Realization of AlN nanowire-based light emitting diodes for UV-C emission

Remy Vermeersch

THÈSE

Pour obtenir le grade de

DOCTEUR DE L'UNIVERSITÉ GRENOBLE ALPES

École doctorale : PHYS - Physique
Spécialité : Physique de la Matière Condensée et du Rayonnement
Unité de recherche : PHotonique, ELectronique et Ingéniérie QuantiqueS, CEA et l'Insistut Néel, CNRS

Réalisation de diodes électroluminescentes à base de nanofils d'AlN pour l'émission dans l'UV-C

Realization of AlN nanowire-based light emitting diodes for UV-C emission

Présentée par :

Rémy VERMEERSCH

Direction de thèse :

Bruno DAUDIN INGENIEUR HDR, Université Grenoble Alpes	Directeur de thèse
Julien PERNOT PROFESSEUR DES UNIVERSITES, Université Grenoble Alpes	Co-directeur de thèse

Rapporteurs :

Maria TCHERNYTCHEVA
DIRECTEUR DE RECHERCHE, CNRS Ile-de-France
Andreas WAAG
PROFESSEUR, Technische Universität Braunschweig

Thèse soutenue publiquement le **17 janvier 2023**, devant le jury composé de :

Maria TCHERNYTCHEVA DIRECTRICE DE RECHERCHE, CNRS Ile-de-France	Rapporteure
Andreas WAAG PROFESSEUR, Technische Universität Braunschweig	Rapporteur
David FERRAND PROFESSEUR DES UNIVERSITES, Université Grenoble Alpes	Président
Fabrice SEMOND DIRECTEUR DE RECHERCHE, CNRS Cote d'Azur	Examinateur
Marc HOFFMANN INGENIEUR DOCTEUR, OSRAM Opto Semiconductors	Examinateur

Invités :

Pierre TCHOULFIAN
INGENIEUR DOCTEUR, Aledia

Remerciements

Je souhaite vous remercier pour l'intérêt que vous portez à ma recherche et qui vous aura motivé à ouvrir ce document, lire mes mots, explorer mes travaux, developper vos idées.

Je souhaite remercier mes encadrants Bruno, Julien et Gwenolé, pour m'avoir transmis des savoirs riches et précieux, scientifiquement comme humainement. Puis-je en faire le meilleur usage et m'enrichir encore de bien d'autres.

Je souhaite remercier les chercheur.euse.s, ingénieur.e.s et technicien.ne.s qui m'ont aidé.e.s, appris, ou simplement ouvert à d'autres sujets que les LEDs AlGaN. Je suis chanceux d'avoir eu cet environnement riche, motivant et stimulant, duquel j'ai beaucoup reçu.

Je souhaite remercier mes amis et collègues de tous les jours avec qui j'ai pu partager des moments de gastronomie, de culture et de voyage, de sport, de joie, de déception, de réussite, d'anxiété ou de fatigue.

Je souhaite remercier mes parents, les meilleurs qui soient, qui m'ont façonnés, accompagnés et soutenus, et que j'aime. Remerciez les car sans eux, vous ne liriez pas ces mots à cet instant.

Je souhaite remercier le Rémy du passé, bien different de celui d'aujourd'hui, pour l'audace d'avoir choisi de faire ce qui lui plaisait le plus. Grâce à toi, je suis fier et je n'ai pas de regrets.

Finalement, cette thèse est terminée.

Acknowledgements

I would like to thank you for your interest in my research and for motivating you to open this document, read my words, explore my work and develop your ideas.

I would like to thank my supervisors Bruno, Julien and Gwenolé, for having passed on to me rich and precious knowledge, both scientifically and personally. May I make the best use of it and be enriched by many others.

I would like to thank the researchers, engineers and technicians who helped me, taught me, or simply opened me to other subjects than AlGaN LEDs. I am lucky to have had this rich, motivating and stimulating environment, from which I received a lot.

I would like to thank my everyday friends and colleagues with whom I have been able to share moments of food, culture and travel, sport, joy, disappointment, success, anxiety or fatigue.

I would like to thank my parents, the best there are, who have shaped me, accompanied and supported me, and whom I love. Thank them because otherwise you would not be reading these words at this moment.

I would like to thank the Remy of the past, quite different from the one of today, for the daring to have chosen to do what he liked the most. Thanks to you, I am proud and I have no regrets.

Finally, This thesis is finished.

Résumé

La récente pandémie de SARS-COV2 aura mis en lumière une des nombreuses applications des rayonnements UV : la stérilisation. Dans l'optique de remplacer les polluantes et encombrantes lampes à vapeurs de mercures émettant à 255 nm, la recherche se concentre désormais sur le développement de solutions à l'état solide à base de semiconducteurs. Les diodes électroluminescentes (DELs) en nitrure d'aluminium et de gallium (AlGaN) répondent aux prérequis. En pratique, la réalisation de tels dispositifs en géométrie planaire est limitée par des conductivités électriques réduites et par une difficile extraction de la lumière, entre autres. En réponse, une géométrie alternative et prometteuse est explorée dans le cadre de ma thèse: la géométrie nanofil. Mon travail de thèse a consisté à accroitre les connaissances sur la physique régissant le transport du courant dans les diodes à nanofils d'AlN crûes par épitaxie par jets moléculaires (EJM) ainsi que sur les techniques de croissance et les technologies pour la réalisation de DELs émettant dans l'UV-C.

Dans un premier temps, mon travail s'est concentré sur la croissance et la caractérisation de zones émettrices de photons UV. Des nanofils d'AlN contenant des multi-puits quantiques de GaN ont été crûs. Après caractérisation par microscopie électronique et par cathodoluminescence, les puits d'épaisseur comprise entre 1 et 4 monocouches montrent une luminescence entre 239 et 304 nm. Je me suis également intéressé aux nanofils AlGaN comportant de très faibles compositions en Ga ($< 1\%$) présentant des propriétés optiques très différentes de celles d'alliage standard, régies par une forte localisation de l'exciton autour d'amas d'AlGaN.

Dans un second temps, j'ai travaillé à l'amélioration du dopage de type n des nanofils d'AlN avec du silicium. Grâce aux caractéristiques électriques (I-V), la conductance des nanofils a été mesurée. Elle décrit une courbe en cloche en fonction du dopage, typique de phénomènes d'autocompensation. Une étude approfondie du transport électrique en fonction de la température a aussi permis d'établir qu'une part significative des dopants restait en site Al avec une énergie d'ionisation de 75 meV, contrairement au donneur profond qui communément est identifié avec une énergie de 270 meV.

Dans un troisième temps, j'ai étudié les propriétés de transport électrique de jonction p-n d'AlN pour différents dopages et structures, par mesures I-V et par courant induit par faisceaux d'électrons (EBIC). Toutes les diodes montrent des comportements rectifiant typiques de jonctions pn. En revanche, la présence d'une barrière tunnel limitant l'injection de trous à fortes tensions ($V > 6$ V) a été mis en évidence. En corrélant les mesures I-V, EBIC, CL et d'électroluminescence (EL), une structure et des paramètres de croissance optimum ont été identifiés.

Finalement, j'ai réalisé un dispositif DEL à 285 nm. Les différentes DELs testées montrent une bonne reproductibilité ainsi qu'un comportement de diode prometteur. L'intensité de luminescence est proportionnelle au courant injecté et la luminescence des défauts reste très faible même à très haute tension. Une efficacité quantique externe a pu être mesurée à environ 5.10^{-3} %, limitée principalement par un difficile compromis entre injection électrique et extraction des photons.

Abstract

The recent SARS-COV2 pandemic has highlighted one of the many applications of UV radiation: sterilization. Aiming at replacing bulky and environmentally hazardous mercury lamps emitting at 255 nm, research is directed towards the development of solid-state solutions based on semiconductors. Aluminium gallium nitride (AlGaN) light-emitting diodes (LEDs) meet the requirements. In practice, the realization of such devices in planar geometry is limited by low electrical conductivity due to deep dopants and by difficult light extraction. In response, a promising alternative is being explored in my thesis: the nanowire geometry. My thesis work consisted of increasing the knowledge on the physics governing the current transport in AlN nanowire diodes grown by molecular beam epitaxy as well as on the growth techniques and technologies in order to allow the realization of deep UV LEDs.

Firstly, my work focused on the realization and characterization of active areas emitting in the deep UV. AlN nanowires containing ultra-thin GaN quantum wells were grown. After transmission electron microscopy observations and cathodoluminescence (CL) measurements, quantum wells with thicknesses between 1 and 4 GaN monolayers are identified and show emission between 239 and 304 nm. I also studied AlGaN nanowires with very low Ga compositions ($< 1\%$). The observed optical properties are very different from those of standard alloys with a spectrally broad emission, governed by a strong exciton localization on AlGaN clusters.

Secondly, I was interested in the n-type doping of AlN nanowires with silicon. Using current-voltage characteristics (I-V), the conductance of nanowires was measured. It exhibits a bell-shaped curve as a function of doping, typical of self-compensation phenomena. A detailed study of the electrical transport as a function of temperature also established that a significant part of the dopants remained in Al site with an ionisation energy of 75 meV, in contrast to the deep Si donor with an energy of 270 meV commonly reported.

Thirdly, I studied the electrical transport properties of AlN pn junctions for different doping range and designs, by I-V and electron beam induced current (EBIC) measurements. All diodes show typical rectifying behaviour of pn-junctions. However, the presence of a tunnel barrier limiting the injection of holes at high voltages ($V > 6$ V) has been demonstrated. Furthermore, by correlating I-V, EBIC, CL and electroluminescence (EL) measurements, optimal structure and growth parameters were identified.

Finally, I realized a broadband LED centered at 285 nm. The different LEDs tested show good reproducibility as well as promising diode behavior. The luminescence intensity is found to be proportional to the injected current and luminescence of defects remains very low even at very high voltage. An external quantum efficiency could be measured at about 5.10^{-3} %, mainly limited by the difficult compromise between electrical injection and photon extraction.

Table of contents

Introduction **1**

UV light: Generalities and Applications . . . 1
Technological path and performances . . . 4
This thesis and its motivations . . . 11

1 III-Nitride materials: Basics and growth **15**
1.1 Generalities about nitride semiconductors . . . 16
1.1.1 Crystal structure . . . 16
1.1.2 Electronic properties . . . 19
1.2 Basics of growth of III-Nitrides . . . 22
1.2.1 Introduction to epitaxy of III-Nitrides . . . 22
1.2.2 From layers to nanowires . . . 25
1.2.3 Growth techniques . . . 27
1.3 Characterization techniques . . . 31
1.3.1 Electron microscopy . . . 31
1.3.2 Energy dispersive X-ray spectroscopy . . . 32
1.4 Summary of Chapter 1 . . . 33

2 From the material to the LED **37**
2.1 Physics of light emitting diodes . . . 38
2.1.1 Electrical transport in doped semiconductors . . . 38
2.1.2 The pn-junction as building block . . . 42
2.1.3 Light emission mechanisms . . . 44
2.1.4 Performance and figures of merit . . . 45
2.1.5 LED architectures . . . 47
2.2 Processing of the NWs . . . 49
2.3 Characterization techniques . . . 50
2.3.1 Current-Voltage characteristics . . . 50

2.3.2 Electron beam based techniques . . . 52
2.4 Summary of Chapter 2 . . . 55

3 Controlling light emission in the UV-C range in AlN NWs 57
3.1 Routes to UV-C emission . . . 58
3.1.1 AlGaN based structures . . . 58
3.1.2 Nanowires specificity . . . 59
3.1.3 Binary heterostructures . . . 59
3.2 GaN wells into AlN barriers . . . 60
3.2.1 Standard growth . . . 60
3.2.2 Alternating fluxes . . . 63
3.3 Ga doped AlN NWs . . . 69
3.3.1 Beyond GaN wells . . . 69
3.3.2 Structural and optical properties of Ga doped AlN NWs. . . . 72
3.3.3 At the edge of alloying . . . 76
3.4 Summary of Chapter 3 . . . 78
3.4.1 Conclusion on active area realization . . . 78
3.4.2 To go further . . . 78

4 Unraveling transport mechanisms in Si doped AlN NWs 81
4.1 A difficult n-type doping of Al-rich AlGaN thin films . . . 82
4.1.1 General state of the art in Al-rich AlGaN and AlN . . . 82
4.1.2 Substitutional or DX state . . . 82
4.2 Structural study of AlN:Si NWs . . . 84
4.2.1 Growth and morphology . . . 84
4.2.2 Quantification of Si concentration by EDX . . . 86
4.2.3 Raman spectroscopy . . . 87
4.3 Coexistence of shallow donor and DX center . . . 87
4.3.1 Basic electrical characterizations . . . 87
4.3.2 Shallow donor and DX center . . . 88
4.3.3 Effect of Fermi level pinning on the electrical conduction . . . 90
4.4 Study of space charged limited current regime . . . 94
4.4.1 Trap assisted space-charge limited current theory . . . 94
4.4.2 Additional trap in highly Si-doped AlN NWs: a new DX state? . . . 96
4.5 Summary of Chapter 4 . . . 100
4.5.1 Conclusion on Si-doping of AlN NWs . . . 100
4.5.2 To go further . . . 101

5 AlN Nanowires pn-junction: Doping and contact optimization 105
5.1 Do AlN pn-junctions exist? . . . 106
5.2 Influence of dopants and their concentration . . . 107
5.2.1 Mg/In codoping of p-AlN . . . 107
5.2.2 Balance between n and p sides . . . 111
5.3 Top interface and hole injection issue . . . 116
5.3.1 Fowler-Nordheim tunneling . . . 116
5.3.2 On the identification . . . 118
5.3.3 Influence of p-GaN cap . . . 119
5.4 Summary of Chapter 5 . . . 121
5.4.1 Conclusion on AlN NWs pn-junctions . . . 121
5.4.2 To go further . . . 121

6 UV light emitting diodes from AlN nanowires 123
6.1 Insight about deep UV LEDs . . . 124
6.1.1 State of the art in thin films . . . 124
6.1.2 Reports on NW based UV LEDs . . . 125
6.2 Design of the device . . . 126
6.3 Device characterizations . . . 127
6.3.1 Optical characterization . . . 127
6.3.2 Electrical characterization . . . 128
6.3.3 Electro-optical characterization . . . 130
6.4 Light emission behavior . . . 132
6.4.1 Electroluminescence . . . 132
6.4.2 About efficiency . . . 133
6.5 Summary of chapter 6 . . . 135
6.5.1 Conclusion on AlN NWs LED . . . 135
6.5.2 To go further . . . 135

Conclusion 139

Publications and Communication 144

Bibliography I

Appendix A MBE calibrations by RHEED XXXI

Appendix B Quantification of carrier density XXXV

Appendix C NextNano simulations XXXIX

Appendix D Literature review on transition energy level of AlN:Si XLI

Appendix E Growth on TiN buffer on (111)-Si XLIII

General Introduction

For decades, researchers have been working to discover physical mechanisms that have paved the way for the development of new technologies, which changed our societies. Among these breakthroughs, those resulting from the work of Akasaki, Amano and Nakamura were particularly impactful, and earned them the Nobel Prize in 2014. Their works have led to the understanding of various phenomena in GaN-based materials, from which visible light emitting diodes have greatly benefited. Today challenges remain numerous, ultraviolet domain being one of the most impactful among them.

UV light: Generalities and Applications

Ultraviolet radiation

Ultraviolet — literally *beyond violet* — light corresponds to an electromagnetic radiation which wavelength is comprised between 10 nm and 400 nm. It is composed by several subparts: Vacuum UV from 10 nm to 200 nm, UV-C from 200 nm to 280 nm, UV-B from 280 nm to 315 nm and UV-A from 315 nm to 400 nm. Deep UV (DUV) can also be used to describe radiations between 200 nm and 300 nm. Natural UV light is produced either by electric arcs or by very hot materials through black body emission. In particular, the sun emits around 10% of its light in the UV range which is more or less absorbed by the atmosphere. Only a small fraction of this UV light (predominantly UV-A), reaches the ground and causes human's skin darkening.

UV is not just a way to tan, depending on the wavelength a wide variety of applications exists, as illustrated in the figure 1. As an amateur photograph myself, I wanted to share two pictures related to UV below. Even if not considered as an application — it *only* allows skin damage investigation —, science can also be aesthetically pleasing as these photographs and bring something else than pure brain activity. Among all of these applications, one has become particularly attractive as the recent *COVID-19* pandemic has hit our societies.

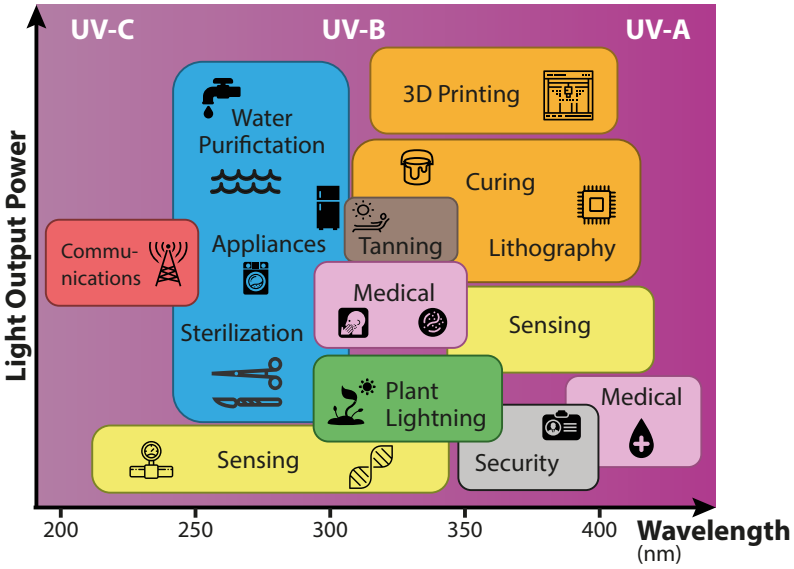

Figure 1: Applications of UV radiations. Redrawn from [1].

UV light reflection photograph of a body with (left side) and without (right side) sunscreen.
From M. Stern and P-L. Ferrer.

Photograph of a *coreopsis* under UV light.
From C. Burrows for *Sciences et Avenir*.

Disinfection and sanitation purposes

UV radiations have the particularity of causing photo-chemical reactions to happen in molecules by giving them enough energy to break bounds, thus rearranging their structure. This property is being exploited in chemistry to activate the polymerization of photopolymers, for instance used in dentistry or in coatings and photoresists.

In a similar manner, DNA and RNA nucleotides can experience a dimerization (a kind of polymerization with only two monomers) under UV light. In DNA, the hydrogen bound between nucleotides from the two strands breaks and two adjacent bases will bound together (figure 3a). It can also results in cross-linking of strands originating from different DNA and/or RNA.

As a result of all these mutations, microorganisms experience effects causing them to die or preventing their replications. Only some wavelengths are absorbed by nucleotides and are therefore targeted for disinfection purposes. Absorbance spectra, shown in figure 3b, indicate that UVs are absorbed mainly below 290 nm with a peak at around 260 nm where three out of four nucleotides are sensitive. Thus, depending on the UV dose, the bacteria and its environnement, it is possible to drastically reduce the number of microorganisms after few tens of secondes of exposition to the radiation [2]. Therefore, UV light is being used for water purification, sterilization of medical tools and appliances prior to be widely used during the SARS COV-2 pandemic in public transports and other places at risks.

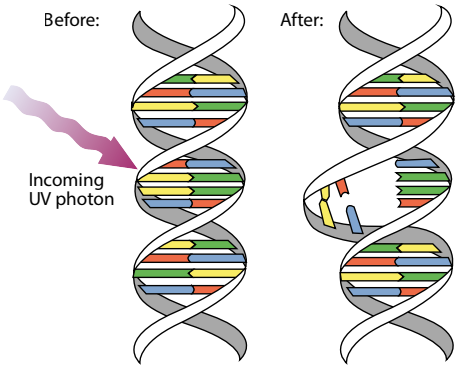

(a) UV photons acting on DNA nucleotides and provoking their cross-linking.

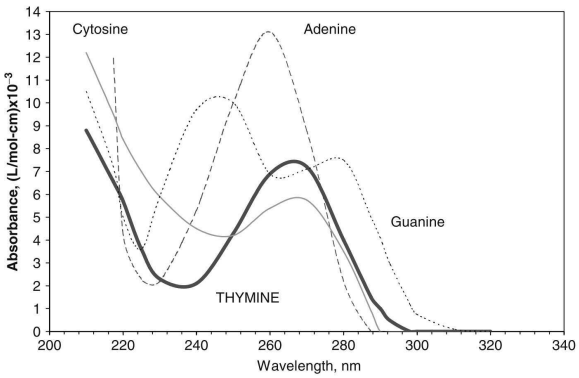

(b) Absorbance spectra of the four DNA nucleotides [3].

Figure 3: UV effects on DNA and absorption spectra of its components.

Health-related effects

If this light is particularly efficient at damaging DNA, it can be harmful for human and requires careful usage. In addition to premature aging of skin cells and its pure aesthetic consideration, overexposure to UV-A and B causes sunburns and skin cancers. Regarding the eyes, UV-B and UV-C (310 nm to 260 nm) are responsible for cataracts and other damages to cornea and retina such as simple, but painful, cornea inflammation (photokeratitis)

UV-C is the most energetic of the three UV subparts and therefore is the most dangerous radiation. However, as the emission wavelength decreases, penetration depth of the photons also decreases. As depicted on figure 4, a 222 nm radiation is stopped before entering the epidermis and the cornea whereas a light at 300 nm in the UV-B can reach the dermis and get through the pupil. Therefore exposure to UV-B will be much more harmful for human health than exposure to far UV-C. For these reasons, standard UV lamps emitting at 254 nm must be used with care when people are nearby. The reduction of emission wavelength could open up new applications in the field of sanitation and allow

their use on human skin for example.

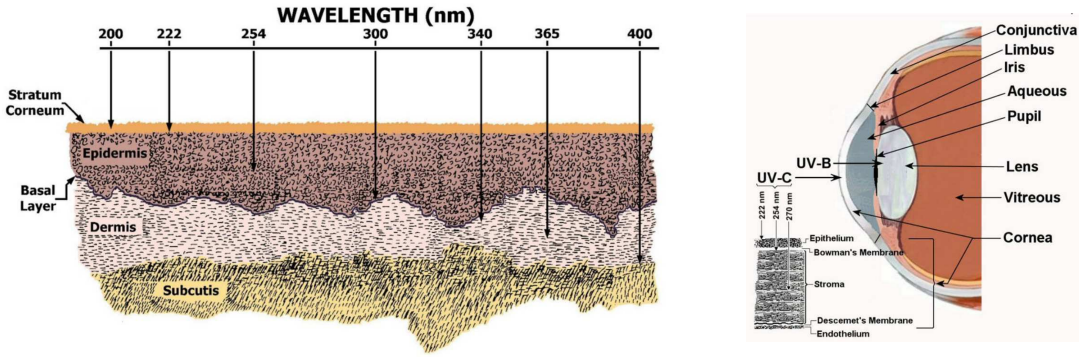

Figure 4: Sketch of UV penetration in skin tissues and eye at different wavelengths [2].

UV market

Because of the Sars Cov-2 pandemic, there has been an increasing need for UV emitters over the last two years, which has led to a growth in the market. Currently, two types of UV emitters can be purchased: lamps and light emitting diodes. Their technical differences will be detailed in the next section. Historically, UV lamps were the first ones to be used and therefore logically represent the majority of the market. According to a study by Yole Developpement [4], the global UV lighting market was worth $400M in 2008 with only a few millions of dollars for UV LEDs. The market has reached $1B in 2019, LEDs accounting for nearly a third of it. As the demand increases, the forecast is for an annual growth rate of 15 to 20% to reach between $1.7B and $8B in 2027 [4–6]. However, the majority of this growth is expected to be driven by LED products with total revenue increasing by 17 times between 2019 and 2025 [7].

To meet the demand, the market is split between a large number of suppliers. The two largest are Signify (*Netherlands*), which sells UV lamps and Seoul Viosys (*South Korea*), which sells LEDs. Behind them are many players mainly from China, and the USA, who want a share of this growing market.

Technological path and performances

After reviewing general considerations about UV light, its applications and current market, let us address the question of the production of such light and clarify differences between lamps and LEDs.

UV Lamps

In lamps, UV light is produced by the de-excitation of molecules that are originally in an excited state. In conventional discharge lamps, an electric discharge is sent through a gas to ionize it. In doing so, the gas molecules are put into an excited state and can de-excite, producing photons whose energy depends on the molecule. Some famous lamps use this principle, such as sodium vapour lamps (orange) and neon lamps (red). Fluorescent lamps, which are increasingly rare nowadays, are actually low pressure mercury lamps emitting in the UV and covered by a phosphor layer which converts UV light into white light. Mercury exhibits many emission bands ranging from 184 nm up to 650 nm, and by adjusting the amount of mercury present in vapour phase, it is possible to adjust the emission wavelength. Low pressure mercury lamp is a high purity 254 nm light source.

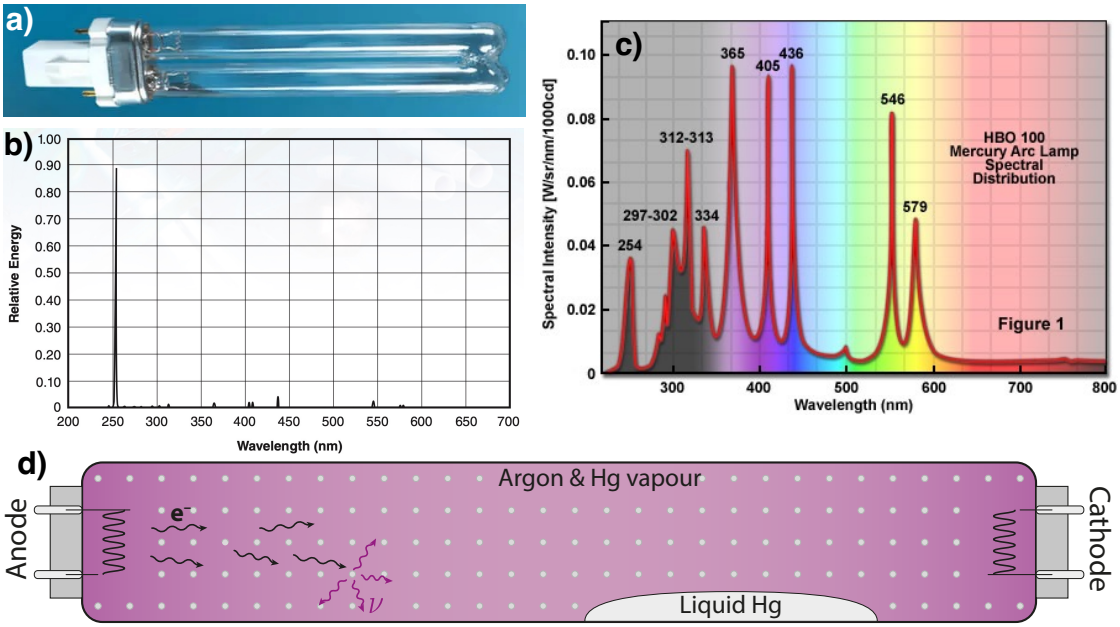

Figure 5: a) Image of a low pressure mercury lamp and b) its emission spectrum from Ushio America. c) Emission spectrum of a high pressure mercury lamp from Zeiss HBO 100. d) Cartoon of the working principle of mercury lamps.

If they can be easily manufactured, they are also quite efficient and of reasonable size. Nevertheless, they have many drawbacks. Life span of such devices is of only few thousands hours. They cannot be miniaturized and implemented in small devices and some minutes are required before their switching on. Most of all, they are fragile and contain mercury which is highly hazardous for the environment and people.

Recent public policies aim to reduce the use of mercury. The EU banned its use in lighting in 2015. In 2013, Minamata convention was established in order to organize the progressive ban in the world, which is now effective since 2020. Manufacture, import and

export of mercury-containing products are now supposedly forbidden in the 127 countries that are party of the convention. However, low pressure mercury lamps emitting in the UV are excluded, at least for the time being.

Figure 6: UV lamp used to disinfect a bus during Covid-19 pandemic.

Other species than mercury can be used to produce UV. Excimer lamps and laser are comparable in term of functioning and can have different emission wavelength in the whole UV. Instead of using gases, atoms from certain diatomic molecules (so called excimers) are able to bound or unbound under an electric excitation, giving rise to light. Noticeably, KrCl (222 nm), ArF (193 nm) are used as light source for disinfection or in research laboratories. Their drawbacks are the relative low efficiency ($\sim$ 1%), high voltage, short life-span and the use of rare gases which kills the viability of this technology for the large needs.

Solid state solutions

Contrary to lamps, solid state devices are fully based on semiconductors and, among them, LEDs are based on a mechanism called electroluminescence. When electrons flow in a semiconductor driven by a electromagnetic force, they may get to lower energy states releasing their energies in the form of light. This process can be highly efficient and cost-effective as the majority of the charges can be turned into light. This kind of device presents several advantages with respect to lamps. LEDs require smaller operating voltages and have no turn on time. Adjusting the current allows to tune the optical output power of the device. Their emission spectrum is narrow over few nanometers without requiring filters.

Their life span is very long. They are free of hazardous materials. Moreover, they can have reduced sizes and be better integrated into other systems of our today's life. These assets are particularly important for the democratization of UV disinfection products and their integration into common objects such as fridge or tap. All of this make solid state devices a solution of choice for production of light in general and UV light particularly.

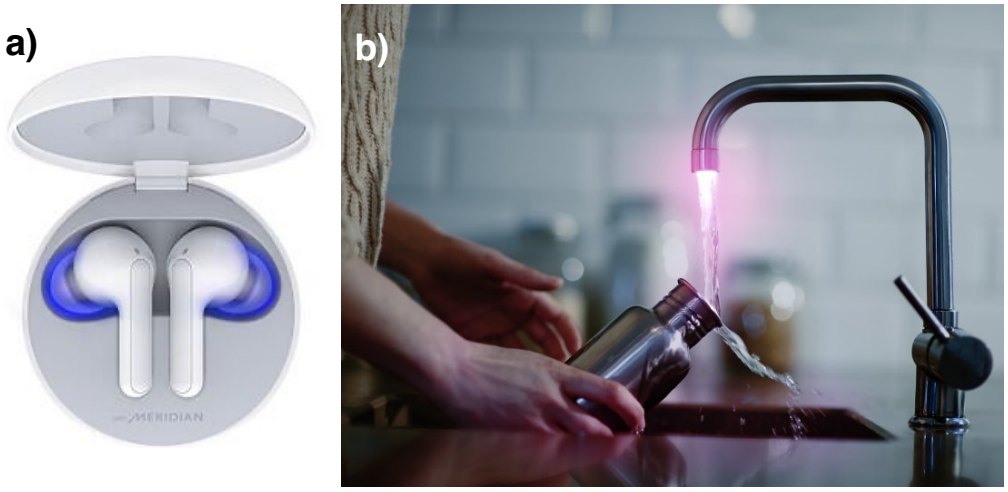

Figure 7: a) UV LEDs embedded in headphone case in the LG Tone. b) Concept of UV LEDs embedded in water tap for disinfection of everyday water, from Osram.

State of the art and current limitations

Thanks to its direct and tunable bandgap, AlGaN alloy is a material particularly suited for this purpose. Its energy band gap varying from 3.5 eV (360 nm) and up to 6 eV (200 nm) allows to cover UV-A, UV-B and UV-C. However, efficiencies of AlGaN based UV emitters are still limited and require further research and development. Blue LEDs made of InGaN alloy reaches extremely high efficiencies and performances, with 90% of injected electrons converted into photons. Adding AlN into GaN leads to a reduction of the emission wavelength, associated to a reduction of device performance, as shown in figure 8. Efficiency drastically decreases, with a peak at 275 nm coming from the large efforts of research centers to improve this wavelength in particular for all the reasons mentioned above.

A standard AlGaN UV-LED structure is represented in figure 9 along with some of its associated challenges. Devices are grown on sapphire substrate, transparent to UVs and inexpensive thanks to the advent of blue LEDs. A n-type doping AlGaN layer is first grown to provide electrons to the $Al_xGa_{1-x}N$ / $Al_yGa_{1-y}N$ multiple quantum wells area. On top of which are grown p-type doped AlGaN and GaN layers in order to provide holes. Increasing AlN molar fraction in the AlGaN layers allows to reach deeper UV but at a certain cost.

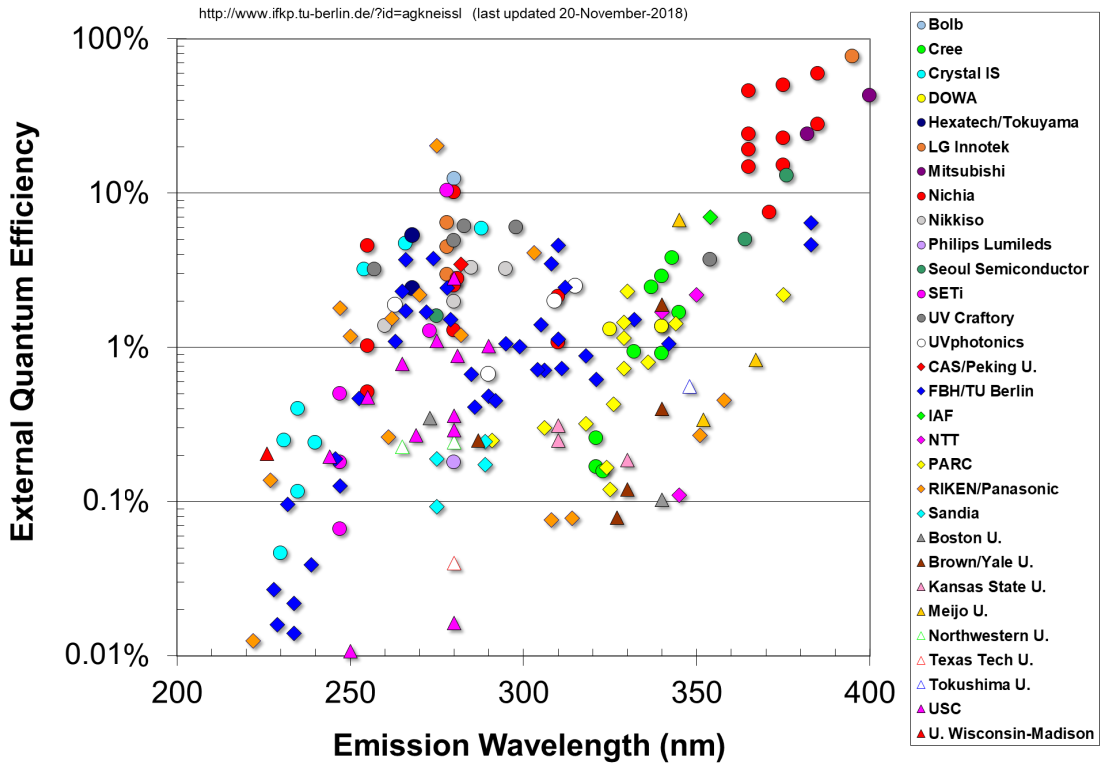

Figure 8: Reported external quantum efficiencies (EQE) of UV LEDs from [8]. Last updated on November 20th 2018. y-axis is on a log scale.

Because of deeper dopant energy levels, resistivity of n-type and p-type AlGaN thin films increases which increases losses by Joule effect and limits spreading of the current over large areas [9–12]. Large extended defect densities can also kill radiative recombinations, although important progress have been achieved allowing to reduce this effect. This point is not considered as a major issue anymore but still requires complex growth techniques to achieve acceptable crystal quality [13–16]. Moreover, a non-negligible part of UV photons are lost before they can exit the structure. Indeed, a compromise between adequate metal contacts and light extraction is to find. In addition, photons can be trapped because of a low difference in refractive index, favouring internal reflections.

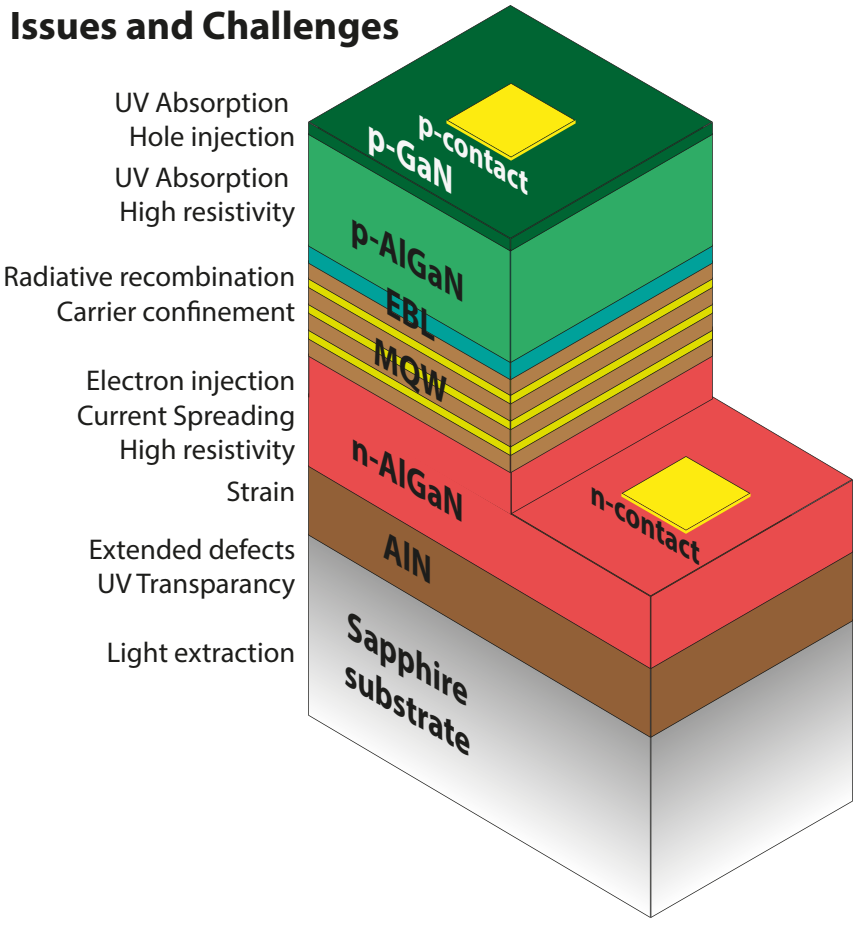

Figure 9: Schematics of a standard UV-LED structure with its issues.

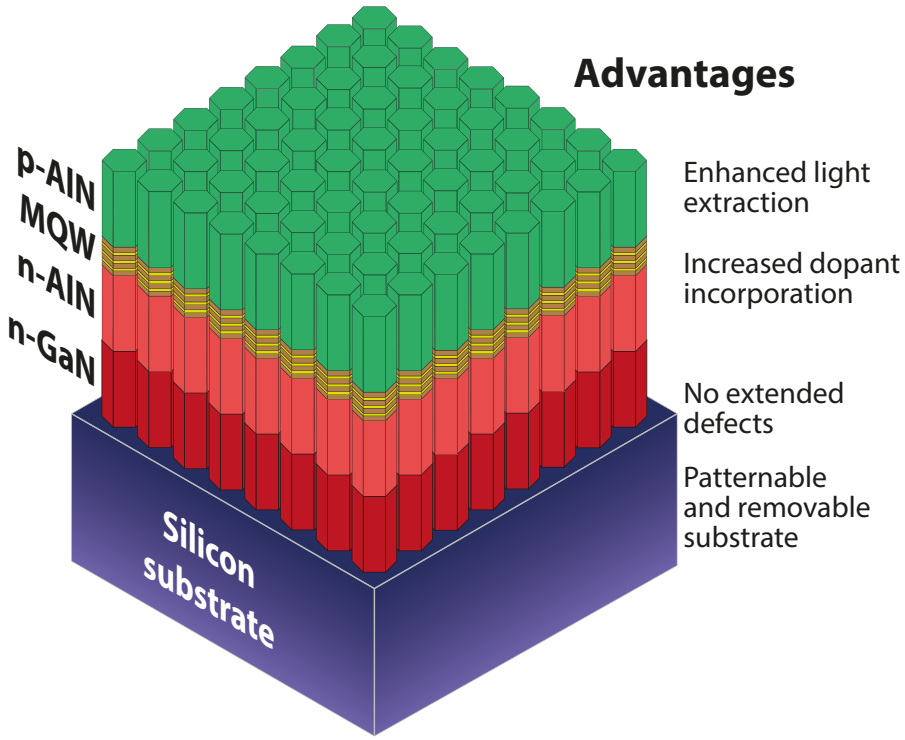

Figure 10: Schematics of a NW based UV-LED structure studied in this work and its advantages.

This thesis and its motivations

Alternative structure for improved efficiency: Nanowires

In the light of the actual limitations of the state-of-the art, a different approach is being investigated using 3D objects. Nanowire structures have several advantages with respect to 2D layers as presented in figure 10.

Because of their unique formation mechanism, self-catalyst nanowires are free from extended defects. Therefore, they are objects which can be studied without questioning about the influence of dislocations on diverse properties.

Moreover, nanowires exhibit a large surface to volume ratio which allows strain relaxation at the side-walls. This feature allows the reduction of strain induced by foreign atoms incorporation and is responsible for an increased solubility limit of dopants in the crystal. This property is highly beneficial in wide bandgap semiconductors as dopants are deep and require larger concentration to overcome their poor ionization ratio at room temperature.

In addition, this geometry can be beneficial to light extraction, primarily due to an effective refractive index closer to the environnement. It is further possible to pattern the nanowire array to create photonic crystal and enhance the out-coupling of the light.

In spite of all these advantages, research is scarcer — yet no less interesting — and drawbacks exist such as a variability from wires to wires and somewhat challenges in technological solution for processing the device.

Scientific questioning

Questions remain numerous and must be addressed in order to compare the two devices geometry. The followings will pave the way of this manuscript.

(i) How can UV emission be achieved from an AlN nanowire? Which solution is the more adequate to NWs?

(ii) How does Si incorporation change AlN nanowires structural and electrical properties?

(iii) In what state are Si donors in AlN nanowires?

(iv) What are the electric transport mechanisms at play in AlN nanowires pn-junction?

(v) Is the realization of an AlN nanowires LED possible? With which performances?

Organization of the manuscript

The organization I have chosen for this manuscript is as follows:

Chapter 1 focuses on giving the key elements on III-Nitride family and the specificities of GaN and AlN materials. Crystal structure and electronic properties are presented.

Growth basics and different techniques are also exposed and discussed. A focus on structural characterization techniques used in this work is also done.

After looking at the material, **Chapter 2** is concerned with device properties and their link with the material. The physics of light emitting diodes is presented from the electrical transport and light emission mechanisms up to state-of-the-art architectures for UV emission. Characterization of the devices were performed by several techniques presented in this chapter as well.

Chapter 3 is the first chapter containing results. It looks at different way of achieving controlled and efficient UV-C emission from AlN nanowires. A first part is dedicated to the control of monolayer thin GaN quantum wells. Leveraging adatom diffusion and self-limiting processes, it is possible to manufacture ultra-thin layers and achieve emission down to 239 nm. In a second time, the unexpected large exciton localization in low gallium content AlGaN is described. With gallium concentration below one percent, these AlGaN nanowires exhibit good UV emission properties in a large spectral range. It is also a much simpler realization than a multi-quantum well structure.

Chapter 4 dives into the electrical properties of silicon doped AlN NWs. The n-type doping properties of Si are known to be complex because of early self-compensation and DX transition. In this work, Si is found to be a shallow donor in a certain doping range. Taking advantages of electrical transport mechanisms, it is stated that Si could be in three different sites within the lattice: one shallow donor and two deeper states.

Chapter 5 studies the influence of doping concentration on electrical properties of pn-junctions. This chapter allows the optimization of the different section of the diode. Its design is also discussed as top interface between metal contact and p-AlN or p-GaN is of particular importance and limiting the device performances.

In conclusion to this thesis work, entitled *Realization of AlN NWs based UV-C LED*, **Chapter 6** presents the realization of an AlN NWs LED and its global properties. Electrical and optical ones are briefly exposed as they are discussed in previous chapters. Electro-optical experiments are performed and show good characteristics for light emission. Electroluminescence at 285 nm is successfully achieved and discussion on thee device performance is done to pave the road of future works.

This work has been carried out between *CEA IRIG* and *CNRS Neel Institute* both in Grenoble. In the first one, I was growing my samples in a molecular beam epitaxy (MBE) system and assisting for its maintenance. Structural characterizations occurred in *CEA PFNC* mainly by scanning electron microscopy. Transmission electron microscopy would not have been made possible without the help of Dr. J-L. Rouviere (senior scientist) and F. Castioni (PhD student). Dr. E. Robin (senior scientist) performed energy dispersive X-ray spectroscopy experiments and analysis in both SEM and TEM. Its work and rigour

were essential in this work. Raman spectroscopy experiments were done by Dr. A. Cros in the Materials Science Institute from the University of Valencia, Spain.

In Neel Institute, I performed electrical and optical characterizations and manufactured the studied devices. Current-voltage, cathodoluminescence, electron-beam induced current and electroluminescence experiments were carried out by myself. I was trained and assisted by Dr. F. Donatini, research engineer in charge of the different setups. The use of Neel Institute clean room *NanoFab* was a great asset in this work as it made easy the realization of LEDs and test structures.

CHAPTER 1

III-Nitride materials: Basics and growth

This chapter aims at giving general knowledge about III-Nitrides materials. GaN and AlN crystal structures and their specificities will be presented and discussed in relation with this work. Basics of growth of these materials are also given. Structural characterization techniques used will be also presented.

Contents

1.1 Generalities about nitride semiconductors 16
1.1.1 Crystal structure 16
1.1.2 Electronic properties 19
1.2 Basics of growth of III-Nitrides 22
1.2.1 Introduction to epitaxy of III-Nitrides 22
1.2.2 From layers to nanowires 25
1.2.3 Growth techniques 27
1.3 Characterization techniques 31
1.3.1 Electron microscopy 31
1.3.2 Energy dispersive X-ray spectroscopy 32
1.4 Summary of Chapter 1 33

1.1 Generalities about nitride semiconductors

1.1.1 Crystal structure

III-Nitrides or III-N, refers to a family of semiconductor composed by a nitrogen atom and a third column atom. In the context of this thesis, the focus will be set on aluminum nitride (AlN), gallium nitride (GaN) and the AlGaN alloy, but other semiconductors, namely, indium nitride or boron nitride exist alongside ternary and quaternary alloys. III-Nitrides is a sub-family of the III-V family composed by one element of the third column and one of the fifth column, other than nitrogen, such as phosphorus or arsenide for instance.

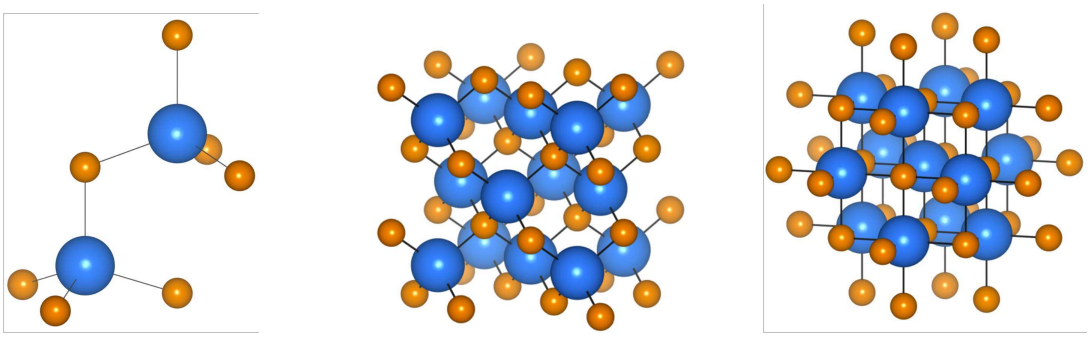

(a) Wurtzite structure (b) Zinc-Blend structure (c) Rock salt structure

Figure 1.1: Representation of the three crystallographic structures of III-N materials. Metal atoms are depicted in blue, nitrogen atoms are depicted in orange.

Crystallography

AlN and GaN exist in three different crystallographic phases:

- **Wurtzite:** It is the most thermodynamically stable structure hence the most widely found, and is the one this work focuses on. It is a hexagonal crystal system, also referred to as the $P6_3mc$ space group, which lattice is represented in 1.1a. Wurtzite phase can be seen as two hexagonal close-packed sub-lattices interlaced and shifted by a vector $< \frac{1}{3}, \frac{1}{3}, \frac{1}{2} >$. Each atom hybridizes into sp^3 configuration, leading to the formation of tetrahedrons: metal atoms are surrounded by three nitrogen atoms and vice-versa. Wurtzite has not as many symmetries compared to other structures thus it exhibits peculiar properties, which will be discussed later on.

- **Zinc Blende:** Sometimes called *cubic* phase, the space group related to Zinc Blende is $F\bar{4}3m$ (1.1b). If its higher symmetry makes Zinc-blende III-V material more convenient for optoelectronic purposes, its challenging growth prevents advances in this direction. Few papers report the growth of cubic GaN by using appropriate substrates

and controlling the growth condition carefully [17–21].

- **Rock Salt:** Not commonly found, rock salt structure is also a cubic structure and requires high pressure and high temperature conditions to be stabilized. Its space group is Fm$\bar{3}$m (1.1c).

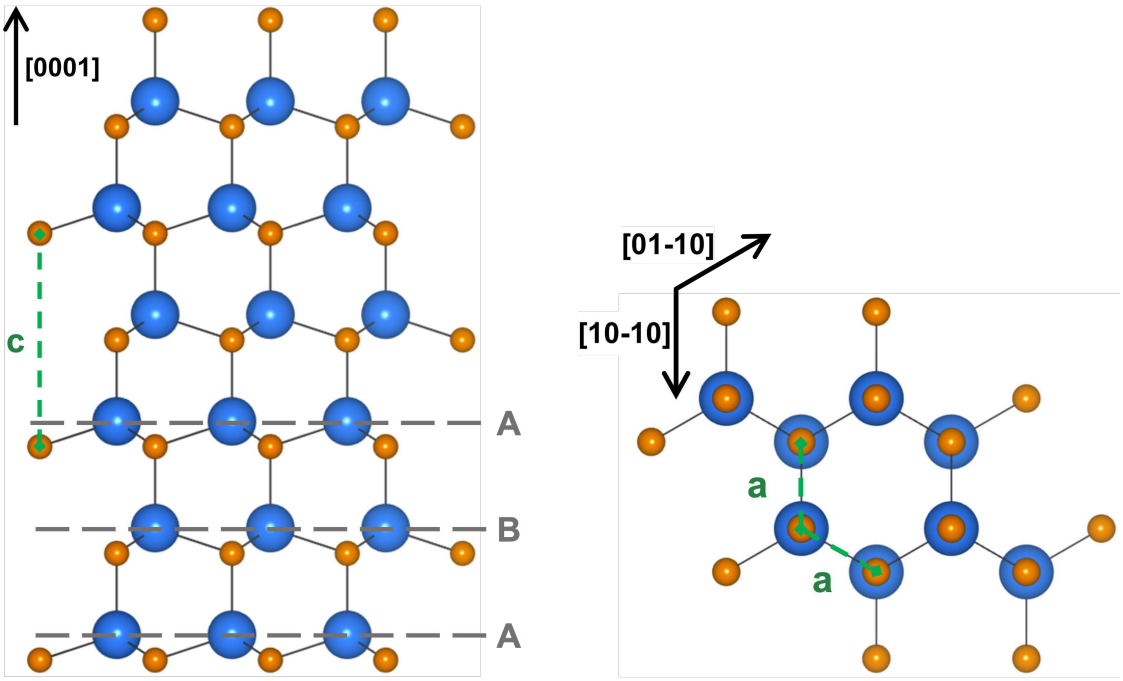

(a) (b)

Figure 1.2: Representation of Wurtzite structure from (a) [10$\bar{2}$0] zone axis and (b) [0001] zone axis. *A* and *B* dotted lines refer to the stacking sequence of the hexagonal structure. Lattice parameters *c* and *a* are shown. Metal atoms are depicted in blue, nitrogen atoms are depicted in orange.

Figure 1.2 presents in details the hexagonal structure. It can be defined by only two lattice parameters: *a* along [10$\bar{1}$ 0] and [01 $\bar{1}$ 0] axis and *c* along [000$\bar{1}$] axis, which represents the "heigh" of the unit cell. Table 1.1 gives the lattice parameters *a* and *c*. One common unit that will be also used in this manuscript is the monolayer (ML). By definition, one monolayer is one single packed layer of atoms hence, in our case it is $c/2$, rounded to 2.5 Å for both AlN and GaN for convenience. Zinc-Blende and Wurtzite structures differ only by a stacking period: ABC-ABC stacking along the [111] axis for cubic structure and AB-AB along the [00.1] axis for hexagonal one (1.2a).

Polarity

The hexagonal structure of III-Nitrides has a distinctive feature: it is non centrosymmetric. In other words, the c-axis [0001] is unique and is in particular different [000$\bar{1}$],

Table 1.1: Lattice parameters for AlN, GaN and InN at room temperature from [22].

	AlN	**GaN**	**InN**
a (Å)	3.112	3.189	3.545
c (Å)	4.982	5.185	5.703

as depicted in figure 1.3. Therefore, depending on the arrangement of the atoms along the c-axis, the structure will be called N-polar or Metal-polar. By convention, the metal polarity refers to the vector pointing from the metal atom to the nitrogen atom along the [0001] (1.3a), and the inverse stands for nitrogen polarity (1.3b).
Several studies have evidenced the importance of polarity on several points. Surface roughness and structural properties [23], impurity incorporation [24, 25], dopant incorporation [26], optical properties [27, 28] are examples of the properties that are influenced by the polarity. X-Ray diffraction [29], potassium hydroxide (KOH) etching, Kelvin probe force microscopy (KPFM) [30] and TEM studies allow polarity determination [31–33].

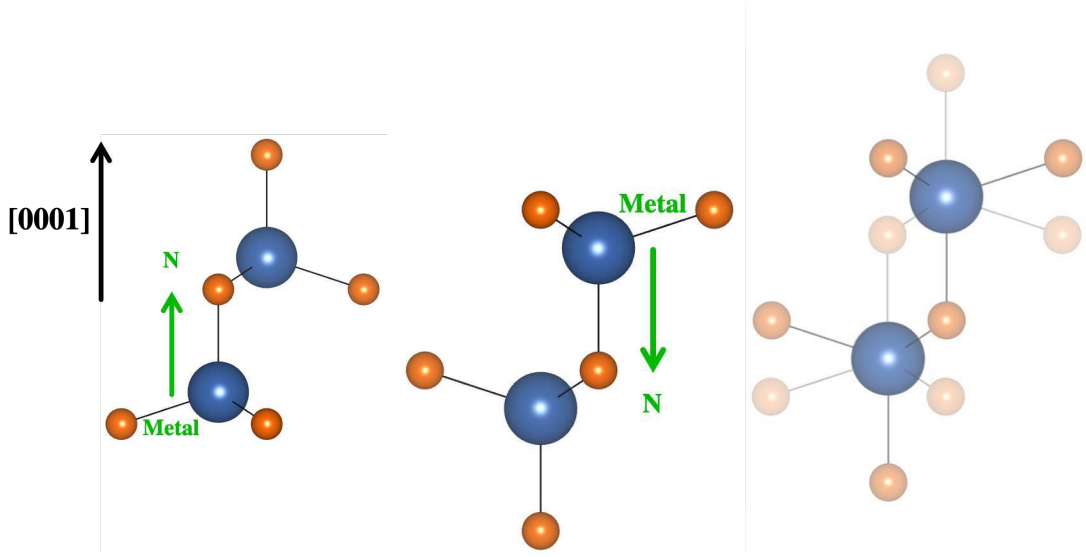

(a) Metal-polar (b) Nitrogen-polar (c) Superposition of the two.

Figure 1.3: Representation of the unit cell view from $[10\bar{1}0]$ zone axis for different polarity. (a) Metal-polar. (b) Nitrogen-polar. (c) Highlights the non equivalence between [0001] and $[000\bar{1}]$ axis where the concept of polarity originates.

If c-plane is particular and remains the main growth direction, other planes are of interest as they can be semi-polar or non-polar and therefore exhibit slightly different behaviors [34–36] (Figure 1.4).

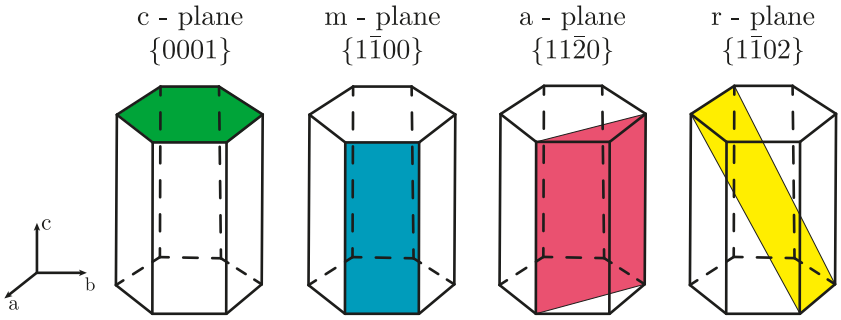

Figure 1.4: Representation of four families of planes in wurtzite structures.

1.1.2 Electronic properties

Energy band gap

Semiconductors of the III-N family have a direct bandgap, meaning that the top of valence band and the bottom of conduction band have the same wave-vector. Specifically, AlN is known for being the semiconductor with the largest direct bandgap (6.2 eV) [37, 38]. It belongs to the family of the ultra wide-bandgap semiconductors ($E_g > 4\ eV$) along with diamond, BN and Ga_2O_3. On its side, with its bandgap of 3.5 eV, GaN belongs to the wide-bandgap semiconductor family [39, 40]. A direct and large bandgap make AlGaN alloy the most suitable optoelectronic material to achieve UV and DUV light emission. Table 1.2 summarizes bandgap energies of wurtzite III-N at room temperature in addition to the corresponding wavelengths while figure 1.5 shows the whole III-N family energy bandgap as function of the lattice parameter a. However, the wide bandgap characteristic makes more difficult to handle impurities and crystal quality.

In order to compute the bandgap of a ternary alloy such as $Al_xGa_{1-x}N$, according to the Al molar fraction x, an empirical model is widely used, derived from Vegard's equation:

$$E_g^{AlGaN} = x \cdot E_g^{\mathrm{AlN}} + (1-x) \cdot E_g^{\mathrm{GaN}} + x(1-x)b \tag{1.1}$$

with b is a bowing factor accounting for the non-linearity of the evolution. Using this equation, one is able to draw the line between two binaries as represented in figure 1.5. Nonetheless, one issue is that the bowing factor can be non-constant with the composition hence difficult to access, especially in III-N and AlGaN. Several values have been reported such as 0.53 eV [19], 0.63 eV [42] for $x < 0.45$ or 1.0 eV[43] and 1.32 eV [44] over the whole range. Despite a lot of efforts, the curve is not well described for composition higher than 50% Al in AlGaN and the situation is even more complex in the case of AlInN.
To expect an emission of light at around 260 nm or 4.75 eV, the composition that is required appears to be $Al_{0.67}Ga_{0.33}N$, or in other words, a ratio of two Al atoms for one Ga atom.

Because of thermal expansion, the lattice size changes with the temperature and so

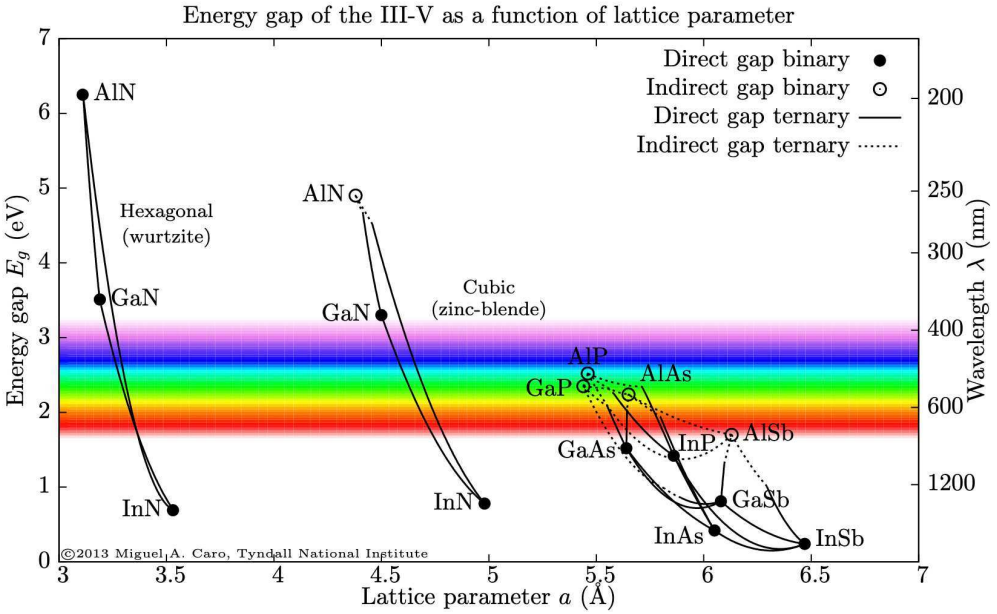

Figure 1.5: Representation of the bandgap energy and the corresponding wavelength of III-V semiconductors as a function of their lattice parameter a, at room temperature. Adapted from [41]

the bandgap with it. The Varshni model predicts the bandgap at a certain temperature depending on few parameters:

$$E_g(T) = E_g(T = 0K) - \frac{\alpha \cdot T^2}{\beta + T} \tag{1.2}$$

where α and β depends on the material and are summarized in table 1.2.

Table 1.2: Varshni parameters, bandgap and corresponding wavelength values for AlN, GaN and InN at room temperature from [22].

	α (meV/K)	β (K)	E_g (eV)	λ_g (nm)
AlN	1.799	1 462	6.20	200
GaN	0.909	830	3.51	353
InN	0.245	624	0.78	1 588

Light polarization considerations

In this section, band structure of wurtzite AlN and GaN is being discussed, especially its consequences on the light polarization. Figure 1.6 shows a schematic representation of the band structure of GaN and AlN near the center of Brillouin zone. In this region, one conduction band (CB) and three valence bands (VB) are present. Because of the absence of symmetry along the c-axis, a degeneracy appears due to crystal field splitting (CF),

corresponding to the p_z orbital, whereas p_x and p_y orbitals are discretized by spin-orbit coupling, giving rise to the two other bands, light hole (LH) and heavy hole (HH). From the transitions between CB and one of the VB result the properties of light, including its polarization. Table 1.3, summarizes the energy involved in the diagram. In the case of GaN, topmost valence band is HH band, which results in most of the transition being made perpendicularly to the c-plane, in the so-called transverse electric (TE) polarization. Unlike GaN, AlN topmost valence band is CF band due to its strong ionic bonding [45]. Therefore, electronic transitions will be mainly done along the c-axis causing light polarized along the transverse magnetic (TM) polarization.
In concrete terms, TE-polarized light will be propagating along the c-axis and will be able to escape the device from the top or bottom part, while TM-polarized one will propagate in-plane, making its extraction more difficult in 2D layers. Here however, nanowire geometry can be a feature of great interest in order to increase the extraction of light allowing the light to exit the structure by the sidewalls preferentially.

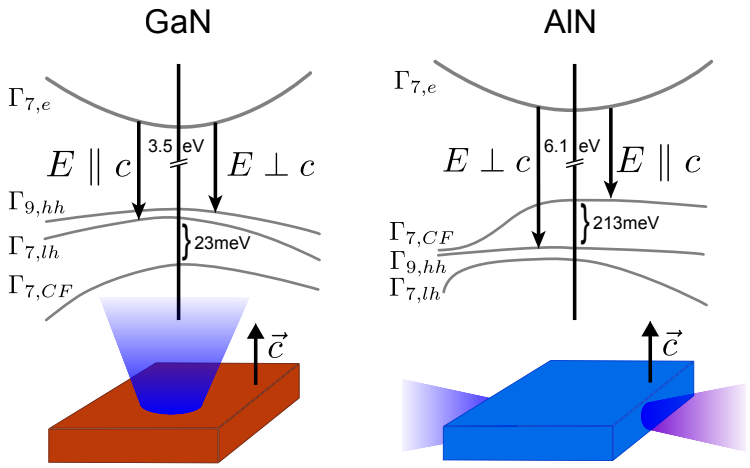

Figure 1.6: Band structure of GaN and AlN semiconductor around Γ point from [46]. $\Gamma_{7,\mathrm{CF}}$ refers to the band splitting by crystal field.

Table 1.3: Band structure parameters for AlN and GaN from [1].

	AlN	**GaN**
Δ_{cr} (meV)	-200	10
Δ_{so} (meV)	19	17

Knowing the composition at which an AlGaN alloy will change its light polarization can be useful. However, lots of discrepancies have been reported on the composition switching from 8% up to 83% [46–50] depending on the strain or the film thickness, or on the electric field in the structure.

Polarization effects

Other consequence of the asymmetry of wurtzite crystal is the creation of spontaneous polarization arising from the fact that N atoms are more electronegative than metal atoms ($\chi_N \approx 3$ and $\chi_{\text{metal}} \approx 1.5$). Electronic densities are therefore non-evenly distributed between atoms, leading to a spontaneous electric field within the crystal. This effect cancels out from one neighbor to the other but at the boundary of the material, charges accumulate and are not compensated. The spontaneous polarization coefficient is reported to be of $-90\ mC/m^2$ in AlN and $-34\ mC/m^2$ in GaN [22, 51].
One can leverage this effect as it generates two dimensional hole or electron gas (2DHG / 2DEG) at interfaces, allowing to reach a very low in-plane sheet resistance. AlGaN-based high electron mobility transistors (HEMT) take advantages of this effect.

In a complementary way, displacing atoms by the strain can modify the distribution of charges: this is the piezoelectric effect. However, contrary to InGaN alloys, in which the difference in lattice parameter is high, AlGaN is not very sensitive to this phenomenon and it will be negligible in our nanowire structures.

1.2 Basics of growth of III-Nitrides

During this work, growth of AlGaN NWs were achieved by the mean of molecular beam epitaxy. This section aims at giving key elements to understand and dive into epitaxy of III-Nitrides. If this section is not meant to explain all the physic and complex mechanisms involved in the growth of nitrides, I would like the reader to understand that growth is the foundation of all devices. Growth rules defect and impurity levels within the material and governs atomic arrangements, defining the overall quality of your device.

1.2.1 Introduction to epitaxy of III-Nitrides

Epitaxy?

Starting from a substrate, one is able to grow layers on top. If the two materials are linked by any crystallographic relationship then, the growth is called epitaxial. As its etymology means, epitaxy refers to any crystal growth which has specific orientation with respect to the crystal beneath it. When the seed crystal is the same as the new one it is called homoepitaxy, when the two differ it is called heteroepitaxy.

In order to grow the layer, one needs to send atoms, which will be able to crystallize making bound with the substrates and other impinging atoms. The substrate is the crystal imposing the crystal orientation to the grown layer. Atoms impinging on the surface can undergo different phenomena. Atoms can diffuse on the surface over a characteristic length λ_D. Then, they can be linked to the substrate in two ways: *physisorption* which is a weak

link by Van der Walls bonds or *chemisorption* which involves strong bounds with the formation of crystal. The atom moves from one site to another as they are energetically separated by a diffusion barrier $D = D_0 \exp(-E_D/kT)$. However, in the meantime, atoms can be re-evaporated from the surface. The resident time $\tau = \tau_0 \exp(E_A/kT)$ is the characteristic time an atom stays on the surface.
Finally, diffusion length λ_D depends on both diffusion barrier height to jump from one state to the other and on the time spent on the surface giving $\lambda_D = \sqrt{2\tau D}$ Important note: these relationships hold because the growth does not occur at thermodynamic equilibrium and is governed by kinetics and therefore by diffusion phenomena. The temperature is a key point in the growth process. Indeed, growing at high temperature will increase the diffusion coefficient but lower the resident time of the atoms on the surface.

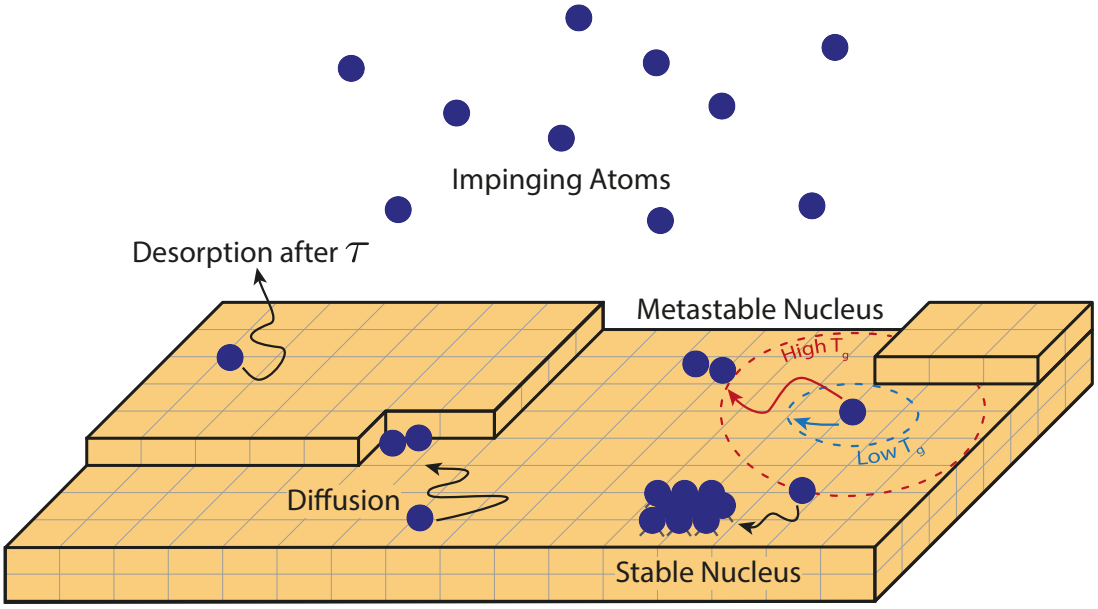

Figure 1.7: Illustration of a surface during epitaxial growth with different mechanisms occurring.

Strain and relaxation

To begin with, one must introduce the so-called lattice mismatch $\Delta a/a$ and strain ε coefficient. If a_l is the lattice parameters of the layer and a_s the one of the substrate then we have:

$$\frac{\Delta a}{a} = \frac{a_s - a_l}{a_s} \tag{1.3}$$

$$\varepsilon = \frac{a_l - a_s}{a_l} \tag{1.4}$$

In homoepitaxy, the lattice mismatch is equal to zero since $a_l = a_s$ and no strain

is induced. However, in heteroepitaxy the grown layer has to adapt to the substrate. The accommodation is done first by elastic deformation of the layer inducing strain: it is a pseudomorphic (or coherent) growth. The larger the mismatch, the larger the deformation. A limited amount of elastic energy can be stored, depending on the material. At a certain threshold, called critical thickness, the system evolves in a plastic relaxation mode. The elastic energy is enough for the layer to create a defect, such as a dislocation, in order to relax. Dislocations can be either screw dislocations, edge dislocations or a mix of the two. Screw dislocations have a direct impact on the growth because of its characteristic: they results in the creation of an additional plane on the surface, or in other terms, beautiful helicoidal looking terraces [52, 53]. Additional strain can be added once the material is cooled down after the growth. It is particularly the case of GaN on Si, because of the large difference in thermal expansion coefficient (table 1.4), when cooled down GaN layers will show cracks.

The strain accommodation of the epitaxial layer can lead to different growth modes:

- *Frank — van der Merve (FM)* mode refers to the classical layer-by-layer growth. When adatom-surface interaction is stronger than adatom-adatom interaction, the substrate surface is wet by impinging atoms that are incorporated progressively. This is typically the case for homoepitaxy.
- *Stranski — Krastanov (SK)* mode (Figure 1.8 *left*). After reaching the critical thickness, the accumulation of strain becomes high enough in the layer for it to relax and results in the creation of free surfaces, i.e. 3D islands, built on a 2D layer, called wetting layer. SK growth is mainly used for GaN/AlN or InGaN/GaN quantum dots heterostructures.
- *Volmer — Weber (VM)* mode (Figure 1.8 *middle and right*) is the extreme case in term of lattice mismatch. Because of the large difference in lattice parameters, adatoms prefer to be linked to other adatoms rather than the surface. It results in the formation of 3D islands in order to reduce the strain, without any wetting layer on the substrate.

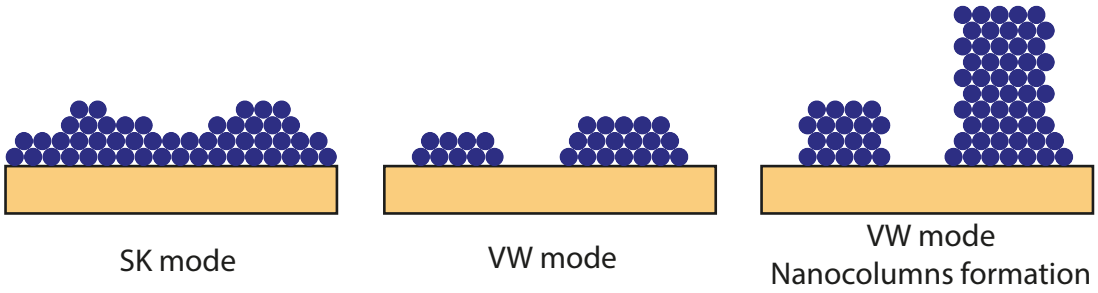

Figure 1.8: Schematics of layer growth mode in SK mode and VW mode and VW after longer growth duration up to nanocolumns formation.

Table 1.4: Lattice mismatch and thermally induced strain of materials with respect to GaN (0001) (from [54, 55]).

Material Orientation	GaN (001)	AlN (0001)	Sapp. (0001)	Si (111)	6H-SiC (0001)
Lattice constant (Å)	3.189	3.112	4.758	5.43	3.08
Lattice mismatch (%)	0	-2.4	$\sim$ 16	-17	-3.5
Thermal expansion (µK)	5.59	4.15	$\sim$ 7	3.6	4.3
Thermal mismatch (%)	0	34	-20	$\sim$100	30

1.2.2 From layers to nanowires

The latter scenario is indeed the growth mode of III-N NWs which is a catalyst-free mode. They can only be grown on substrates exhibiting large lattice mismatch, or in growth conditions reducing the adatom diffusion on the surface. The use of a masking layer, carefully chosen, is also possible in order to perform selective area growth (SAG) and get arrays of well ordered NWs [56]. The following describes the growth mechanisms of NWs by molecular beam epitaxy, even if part of the discussion holds for other techniques. GaN and AlGaN NWs grown on various substrates have been studied extensively in different research laboratories and by former PhDs of the team. Therefore, the following paragraphs will detail the mechanisms ruling NWs growth, without going into the details. To go further, I encourage the reader to have a look at the work of Karine Hestroffer, Thomas Auzelle, Sergio Fernandez-Garrido and Raffella Calarco and many others [29, 57–64].

First of all, a nanowire is defined as a column-shaped crystal, self-organized, having an aspect ratio of few tens and typically of below 200 nm diameter.

Starting with a clean (111)-Si substrate, we will work at a high growth temperature for GaN ($\sim$800°C) in order to increase Ga diffusion length with a III/N ratio below one. In such conditions, Ga can diffuse on the surface until it finds a N atom to bound to: the nuclei is formed. At this stage, it can either dissociate and re-evaporate or grow if other atoms reach it and bind. Once the nuclei is large enough, it will stop growing laterally because of the accumulated strain and rather grow vertically in order to relax. The 3D island is now formed and will act as a "diffusion pump". Indeed, Ga atom diffusing on the substrate surface will be able to reach a nuclei, and contribute to its growth rather than forming a new one. The NWs are grown catalyst-free since no external element acts in order to perform the growth, contrary to II-VI NWs for instance which are assisted by gold droplets [65].

How does this scenario change with growth parameters? If the Metal/Nitrogen ratio increases, Ga atoms won't be able to diffuse much on the surface because the probability

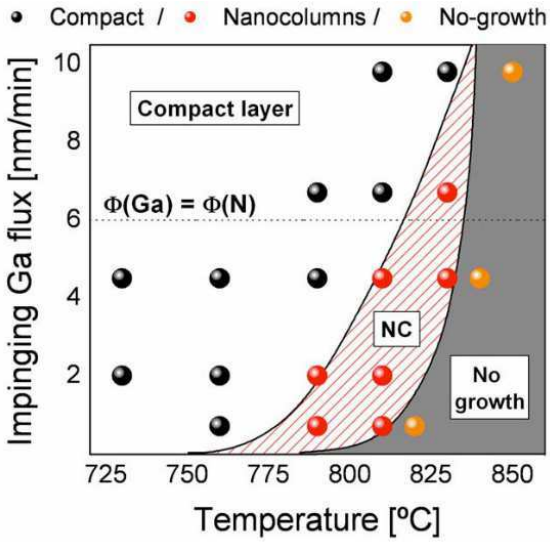

Figure 1.9: Diagram of growth regimes from [63].

to bind to a N atom will be larger, favoring the nucleation process. The limit case of Metal rich corresponds to an infinite density of nuclei on the surface, leading to a 2D layer. The temperature is also a key parameter since it plays a role on the diffusion length but favors desorption and dissociation. Thus, a too low temperature will result in a high degree of coalescence while a too high temperature will give rise to inhomogeneous and sparse NWs or no nanowire at all. This is summarized in the diagram in figure 1.9.

Nucleation time is also a key parameter as it rules the beginning of the NW growth [66]. Under high temperature or low Ga flux, dissociation rate is high and the nucleation happens in an asynchronous manner. This delay between NWs nucleations will translate into height inhomogeneities since all of them grow at the same rate. Height inhomogeneities are detrimental because it increases shadowing effects and makes metal deposition difficult for further electrical characterizations. Tuning substrate temperature and Ga flux accordingly, allows one to have a relatively quick nucleation time (typically between 3 to 8 minutes) and get homogeneous NWs. Figure 1.10 shows typical NW morphologies one can get by changing growth parameters at nucleation in MBE.

The case of GaN was used but what would happen with AlN NWs? Since Al has a small diffusion coefficient compared to Ga, the direct growth of AlN NWs on Si is difficult to achieve and would require growing at around 1200°C, which is challenging. The feasibility has been demonstrated on sputtered TiN on Si in the work of *Azadmand* et al. in the Paul Drude institute [67]. Otherwise, the main strategy is to first grow GaN NWs stems as template to further grow the AlN NWs on top of it.

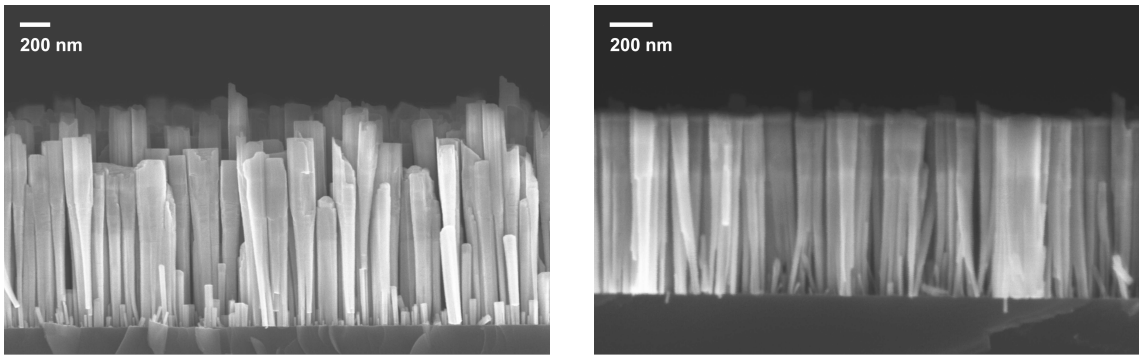

(a) N3522: $T_{\text{sub}} = 850$C (b) N3784: $T_{\text{sub}} = 820$C

Figure 1.10: Scanning electron microscope cross sectional images of N3522 (a) and N3784 (b) highlighting different morphologies depending on the substrate temperature during the nucleation stage. Both were grown with a Ga/N flux of ~ 0.3.

1.2.3 Growth techniques

To achieve epitaxial growth, three main techniques exist:

- *Hydride Vapor Phase Epitaxy* (HVPE) is one of them. A HCl gas flow reacts with a hot liquid Ga in order to produce GaCl gas, which will meet NH_3 at the surface of the substrate. This technique presents several advantages. It does not introduce oxygen or carbon, increasing the crystal purity, the growth takes place at high temperature and high pressure, and therefore close to thermodynamic equilibrium, in addition to a growth rate as high as 500 µm/h. Nevertheless, it is not possible to dope or get a structured material. It is particularly well suited for the realization of thick buffer layers or the production of substrates such as free-standing GaN.

- Most widely used in the industry, *Metal Organic Vapor Phase Epitaxy* (MOVPE) or *Metal-Organic Chemical Vapor Deposition* (MOCVD) is close to HVPE. Major difference is the use of carbon-based precursors such as trimethylgallium $Ga(CH_3)_3$ or trimethylaluminum ($Al_2(CH_3)_6$) along with NH_3. Again, precursors are brought to the substrate surface, which is heated and allows the reaction of the species. The adjustable growth rate and substrate temperature make it useful in order to precisely control thickness or alloy composition compared to HVPE. However, growers have to be careful on the level of oxygen, carbon or hydrogen incorporated in the structure, which could be to the expense of crystal quality and device performances.

These two first techniques are chemical deposition techniques because they both involve chemical reactions between provided molecules. A schematic of their functioning is given in figure 1.11. A third one is classified as a physical technique since the source material are atoms and no longer molecules.

- *Molecular Beam Epitaxy* (MBE) is the technique used to grow the samples presented in this manuscript, the machine being sketched on figure 1.12. The growth takes

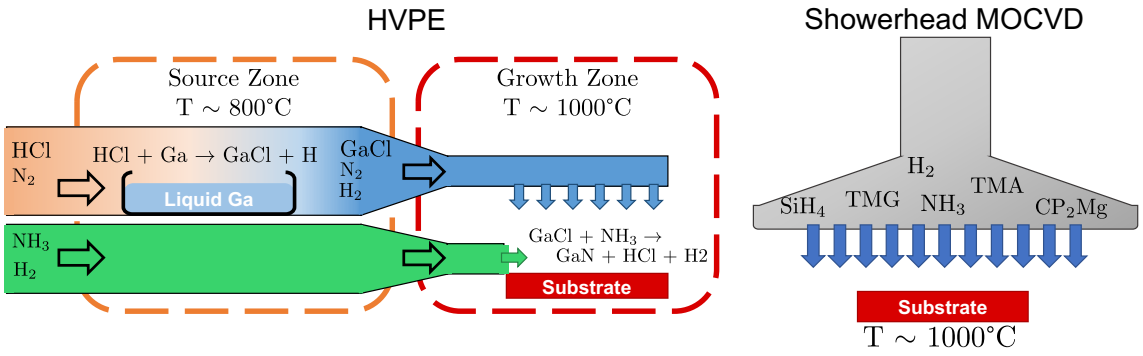

Figure 1.11: Schematics of HVPE and MOCVD growth process.

place in general in an ultra-high vacuum chamber ($\sim 10^{-8}$ mbar) in which the substrate is facing different cells, each sending atomic flux. Thanks to the high vacuum, mean free path of atoms in such conditions is veery large, which ensures no interaction between them and a ballistic regime. Also the lower growth rate and the nature of the interaction makes MBE most suited for sharp interfaces and controlled heterojunctions. The growth usually occurs at lower temperature than in MOCVD and further away from thermodynamic equilibrium, allowing a high degree of freedom on the growth, which is primarily governed by kinetics.

Next section will focus more on the technical details of MBE and especially of the machine used.

PAMBE technical details

Molecular beam epitaxy of III-Nitride is done using Knudsen cells in order to provide metallic species such as Al, Ga, In, Mg or Si. In those Knudsen cells, a high purity material is put in a crucible (either made of pyrolytic boron nitride or graphite), which will be heated by Joule effect thanks to a filament. The material is evaporated (Al, Ga, In) or sublimated (Si or Mg) giving rise to the atomic beam. On its side, nitrogen source can be achieve by two means: ammonia dissociation in so-called NH_3-MBE or through nitrogen plasma, which is our case. A nitrogen flow is sent through a plasma cell which will dissociate N_2 into N radicals by radio-frequency power, giving the name of radio-frequency plasma assisted MBE or RF-PAMBE. Two plasma cells can be used in our chamber depending on the growth condition one wants, one working at a N_2 flow of 0.8 sccm and a RF power of 300 W, the second working at 2.5 sccm and 600 W. Samples are mounted on two inches In-free molyblocks and are held by a manipulator equipped with a heater made of a SiC filament, allowing growth at high temperature (up to 1100°C). Temperature is recorded by a thermocouple put at the rear face of the sample. The manipulator can move along four degrees of freedom and is placed so that it gets the most of the beams with the best homogeneity. A quadrupole mass spectrometer is installed in the chamber and allows

control of the atomic species present in the chamber. An additional chamber is also present which allows us to do oxygen plasma treatment and outgasing of the substrates by heating them up to 300°C.

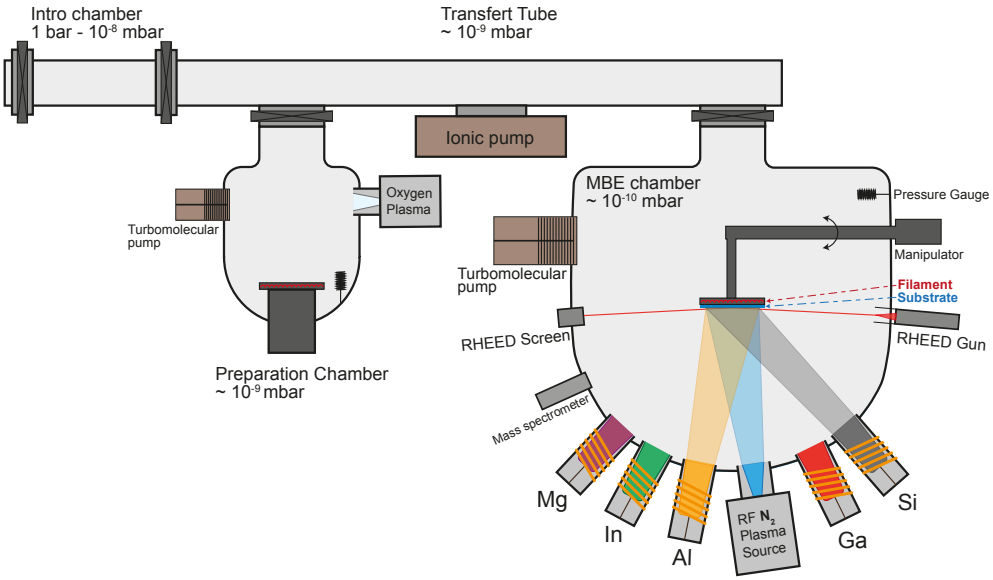

Figure 1.12: Schematics of the molecular beam epitaxy system used during this work.

Monitoring by reflection high energy electron diffraction

Working under ultra-high vacuum can be difficult, for maintenance for instance, yet it is an advantage as it allows the use of electron beam. Reflection high energy electron diffraction (RHEED) technique is the main tool to monitor growth in-situ and perform a first characterization. An electron beam is sent onto the sample with a grazing incident ($\sim 2°$) and an energy of 32 keV. The electrons will be diffracted by the surface features and form a pattern corresponding to its structure.

On a perfectly smooth surface, the direct reflection of the beam can be seen alongside some infinitesimally small spots resulting from the intersection of Ewald's sphere with the reciprocal space of the lattice. Dealing with substrate with long terraces, at high temperature and with a non-ideal beam, allows one to instead observe elongated lines separated by a distance corresponding to the inverse on the in-plane lattice constant. If the surface roughens, the beam is partly transmitted through the asperities. The resulting signal will be streaky lines. If the roughness is large and 3D structures appear, the corresponding out-of-plane periodicity can be found in the RHEED signal. Spots will be predominant with both in-plane and out-of-plane lattice parameter accessible from the distance between the spots.

RHEED is the most useful tool in the MBE chamber. Firstly, it is used in order to

calibrate the growth rate by observing so-called RHEED oscillations. They are oscillations in reflected beam intensity arising from the periodic completion of layer in monolayer by monolayer growth. Thus, their periodicity is directly linked to the rate at which the surface is being grown. To get more details, see appendix A. Secondly, (111)-Si has a specific feature in that it presents a surface reconstruction transition from a 7×7 to a 1×1 at around 860°C [68]. This pattern, shown in figure 1.13a, is therefore used in this work to calibrate substrate temperature and to check the surface deoxidation. Thirdly, RHEED can monitor the nucleation time of nanowires. Indeed, NWs being columnar crystallites, the nucleation corresponds to a roughening of the surface with formation of spots on the RHEED signal (Figure 1.13b — 1.13d). Therefore, the grower can have a clue on the density of NWs thanks to the speed at which the dot appears. At the beginning NWs can be tilted, resulting in an annular shaped RHEED signal vanishing with growth duration.

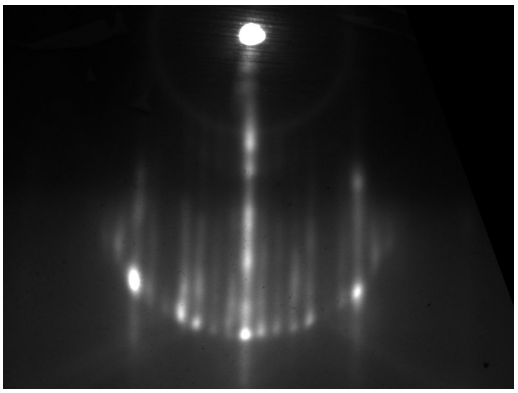

(a) Clean (111)-Si substrate exhibiting a 7×7 surface reconstruction at T_{sub}=820°C.

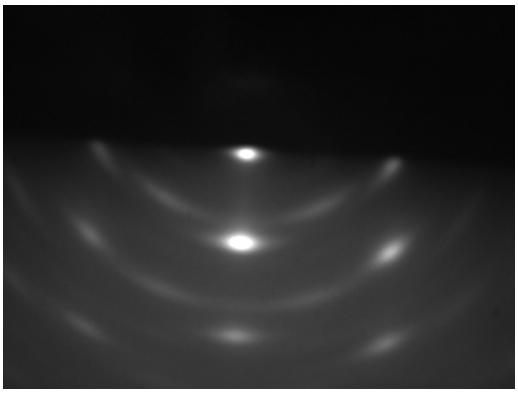

(b) 9 minutes after the beginning of NW growth.

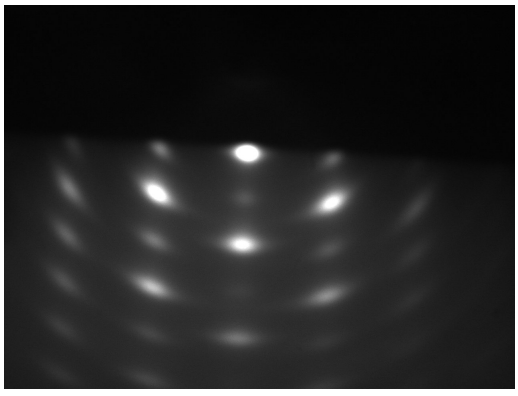

(c) 12 minutes after the beginning of NW growth.

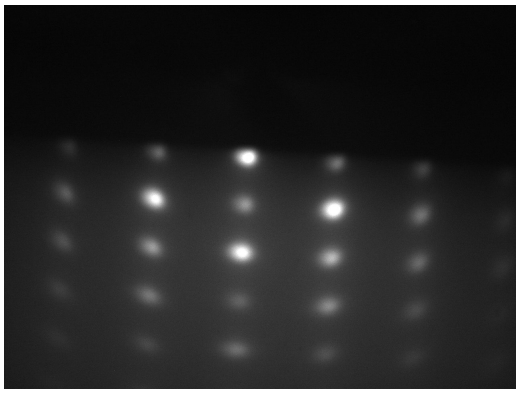

(d) 4 hours after the beginning of NW growth.

Figure 1.13: RHEED patterns observed in various cases.

1.3 Characterization techniques

After the growth, structural characterizations can be performed in order to assess structural quality and overall morphology of the samples.

1.3.1 Electron microscopy

Electron microscopy techniques are a must when one wants to image nanostructured objects. Because of diffraction, the resolution of an image can not be lower than the wavelength of the probe. In case of optical microscopy, this limit is around 800 nm, which is too large compared to the studied structures. Using an electron beam allows to get higher resolution since the wavelength of the beam is typically less than an angstrom. The beam is formed by a field effect gun producing a highly coherent and bright source. Afterwards, the beam goes through a series of electromagnetic lenses in order to be shaped and focused on the sample.
Depending on the acceleration voltage and the atomic number of the species, the interaction volume, so-called interaction pear, can be tuned to probe the near surface or deeper in the volume. It exists several interactions between the incoming electrons and the sample arising from ionization, elastic or inelastic scattering or absorption of the electrons in the material.

- **Secondary electrons** (SE) which are low energy electrons and originate from the ionization of atoms close to the surface.
- **Back-scattered electrons** (BSE) which arise from the 'reflected' electron beam and exhibit higher energy.
- **X-rays** generated from the interaction between the beam and the atom's electrons (see 1.3.2).
- **Light** or **current** induced by injection related phenomenon (see 2.3.2 or 2.3.2).
- Interactions acting on the transmitted beam if any.

Because of the wide variety of interactions between electron and matter, a lot of information can be extracted. In addition, each signal comes from a certain area of the interaction pear, as highlighted in figure 1.14. Electron microscopes are of two kinds, which are schematically shown below (1.15):

Scanning electron microscope (SEM): The sample surface is scanned by the electron beam, which has a typical acceleration voltage between 3 to 30 kV. It allows to have a spatial resolution down to ten nanometers in SE mode. Easy to use, it can perform a lot of experiments. In this work, a ZEISS Ultra55 model was used to observe NWs morphology, characteristic dimensions, density and to measure atomic concentration by EDX.

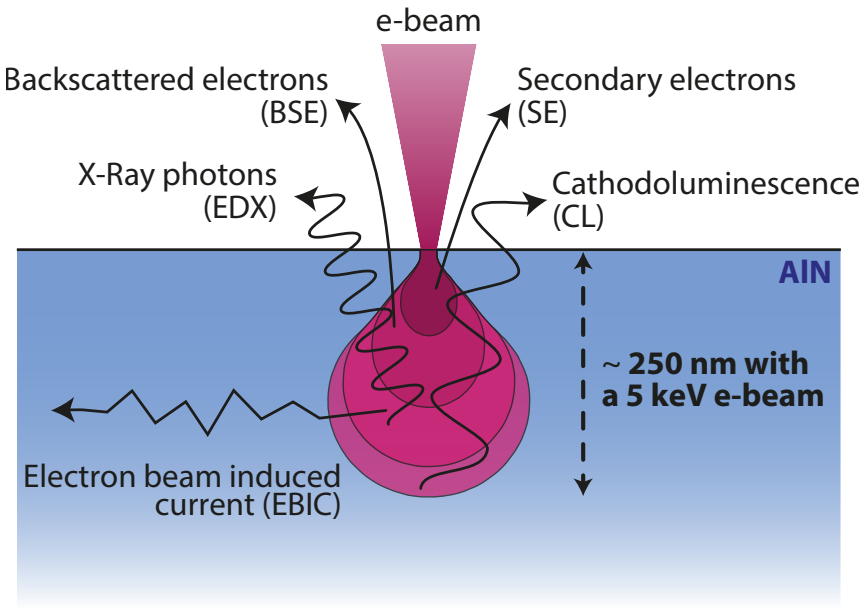

Figure 1.14: Cartoon of an interaction pear and associated signals.
Depth of the interaction pear is extracted from simulations using *Casino* software.

Transmission electron microscope (TEM): In a TEM, the electron beam is collected after having passed through the sample. It needs to be transparent to electron usually by thinning a lamella or directly in the case of nanostructures such as thin NWs. Operating at higher acceleration voltage than a SEM (between 60 kV to 300 kV) and on thin specimen allows the spatial resolution to be considerably improved. Several techniques are available depending on the information one wants to get. For instance, high-resolution scanning TEM (HR-STEM) by high angle annular dark field (HAADF) is a technique that has been used in order to image atomically thin layers of material based on atomic Z-contrast.

1.3.2 Energy dispersive X-ray spectroscopy

As mentioned hereabove, X-rays can be produced in the material as electrons from atom's inner shell may be ejected by the impact with the beam and leave a hole. This hole will, shortly after, be filled by an electron coming for the outer shell. This transition will be the responsible for the X-ray generation, with a characteristic energy according to the atom electronic structure and the involved transition. Every atom has a distinct structure making its set of X-rays energy peak unique, similar to an ID card (table 1.5). By recording the energy spectrum from the material, the chemical composition of a sample can be deduced with a spatial resolution being the one of the interaction pear. The emission of X-rays is a random process following Poisson's law. In order to get an accurate spectrum

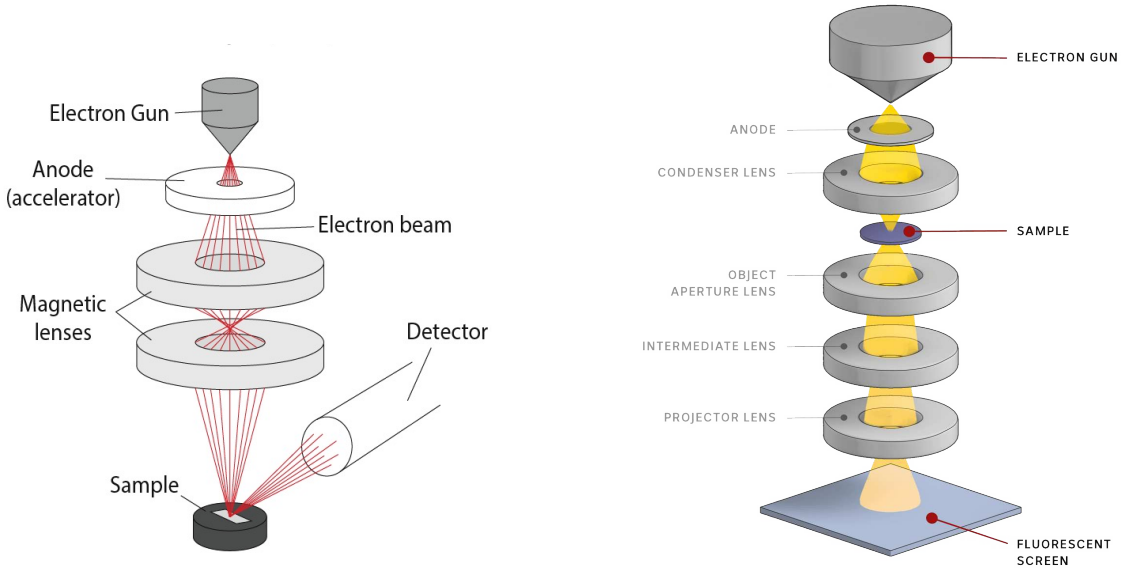

(a) (b)

Figure 1.15: Sketch of (a) a scanning electron microscope and (b) a transmission electron microscope (from [69, 70]).

and therefore an accurate measure of sample composition, it is important to acquire a lot of X-ray photons. Peaks can overlap making the de-correlation of species difficult and the counting yield important in order to best fit the data. A concrete case is the case of Mg doped GaN in which Mg K_α line (1.25 eV) is close to the Ga L_β line (1.24 eV). Nevertheless, it is possible after a rigorous work of calibration of the detectors and counting to be able to reach a detection limit of few 10^{18} at/cm^3

Table 1.5: X-ray energy of various transitions and atoms. Energy values are given in keV.

	$\mathbf{K}_\alpha$	$\mathbf{K}_\beta$	$\mathbf{L}_\alpha$	$\mathbf{L}_\beta$
N	0.39	—	—	—
Al	1.49	1.56	—	—
Ga	9.24	10.3	1.10	1.24
In	24.1	27.2	3.28	3.49
Si	1.74	1.84	—	—
Mg	1.25	1.30	—	—

1.4 Summary of Chapter 1

Chapter 1 was primarily designed to introduce the material family, and highlight its relevant specificities in the scope of this work. Therefore, a focus on AlGaN is done from a

crystallographic and electronic point of view. Growth of nitrides was also detailed in order to give a glimpse on how one can obtain high quality crystal and how to grow AlN and GaN nanowires specifically. An overview of the experimental techniques used to characterize the samples after the growth was finally done, in a brief manner.

CHAPTER 2

From the material to the LED

This chapter is dedicated to the semiconductor physics behind light emitting diodes and other devices. Light emission mechanisms as well as electrical transport mechanisms will be presented. Lastly, device realization and characterization techniques used in this work are detailed.

Contents

2.1 Physics of light emitting diodes 38
2.1.1 Electrical transport in doped semiconductors 38
2.1.2 The pn-junction as building block 42
2.1.3 Light emission mechanisms 44
2.1.4 Performance and figures of merit 45
2.1.5 LED architectures 47
2.2 Processing of the NWs 49
2.3 Characterization techniques 50
2.3.1 Current-Voltage characteristics 50
2.3.2 Electron beam based techniques 52
2.4 Summary of Chapter 2 55

2.1 Physics of light emitting diodes

A light emitting diode can be decomposed in several parts. Firstly, it is a diode and therefore a pn-junction, which implies to understand how the current can flow in such structure and its limitations in the case of wide bandgap semiconductors. The physics of a pn-junction will be detailed after discussing the transport mechanisms occurring in doped semiconductors. Secondly, optical properties of semiconductors in general and of LEDs in particular will be discussed in a third part before having a look on figures of merits and architectures.

2.1.1 Electrical transport in doped semiconductors

Doping

A recall of the quantities and their meaning might be useful before diving into the topic. Especially, I want to emphasize the differences between impurity concentration denoted $[X]$, dopant concentration, effective doping and free carrier concentration, which can be summarized in figure 2.1. The concentration of atom X, refers to the number of atoms per volume of material. A dopant can be characterized by its ionization energy which defines the position of its energy level with respect to either valence or conduction band, according to its type: E_A or E_D for acceptor and donor respectively. If this energy is of the order of kT, the dopant will be called shallow, otherwise it will be called "deep". The deeper the energy level, the strongest the interaction between the atom and its charge, the lower the ratio of ionized atoms, hence free carriers at a given temperature. Finally, the carrier density refers to the number of free carriers available in the band, either p holes in VB or n electrons in CB.

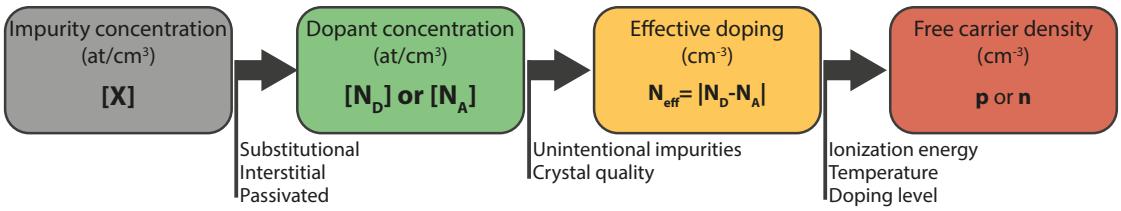

Figure 2.1: Illustration of the link between dopant concentration, effective doping and free carrier concentration (adapted from [71]).

As one dopes a semiconductor in-situ (i.e.ḋuring the growth), Fermi level shifts toward either VB or CB. Because of this, the formation energy of defects can be changed. In general, the thermodynamic will have tendency to compensate the doping induced by creating certain intrinsic defects such as vacancies or complexes. This effect is especially true in wide bandgap semiconductors since plethora of states can lie in their large gap. Those can act as compensating centers and reduce the doping efficiency (figure 2.2a vs

figure 2.2b). Effective doping N_{eff} is defined as the difference between donor and acceptor concentrations $|N_D - N_A|$. In III-N, metal vacancies are known to act as acceptors while N vacancies as donors [72–74]. In order to increase free carrier concentration, one can adjust the amount of dopant. However, the effective doping is the quantity referring to dopants still able to be ionized excluding the one that have been compensated. One can act on the growth in order to decrease the compensation and reduce the difference between dopant concentration and effective doping. Then only a fraction of this concentration will be ionized depending on the ionization energy of the dopant and the temperature. Figure 2.2c aims at describing the phenomenon from an energy band diagram point of view. For a more quantitative perspective, following the book of Look [75], appendix B gives a modeling and simulation result of the carrier concentration depending on these parameters.

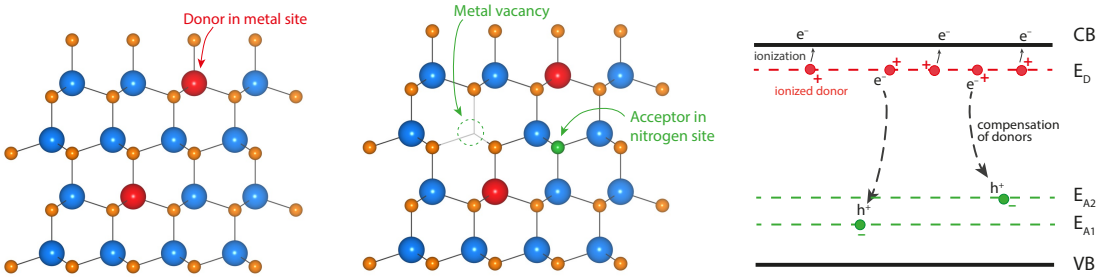

(a) Donor in metal substitution.

(b) Donor in substitution with an acceptor in nitrogen substitution and a metal vacancy.

(c) Schematic of band diagram in case of five donors located at a single level E_D, compensated by two different acceptors at energy levels E_{A1} and E_{A2}.

Figure 2.2: Schematics of a n-type nitride lattice in the case of non-compensation and compensation and a sketch of its associated band diagram. E_D line represents the single energy level of the donor in metal site, while E_{A1} and E_{A2} lines represent the two acceptors energy levels of this example namely a metal vacancy and an acceptor in nitrogen site.

Ohmic conduction

The most common transport behavior in doped semiconductors is Ohmic transport or band transport. Free charges are delocalized in conduction or valence band and their mean free path is large. When an electric field E is applied, free charges are set in motion and flow: Ohm's law applies as written in equation 2.1 in the case of a n-type semiconductor:

$$J_{\text{Ohm}} = nq\mu E = \sigma E \tag{2.1}$$

J being the current density, σ the conductivity and n the free electron concentration. μ is the mobility which represents the ease with which the charged particles can move in

the material. This mobility is directly affected by scattering centers (i.e.ṕoint defects, dislocation, foreign atoms, or phonons) and is, in general, dependent on the temperature. Mobility ranging between tens to a several hundreds of $cm^2/(V.s)$ have been reported in n-doped GaN and AlN [76–80]

Hopping conduction

When few electrons are present in conduction band and lots of available states lie into the forbidden gap, hopping conduction can be favored. Instead of being delocalized in CB like in ohmic conduction, charge carriers are localized around a discrete level. If another available state is in the close environment with respect to its wave-function, it exists a probability for it to tunnel and hop from one to another. Hopping conduction is highly dependent on the number of states, being for instance dopants or defects. The higher their density, the easier the probability to tunnel to an available level: the so-called Nearest-Neighbor (NN) hopping model. It is also dependent on the temperature as it allows the charges to reach levels that would be at energy levels slightly different. In this case, variable range (VR) hopping model applies. The mechanism is schematically drawn in figure 2.3 and compared with Ohmic conduction regime.
Mott was one of the first to have modeled this regime. He predicted and experimentally assessed the temperature dependence of the conductivity in hopping regime [81]:

$$\sigma = \sigma_0 \exp\left(-\frac{T_0}{T}\right)^{\beta} \tag{2.2}$$

However, the value of β reveals the hopping conduction at play: NN hopping if $\beta = 1$ or VR hopping $\beta = 1/4$ [82, 83].

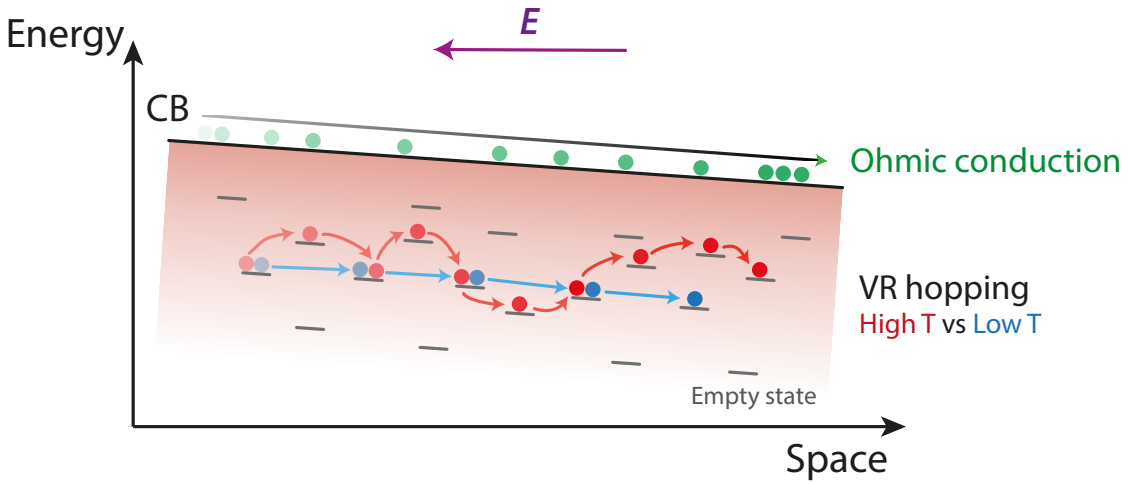

Figure 2.3: Schematics of ohmic and hopping conduction of electrons. Red, blue and green circles correspond to electron in one of the three transport regimes.

Impact ionization

In the case of high electric field, the total energy of charges flowing in a material can become large. To a certain extent, this energy can become large enough to ionized electron from the lattice atoms in a so-called impact ionization process. Current flows in a so-called avalanche where multiplication of charges occurs in a self-sustaining manner. Detrimental from a material point of view, multiplication can lead to breakdown of device. The so-called breakdown field quantifies the electric field a material can sustain before it undergoes breakdown but greatly depends on crystal quality. Some values for various materials are reported in table 2.1 along with their energy bandgap. Avalanche photodiodes and single photon detectors take advantage of this phenomenon in order to create a non negligible current once a single photon is absorbed in the high electric field region.

Table 2.1: Energy band gap and breakdown field of several semiconductors (from [84–87])

	AlN	**GaN**	**Diamond**	**SiC**	**Si**
Bandgap (eV)	6.2	3.4	5.5	3	1.1
Breakdown field (MV/cm)	10	5	20	2	0.2

Space-charge limited current

In material exhibiting low free carrier densities, space-charge limited current can be observed as electrical transport regime. It occurs when electrons are directly injected from the contact into conduction band and can be assisted by traps. Primarily described by Lampert [88] and Rose [89], the current flow follows a power law $J \propto V^{\alpha}$ with $\alpha \geqslant 2$. In most cases, at low bias, Ohm's law applies thanks to background free charges that might be present in the material. At a certain voltage, CB band bends enough so that the carriers injected from the contact become in excess with respect to the ones present in the material at thermodynamic equilibrium. Once this regime is established, current follows Child's law:

$$J = \frac{9\varepsilon\mu}{8a^3} \cdot V^2 \tag{2.3}$$

where, ε is the dielectric permittivity of the material, μ the mobility of carriers in the band and a the distance between the anode and cathode. Traps can influence the electrostatics at the interface between the metal and the semiconductor. In particular, being charged or not, different dependencies can be present at different voltage regimes. Transition between Ohm's law and Child's law can be abrupt because of the repulsion from deep traps or smooth in the case of shallow trap. More details will be given on this theory in Chapter 4 as it is a mechanism found in Si-doped AlN NWs.

2.1.2 The pn-junction as building block

The pn-junction is the base of the diode in the LED. It aims at providing electrons and holes in the active media where their conversion into light occurs. As any diode, pn-junctions are non-linear electronic devices, governed by mechanisms which could seem simple at first sight but may exhibit a high level of intricacy in complex device structures.

Electrostatics of an ideal pn-junction

A schematic of a pn-junction is given in figure 2.4. At the metallurgic interface between a n-doped and p-doped semiconductor, diffusion of free electrons from the n-side and holes from p-side occurs. It results in the recombination of nearby carriers, leaving an interface with only ionized donors and acceptors called space charge region (SCR). In this region charges are fixed and unbalanced leading to the creation of an electric field and a corresponding built-in voltage V_{bi}. For N_D donors and N_A acceptors in either side, the charge neutrality equation gives the following relationship:

$$V_{bi} = \frac{kT}{q} \ln\left(\frac{N_D N_A}{n_i^2}\right) \tag{2.4}$$

with k Boltzmann's constant, T the temperature in K, q the elementary charge, n_i the intrinsic carrier density of the material. Solving Poisson's equation $\frac{d^2V}{dx^2} = -\frac{\rho}{\varepsilon}$, with the adequate boundary conditions, leads to the following expression of the width of the depletion region as function of the applied bias:

$$W = \sqrt{\frac{2\varepsilon(V_{bi} - V)}{q}\left(\frac{1}{N_A} + \frac{1}{N_D}\right)} \tag{2.5}$$

At equilibrium, only few minority carriers might be able to diffuse to the SCR and generate a current. This current is called saturation current and can be expressed as:

$$I_s = qAn_i^2\left(\frac{D_n}{L_n N_D} + \frac{D_p}{L_p N_A}\right) \tag{2.6}$$

where A is the junction area, $D_{n,p}$ the diffusion coefficient and $L_{n,p}$ the diffusion length. Under a reverse bias, electrons and holes are pulled away from the SCR increasing its width and avoiding current to flow (figure 2.4c). On the contrary, when the junction is forward biased, the potential barrier is decreased and electrons and holes are allowed to flow across the junction. Shockley equation dictates the current behavior of pn-junction as:

$$I = I_s\left[\exp\left(\frac{qV}{\eta kT}\right) - 1\right] \tag{2.7}$$

with η the ideality factor which is equal to 1 in perfect diode and in low injection regime. In passing mode, current flows exponentially as the voltage is increased and the pn-junction barrier is lowered.

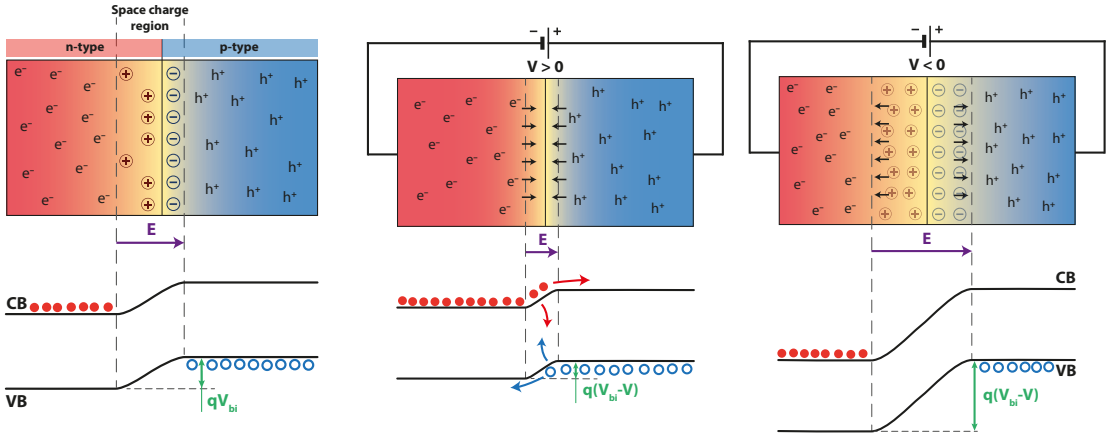

(a) At equilibrium (b) Forward bias (c) Reverse bias.

Figure 2.4: Schematics of a pn-junction and its band diagram at equilibrium and under a forward and reverse bias.

Real diode current-voltage characteristics

In reality, a device is not so simplistic. Especially, current cannot increase exponentially to infinity. Once the barrier is fully lowered, other resistances will be predominant. Neutral regions, because they are doped semiconductors, have non null resistivity which will limit the current at high bias. Parasitic parallel resistances are often seen as they will act as favored current path and lead to leakage current. If this resistance is low enough a non-negligible part of the current will shunt the pn-junction. This effect can be seen at low bias and mostly in reverse bias. Taking into account possible parasitic and series resistances, the corresponding electrical circuit can be drawn as in figure 2.5. Since the potential drop applied on the diode is now different than the potential drop at the pn-junction, Schokley equation can be rewritten as:

$$I - \frac{V - IR_s}{R_p} = I_s \exp\left(\frac{q(V - IR_s)}{\eta kT}\right) \tag{2.8}$$

with $V_D = V - IR_s$ and $i_D = I - V_D/R_p$.

An equivalent circuit can be drawn as in figure 2.5. Parallel resistance will have a strong impact on the reverse current, as it will be able to shunt the pn-junction. Whereas, series resistance will be more limiting the current flow once the pn-junction barrier is lowering and therefore seen in forward bias.

Beside, diodes and especially GaN based diodes are not ideal pn-junctions. An ideality

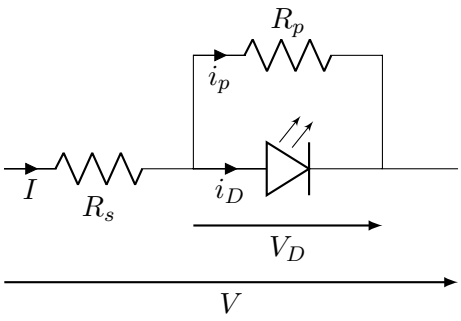

Figure 2.5: Equivalent circuit of a real diode. Potential drop V_D and current flowing into the LED i_D are no longer equivalent to the total potential drop V and current I.

factor greater than one is often needed to fit the I-V characteristics of such components. If usually $\eta \sim 1$ is reported for silicon diodes, the case of III-V materials is more problematic. Values of around 2 have been reported for III-Phosphide [90] and ranging from ~ 1 up to 6.9 have been reported in nitride pn-junctions [91–94]. Metal-semiconductor interfaces, trap-assisted recombination or tunnelling are the candidates accounting for those discrepancies, yet without clear understanding.

2.1.3 Light emission mechanisms

In semiconductors, electrons and holes can either recombine radiatively or non-radiatively. In a LED, as in any optoelectronic devices, the non-radiative recombination will be detrimental for the overall performances.

In the first place, electrons in conduction band and holes in valence band are needed. This excitation step can be realized by absorption of photons with an energy higher than the bandgap (optical pumping), by direct injection of carriers through electron irradiation (electronic pumping) or by electrical injection thanks to a pn-junction. For carriers to recombine, they must be spatially close enough and for a sufficiently long period of time. Or in other words, the recombination is directly linked to the overlap of electrons and holes wave-functions. Optical confinement of carriers by the mean of adequate structuration of the material is therefore an option to adjust their localization. More details will be given in part 2.1.5.

Once electrons and holes are in their respective bands, the system tends to reach a lower energy level putting the electron back in valence band, making them recombine. This recombination can involve several transition and several paths (figure 2.6).

- **Direct transition** from the band edge leads to a photon with energy equal to the bandgap of the material.
- **Free excitonic (FX)** recombination is similar to the direct one but involves an electron hole pair interacting and forming quasi particle called an exciton. The total

energy is reduced by a value corresponding to the Coulomb interaction between the two particles. Exciton binding energy being large even in bulk GaN (22 meV [95]) and AlN (50 meV [96]), they can remain stable at room temperature, while dissociated in other materials such as GaAs or Si.

- **Donor / acceptor** related luminescence arises from the interaction of electrons and holes with charged impurities. As donors and acceptors are charged, Coulomb interaction between them and charge carriers reduce photon energy depending on those impurity levels with respect to bandgap. In addition if an acceptor and a donor are close to each other, they can attract electrons and holes and produce light with an energy depending on the species and their distance, this is the so-called donor-acceptor pairs (DAP) luminescence.

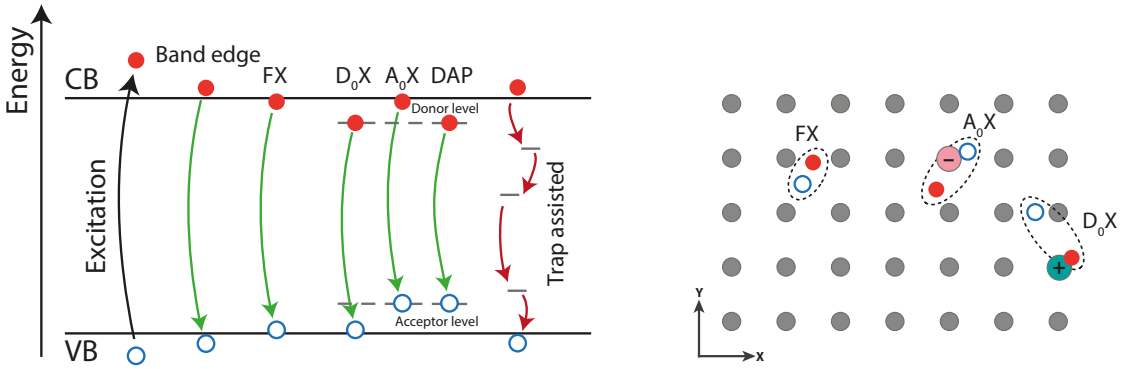

(a) Recombinations processes possible in semiconductors. Red arrow: non radiative recombination. Green arrow: radiative recombination.

(b) Schematics of free exciton (FX), neutral donor — exciton (D_0X) and neutral acceptor — exciton (A_0X)

Figure 2.6: Representation of different types of recombination in semiconductors. Non exhaustive list.

In general, the most efficient way to make light is excitonic and direct recombination because it is the fastest mechanisms to emit light. On the other hand, emission from DAP is very slow because electron and hole are not spatially at the same location and the overlap of their wavefunctions is low.

2.1.4 Performance and figures of merit

The physical background of both electrical and optical properties of semiconductors being set, it is time to discuss LED performances. In an ideal and perfect LED, *one* electron injected recombines with one hole and creates *one* photon. The yield is then of 1 as one electron is converted into one photon. But the reality is more complex and the plurality of figure of merits in the field of light source emphasizes it.

From a wide-angle perspective, the simplest efficiency to be considered is the power efficiency or **wall-plug efficiency** WPE. It is the ratio between the output optical power P_{optical} and the input electrical power $P_{\text{electrical}}$:

$$\text{WPE} = \frac{P_{\text{optical}}}{P_{\text{electrical}}} = \frac{P_{\text{optical}}}{IV} \tag{2.9}$$

with I the current flowing through the diode and V the voltage. Behind the wall-plug efficiency lies the idea of power of the photon, which is not relevant when one wants to compare the efficiency from a particle point of view.

The **external quantum efficiency** EQE is defined as the ratio of photons $N_{\bar{\nu}}$ emitted per electrons injected N_{e^-}:

$$\text{EQE} = \frac{N_{\bar{\nu}}}{N_{e^-}} = \frac{q \cdot P_{\text{optical}}}{h\nu I} \tag{2.10}$$

with ν the photon frequency and h Planck's constant. EQE gives the direct conversion efficiency in the sense that it answers to the question: *How many photons do I generate when I inject N electrons?*. This quantity represents the Holy Grail for light emitters and is the most important figure of merits. It only differs from the WPE by the ratio of photon energy over electron energy $h\nu/qV$. However, between the injection of electrons and the detection of photons, a lot of phenomena occurs. Therefore, EQE can be decomposed in several components, tracing back the story of the emission.

The **injection efficiency** η_{inj} quantifies the proportion of electrons reaching the emitting area with respect to the injected ones. Sometimes it is merged with the **internal quantum efficiency** IQE, which quantifies the percentage of radiative recombination with respect to all the recombination occurring in the active area. A well known model is the so-called ABC model of *Shockley*, *Read* and *Hall* [97]. In the assumption of hole and electron density being equals, one can state:

$$\text{IQE} = \frac{B \cdot n^2}{A \cdot n + B \cdot n^2 + C \cdot n^3} \tag{2.11}$$

with B the radiative recombination term, A the term accounting for trap-assisted non-radiative recombination and C the term accounting for high injection regime non-radiative recombination.

Finally, generated photons still need to escape the device, which can be difficult in particular for UV light and planar device. The ratio of escaping photons over the total number of photons generated is called **light extraction efficiency** LEE.
All in all EQE can be written as:

$$\text{EQE} = \eta_{\text{inj}} \times \text{IQE} \times \text{LEE} \tag{2.12}$$

Figure 2.7 is a schematic view of the progress of electrons that are injected in a LED till the extraction of generated photons, and aims at illustrating some of the main losses.

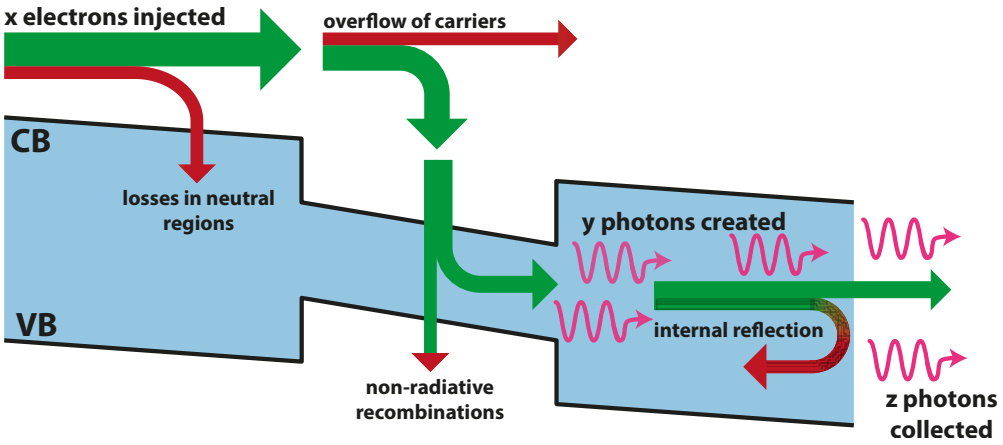

Figure 2.7: Simplified schematic of the process of conversion of x electrons into z collectable photons by the mean of LED heterostructure.

Knowing the number of photons generated inside the structure is almost impossible, thus making impossible the exact measurement of the LEE of LED. Computation and simulation however are of great help in this field [98, 99]. Similarly, it is difficult to dissociate η_{inj} from the IQE, which can be estimated by the mean of approximations (more or less *"true"*) or based on models such as the ABC model. In order to bypass those limitations, often efficiencies are gathered together or assumed to be constant with respect to a setup parameter.

2.1.5 LED architectures

The physic of a LED is simple: a bias is applied on a pn-junction, electrons and holes are injected from their respective sides, they gathered at the interface where they can recombine giving rise to a photon of the energy corresponding to the bandgap of the material. As described in figure 2.7, several phenomena can lead to losses, therefore strategies to overcome them have been developed.

Electrical improvements

p-type conductivity: In order to increase the number of charge carriers reaching the active area, the neutral regions must have a conductivity as high as possible. In the case of AlGaN, p-type doping is usually the limiting factor since ionization energy of Mg ranges from 250 meV in GaN to 600 meV in AlN [100–102] which leads to a hole concentration of around 0.1% of N_A at room temperature. Various approaches have been investigated

such as p-doped superlattice [103], tunnel junctions [104] or codoping with indium in nanowires [105] in order to promote hole injection.

Blocking layers: Electron Blocking Layer (EBL) and its counterpart Hole Blocking Layer (HBL) are structures used to reduce electron and hole overflow and increase the amount of carriers confined into the active area. EBL (resp. HBL) consists in the juxtaposition of the active area and a material with a higher bandgap with a band offset making it suitable to create a barrier inside conduction (resp. valence band) without blocking the hole (resp. electron) flow. Several studies especially in shorter wavelength emitters have demonstrated its efficiency [106–109]. However, no semiconductor has higher bandgap than AlN hence, it is not possible to make those structures in pure AlN-based device.

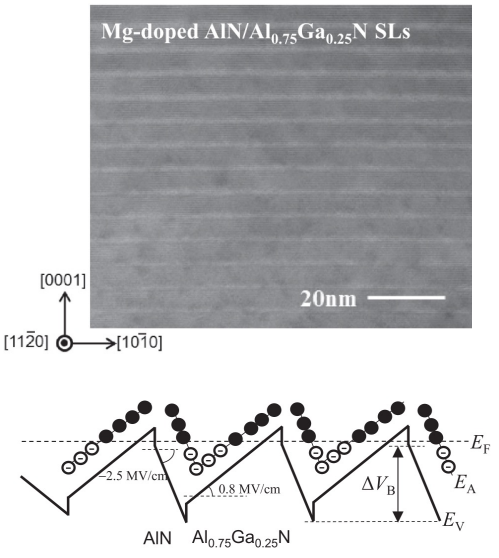

(a) Mg doped AlN/$Al_{0.75}Ga_{0.25}N$ superlattice from [103].

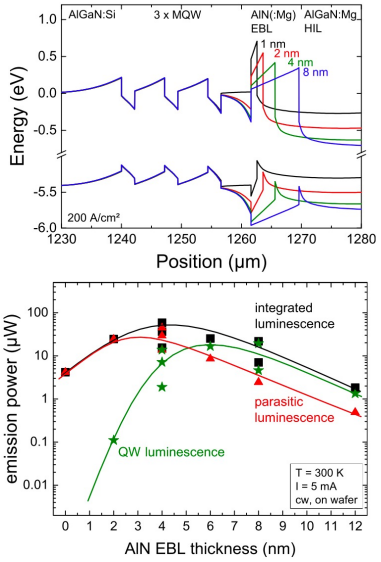

(b) Band diagram and optical power for different EBL sizes from [106].

Figure 2.8: Two architectures used in order to improve LED efficiency: (a) by increasing Mg ionization rate and free hole concentration in p-AlGaN layers and (b) by the use of an EBL in order to reduce electron overflow.

Optical improvements

Active area design: To get a high photon generation rate, electrons and holes must be spatially close to each other and have an energy level difference corresponding to the desired photon energy. In order to obtain this combination of effects, quantum well structures are widely used. It consists of a region called well in between two higher bandgap regions called barriers. Doing so, carriers will be localized within the well and spatially confined. In addition, for thin enough wells, energy levels are discrete and depend on the thickness, allowing one to tune the emission wavelength of the device. Extending this concept, the

three dimensional quantum well is called quantum dot and implies a stronger confinement of carriers. Further discussion along with experimental results are presented in Chapter 3.

Surface patterning: The photon extraction can be particularly difficult in the case of DUV AlGaN emitters because of TM polarization and the lack of transparent electrodes. Because of the lack of efficient p-type transparent materials the main strategy is to extract the light from the transparent sapphire/AlN substrate. However, it implies the loss of half of the photons in the p-side and the low refractive index difference makes the amount of internal reflection important. In this context, pattering of sapphire substrates and the use of a reflector, can improve LEE as shown in [110], [111], [99] or [112]. Nanowires appear as a non-conventional solution: indeed their patterning into photonic array, the average refractive index being different than the one of compact layer and their ability to be detached from their substrate make them interesting, to say the least.

2.2 Processing of the NWs

Between the growth of the NWs and their electrical characterizations, device has to be realized. Due to their small size, contacting of individual NWs is tedius and can result in bad electrical contact. In order to have a more reliable electrical contact and probe more than a single NWs, large arrays composed of several thousands of them are realized in clean room. To do so, metal is being deposited on the top of the sample, ensuring their electrical connection.

Therefore, this section aims to give the reader the recipe used to process the as-grown samples and turn them into devices. Processing of the samples took place at Neel Institute's clean room *NanoFab*. Standard single step optical lithography was applied in order to deposit metal on top of the sample and electrically connect thousands of nanowires.

1. The first step consists of spin coating a bilayer positive UV photoresist:
   (a) 200 nm of LOR 3A at 4000 rpm/s acceleration and 4000 rpm speed for 30 seconds followed by a 2 minutes baking at 200°C
   (b) 400 nm of S1805 at 6000 rpm/s acceleration and 4000 rpm speed for 30 seconds followed by a 1 minute baking at 115°C

2. Optical lithography is performed either by laser lithography (DWL 66 fs 405 nm laser diode) or by a Smartprint projector equipped with different lenses in order to obtain different resolution.

3. A 60 seconds bath in pure MF26 is done to develop the resist, followed by a rinsing in two water beakers before nitrogen blow drying.

4. In order to remove potential residue of resist, an oxygen plasma is applied for 6 — 8 secondes at 10 W and 50 sccm in a Reactive Ion Etching system.

5. Metal deposition is done by electron beam evaporation from pure metallic crucibles for most of the metals. A deposition rate of 1 Å/s was used and a 10° angle was set in order to avoid direct deposition of the metal at the bottom of the wires. Only ITO was deposited using magnetron sputtering at 50 W and an argon flow of 10 sccm.

6. The lift-off step is realized in pure N-Méthyl-2-pyrrolidone (NMP or Remover PG) at 80°C for at least 3 hours followed by an isopropanol cleaning prior to dry the samples with dry nitrogen. A gentle ultrasonic bath could be useful in order to help the lift-off.

7. Finally, when needed, annealing of metals took place in a tubular oven under a nitrogen flow. Temperatures are set and kept constant at 500°C for Ni/Au and 600°C for Ti/Al and Pt/Pd/Au metal stacks.

Morphology of the nanowires are of major importance. If the roughness is too large and the coalescence too little, the metal deposition step would be difficult. In order to make a proper layer, the metal has to stick and remain on the sample surface. Sometimes, the deposition is made impossible as NWs do not exhibit the same height and a coalescence degree smaller than at least 90%. As an example, figure 2.9 shows two NW morphologies from SEM images as well as the result after the same process. After lift-off, no metal remained on the top of the NWs which have structural inhomogeneities (figure 2.9a).

Clean room process can be tedius and disappointing sometimes. I hope people willing to continue this technique, will be able to reproduce the process and adapt it if needed.

2.3 Characterization techniques

2.3.1 Current-Voltage characteristics

Current voltage characterization is the most simple technique to characterize electrical behavior of a device. After processing of the nanowires, the sample is glued on an alumina plate using silver paste in order to electrically isolate it from sample holder. Using tungsten tip mounted on nano-manipulators, the deposited metal is connected to make the *top* contact. A second tip is put on the silver paste or directly on the Si wafer which is highly conductive; it is the *bottom* contact. The tips are then connected with triaxial cables to source measurement units (SMU) which can be:

- *Keithley* 2612 / 2636: standard current and voltage source units (detection limit down to 100 fA and 0.1 fA)

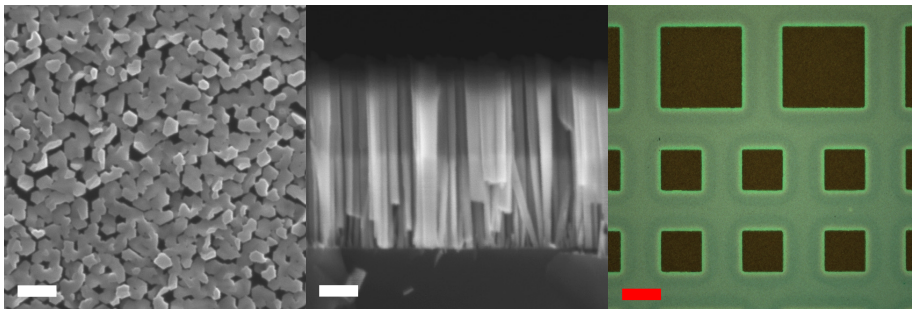

(a) Lower density and coalescence.

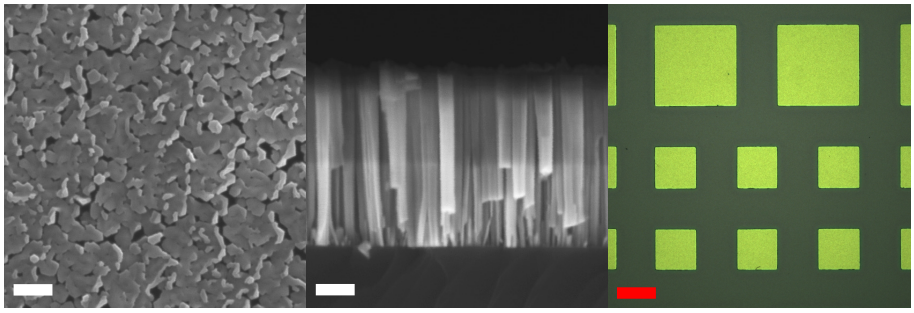

(b) Higher density and coalescence.

Figure 2.9: Top view (left) and cross sectional view (middle) of AlN NWs. Optical microscopy of after lift-off of Pt/Pd/Au (10 nm/10 nm/50 nm) metal stack. White scale bar is 200 nm. Red scale bar is 100 µm. On the low density sample, metal did not formed a layer onto the NWs and has been removed during lift-off.

- *Keithley* 6517: high impedance electrometer, made to measure high resistances (detection limit down to 1 fA)

- *Solartron ModulabXM* equipped with high voltage and low current modules: a system which can perform simple DC measurements as well as more complex AC and impedance measurements (sourcing up to 100 V a detection limit down to 0.2 fA).

Detection limit of the full measurement line is higher than the one datasheet reports because of leakage from ground, discharging time and technical considerations. *Keithley* systems were the most used in my thesis with detection limit around 1 pA for the 2612 and 0.1 pA for the 2636 and 6517 SMUs.

The main setup for IV measurements is shown in figure 2.11, consisting of an enclosed box allowing to reach vacuum down to 10^{-4} mbar. The sample holder can be heated up to 350°C and cooled with liquid nitrogen. Because of temperature gradient in the sample holder, the use of a Pt100 thermocouple glued on the same alumina plate is relevant in order to measure the sample temperature accurately. A Xenon lamp coupled with a monochromator (not shown) can be used in order to inject light on the sample or, complementarily, one can collect light from the sample using a photomultiplicator as detector and the same monochromator.

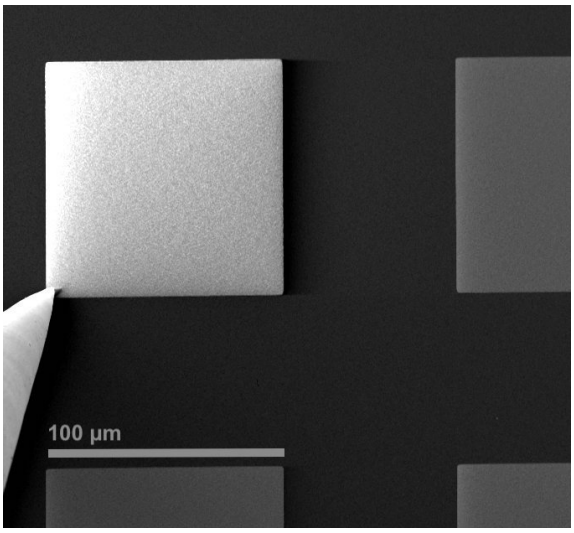

Figure 2.10: SEM image of a contacted pad. The -3 V was applied on the pad is responsible for the different contrast with respect ot the other pads.

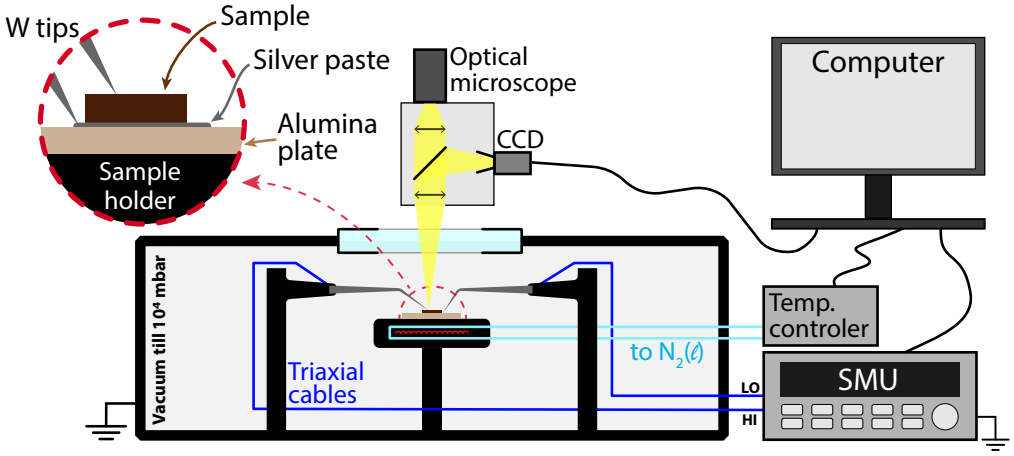

Figure 2.11: Schematic of the probe station used for IV measurements in the enclosed box.

2.3.2 Electron beam based techniques

Two characterization techniques based upon the injection of charge carriers by the mean of an electron beam were used many times in this PhD.

Electron beam induced current

Electron beam induced current (EBIC) is a great tool when it comes to map electrical field within a material. A schematic representation of a pn-junction under EBIC measurement is shown in figure 2.12 with relevant values along the junction. The concept is quite simple: an electron beam is focused onto the material and creates many electron-hole pairs. Under the effect of an internal electric field, electron and hole will be separated, generating

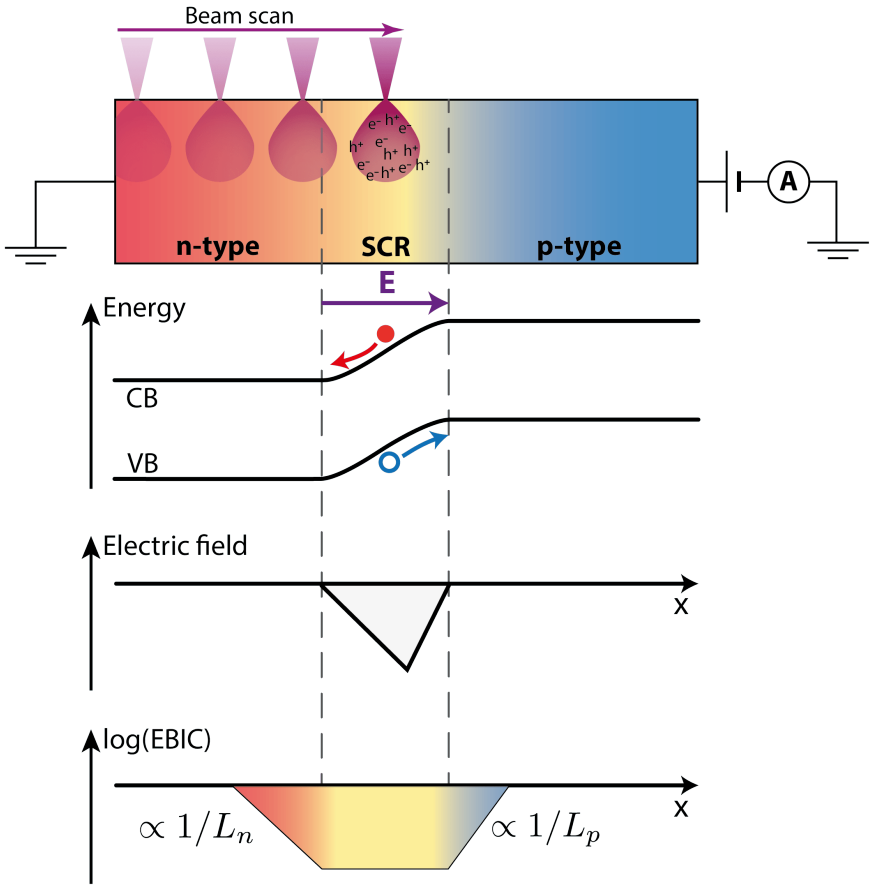

Figure 2.12: Schematic of ideal EBIC measurement setup of a pn-junction along with its band diagram, electric field and EBIC variation.

a current which one can collect and measure. This internal electric field might come from any potential barrier (pn-junction, Schottky contact) and/or from the application of a bias on a structure. If no electric field is present, the particles will recombine and no signal is detected. Therefore EBIC allows to probe the location of any electric field as long as the generated carriers can be collected.

In addition, carriers generated close to this region may diffuse and be collected. This effect being directly linked to the diffusion length of minority carriers, it can be measured as EBIC scales, in these conditions, with $\exp(-x/L_{n,p})$. However, this is true only in low injection regime in which minority carriers are the only contributor to the signal. Otherwise both electrons and holes diffuse and the measured length corresponds to a mix of the two diffusion lengths.

Cathodoluminescence

With the electron beam, many electron-hole pairs are generated in the structure. Contrary to EBIC, one is interested in the light arising from the radiative recombination of those pairs. Therefore the goal is no longer to separated the charges. Cathodoluminescence (CL) is very similar to photoluminescence (PL) but allows to reach a spatial resolution of the size of the interaction pear (few tens of nm) and to excite any material regardless their bandgap. One drawback is the difficulty to inject carrier in sufficiently low concentration in the material and perform accurate injection dependent measurements. Since no laser able to optically pump and excite AlN is available in Grenoble, CL is the main tool used to probe the optical properties of our samples.

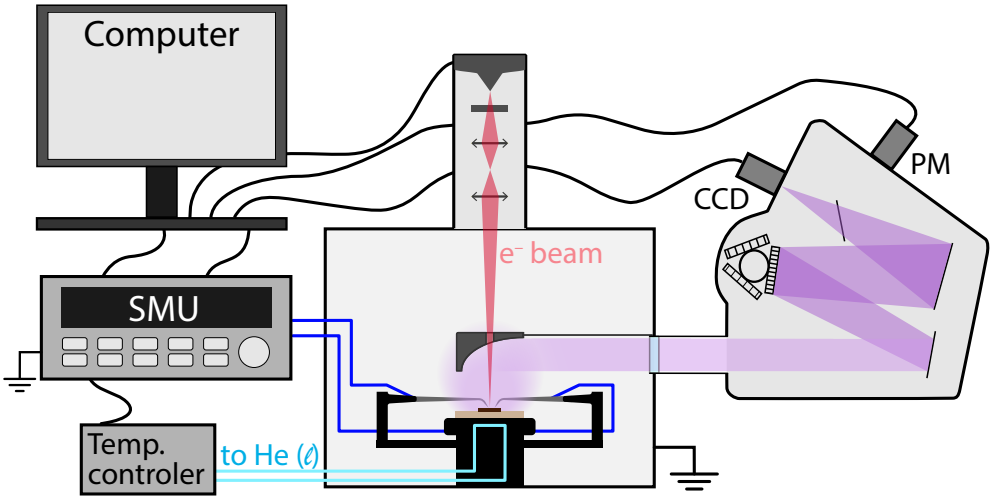

Figure 2.13: Schematic of the SEM setup used for EBIC, CL and EL measurements.

Both EBIC and CL experiments can be performed in the same setup shown in figure 2.13 which is a custom SEM. From the one hand, it is equipped with a parabolic mirror used to collect the light created by the sample and direct it towards a spectrometer for CL experiments. On the other hand, the stage is equipped with four nanomanipulators connected to SMU via triaxial cables for EBIC and IV measurements. Moreover, the sample holder can be cooled with liquid helium down to 5K. Using this versatile tool, electroluminescence can be measured in this setup as well. To do so, the carriers are injected electrically by the tips and the light is collected as in CL.

2.4 Summary of Chapter 2

Chapter 2 is primarily focused on the basics on physics of light emitting diodes and aimed at setting the vocabulary as well as the concept that will be discussed in the following chapters. Clean room process is detailed in order to promote its reproducibility through generations and, perhaps, laboratories. Finally, a focus is made on the two main setup and experimental techniques applied along this research work in order to characterize the sample, either basic material or complex heterostructures.

CHAPTER 3

Controlling light emission in the UV-C range in AlN NWs

In this chapter, means of producing light in the UV-C range are investigated, putting in perspective growth mechanisms and structural and optical characteristics. First, the realization of pure binary AlN / GaN heterostructures is addressed. Then, the particular case of AlGaN with very low Ga content is reported and its properties are studied.

Contents

3.1 Routes to UV-C emission 58

3.1.1 AlGaN based structures 58

3.1.2 Nanowires specificity 59

3.1.3 Binary heterostructures 59

3.2 GaN wells into AlN barriers 60

3.2.1 Standard growth 60

3.2.2 Alternating fluxes 63

3.3 Ga doped AlN NWs 69

3.3.1 Beyond GaN wells 69

3.3.2 Structural and optical properties of Ga doped AlN NWs. 72

3.3.3 At the edge of alloying 76

3.4 Summary of Chapter 3 78

3.4.1 Conclusion on active area realization 78

3.4.2 To go further 78

3.1 Routes to UV-C emission

3.1.1 AlGaN based structures

As stated in the introduction and in Chapter 1, III-Nitrides (except BN) are direct bandgap semiconductors and alloying them allows one to emit light in a wide spectral range. For emission below 350 nm, either AlGaN or AlInN with In content $> 0.25\%$ [113], can be used. The growth of AlInN is known to be challenging because of the large difference in bond strength between Al-N and In-N as well the large difference in typical growth temperatures. In spite of these physical considerations, its growth is still possible but is not in the scope of this work.

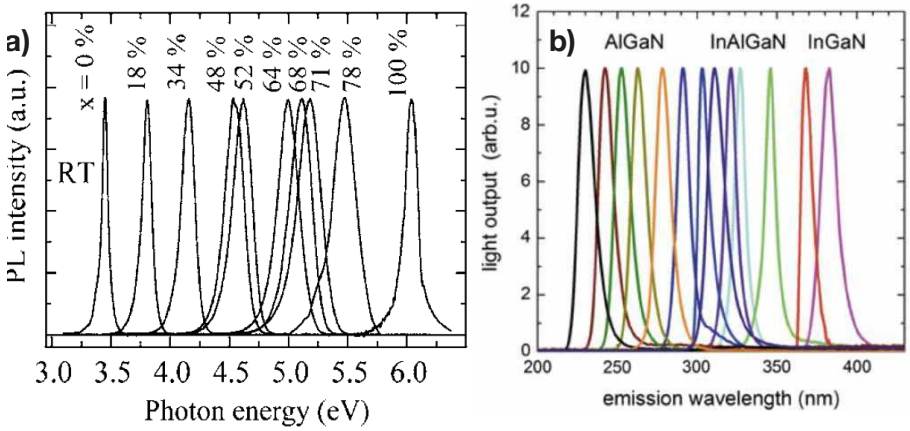

Figure 3.1: (a) Variation of the near band-edge emission energy as function of the Al content in the AlGaN layer (from [114]). (b) Examples of variations of emission wavelength depending on the family of III-N alloy used (from [1]).

In regards of more standard AlGaN thin films, their growth is much easier to control, allowing one to target an emission in the whole UV range (figure 3.1) [1, 114, 115]. The more common structure for this purpose remains a quantum well (QW). Since its thickness controls bandgap energy, engineering of such structure is quite simple and rely on mainly four parameters: AlGaN layer thickness and composition of wells and barriers. However, it requires some experience since interface roughness and overall homogeneity over wells and barriers are key parameters, needing an accurate optimization.
(Al)GaN quantum dots (QD) are also a way to reach deep UV by confining the exciton in three directions and good results have been shown with such structures [116–118]. However because these dots are Stranski-Krastanov (SK) dots, a wetting layer acting as a QW will first form prior to relax in a QD. Strain accommodation is the driving force for their formation and can be limiting in some cases, for instance in AlGaN QDs if the strain is too low.

3.1.2 Nanowires specificity

It is not possible to achieve 3D confinement of excitons in MBE grown NWs because of their diameter of 50–100 nm which is still to large. Firstly, SK QDs can't be grown because of strain relaxation at the NW sidewalls which prevents the transition into island growth mode. Secondly, the exciton size being of roughly 3 nm in GaN, the nanowire itself is too large to confine it in this plane.

The solution left is to create a 1D confinement by growing AlGaN QWs (also called quantum disks) along c-axis. At first sight, it appears to be a reasonably simple solution, supported by the state-of-the-art of DUV LEDs. However, working with nanowires is more difficult as they are not particularly suited for controlled growth of AlGaN alloy. As already reported many times, AlGaN NWs are subject to large compositional inhomogeneities in axial and radial directions. Noticeably, growth often results in self-assembled and irregular AlN/GaN superlattice-like structures as shown in figure 3.2 [119–124]. In addition, fluctuations can be large, nucleation of AlGaN sections can be delayed [119]. The plurality of reports in various systems, such as m-plane MOCVD grown NWs, supports the fact that this property is intrinsic to the material itself under growth conditions commonly used.
Physical explanation lies in several points. Firstly, the difference in diffusion length between Ga and Al leads to an excess of Al on the NWs sidewalls, unable to reach the top facet. This results in a larger radial growth rate compared to GaN NWs as well as a deficit of Al atoms with respect to Ga ones. Furthermore, Al takes priority over Ga when incorporating in a growing layer, leading to Ga accumulation on the surface prior to its own incorporation. Structural properties of AlGaN NWs were associated to their optical properties, which shows strong localization and single-photon emission properties [125]. In view of these considerations, the precise control of both composition and thickness of several quantum wells on an assembly of thousands of NWs is challenging.

3.1.3 Binary heterostructures

To avoid ternary alloys, the solution left is the growth of binary AlN/GaN heterostructures. By reducing the size of GaN QWs down to a few monolayers, the extreme confinement results in a large UV-shift of the GaN QW emission. Advantages are numerous: tunable wavelength between ∼230 nm to 350 nm, high confinement leading to an increased IQE [126] and negligible quantum confined stark effect thanks to reduced thickness. This solution presents also the advantage of producing a TE-polarized light propagating along c-axis, contrary to AlGaN with Al $>$ 60%, which is TM-polarized.

An emission wavelength of 237 nm has already been demonstrated in MOCVD grown short-period superlattices of 0.9 ML GaN QWs [127], and recently reproduced by MBE by the group of Prof *Jena* (figure 3.3) [128, 129]. Although precise control of growth at the monolayer level is very challenging even for MBE systems, it is even more complicated in

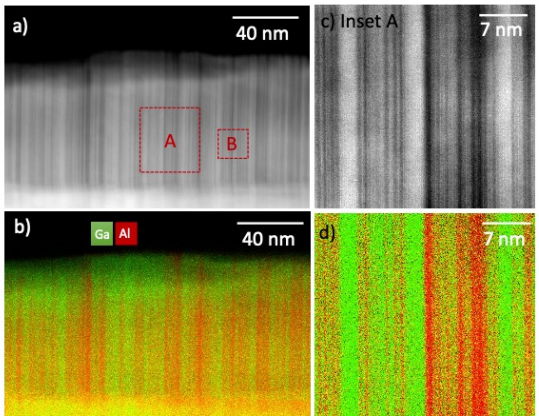

(a) HAADF HR STEM view (top) and corresponding EDX spectrum (bottom) of an $Al_{0.6}Ga_{0.4}N$ NWs [122].

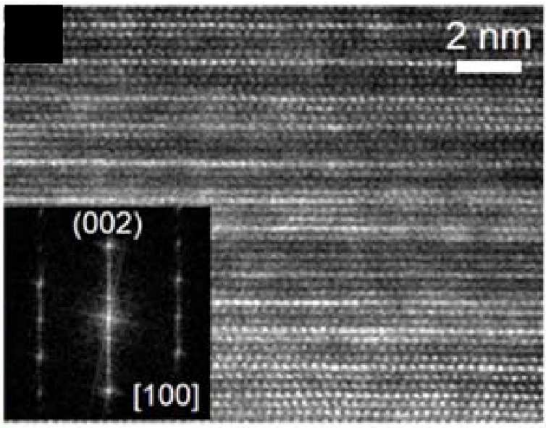

(b) HAADF-STEM of $Al_{0.75}Ga_{0.25}N$ NWs [123].

Figure 3.2: Alloy fluctuations in AlGaN NWs

NWs and a unique report has been published [130]. For all the reasons discussed above, this concept is logically the one chosen in this work to achieve UV-C emission in a controlled manner.

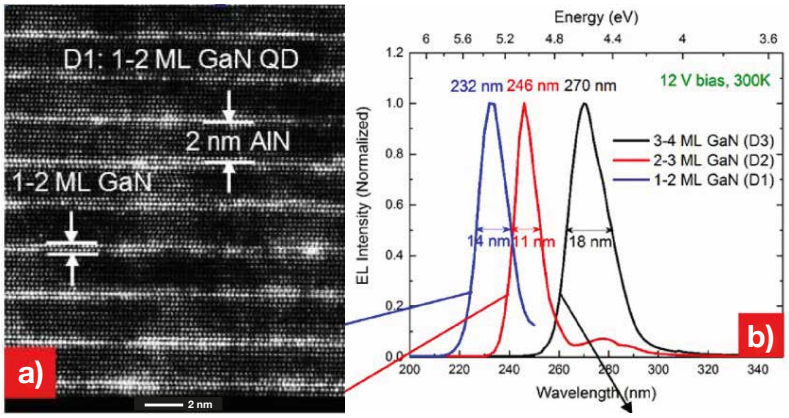

Figure 3.3: a) HR-TEM image of ML thin GaN quantum wells in AlN barriers. b) Electroluminescence ML thin QW LEDs according to the GaN quantum well thickness. Both from *Islam et al.* [129].

3.2 GaN wells into AlN barriers

3.2.1 Standard growth

To start this study, four samples have been grown on 5 nm TiN mask sputtered on (111)-Si substrate. More details can be found in Appendix E. Secondary electron images of one of the samples are presented in figure 3.4, showing a much lower density and few

coalesced NWs thanks to the nucleation on TiN mask. These morphologies are particularly suited for optical characterizations and NW dispersion for TEM observations. After the growth of a 500 nm long GaN stem at a temperature of 790°C, a 200 nm long AlN section was grown at a temperature of 850°C both at III/N ratio of 0.4. Subsequently, the growth of the active region was performed according to the growth procedure detailed in figure 3.5 and at a temperature of 700°C. Finally, a 30 nm thick AlN cap was realized.

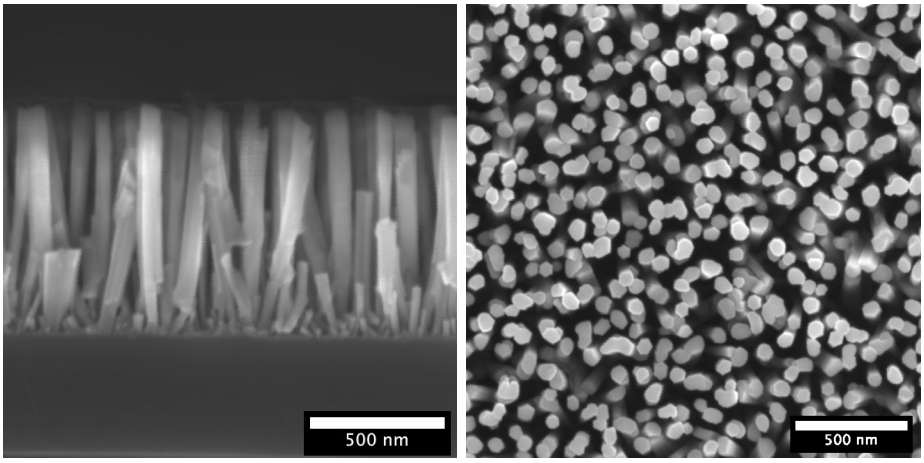

Figure 3.4: SEM cross sectional and top view of one of the four samples of the present study.

Ten quantum wells were grown by applying a nitrogen flux of ∼0.16 ML/s and a Ga flux of ∼0.1 ML/s for a variable duration t_{Ga} ranging between 4 and 40 seconds. For each samples, AlN barriers were grown for 100 seconds with an Al flux of ∼0.1 ML/s. Changes in GaN quantum wells thickness had no influence on the NWs morphology.

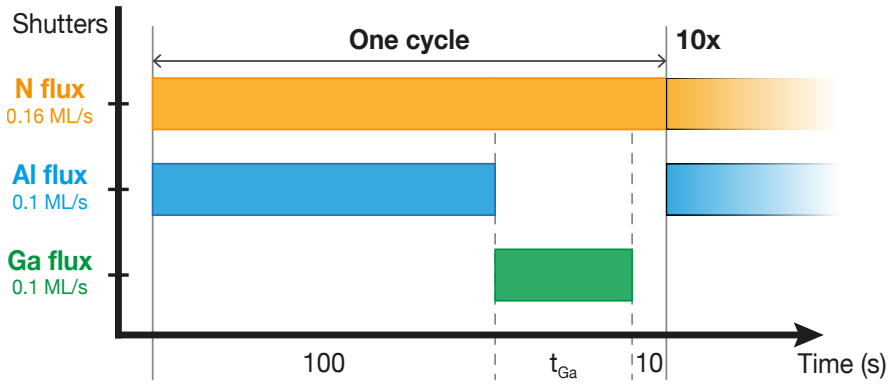

Figure 3.5: Growth diagram of the emitting region of the samples. t_{Ga} stands for GaN growth duration.

Optical characterizations were done by CL at room temperature, scanning a large 100 μm^2 area with a 15 kV e-beam. A comparison of normalized CL spectra can be found in figure 3.6. For 40 seconds exposure, a single peak is observed centered at 340 nm, in agreement with a GaN quantum well emitting at smaller wavelength than bulk GaN. For

duration of 20 seconds, the main peak shifts towards higher energies and reaches 280 nm. The QWs being thinner, confinement energy increases resulting in this emission energy shift.

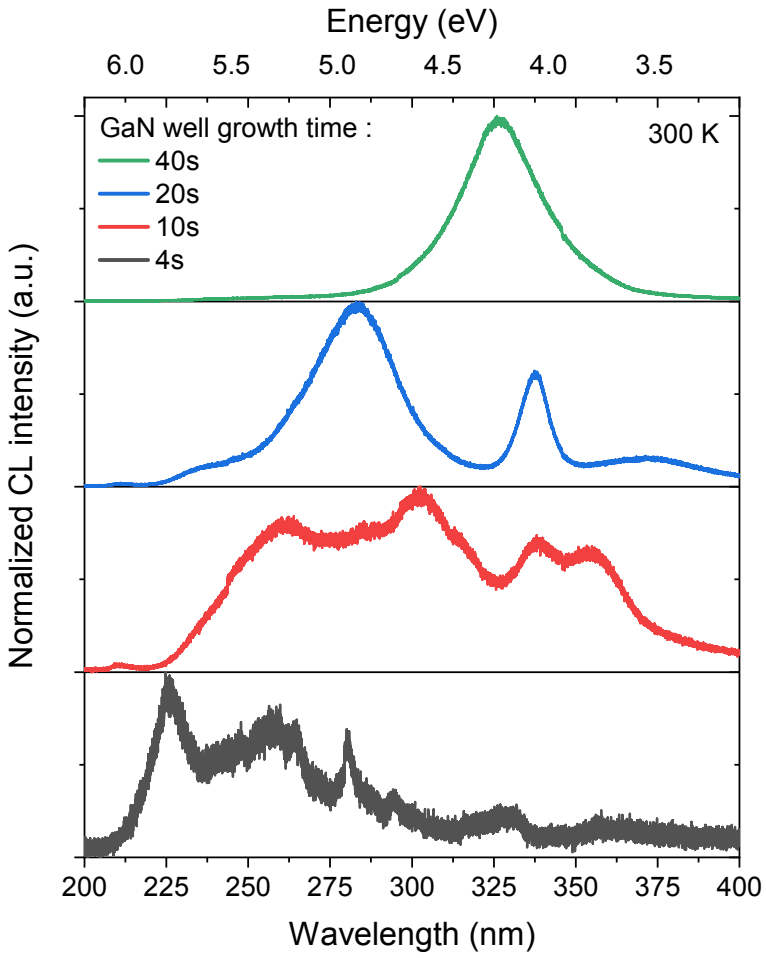

Figure 3.6: Room temperature CL spectra of samples containing GaN QW with various QW growth duration.

This trend changes as the duration is further reduced. In both the 10s and 4s samples, the smaller wavelength emitted shifts towards lower wavelengths, as expected. However, several peaks are present and overlap. This effect is attributed to large QW thickness fluctuations.

This can be understood as the nucleation of a layer is a stochastic process at the scale of a NWs. Especially, the nucleation probability is proportional to the density of adatoms. If one can precisely control this flux on 2D layers, growing such structures on NWs is more troublesome. In the light of *Gruart et al.* [131], the nucleation of the top layer is initiated at the periphery of NW, where adatoms density is the largest. However, depending on its diameter and on shadow effect, the contribution of adatoms coming from the NW sidewalls can be different from one nanowire to another. Therefore, the time for a layer to form can be slightly different from NW to NW.

In the end, growing thin GaN quantum wells in AlN barriers by exposing the nanowires to a simultaneous flux of metal and nitrogen is tedious due to the nature of the nucleation of monolayers and the variability in NW geometries. If the latter would require perfectly identical NWs, made possible by the use of patterned substrates, the first can be adjusted by growth mechanisms, as demonstrated in the next section.

3.2.2 Alternating fluxes

State-of-the-art growth of c-plane GaN thin films relies on the growth in metal rich conditions. In such manner, a liquid Ga bilayer forms which increases diffusion length and reduces surface roughness, among others [132–134]. Particularly, this bilayer is self-regulated and limited to two atomic layers on Ga-polar and one monolayer in the case of N-polar surface [135]. Despite these great assets, growth in metal rich conditions is not suited in the case of nanowires because it implies their enlargement, along with coalescence and structural defects [131]. However, it is still possible to grow in pseudo metal rich conditions by saturating the surface. This technique is used in thin films to grow atomically thin AlN layers [136] or AlGaAs [137] in the so-called migration enhanced epitaxy (MEE). By alternalty supplying Al and N species, MEE allows to enhance surface migration of adatoms on the surface.

Three samples have been grown with the same nucleation steps as the previous ones. Only the active area recipe changes with a growth at 750°C, following the shutter sequence in figure 3.7. One cycle is now composed of a sequence of metal and nitrogen exposures. This permits metal atoms to diffuse and accumulate at the top of the NWs. Once it is filled, this metal layer is exposed to nitrogen to form the nitride layer. The process is repeated twice for the growth of AlN barrier and between one and three times for GaN QW. A longer Al exposure with respect to Ga one is applied in order to balance Al shorter diffusion length. Nitrogen is supplied at a larger flux to make sure no metal atoms remain at the top and they are all incorporated, especially Al which does not desorb at such temperatures.

Table 3.1: Description of samples with the number of (Ga/N) cycle repetition.

Sample name	N3702	N3703	N3704
# (Ga/N) cycle	1	2	3

Figure 3.8 shows CL spectra measured at room temperature of the three samples, acquired at the same position on the three wafers. With 1×(Ga/N) cycle, a weak and wide peak is observed at 245 nm with a large contribution of the GaN stem at ∼350 nm. On the other side with 3×(Ga/N) cycles, N3704 shows similar characteristics as the 40s GaN sample in figure 3.6 with a main peak at 320 nm but with an additional contribution at 265

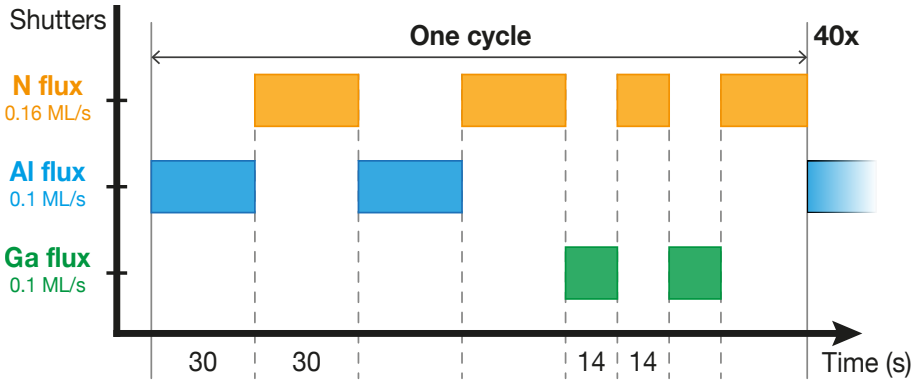

Figure 3.7: Growth diagram of the emitting region of the new samples with N and Metal exposures alternated. Example for N3703.

nm. With 2×(Ga/N) cycles, N3703 exhibits three peaks at 240 nm, 265 nm and 285 nm, in addition to the signal arising from the GaN stem. Remarkably, peaks are aligned from samples to samples. This plurality of peaks is consistent with the supposed discreteness of the GaN well thickness.

To go further, additional CL measurements at 5 K were performed on the latter sample, and at various position along the wafer. Results are shown in figure 3.9. Several peaks from 239 nm to 304 nm appear and are aligned with each others, with variable intensity. As the measurement area is displaced towards the edge of the wafer, peaks shift towards higher

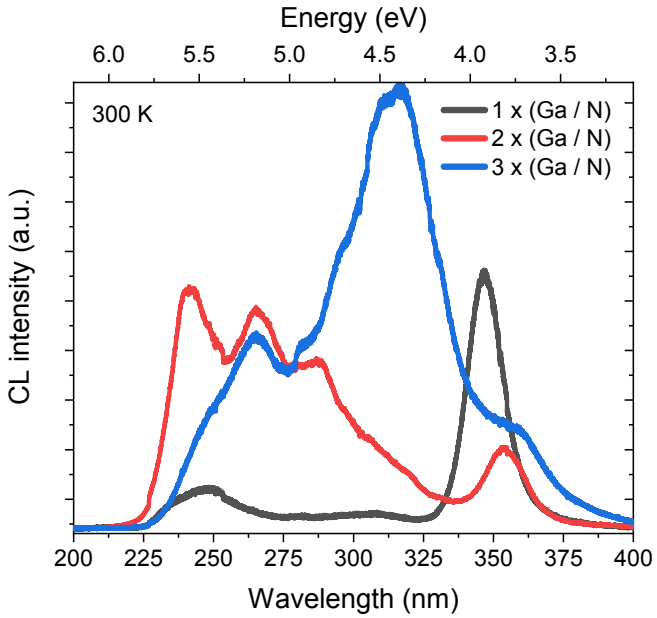

Figure 3.8: Room temperature CL spectra of samples grown with alternate exposures for 1, 2 and 3 × (Ga/N) cycles.

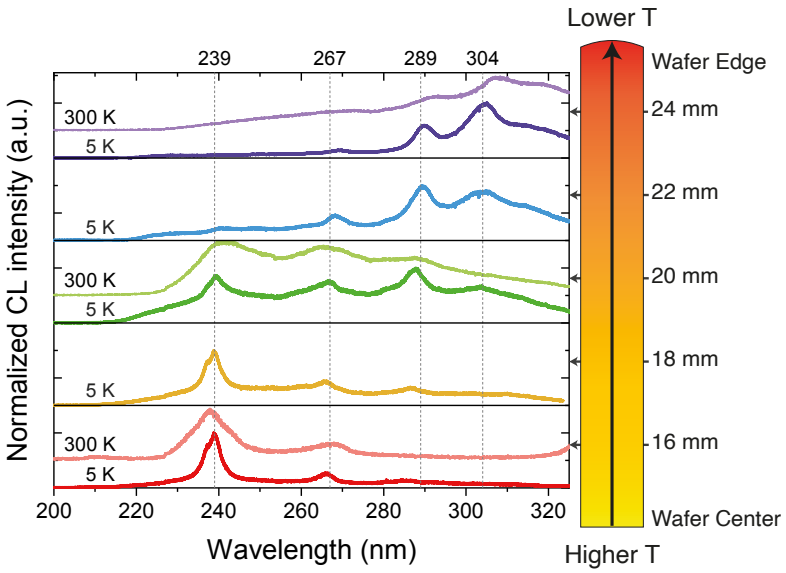

Figure 3.9: Normalized CL spectra of 2 × (Ga/N) sample for various positions along the wafer. Dark curves are at 5 K. When presents, light curves are measured at 300 K. Right cartoon represents a wafer slice with the positions on which CL signal was acquired.

wavelength in a discrete fashion. These observations are consistent with the presence of different GaN well sizes of 1, 2, 3 and 4 monolayers thick. These fluctuations across the sample can be explained by the temperature gradient at the substrate surface. Because the temperature reduces by $\sim$ 20 degrees, desorption of Ga atoms is changed [138]. Thus, the amount of Ga at the top of the wire before nitridation increases as the temperature decreases which leads to thicker well.

High angle annular dark field (HAADF) high resolution (HR) STEM images were taken on a similar sample (N3698) but grown at too high temperature leading to the presence of luminescence only at the wafer edge (not shown). Nevertheless, its CL properties were identical to N3703 at 18 mm. HR STEM images reveal the presence of 1–2 ML thick GaN wells into 5–6 ML thick AlN barriers (Figure 3.10). These slight fluctuations show that even if the active area formation has been improved by alternating the fluxes, interfaces are not perfectly regular and further improvements can probably be made during the growth. The presence of a rather thick AlN shell around the QW area can also be observed in figure 3.10 (a), which will probably introduce strain in an hydrostatic manner and affect the emission energy.

With lighter colors in figure 3.9, room temperature CL spectra at approximately the same positions were recorded and plotted with the one at 5 K in figure 3.9. All the peaks can still be clearly distinguished without changes in their positions. It confirmed the marked robustness of the luminescence and points towards a high degree of localization of excitons in the nanostructure.

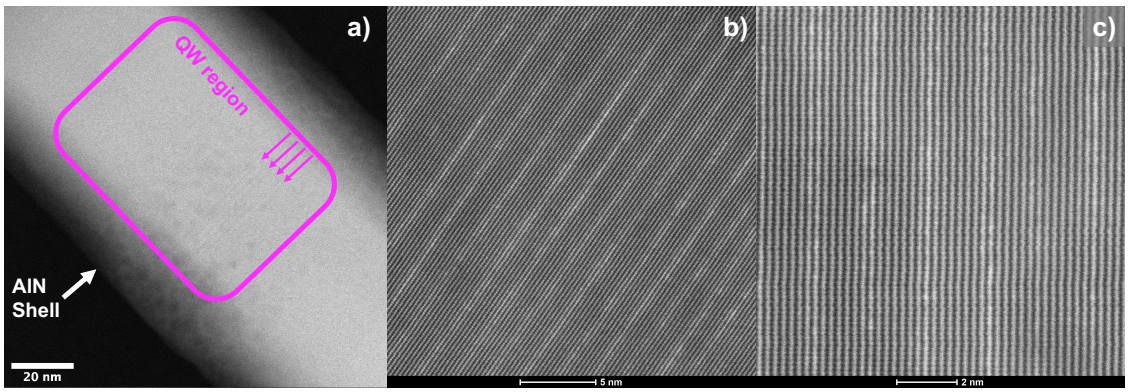

Figure 3.10: HAADF STEM images of N3698 taken at around 24 mm. (a) Large view of the NWs showing the quantum well region, indicated by the pink rectangle and arrows. (b-c) HR-STEM images of the ultra-thin quantum wells.

CL spectra were acquired as function of the temperature at the 20 mm position of N3703 (Figure 3.11 (a)) and CL intensities were integrated around the three peaks denoted by stars (Figure 3.11 (b)). They all show a similar behavior with a ratio CL(300 K)/CL(5 K) of around 20% which is relatively high at these wavelengths.

CL mapping at 5 K were acquired using a photomultiplicator. Images are shown in figure 3.11 (c-e). From the map at 370 nm one can clearly see the contribution of the GaN stems. The hyperspectral map in figure 3.11 (e), color-coded as red, green and blu, correspond to 287, 267 and 240 nm, respectively. Blue, green and red pixels are distinct indicating that each NW emits at a single wavelength and contribute to only one of the three peaks. Therefore, the inhomogeneity observed in figure 3.11 (a) is due to ML thickness variation from NW to NW and not within the NWs. These variations might arise from variations in NW diameter and shadow effect, which would lead to different metal atoms at the top of the wire, thus to different thicknesses.

To conclude this study, its is of good practice to look at this result in the light of previous reports. Figure 3.12 proposes a literature review of luminescence wavelength for GaN ultra-thin quantum wells into AlN barriers grown on c-plane. Except for the work of *Aiello et al.* and *Wu et al.*, all are in 2D layers. The results of the present work follow the trend observed in the literature, however slightly shifted towards higher wavelengths by $\sim$ 20 nm. Two possible facts could account for this shift, one experimental bias and one physical effect.

Firstly, thickness measurement of ML thin QW is challenging and uncompleted monolayers or interface roughness leading to important potential fluctuations and thus different emission energies. Some articles used high-resolution X-Ray diffraction while others relied on direct measurements of HR-STEM images or simulations. Independently of the methodology applied, uncertainties are present on the QW size. In the present work, according to

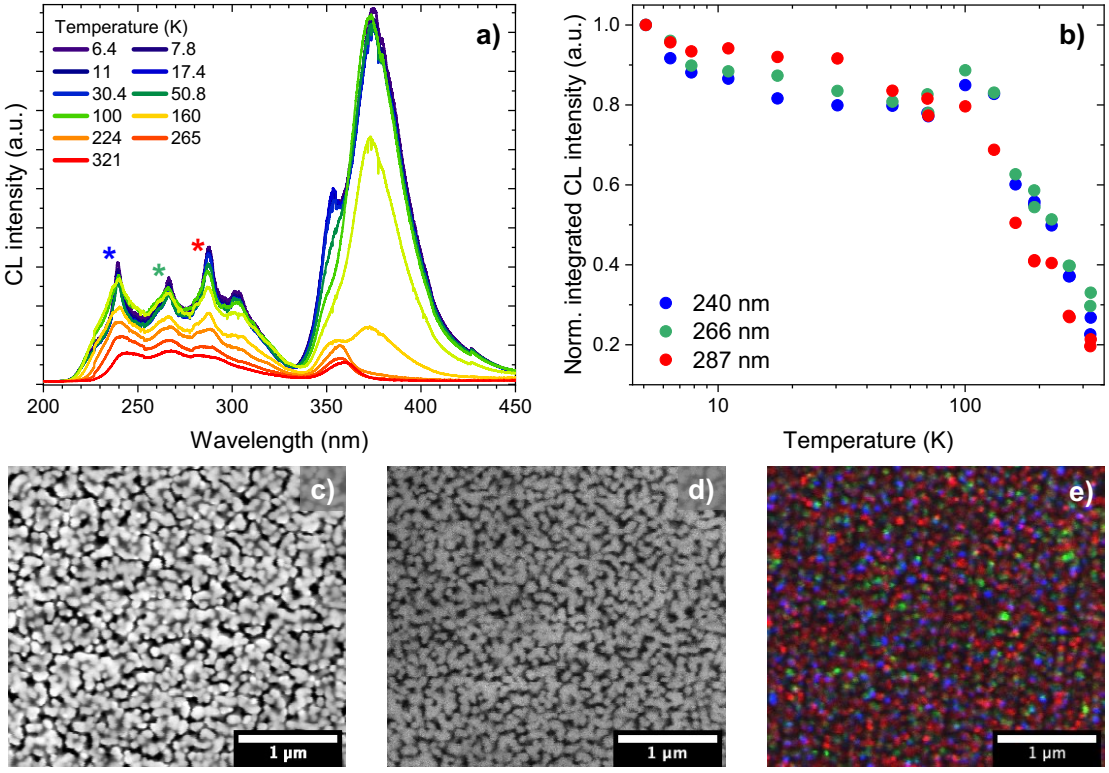

Figure 3.11: (a) Temperature dependent CL spectra of N3703. Stars denote the peaks used in (b) and (e). (b) Integrated CL spectra as function of the temperature. The integration bounds are ± 5 nm centered at the peak position indicated in the legend. (c) Secondary electron image of the scanned area for (d-e). (d) CL map at 370 nm. (e) Hyperspectral CL map of the area. Blue: 240 nm, green: 267 nm, red: 287 nm. Spectral window for maps in (d) and (e) is of ± 3 nm.

TEM images, the shorter wavelengths would correspond more to a 1–1.5 ML than a pure 1 ML and uncertainties on the thickness of ± 0.2 ML is assumed. Moreover, AlN barrier thickness is not always mentioned, even if this value if of importance. Especially, a thinner barrier would lead to an emission shifted towards smaller energies and could account for some of the discrepancies observed.

Another explanation lies in the strain state of GaN QWs. The fact that the emission is systematically red-shifted points towards more relaxed GaN QW in NWs compared to 2D layers. To account for this, several points must be recalled. On the first hand, as previously reported, the critical thickness of GaN layer on AlN is of at least 2.4 ML but highly depends on growth temperature and threading dislocation density [139, 140]. Therefore, NW geometry could be seen as a perfect crystal without extended defects. However, it has been reported that in GaN quantum disks embedded in AlN NWs, misfit dislocations may appear in the AlN shell allowing the crystal relaxation in the case of 2.5 nm thick disks corresponding to about 5 MLs [141]. On the other hand, in the present case of very thin GaN quantum disks between 1 and 4 MLs, the presence of the thick AlN

shell (Figure 3.15) adds a non-negligible strain component along c-axis by contrast to the purely in-plane biaxial strain in 2D layers [142]. All these facts make difficult to conclude on how the strain state of GaN QW in NWs differs from those in thin films.

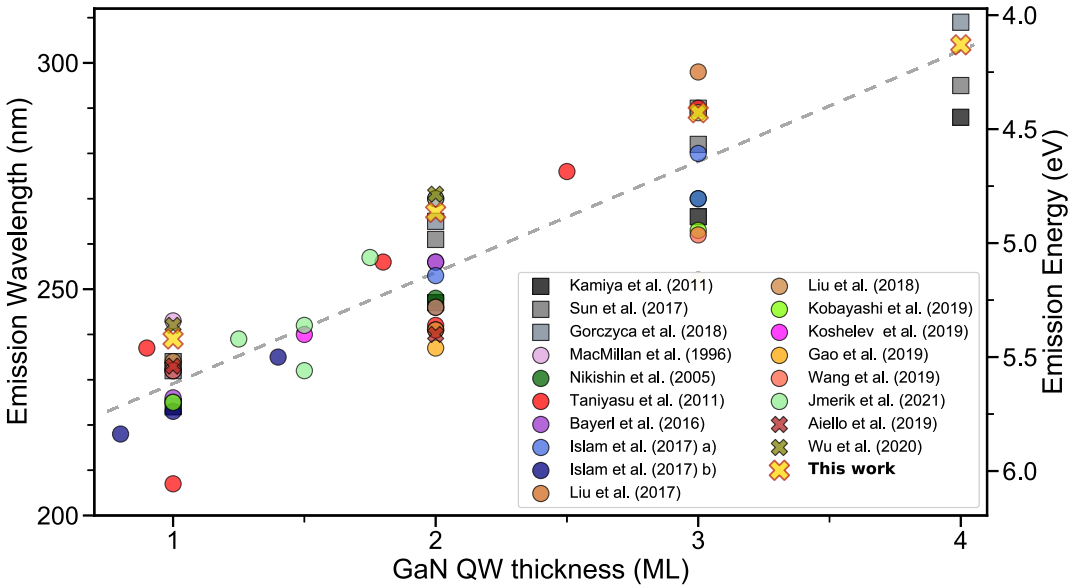

Figure 3.12: Review of reported room temperature luminescence peak wavelength for monolayers thin GaN wells into AlN barriers on c-plane. Squares are for simulated data [143–145], circles and crosses are for experimental values in thin films [126–129, 146–154] and nanowires [130, 155] respectively. y error bars on are of the size of the marker corresponding to ± 2 nm. Grey dashed line is a guide for the eye.

3.3 Ga doped AlN NWs

3.3.1 Beyond GaN wells

In regards of the previous results, the realization of a LED was attempted. The growth of sample N3784 was performed on Si substrate and the overall growth will be detailed in Chapter 6. In order to increase the homogeneity over the wafer and from NW to NW, a modified growth was used for the active area, which is shown in figure 3.13. It consists in 5 repetitions of only 2 × (Al / N) and 1 × (Ga / N) cycles. To further increase Ga diffusion, growth temperature was raised to 800°C instead of the 750°C previously used. Moreover, gallium flux was tripled compared to previous samples to 0.3 ML/s, in order to increase bi-layer coverage on top of the NWs and counteract its desorption.

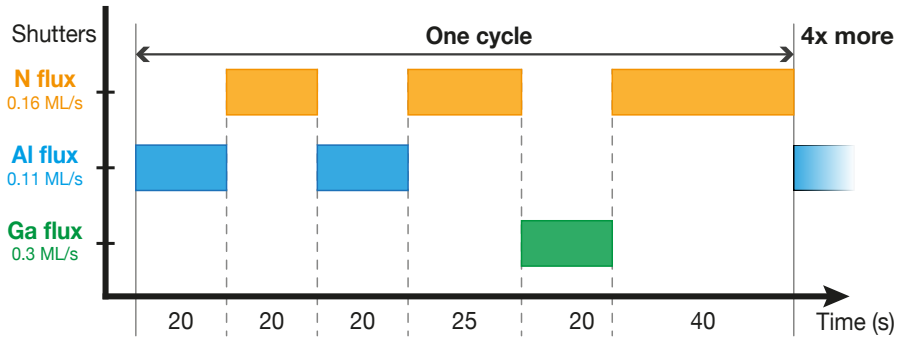

Figure 3.13: Growth diagram of the active area of sample N3784.

Results from CL experiments are displayed on figure 3.14. From CL spectra at room temperature (Figure 3.14a), the main peak centered at 285 nm is attributed to the signal arising from the active region with contribution from GaN sections at around 360 nm and a blue band at ∼ 420 nm, supposedly due to donor-acceptor pairs (DAP) recombination. The main peak at 285 nm is attributed to the active region but is found to be at much higher wavelength compared to the expected value from ML thin well studied previously. However and as intended, the recipe led to a better homogeneity of the signal on several millimeters across the wafer and from NW to NW as shown on the CL mapping of figure 3.14d. Still some brighter spots can be noticed, which will be assigned in the next paragraphs.

To investigate on the discrepancies of emission wavelength between N3703 and N3784, HR-TEM images were taken (Figure 3.15). No evidence of presence of QWs were found, neither any contrast indicating AlGaN section in the AlN nanowires. EDX in TEM measurements were performed on several NWs and indicate a Ga composition of at most 2% in the active area and top section while it is less then 1% at the bottom of the AlN section. The presence of the p-type GaN cap is interfering with the measurements as a this GaN shell is also probed. It therefore increases the number of Ga counts but cannot be

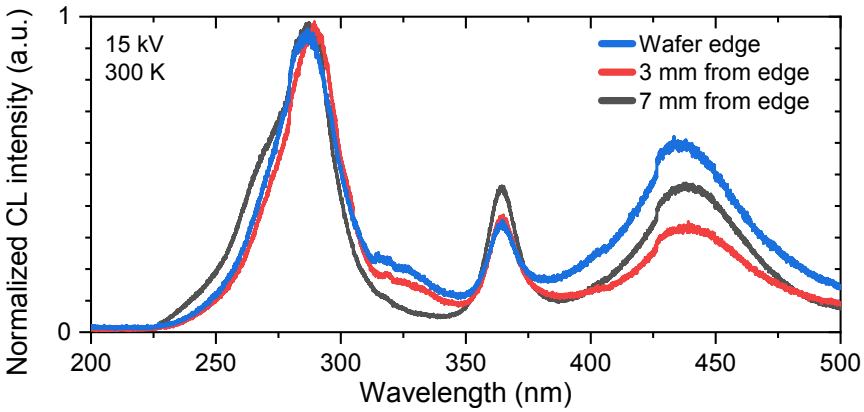

(a) Room temperature CL spectra of a $10 \times 10\ \mu m^2$ NWs array.

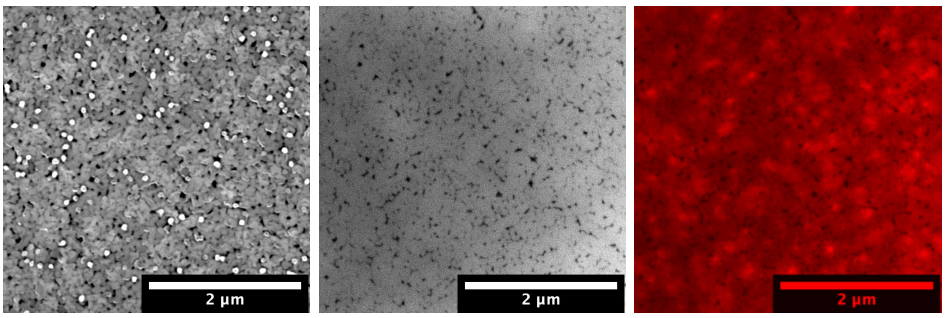

(b) Secondary electrons. (c) CL 360 nm. (d) CL 285 nm.

Figure 3.14: a) CL spectra of N3784 at various position along the wafer. b) SE image and c)-d) CL mapping at 360 nm and 285 nm of N3784 at 7 K.
Spectral resolution is of ± 2.5 nm.

deconvoluted from the number of Ga in the NW core.

At this point, the question to address is the following: *Where does the luminescence come from?* Additional experiments were done in order to answer this question. The first one consists in excitation dependant photoluminescence. A 244 nm laser was used in

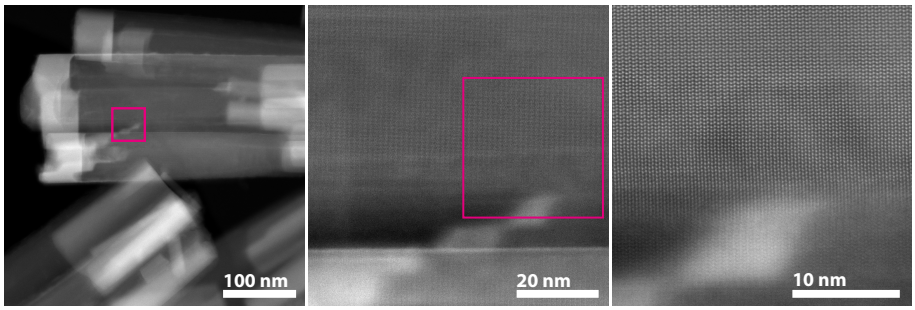

Figure 3.15: HAADF HR-TEM images of sample N3784. Magenta boxes indicates the position of next images. These images are examples, several locations on several NWs were analyzed.

order to excite the sample at 5 K and beam power was varied between 5 µW to 500 µW, measured with a power-meter right before the sample surface. The results are shown in figure 3.16 (a).
The absence of changes in both intensity and peak shape of the PL spectra points towards recombination centers that are not saturated in this range of power. It can further discard the hypothesis of DAP being responsible for the emission as they are known to be very dependent on the excitation power. Indeed by increasing it, one is able to saturate donor-acceptor pairs that are far away and exhibit long life-time, while the ones closer to each others can still recombine. In this case, when DAP are spatially closer, Coulomb interaction is increased, inducing a shift of the emission towards smaller wavelength, which is not observed in the present case.

Furthermore, CL spectra of single NWs were also acquired (Figure 3.16 (b) and reveal that the rather large peak centered at 285 nm is indeed composed of multiple sharp lines. It points towards the presence of an abundance of recombination centers, confining excitons in a QD behavior. As shown from the temperature dependence of CL spectra from single NW in figure 3.16 (c), the confinement is indeed very strong with localization up to around 200 K.

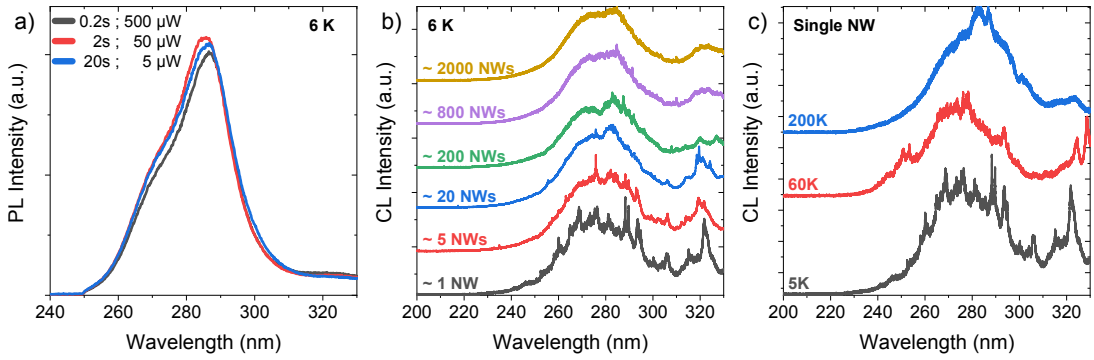

Figure 3.16: a) Low temperature PL spectra of N3784 at various excitation powers and integration times. b) Low temperature CL spectra for different number of NWs probed. c) CL spectra with a focused electron beam on a single NW as function of the temperature.

This collection of observation is compatible with strong localization of the exciton on small GaN clusters in AlN. Especially, since the growth recipe is quite unusual, a peculiar incorporation of Ga in AlN can be explained in our specific case. Because of the growth procedure consisting of an alternation of metal and nitrogen exposures, around one ML thin GaN quantum well was grown prior to be decomposed by the succeeding exposure to Al [156]. With subsequent N exposure, a proper AlN:Ga layer has formed. Exhibiting longer diffusion length than their Al homologue, Ga atoms may have distributed unevenly in the AlN matrix, leading to an AlGaN section with large local compositional fluctuations.

The higher desorption rate of Ga with respect to Al at high growth temperature accounts for the rather low Ga content in the whole structure compared to the nominal flux.

3.3.2 Structural and optical properties of Ga doped AlN NWs.

The scenario proposed above matches experimental measurements, however proofs are weak. To extend the study and strengthen the conclusions, four samples were additionally grown. 300 nm long GaN stems were grown on (111)-Si substrate at 820°C and under a Ga/N ratio of 0.3. A 750 nm long AlN section is further grown on top of this stem at a temperature of 900°C and a Al/N ratio of 0.56. In addition to Al and N fluxes, the samples were exposed to a slight Ga flux ranging between approximately 0.007 and 0.03 ML/s. The corresponding nominal Ga concentrations were comprised between 1.2 and 5%, estimated from calibration of the Ga cell flux by RHEED oscillations on 2D GaN layers. A fifth sample was grown following the same recipe, but without any gallium flux added during the growth of the AlN section in order to serve as a reference. Table 3.2 summarizes the relevant growth information during the AlN:Ga and a scheme of the sample with SEM images are shown in figure 3.17.

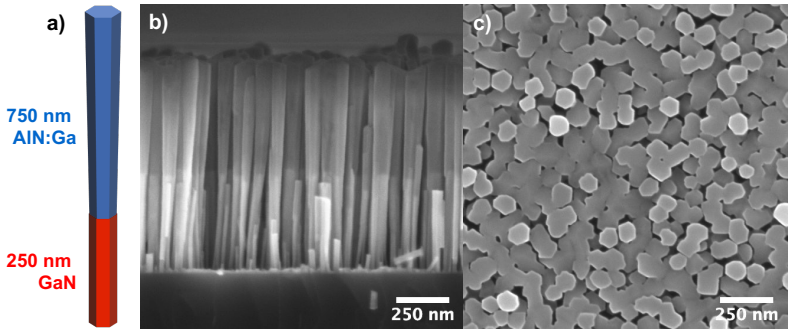

Figure 3.17: a) Scheme of the NWs structure. Cross sectional b) and top view c) SEM images of N3859.

Table 3.2: Gallium cell temperature, equivalent Ga flux and Ga/(Al+Ga) ratio of samples Ga790 and Ga840. The last two columns are derived from RHEED oscillations on 2D surfaces. Variation of sticking coefficient and Ga desorption were not taken in consideration.

Sample name	Sample number	T_{Ga} (°C)	Ga flux (ML/s)	Ga/(Ga+Al) (%)
Reference	N3887	no Ga	—	—
Ga770	N3898	770	0.007	1.2
Ga790	N3859	790	0.01	1.7
Ga810	N3897	810	0.02	3.4
Ga840	N3860	840	0.03	5

Ga identification by EDX in TEM

Thanks to this simple structure, EDX in TEM could be performed and give more accurate Ga quantification than in N3784. Figure 3.18 presents EDX maps of Ga and Al atoms at different scales for Ga790 and Ga840 samples while table 3.3 shows Ga concentration in different areas. At the nanowire scale, it is impossible to distinguish Ga atoms on mappings, but quantification was possible as signal from Ga could be clearly observed (not shown). It indicates an average concentration of around 0.1% in Ga840 and slightly less or equal in Ga790, close to thee detection limit. Once zoomed in the NW structure, presence of Ga-rich areas appears by EDX even if no contrast can be seen from HAADF images. For both samples, the extracted concentrations are of the same order of magnitude, at around 0.3–0.4% in the richest regions, while in the poorest regions, concentrations are below the detection limit.

The difference in Ga composition with respect to the expected values can be easily explained. Firstly, the calibration were made at much lower temperature with a desorption rate of Ga much lower than in the case of NW growth. Secondly, Al has priority over Ga for its incorporation, which can lead to an increased residence time of Ga on the surface further promoting its desorption.

It is worth noting that EDX probes atoms all along NW diameter which is around 100 nm thick. Therefore, the concentration extracted by this technique are given for a certain volume and it is difficult to truly assess the Ga cluster size and local concentration. Nevertheless, it confirms that Ga is being incorporated in AlN NWs at low concentration with important fluctuation at different scales, although the differences between the two samples are difficult to appreciate.

Table 3.3: Ga concentration extracted by EDX in TEM from Ga K_α lines. *b), g)* refer to the whole areas in figure 3.18 b) and g) and *1,2,3,4* refer to the annotated zones of the respective maps.

	Ga790					Ga840			
	1	b)	2	3	4	1	g)	2	3
Ga concentration (‰)	0.5	1.00	4.0	0.1	4.1	1.1	1.52	0.4	3.3
Uncertainty (‰)	0.5	0.04	0.8	0.1	1.1	0.1	0.04	0.1	0.2

Luminescence properties

Luminescence properties of the samples present more differences than EDX can highlight. CL investigations were carried out at low temperature under a 15 kV electron beam and a probe current of ∼1 nA in top-view configuration. Results are shown in figure 3.19 (a). All samples exhibit a wide band emission, extending from about 220 to 300 nm. If Ga840 presents a single peak at 265 nm, its intensity decreases as the Ga flux

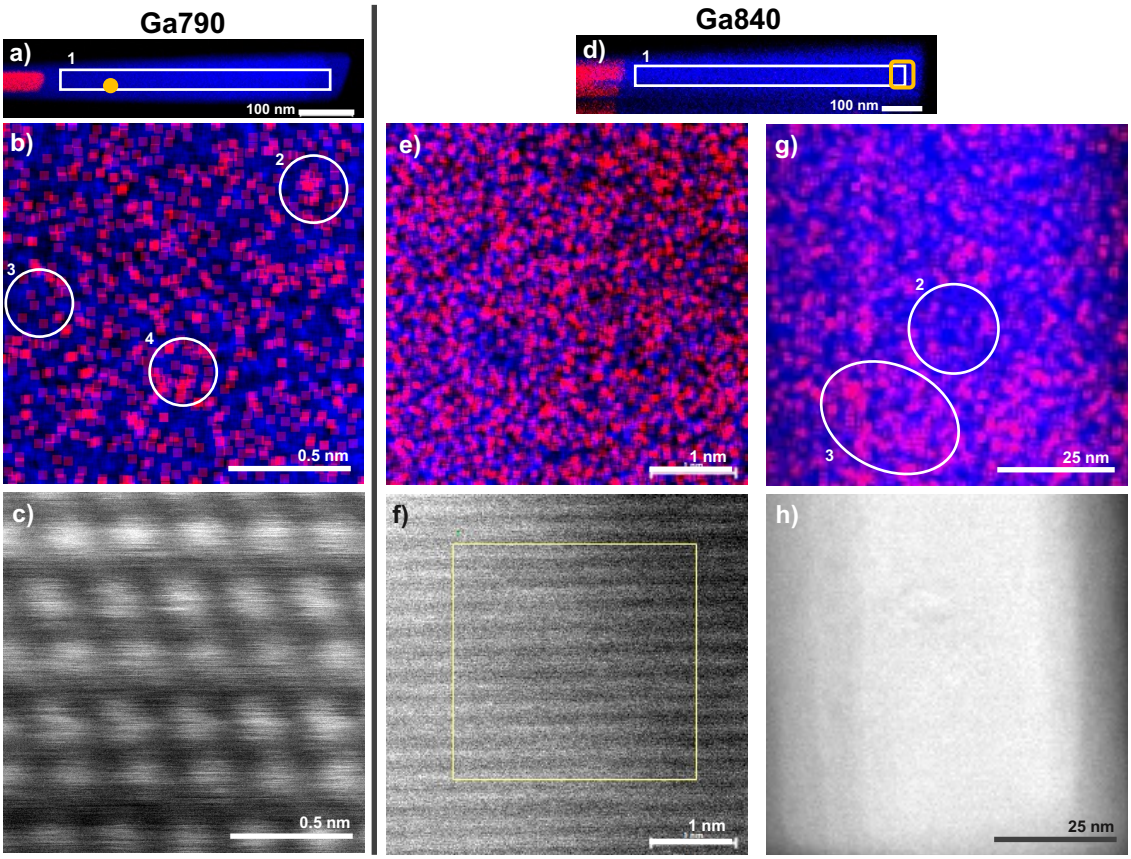

Figure 3.18: EDX maps of Al (blue) and Ga (red) of Ga790 (a-b) and Ga840 (d-e). b) is taken at the orange dot location while (e-h) are zoomed on the orange rectangle. c), f) and g) are the corresponding HAADF images of b), e) and g) maps.

is reduced. In parallel, a second peak at higher wavelength appears. As regards EDX results, the hypothesis of local lower Ga concentration is put forward to account for this. The reference sample presents a band centered at 245 nm, with relatively weak intensity and seems to be out of the trend drawn by the other sample of the series. Sharp luminescence lines are put in evidence when probing a reduced number of NWs, as shown for Ga790 in figure 3.19 (b), suggesting the presence of a wide distribution of carrier localization centers dominating the luminescence properties of single NWs. Averaging signals from several nanowires give rise to a smooth CL spectrumIn addition, low temperature PL spectra were recorded at different excitation power. The results shown in figure 3.19 (c), does not show any change in peak shape and a low variation in intensity, consistent with previous measurements on N3748. Emission from DAP is therefore excluded once again in AlN:Ga samples. Regarding the reference, its behavior is completely different since it shows a large reduction of its intensity as the power is increased (not shown). This points towards recombination center with long lifetime, easily saturated. It is attributed to a standard defect.

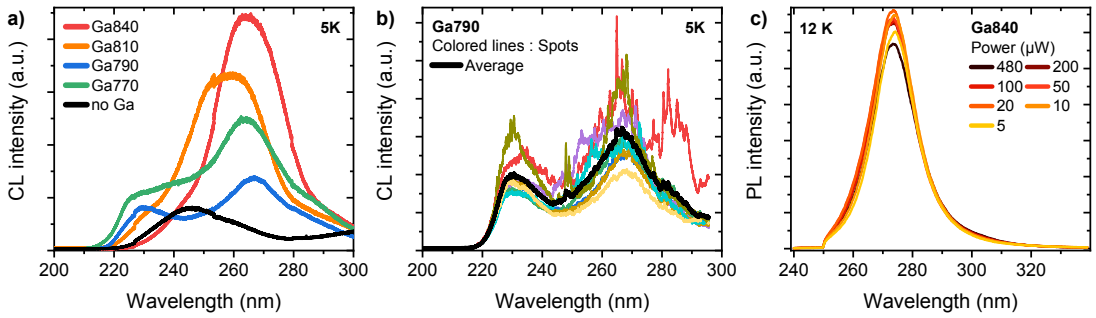

Figure 3.19: a) Low temperature CL spectra of Ga790 acquired with a focused beam on 8 NWs (colored lines) and their average (black line). b) Low temperature CL spectra of a 100 µm^2 area of Ga790 and Ga840. c) Low temperature PL spectra as function of the power. Spectra have been normalized by the integration time.

The variation of CL intensity as a function of temperature is plotted in figure 3.20. The intensity variation as a function of temperature, plotted in inset, shows that at room temperature it is still 20–30% of the low temperature intensity value. Consistent with the EDX results, this limited quenching is assigned to the quantum dot-like behavior of the carrier localization centers resulting from the local Ga concentration fluctuations. Interestingly, it is clear that the higher energy peak in Ga790 is diminishing faster than its lower energy counterpart. This phenomenon suggests a charge transfer from higher energy states to lower ones and is further supported by the variation of intensity as function of the temperature, observed in the inset of figure 3.20. The 230 nm peak intensity starts decreasing at around 30 K while the 270 nm peak intensity remains stable up to much higher temperature. A similar trend, however much weaker, is seen in Ga840 where a shoulder at higher energy disappears prior the reduction of the main peak intensity.

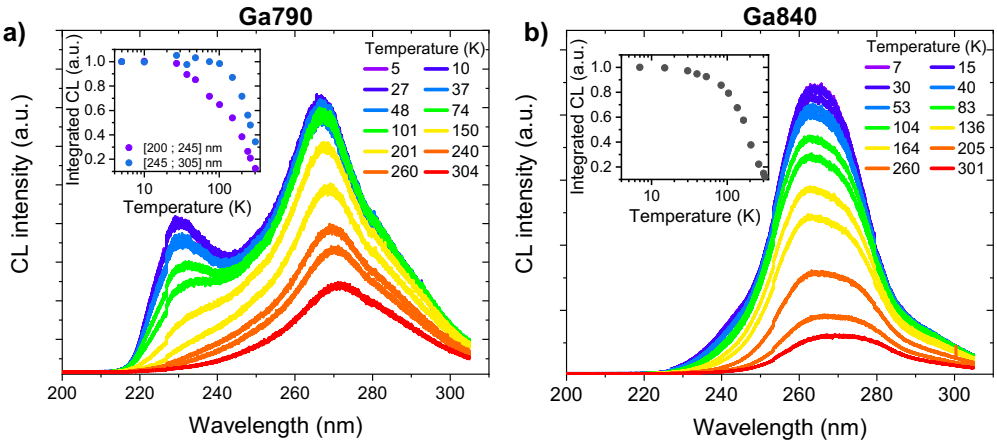

Figure 3.20: CL spectra as function of the temperature for Ga790 (a) and Ga840 (b). Inset: integrated CL intensity as function of the temperature.

3.3.3 At the edge of alloying

After having studied the properties of the two samples, it is difficult to clearly denominate the formed material. The reduced amount of Ga in AlN, its spatial distribution and the strong localization of the exciton points towards a semiconductor doped with an isoelectronic impurity, which would be denoted AlN:Ga. *Callsen et al.* classified alloy into two classes: type I alloy which exhibits bound state within bandgap, and type II alloy which exhibits non discrete band states [157]. A schematic representation of the band structure of a simple GaP:N is drawn in figure 3.21a. It corresponds to a type I alloy as N impurity gives a discrete energy state within GaP bandgap. As N concentration increases more energy levels appear in the band, which correspond to different configurations of N-N complex, up to a point where the large number of nitrogen leads to the opening of a band [158]. The physics behind was investigated also in GaAsP:N [159, 160], GaInAs:N, ZnTe:O [161] or GaN:As and GaN:P [162]. Recent work reports on this effect in GaAsP:N NWs in which a small percentage ($\sim$ 0.1–4 %) of nitrogen is diluted in GaAsP matrix [163, 164]. Their optical properties are close to the one observed in our nanowires.

By opposition to type I alloy, GaAsP and Nitrides are known to belong to group II alloy, also called mixed-crystal alloy. The introduction of the new atom in the lattice introduces levels within the band themselves. Therefore, the exciton is not bound to a state and probe an average potential, leading to broader emission and the bandgap energy shifting monotonously with alloy composition. AlGaN can be seen as special because of the reduced size of the exciton, around 2–4 nm [165]. Therefore, it is more sensitive to local compositional fluctuation which would lead to local potential fluctuation. The effects of the exciton size on the optical properties of AlGaN with large inhomogeneities were many times reported. Noticeably, they can translate into strong localization and QD-like behavior, similarly to type I alloy. [119, 121, 125, 166–168].

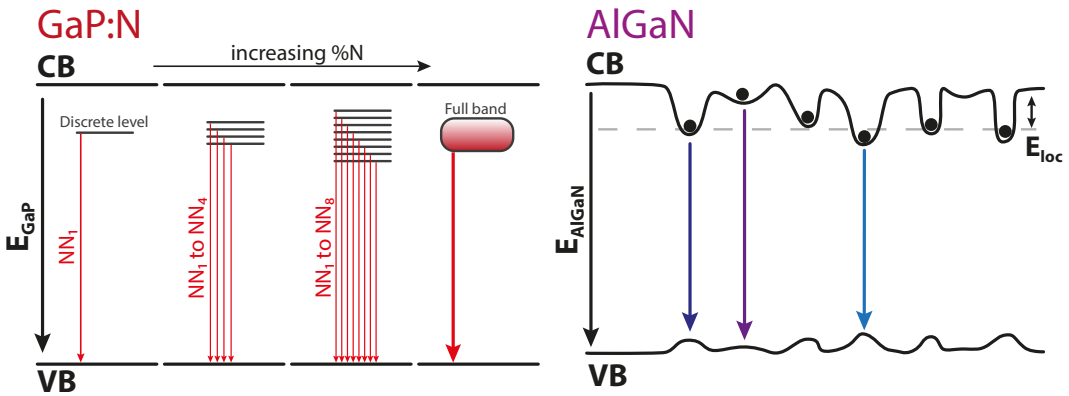

(a) Type I alloy (b) Type II alloy

Figure 3.21: Schematic band structure representation of (a) GaP:N type I alloy [158, 161] and (b) AlGaN type II alloy.

In the present samples, the emission is several hundreds of meV below the AlN band-edge, it shifts with Ga concentration and the emission linewidth on NW ensembles is large. All these experimental facts are in agreement with the definition of type II alloy. Moreover, the abundance of sharp lines is not compatible with the type I alloy as they are too numerous and separated by large energies. A sketch of Ga790 band diagram is proposed in figure 3.22 (a). How CB and VB should be drawn, either flat or in a roller-coaster manner is not clear and does not really change the interpretation, therefore I have chosen to make it flat.

The hypothesis of AlGaN nano-clusters is claimed as it is efficiently matching all observations and compatible with being a type II alloy. EDX measures an average Ga concentration on the NW diameter which is of ∼100 nm. The exciton radius being 50 times smaller, it is possible that the concentration is, at the scale of the exciton, 50 times larger if Ga atoms are closely gathered, giving a concentration up to 10–20%. These AlGaN clusters could indeed behave as QD with strong exciton localization and confinement energy. The fact that Ga790 exhibits two peaks at this location on the wafer points towards the coexistence of two populations of QD varying either in size or in Ga content. However, the observation of a single peak at smaller energy in Ga840, grown at a larger Ga flux, is consistent with the fact that clusters size can be adjusted by tuning ting growth parameters.

Finally, AlGaN remains a type II alloy and we probed its optical properties in the case of an extremely low Ga concentration.

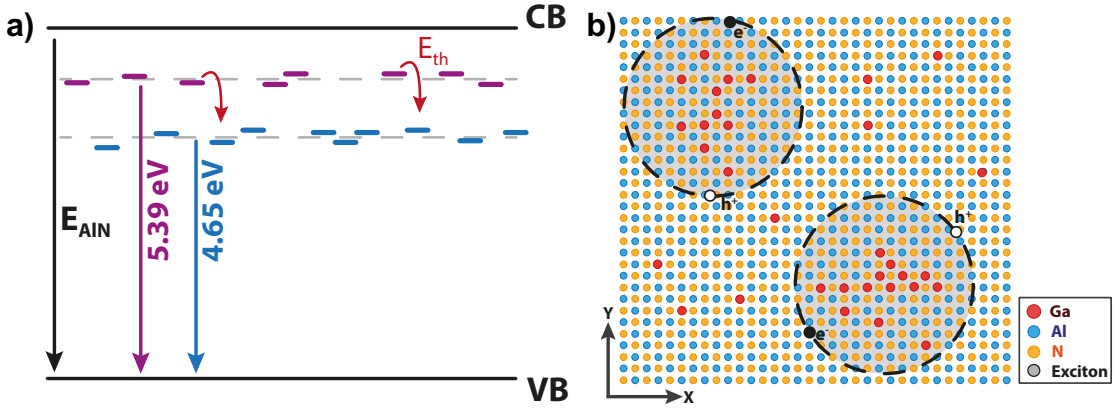

Figure 3.22: a) Proposed representation of band diagram with small AlGaN cluster as in Ga790. CB of AlN is not affected but the GaN inclusions create energy levels within the bandgap. Two different mini-bands are present below AlN CB, spatially randomly distributed. Hopping from one level to the other can be promoted by thermal energy. b) Schematics representation of short range alloy fluctuation. Excitons do not probe the same potential as they have different chemical environments.

3.4 Summary of Chapter 3

3.4.1 Conclusion on active area realization

This chapter was motivated by a unique guideline but gave rise to two studies, touching the limit of two systems: the quantum well and the AlGaN alloy.

In a first part, a set of samples has asserted the growth of monolayer thin GaN quantum wells in nanowire geometry. Leveraging adatom diffusion and alternating metal and nitrogen fluxes, binary quantum wells with thicknesses between ∼1 and 4 ML were achieved covering a large range of emission between 240 nm and 300 nm. Results are in the line of previous reports from the literature, mainly on 2D layers. Luminescence exhibits a high robustness in temperature which is highly beneficial for room temperature operating devices. Limiting factors are the inhomogeneities in NWs morphology, which can be overcome by the use of patterned substrates, and accurate growth conditions to control the amount of metal adatoms thus well thickness and interface sharpness.

In a second part, the adaptation of the ML thin quantum well in a LED structure has led to an unexpected result. Peculiar incorporation mechanisms resulted in Ga-doped AlN NWs. With Ga concentration below 1%, optical properties of the commonly known standard AlGaN alloy are changed. The sparse and random distribution of Ga atoms are found to be able to strongly confine the exciton with high robustness and emission energy spanning in the whole UV-C. This hypothesis of small AlGaN clusters is put forward in order to explain the majority of the experimental observations. Alternatively to a challenging growth of homogeneous AlGaN nanowire, the growth of AlN NWs with a slight Ga flux is found to give the same emission energy, which can be further tuned by adjusting growth parameters.

3.4.2 To go further

These two studies have achieved some of the challenges and questions identified at the beginning of this manuscript. Nevertheless, more studies can be done to go further.

On the monolayer thin quantum well study, the homogeneity is stated as a limitation. Technical development and the use of patterned substrates could pave the way to new studies on the diffusion of Al adatoms on such structures and the incorporation mechanisms of Al and Ga in AlGaN NWs. The equivalent has been done with GaN NWs by *Gruart et al.* [131] and would be of particular interest in the aim of controlling the growth of ML thin AlN/GaN structure. The lowest emission wavelength obtain is 239 nm with such binary system. It would be interesting to see if including 5–15% Al in the GaN well could be used in order to decrease even further the emission wavelength and at what expense.

Study of Ga doped AlN NWs was not expected in the framework on this thesis and

appeared at the end of my work. Exploring the way to control the emission properties of such emitters by varying flux, temperature and growth rate seems to be the most straightforward studies to carry. Questions are plentiful. Can the emission linewidth be decreased? Can single photon emission be achieved from a single Ga cluster located in a single NW? What is the role of impurities, that are plentiful in AlN, on the luminescence properties of these clusters?

In this chapter, IQE measurements are never performed in a proper way. The ratio of CL intensity at room and low temperatures is the main quantity used to assess the quality of the structures. However this ratio is still not 100 % and can be tricked by non-radiative defects remaining active at 5 K. A deep study of point defects in AlN NWs is, to my opinion, a necessity. Literature is sparse and those point defects have to have a detrimental effect on the luminescence efficiency. Time-resolved luminescence and excitation-dependent photoluminescence measurements could be a good way to probe other optical properties of these structures.

CHAPTER 4

Unraveling transport mechanisms in Si doped AlN NWs

Specific investigation of transport mechanism in Si-doped AlN nanowires is conduct in this chapter. Structural study shows that solubility limit of Si in AlN was not reached. Electrical characterizations allow to identify two conduction mechanisms at low and high bias. From them, three silicon levels are identified attributed to different atomic arrangements.

Contents

4.1 A difficult n-type doping of Al-rich AlGaN thin films 82
4.1.1 General state of the art in Al-rich AlGaN and AlN 82
4.1.2 Substitutional or DX state 82
4.2 Structural study of AlN:Si NWs 84
4.2.1 Growth and morphology 84
4.2.2 Quantification of Si concentration by EDX 86
4.2.3 Raman spectroscopy 87
4.3 Coexistence of shallow donor and DX center 87
4.3.1 Basic electrical characterizations 87
4.3.2 Shallow donor and DX center 88
4.3.3 Effect of Fermi level pinning on the electrical conduction 90
4.4 Study of space charged limited current regime 94
4.4.1 Trap assisted space-charge limited current theory 94
4.4.2 Additional trap in highly Si-doped AlN NWs: a new DX state? . 96
4.5 Summary of Chapter 4 100
4.5.1 Conclusion on Si-doping of AlN NWs 100

4.5.2 To go further 101

The results presented in this section gave rise to two publications during this PhD period:

- Rémy Vermeersch, Eric Robin, Ana Cros, Gwénolé Jacopin, Bruno Daudin, and Julien Pernot. "Shallow donor and DX state in Si doped AlN nanowires grown by molecular beam epitaxy". In: *Applied Physics Letters* 119.26 (December 2021), p. 262105. DOI: 10.1063/5.0074454
- Rémy Vermeersch, Gwénolé Jacopin, Bruno Daudin, and Julien Pernot. "DX center formation in highly Si doped AlN nanowires revealed by trap assisted space-charge limited current". In: *Applied Physics Letters* 120.16 (April 2022), p. 162104. DOI: 10.1063/5.0087789

4.1 A difficult n-type doping of Al-rich AlGaN thin films

4.1.1 General state of the art in Al-rich AlGaN and AlN

Silicon is the most widely used n-type dopant in nitrides. Substituting metal atom, it exhibits an ionization energy as low as 15 meV [11] and allows to reach high mobility and electron concentration in GaN thin films and NWs. This relatively low ionization energy allows to reach metallic behavior starting at free electron density of a few 10^{18} cm^{-3} [78]. However as one increases the Al content in the AlGaN alloy beyond $\sim 60\%$, a drastic loss in conductivity is observed, linked with an increasing ionization energy of the dopants [11, 12, 171–173]. The so-called shallow Si donor in GaN turns into a deep donor in Al-rich AlGaN. In pure AlN, this activation energy can be found between 90 meV [173] and 280 meV [80]. It has to be noted that these two values have been found from samples grown within the same group, with the same machine and the same substrates without understanding why they differed. As shown in figure 4.1, discrepancies are observed but the common agreement is that Si_{Al} donors have a ionization energy of ~ 300 meV [76, 174–176].

To account for these discrepancies, several candidates are pointed at. As AlN molar fraction increases the formation energy of aluminum vacancies V_{Al} decreases. These vacancies act as compensating centers with several negatively charged states and can be involved with Si or O atoms [184–186].

4.1.2 Substitutional or DX state

Another effect is present which is already known for years in AlGaAs and GaAsP systems [187–190]. As a matter of fact, Si, Te or S doped AlGaAs exhibits strong dopant-dependant lattice relaxation. It is typically the case of AlGaN:Si with an AlN molar

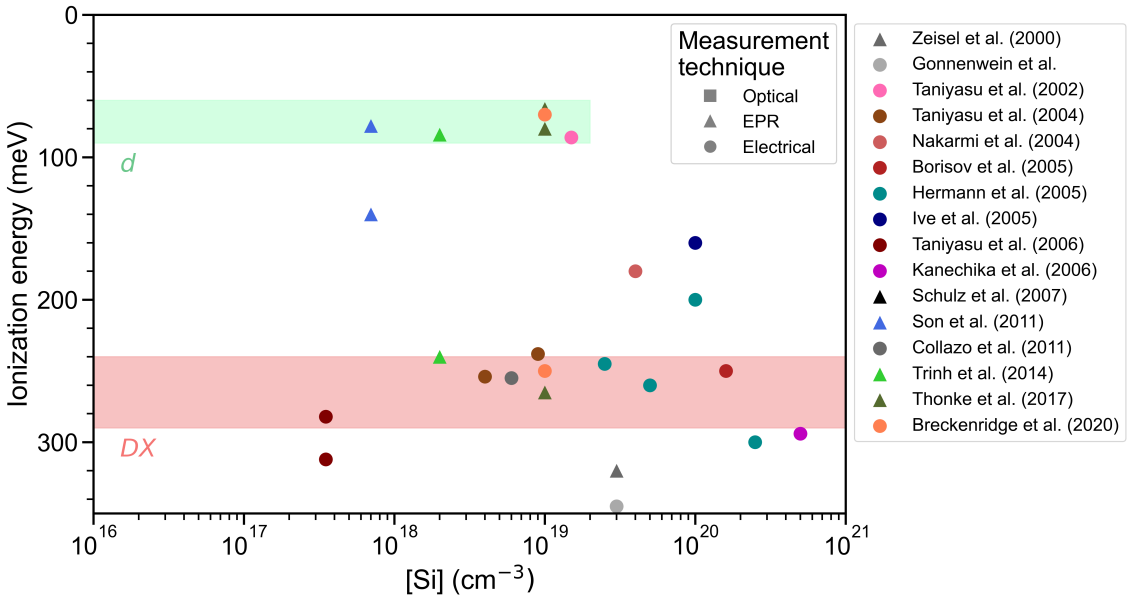

Figure 4.1: Review of transition level energies of silicon in AlN reported in the literature as a function of the silicon concentration [11, 76, 80, 172–183]. Optical refers to photoluminescence techniques, EPR to electron paramagnetic resonance and electrical refers to either Hall or conductivity measurements. Green and red regions are indicative.

fraction higher than $\sim$ 70%. Si atoms no longer remain on cation sites but will rather undergo a transition through lattice relaxation [191, 192], following this relationship:

$$2d^0 \longleftrightarrow d^+ + \mathrm{DX}^- \tag{4.1}$$

This state, called DX for *Donor and Unknown*, is related to Si in interstitial site with ionization energy much larger that the hydrogenic d state (figure 4.2). At rest, DX state is negatively charged but can be ionized as all donors, exhibiting a large ionization energy. The main characteristics of the DX center is its trapping behavior leading to persistent photocurrent. More details can be found in [187], in which *Lang* and coworkers proposed a model for Te-based DX centers in AlGaAs, relying on deep level transient spectroscopy and photocapacitance measurements.

The discussion supported by density functional theory calculations on the nature of the different Si states in AlN was initiated in the late 1990s and is still ongoing. However, no consensus appears neither on Si configuration within the AlN lattice nor on its electronic state and transitions [191, 193–197]. Recently, stabilization of the shallow state of Si impurity was demonstrated in the case of implanted layers annealed at relatively low temperatures [183]. *Breckenridge* and co-workers reported an ionization energy of 70 meV after annealing at 1200°C while a 270 meV ionization energy was found for samples annealed at higher temperature.

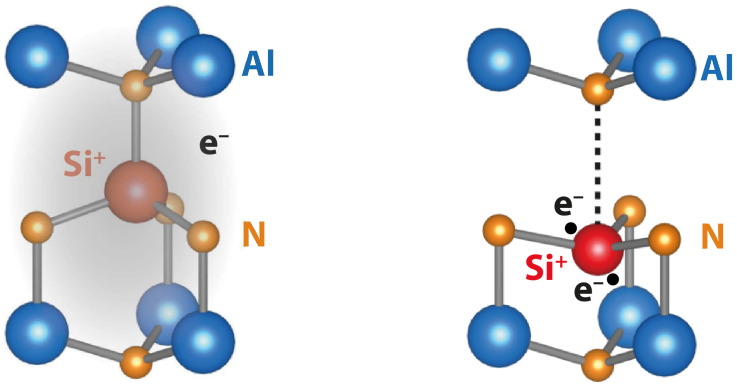

(a) d^+:Si in Al substitution and its delocalized electron

(b) DX^-: Si in interstitial site and its two bound electrons

Figure 4.2: Schematic representation of Si in d and DX configurations [188].

4.2 Structural study of AlN:Si NWs

If all previous studies found in literature rely on 2D AlN, the case of how this system behaves in a nanowire geometry is unreported adn of particular interest in the aim of achieving optimal electron transport in a LED, among other devices.

4.2.1 Growth and morphology

All samples of this study were grown in our plasma assisted MBE, on highly conductive n-type (111)-Si wafer, under N-rich conditions. Prior to growth into the MBE chamber, native silicon oxide was removed by dipping the substrate in a 10% HF solution for around 30 s and annealed in the MBE chamber first at 300°C for at least one hour and at 950°C for 30 min. A 350 nm GaN stem was first grown at a substrate temperature T_g of 817°C and a metal over N ratio of ~ 0.3, then AlN section was grown for 2h10 at the same metal over N ratio and at $T_g = 880$°C. Finally, a 20 nm GaN cap was grown under a Ga / N ratio of 1.2 to promote NW enlargement for further contacting. In all samples, Si cell temperature of GaN sections was kept at 930°C while it was varied between 750°C to 1300°C in the AlN sections. Naming of the sample is done so that S900 is the sample grown with $T_{Si} = 900$°C and S0 refers to a sample in which no Si flux was applied during the AlN growth. Figure 4.3 shows a sketch of the structure and SEM images of S900 and S1200.

From those two samples, a change in NW morphology can be seen. Figure 4.4 shows results of structural study. Following a stable morphology stage for Si effusion cell temperature lower than 1100°C, a transition occurs resulting in the NW widening from 80 to 130 nm, associated with a shortening from 810 to 720 nm, respectively. At very high Si flux ($T_{Si} > 1250$°C), the coalescence due to the widening leads to a plateau of the NW diameter. As previously reported for Si and Mg doped GaN NWs [77, 198, 199], this mor-

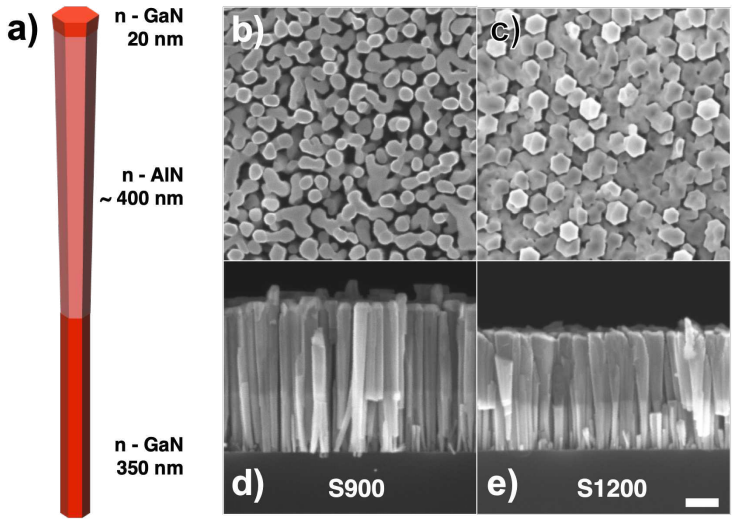

Figure 4.3: (a) Schematics of the NWs structure. Top view and cross sectional view of S900 (b - d) and S1200 (c - e). Scale bar is 200 nm for all four SEM images.

phology change can be assigned to an enhancement of adatom diffusion on the NW lateral m-planes, leading to a higher incorporation on top of the sidewalls and an increase in radial growth rate compared to the axial one. The formation of a defective shell around the nanowire as identified by *Fang* et al. [77] for heavily Si-doped GaN NWs, with a transition from 6-fold to 12-fold symmetry is not observed here.

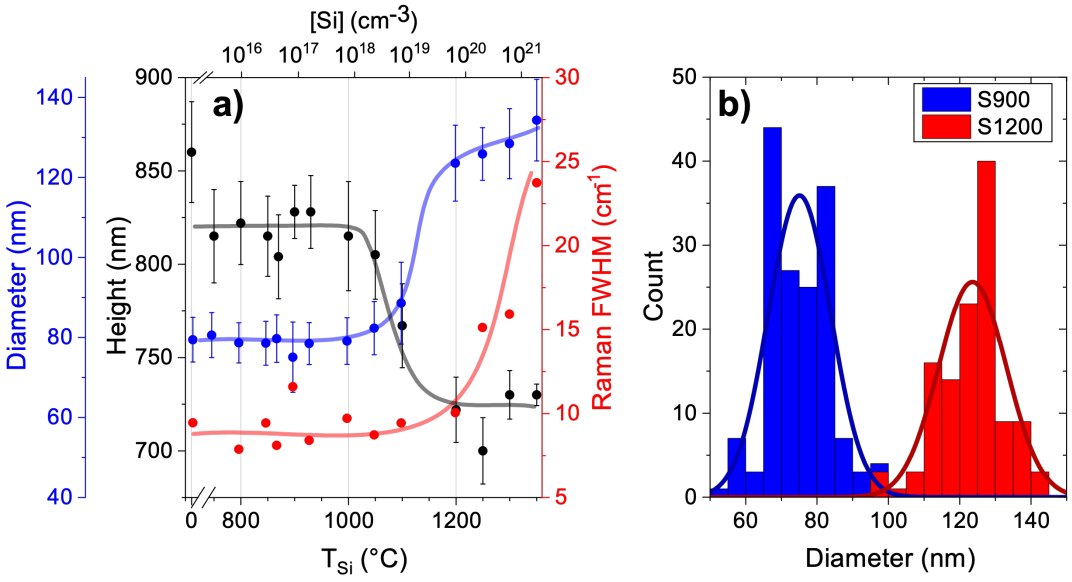

Figure 4.4: (a) NW diameter (blue), length (black) and Raman full width at half maximum (red) as function of T_{Si} and [Si]. Lines are guides for the eyes. (b) NWs diameters histogram for S900 and S1200. Lines are gaussian distribution fits.

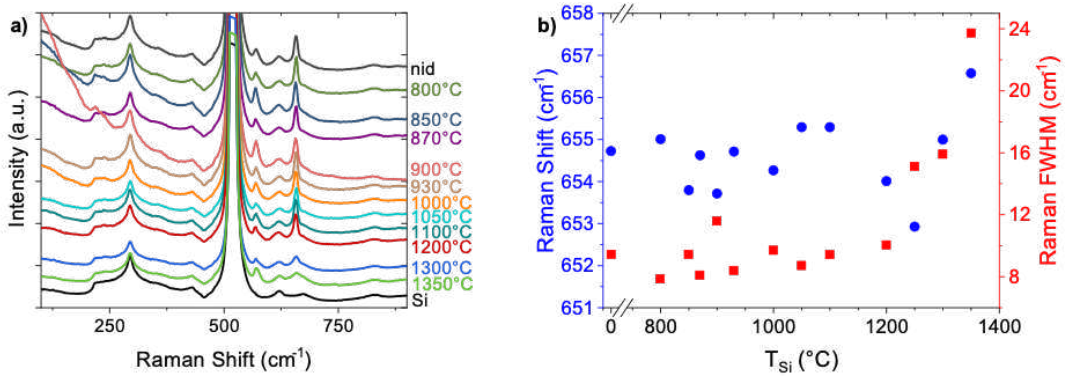

Figure 4.5: (a) Raman spectra of samples under study. The E_{2h} peak of AlN is at 655 cm $^{-1}$. Silicon reference is added as the bottom spectrum. (b) Raman shifts and full width at half maximum extracted for gaussian fits of the E_{2h} peak.

4.2.2 Quantification of Si concentration by EDX

Si content was determined by EDX as reported on the top x-axis of figure 4.4. In order to perform this measurement without being sensitive to the Si signal arising from GaN and substrate, samples have been dispersed onto a molybdenum sheet. Signal was furthermore treated and normalized based on signal from undoped AlN thin film obtained under the same operating conditions. With a detection limit of around 1×10^{19} cm^{-3}, only an average Si concentration from S1200 to S1350 was measured ranging from 6.5×10^{19} cm^{-3} to 1.8×10^{21} cm^{-3} and extrapolation was done for the rest of the samples as shown in

Table 4.1: Description of studied samples with their structural parameters, conductance at room temperature G_{300K} and ionization energies $E_{D1,2}$ used for the fits. A unique value for E_{D1} and E_{D2} have been used to fit the whole set of samples. Si concentration from S750 to S1100 are extrapolated from EDX data (fig. 4.6).

	T_{Si} (°C)	[Si] (cm^{-3})	Diameter (nm)	Length (nm)	G_{300K} (S)	E_{D1} (meV)	E_{D2} (meV)
S0	no Si	—	79	860	2.0×10^{-8}	75	700
S750	750	2.4×10^{14}	81	815	5.6×10^{-7}	*not measured*	
S800	800	1.7×10^{15}	79	822	1.2×10^{-7}	75	700
S850	850	1.0×10^{16}	79	815	4.6×10^{-7}	*not measured*	
S870	870	2.2×10^{16}	80	804	7.8×10^{-7}	75	270
S900	900	5.2×10^{16}	75	828	1.4×10^{-5}	75	270
S930	930	1.3×10^{17}	79	828	1.1×10^{-6}	*not measured*	
S1000	1000	9.5×10^{17}	79	815	1.7×10^{-7}	75	270
S1050	1050	3.4×10^{18}	82	805	1.1×10^{-7}	75	270
S1100	1100	9.4×10^{18}	89	767	3.1×10^{-8}	75	270
S1200	1200	6.5×10^{19}	125	722	6.2×10^{-6}	*not observed*	270
S1250	1250	2.0×10^{20}	128	700	3.6×10^{-8}	*not observed*	270
S1300	1300	6.0×10^{20}	128	730	1.0×10^{-8}	*not observed*	270
S1350	1350	1.7×10^{21}	134	730	2.0×10^{-8}	*not observed*	64

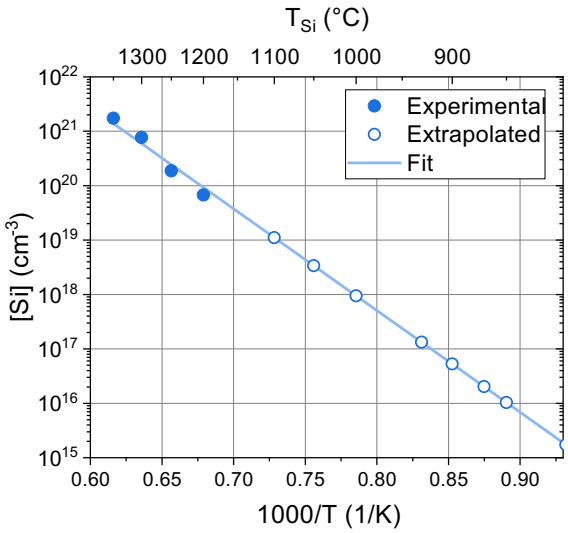

Figure 4.6: Silicon concentration as a function of silicon cell temperature extracted from EDX measurements. Open circles are extrapolated points from the Arrhenius law and with an activation energy of 3.8 ± 0.2 eV [175].

figure 4.6. EDX results indicate a Si content lower than the solubility limit in AlN, reported to occur for 6×10^{21} cm^{-3} in layers [175, 196] consistent with the absence of symmetry alteration. Si concentration in GaN sections was also measured at a level of 2×10^{20} cm^{-3}.

4.2.3 Raman spectroscopy

Figure 4.5 shows the results of Raman spectroscopy performed at University of Valencia. These measurements were realized in backscattering geometry along growth direction with a 532 nm Laser operating at 8 mW and focused on the sample. Full-width at half maximum (FWHM) were extracted from lorentzian fit of the spectrum. Interestingly, no shift of the E_{2h} peak energy is observed even for the highest doping level. However, there is a clear increase in FWHM starting at a $T_{\mathrm{Si}} \sim 1200$°C corresponding to a Si flux higher than the flux corresponding to the onset of NW widening (figure 4.4 (a)). Then, it appears that the increased Al adatom diffusion length on the side-walls assigned to a Si-induced surfactant effect will impact the NW morphology at a Si flux significantly lower than the flux responsible for the increase in E_{2h} peak FWHM. In conclusion, Raman spectroscopy points toward a non-strained ensemble of NWs in average, with large inhomogeneities at the single NW scale without dopant induced strain change.

4.3 Coexistence of shallow donor and DX center

4.3.1 Basic electrical characterizations

In order to investigate electrical behavior of Si doped AlN NWs, Ti (30 nm) / Al (70 nm) 100 × 100 μm^2 square pads were deposited. Measurements were carried out in two probe configuration in the setup in the box displayed in figure 2.11 of Section 2.3.1, with

a Keithley 6517 high impedance electrometer. Thanks to the high doping level of GaN sections, they are assumed to have a metallic behavior [77], making the GaN contribution negligible with respect to the high resistance of the n-AlN section. Contact resistances are also assumed to be of much less importance than the resistance of n-AlN sections.

I–V characteristics presented on a log–log plot in figure 4.7 (a), show a linear regime $I \propto V$ at bias lower than ~ 0.1 V corresponding to Ohmic transport followed by a supra-linear regime. Due to its V^2 dependence, this behavior is attributed to a space-charge limited current (SCLC) regime in which electrons are injected from the contact into a material with a low free carrier concentration [88, 89, 200] as previously reported in GaN and AlGaN structures [201–204]. This phenomenon will be studied in a detailed manner in Section 4.4.

Fitting of the linear regime (below 0.1 V) with Ohm's law gives access to the conductance $G = I/V$, which is reported on a log-scale in figure 4.7 (b). The room temperature conductance vs Si cell temperature describes a bell-like curve for the samples with the lowest Si cell temperatures ($T_{\mathrm{Si}} < 1200$°C) where the maximum of conductance reaches a value of 1.4×10^{-5} S for S900 at [Si] $\sim 6 \times 10^{16}$ cm^{-3}. This behavior is expected from the self-compensation of Si already observed by *Harris et al.* [186] in the same range of concentration in the case of thin films. The conductance for the samples with the highest Si cell temperatures ($T_{\mathrm{Si}} > 1200$°C) shifts toward higher values. This increase is assigned to the enlargement of the NW, which reduces the impact of the depletion on the wire conductance. This point will be detailed below.

4.3.2 Shallow donor and DX center

Temperature dependent I–V measurements were performed in order to probe the ionization properties of the donors. Figure 4.8 (a) shows typical I–V curves for samples S900 at different temperatures. For each temperature, the conductance was extracted from a fit of the linear regime and plotted as a function of 1000/T in figures 4.8 (c) and (d). Values can be found in table 4.1.For samples with $T_{\mathrm{Si}} < 1200$°C (figure 4.8 (c)), two regimes are present in all measured samples and fitting with:

$$G = G_1 \exp\left(-\frac{E_{D1}}{kT}\right) + G_2 \exp\left(-\frac{E_{D2}}{kT}\right) \tag{4.2}$$

was used to extract conductance values and activation energies of the different regimes. At lower temperatures, an ionization energy of 75 meV is extracted, which is consistent with the shallow donor state of Si in AlN [183, 198] and predicted to be the hydrogenic one. At higher temperature, an ionization energy of 270 meV is found, which is attributed to the DX state of Si [174, 176, 181–183]. Interestingly, S0, S750 (not shown) and S800 exhibit a higher activation energy of around 700 meV at high temperature, which is inferred from

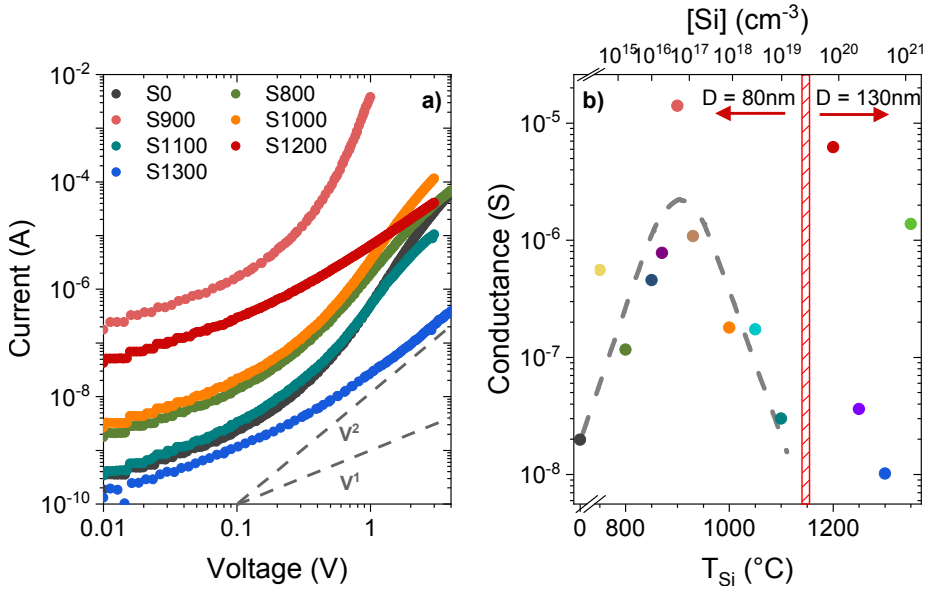

Figure 4.7: (a) Room temperature I–V characteristics of samples obtained from two probes experiments. The black vertical dashed line represents the transition between Ohmic and space-charge limited current behavior. (b) Conductance extracted from the low voltage Ohmic regime as function of the Si cell temperature for all samples under study. The dotted line is a guide for the eyes and the red crosshatched rectangle materializes the morphology transition boundary.

the ionization energy of residual oxygen in DX state in AlGaN [205]. The energy of 75 meV found in the lower temperature range for these samples probably arises from the hydrogenic state of residual O, indistinguishable from the Si one [173, 193, 206]. Regarding samples grown with $T_{Si} > 1200$ °C (figure 4.8(d)), the signature of the DX state is predominant.

Sample S1350 is different, exhibiting an activation energy of 64 meV over the whole range of studied temperature. This difference makes understandable the different conductance value at 300 K observed in figure 4.8 (b). The lowering of the activation energy could be due to the apparition of an impurity band instead of a discrete level, supported by the large Si concentration of 2×10^{21} Si/cm^3 measured in this sample. This could give rise to electrostatic screening between Si dopants as seen in Si-doped GaN for instance [78] and detailed in the Appendix B (figure B.2) or to variable range hopping conduction as reported in AlN:Si in ref [175]. However, the high coalescence degree could also be responsible for preferred conduction path at grain boundaries and therefore no solid conclusions have been drawn to explain this behavior.

As shown in figure 4.8 (e), persistent photocurrent (PPC) was observed in S1200 whereas absent in S900, under a 500 nm illumination. Below bandgap illumination of the sample under test does not generate electron–hole pairs, which discard the effect of

charge splitting induced by Fermi level pinning, as reported in *Calarco* et al. in the case of GaN NWs [203]. It rather indicates that the deep donor behaves like an electron trap when the light is turned off, which could be due to optical excitation of DX center [174, 181, 187, 189].

The presence of both shallow and deep Si donors can have multiple origins. DX state formation is directly linked to thermodynamic equilibrium in which a Si atom lowers its energy through lattice relaxation. Being out of equilibrium is the reason claimed by *Breckenridge* and coworkers for the presence of shallow donors in implanted Si:AlN [183]. Due to NW dimensions, surface level pinning arising from surface states at the side walls significantly modifies the near-surface energy band diagram. A Fermi level pinning on m-plane AlN at 2.1 eV below conduction band (CB) was reported [207]. In the work of *Gordon* et al., the formation energy diagram of d and DX states was computed and showed a transition between the two occurring at 150 and 640 meV below CB for Si and O, respectively [193]. Because of the large pinning, an effective Fermi level in NWs is expected to lay below these values for which Si incorporation in d state is favored. This hypothesis matches the experimental data where shallow donors are found to be the main contributors for the smallest diameter where the influence of Fermi level pinning is higher. For 130 nm diameter NWs, growth occurs closer to the bulk case in which DX state formation might be more favorable.

4.3.3 Effect of Fermi level pinning on the electrical conduction

As seen in figure 4.7 (b), an increase by two orders of magnitude in the conductance occurs for a T_{Si} between 1100°C and 1200°C. This sudden increase is opposite to the observed trend and to the higher ionization energy found previously. It is assumed to result from the increased diameter from ~ 80 to ~ 130 nm for the highest Si cell temperatures. Indeed, the small diameter of AlN NWs makes them particularly sensitive to surface states and Fermi level pinning. Nanowire free surfaces are indeed prone to adsorption of foreign species, which can modify surface states, leading to a change in band structure. In the case of non-intentionally doped GaN NWs, *Calarco* et al. found a Fermi level pinned around 0.55 eV below CB on m-planes [203]. The complete depletion of GaN NWs doped with a Si concentration of 1.8×10^{18} cm^{-3} was reached for a NW diameter of 50 nm. In the present case, the large value of 2.1 eV is consistent with a full depletion of the AlN NWs especially for the lowest Si flux.

This hypothesis is further supported by the improved electrical conduction properties after heating under vacuum or exposed to electron beam, as illustrated in figure 4.9. S1250 exhibits almost two orders of magnitude higher current after one hour of baking at 300°C in vacuum (figure 4.9). After exposing the sample to air for few minutes, I-V characteristic returned to its original state assessing the influence of surface states. The same increase

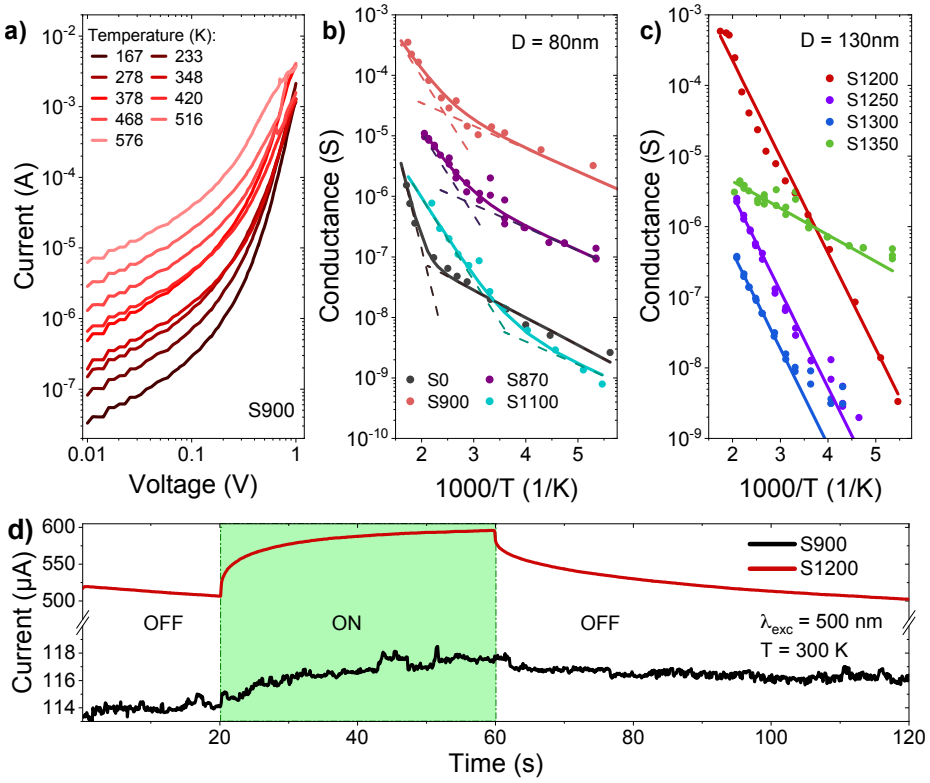

Figure 4.8: (a) I–V characteristics for different temperatures for samples S900. (c) and (d) Arrhenius plot of the conductance extracted from Ohmic regime for the samples with a diameter of 80 nm (c) and 130 nm (d). (e) Current at 1 V over time for S900 and S1200 at room temperature with or without illumination under a 500 nm light.

in current is observed after exposing the sample to an electron beam as shown in figure S.4.b. The surface modification by electron irradiation results in half a decade increase in current after a dose of 0.4 mC/cm^2. Further increasing, the dose allowed to increase again the current up to a given point at which surfaces is expected to be clean.

To quantitatively investigate the depletion and surface effect on AlN NWs properties, *NextNano* simulations were performed in order to solve neutrality equation in the studied system. Appendix C gives details on this software and on how the simulations were done. Results are displayed in figure 4.10. An ionization energy of 75 meV and no compensation were assumed. Figure 4.10 (a) displays the CB minimum in the NW plane with a Fermi level pinning at 2.1 eV from the CB, whereas Figure 4.10 (b) displays the local electron density for 10^{19} donors/cm^3. In this case, it appears that the NW is not fully depleted but electrons are only located in the core of the wire. In order to evaluate the depletion region width, we compared the calculated electron densities n in the case of the NWs with the value n_{FB} obtained for bulk-like conditions (i.e., with flatband at surfaces) and plotted

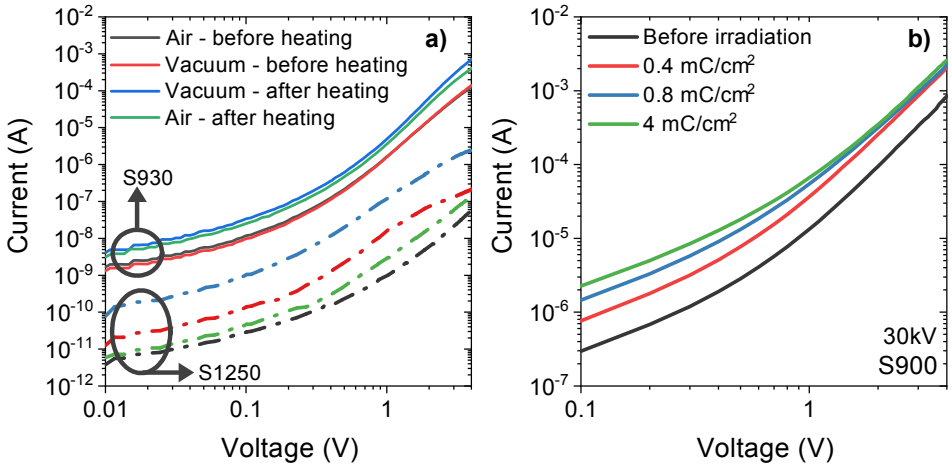

Figure 4.9: (a) I-V characteristics at 300K of S930 (full line) and S1250 (dashed line) in air (black), in vacuum (red), in vacuum after annealing at 300°C for an hour (blue) and in air after being heated (green). (b) I-V characteristics of S900 under e-beam for different electron irradiation doses

the ratio of the two. Figure 4.10 (c) shows a cross section of the NWs with band-edges in blue for a donor concentration of 10^{19} cm^{-3}, in addition to the ratio $n = n_{\mathrm{FB}}$ versus the position for three donor concentrations. For a diameter of 80 nm and $N_D < 2\times10^{18}$ cm^{-3}, the wire is fully depleted, whereas for $N_D = 3 \times 10^{18}$ cm^{-3}, only the core is expected to have an electron density equal to 70% of the bulk one. Full or partial depletion of the wire results in drastic reduction of the free carrier density and consequently of the conductance. An effective free electron density in the NW n_{eff} is defined as the average electron density in the nanowire as follows:

$$n_{\mathrm{eff}} = \frac{1}{S}\int_S n(x,y)\,dxdy \tag{4.3}$$

As shown in 4.10(d), the NW width increases from 80 to 130 nm leads to an increase of several orders of magnitude in the effective carrier density in the 10^{18} cm^{-3} range, the smaller wires being fully depleted while the larger are not. Moreover, the effect is similar if instead of widening the wire, the Fermi level pinning is lowered to 1 eV. This demonstrates the relevance of surface passivation in AlN NWs to enhance conduction properties. In this figure, values from the literature are also reported, highlighting the increase of more than one order of magnitude in free carrier concentration by changing the ionization energy from 270 to 75 meV. Since all samples are conductive at room temperature, none of them were fully depleted, which seems to indicate a lower Fermi level pinning or the presence of residual O donors in the low Si doped and undoped samples (figure 4.8 (a)) with donor density $N_D = [\mathrm{Si}] + [\mathrm{O}]$ larger than 2×10^{18} cm^{-3}.

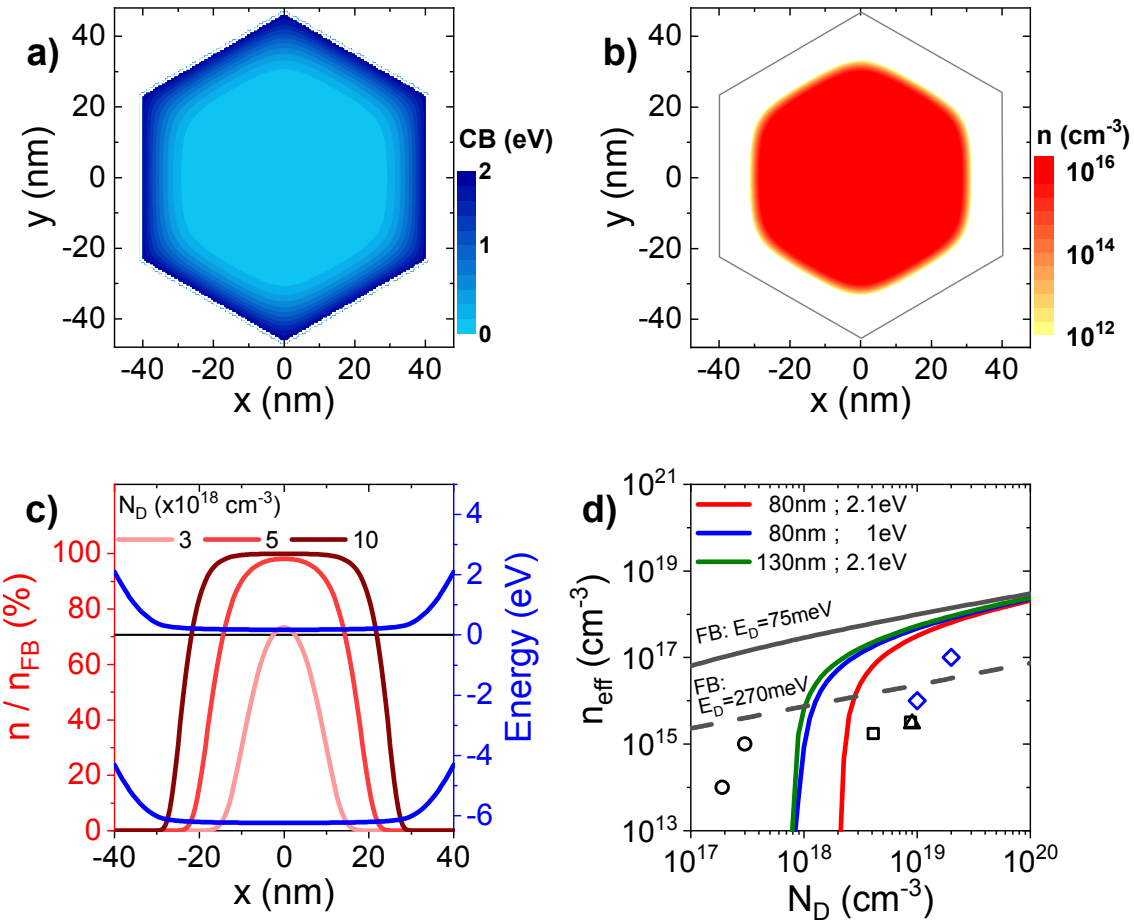

Figure 4.10: (a) Simulated conduction band minimum and (b) electron density in the NW plane. (c) Ratio between NW and bulk electron density (red) and conduction and valence bands (blue) as a function of the position in the NW. Fermi level is represented by the black line at 0 eV. All simulations have been computed for a Fermi level pinning of 2.1 eV on m-plane, $N_D = 10^{19}$ cm^{-3}, and $E_D = 75$ meV. Only n/n_{FB} ratio simulations were performed for various N_D. (d) Simulated effective electron density for two different NW diameters and Fermi level pinning as a function of the donor concentration. Black circles from [80], black square from [76], black triangle from [186] with $E_D = 270$ meV. Blue squares from [183] with $E_D = 86$ meV.

4.4 Study of space charged limited current regime

Lots of information are still to be discussed and analyzed from the IV experiments shown in figure 2.11. If one would have expected a linear behavior of current on a large voltage range like in standard conductors, experiments tell a different story. The dependance of current with voltage is indeed corresponding to a transport mechanism called space charged limited current (SCLC).

4.4.1 Trap assisted space-charge limited current theory

Theoretical background

As described by Lampert [88], the simplified theory of SCLC is designed in order to model current flow in insulator containing traps based on Poisson's equation and the charge neutrality equation at quasi-thermal equilibrium. The case of a material with free electron concentration n containing a single trap with concentration N_t located within the forbidden gap at a single energy level above the Fermi level and a homogenous electronic transport is hereafter considered. At low bias, Ohmic conduction occurs thanks to the drift of charge carriers present at thermodynamic equilibrium, following Ohm's law:

$$I_\Omega = \frac{qn\mu SV}{a} \tag{4.4}$$

where q is the electronic charge, μ the carrier mobility, V the applied voltage between the anode and cathode separated by a distance a, and S the contact surface. Depending on the trap nature and its energy position with respect to the Fermi level, a number of them can be charged close to the contact, repulsing carriers and preventing their direct injection from the contact. In the case of deep traps, a certain voltage threshold is needed to overcome this repulsion, which is equal to $V_{\mathrm{TFL}} = \frac{qa^2N_t}{2\varepsilon}$, ε being the dielectric constant of the material. In the case of nanowires with high surface/volume ratio, V_{TFL} may be significantly reduced due to poor electrostatic screening [201]. Once this voltage is reached, the current flow arises from injected carriers at the contact resulting in a steep increase in current, sometimes wrongly assigned to impact ionization [89]. Starting from V_{TFL} and for higher voltages, the current follows Child's law and is only dependent on the carrier mobility μ , but no longer on the density of electrons n present in the material:

$$I_C = \frac{8q\varepsilon\mu SV^2}{9a^3} \tag{4.5}$$

However, in the case of shallow traps, and as the Fermi level lies below the trap level close to the anode, only a fraction might be already neutralized. Accordingly, direct injection from the contact can occur at voltages lower than V_{TFL}, ensuing the onset of

Child's law at a voltage, $V_{\Omega-\theta} = \frac{ea^2n}{2\varepsilon\theta}$. Here, the free/trapped carrier ratio θ is defined by the following equation:

$$\theta = \frac{N_C}{N_t} \exp\left(-\frac{E_C - E_t}{kT}\right) \tag{4.6}$$

with N_C being the effective density of state of the conduction band, k Boltzmann's constant, T the temperature, and $E_C - E_t$ being the relative position of the trap level with respect to the conduction band. This ratio, smaller than unity, is independent of the applied voltage. For $V_{\Omega-\theta} < V < V_{\mathrm{TFL}}$, the current flows following Child's law corrected from θ smaller than 1,

$$I_C = \frac{8q\varepsilon\theta\mu SV^2}{9a^3} \tag{4.7}$$

In the case of $V \approx V_{\mathrm{TFL}}$, filling of all traps occurs, and the current flows in standard Child's law regime where θ takes the value 1.

Experimental facts

IV measurements were redone in order to access higher voltages. To avoid self-heating due to high electrical power at large bias, a pulsed voltage was used with an optimized ON state duration of 50 µs and a duty cycle of 2%. Figure 4.11 shows the coefficient m of the power law $I = V^m$, defined by

$$m = \frac{d\log(I)}{d\log(V)} \tag{4.8}$$

At higher bias, this linear Ohmic regime evolves toward a space-charge limited regime. Two behaviors can be distinguished depending on the doping level. For the lowest doped samples ([Si] $< 5 \times 10^{18}$ cm^{-3}), the transition is associated with a m value reaching more than 3 at voltages around 1 V. Following the transition regime, a quadratic behavior is observed. For the most doped samples ([Si] $> 10^{19}$ cm^{-3}), the transition from $m = 1$ to $m = 2$ is monotonous and smooth. For S1200 and S1250, m reaches a value of 2 in a range of a few volts for which Child's law regime is obeyed before increasing sharply above 10 V while it increases for a voltage as low as 4 V in S1300.

These observations are consistent with the theory of SCLC as formalized hereabove following ref. [88]. The different behaviors between the first and second NW population can be explained by assuming different trap characteristics (i.e., the energy level or concentration). In the case of the first population, the high m value extracted at 1 V is assigned to the trap filling limit, followed by a $I \propto V^2$ corresponding to Child's law regime. Equation 4.5 is used to fit the I–V curve, assuming $S = 10^{-4}$ cm^{-2}, a= 450 nm, $\varepsilon = 9\varepsilon_0$ [208] and $\theta = 1$, leading to an electron mobility value around 0.01 cm ^{2}/(V.s) for almost all samples with [Si] $< 10^{19}$ cm^{-3}. Only S900 and S930 exhibit a mobility of 0.8 and 0.08 cm ^{2}/(V.s), respectively. These values are surprisingly low compared to values reported in the literature in the case of bulk materials [76, 209]. One explanation could arise from the

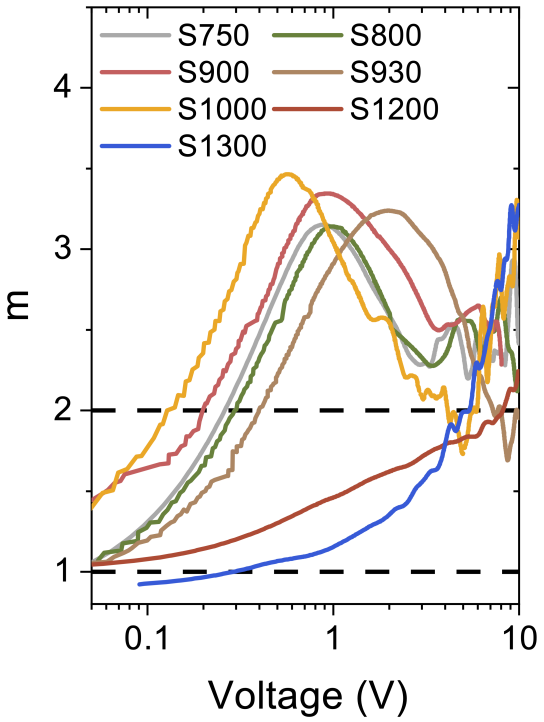

Figure 4.11: Plot of $m = d(\log(I))/d(\log(V))$ vs voltage for different samples. Horizontal dashed lines are guides for the eyes.

overestimation of the conduction area S under consideration. Indeed, part of an individual wire can be depleted due to Fermi level pinning on the NW sidewall. Additionally, a certain amount of NWs within the probed array may not contribute equally to the current flow due to height or diameter inhomogeneities.

As shown in figure 4.11, the slope increase from 1 to 2, for the most doped samples, indicates the predominance of a trap filling regime. This difference in behavior between low and high doping could arise from either a drastic increase in the trap density or the formation of a new trap located above Fermi level. Conversely, the Ohmic regime observed for those samples points toward a conduction exclusively related to the DX state (4.8). Thus, it highlights a correlation between the increase in Si doping and the DX concentration and the apparition of a regime of trap filling in the line of other studies [174, 176].

4.4.2 Additional trap in highly Si-doped AlN NWs: a new DX state?

Trap characteristics

In order to further characterize the trapping behavior in AlN:Si NWs, temperature dependent current-voltage measurements were carried out between 200 and 500 K. I–V characteristics of S1250 are shown in figure 4.12 (a). At high bias, the contrast between S1250 and S900 showed in figure 4.8 (a) emphasizes the difference in trap population

previously highlighted. Almost no temperature dependence is found for the low doped samples in agreement with a trap filled space-charged limited regime. In this regime, equation 4.6 with $\theta = 1$ holds, in which the only temperature dependent term is the mobility, expected not to vary on several orders of magnitude [80]. In the case of S1250, a clear temperature dependence is seen in the V^2 regime, which is consistent with the trap filling mechanism and the θ dependence with temperature (equation 4.7). Fitting the quadratic region with modified Child's law function (equation 4.7), the quantity $\theta\mu S$ was extracted. Taking $N_C = N_C^0 T^{3/2}$, equation 4.6 is rewritten as

$$\theta\mu S T^{3/2} = \frac{\mu S N_C^0}{N_t} \exp\left(-\frac{E_C - E_t}{kT}\right) \tag{4.9}$$

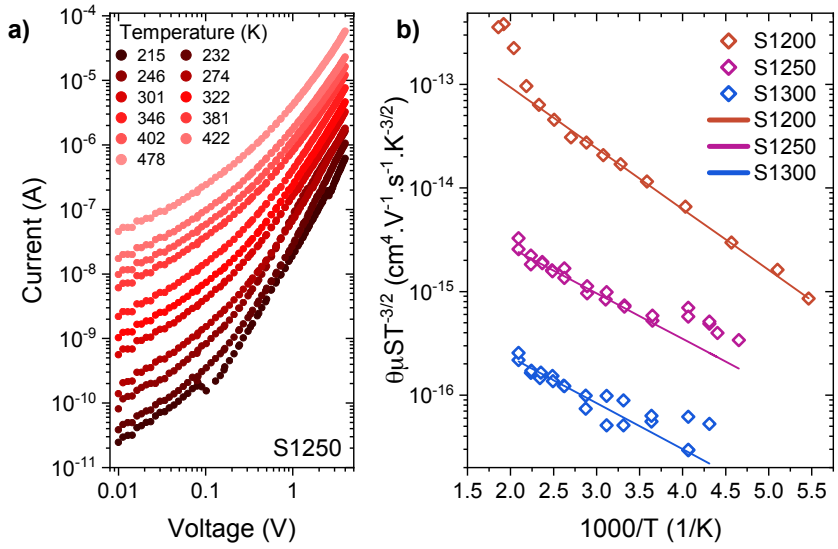

Figure 4.12: (a) I–V characteristics for different temperatures for S1250. (b) Evolution of $\theta\mu S T^{3/2}$ as a function of $1000/T$ for S1200, S1250 and S1300. Straight lines are exponential fits

Figure 4.12 (b) shows the evolution of the quantity $\theta\mu S T^{3/2}$ as a function of $1000/T$ in a semi-logarithmic scale. Assuming no variation of mobility with temperature [80], $E_C - E_t$ values equal to 162, 144, and 132 meV were extracted for S1200, S1250, and S1300, respectively. Taking a mobility of 0.01 cm ^{2}/(V.s) and a surface of 100×100 cm^2, fitting of S1250 gives a trap density of 1.1×10^{20} cm^{-3} to be compared with [Si] $= 2 \times 10^{20}$ cm^{-3} in this sample. As extracted from study of the Ohmic regime, the main donor exhibits an ionization energy of 270 meV designated as the transition level energy of DX center. Interestingly, the trap is found to be at around 150 meV and, therefore, shallower than the DX state at 270 meV. Moreover, with the increase in the Si flux, an increasing proportion of trap with respect to [Si] is measured. This cannot be compatible with a two levels system in which Si is either in a shallow substitutional state or in a DX state but rather suggests the

implication of a third Si-related state. Although the presence of defects, such as $V_{Al} - Si_{Al}$ complexes, cannot be discarded, the ionization energy of such complexes is not in agreement with our experimental data [186]. By contrast, our results are consistent with *Aleksandrov* et al. [197], who proposed two metastable configurations of Si in AlN, perpendicular to and along the c-axis, denoted DX_c and DX_a, respectively. Their transition energy levels of around 170 and 230 meV, respectively, are in line with our results, suggesting that the trap level identified at $\sim$ 150 meV indeed corresponds to a second DX center. However, it is worth stressing that other published works based on the DFT provide a wide variety of DX states and ionization energies [191, 193, 194, 210]. More generally, those three levels were identified both experimentally and by calculations. However, they were never observed in the same sample set.

Relative distribution of the different states

Thereafter, we assume that this trap with a transition level energy of $\sim$ 150 meV is a DX center, denoted DX_1. The deeper state at 270 meV will be denoted DX_2. First, one can postulate that the configurations of Si atoms can be either shallow d or one of the two DX_1 and DX_2 centers, leading to the equation:

$$[\mathrm{Si}] = [d] + [\mathrm{DX_1}] + [\mathrm{DX_2}] \tag{4.10}$$

Second, in the lowest doped sample, d states participate in the Ohmic conduction, DX_2 centers appear only at higher temperatures, and no thermal activation of DX_1 is observed (figure 4.8). Hence, we can write: $[d] > [\mathrm{DX_1}] + [\mathrm{DX_2}]$. In other words, part of shallow donors is not involved in DX formation, no self-compensation occurs for those ones, and they can be ionized with a 70 meV ionization energy to deliver electrons to the conduction band.

On the other hand, in the most doped samples, all d and DX_1 states are depleted, and so positively charged, i.e., in a d^+ and neutral DX_1^0 state, respectively, while DX_2 are shared between neutral DX_2^0 and negatively DX_2^- charged states. This results from the fact that only the DX_2 transition energy of 270 meV is measured by the temperature dependence of the conductivity while the DX_1 transition energy of 150 meV is exclusively evidenced as an electron trap during trap assisted SCLC measurement.[1] Such a situation indicates that an additional acceptor N_A must be lying within the bandgap to compensate Si donors. Aluminum vacancies (V_{Al}) formation is predicted to be favored in n-type AlN. They could play this role by compensating DX centers as several studies reported [186, 211]. When introducing this acceptor in our model and in the specific case of these highly

[1] Because the compensated hydrogenic state d^+ is too close to CB, equation 4.6 based on Boltzmann's distribution is no more valid and the trap filling regime tends to trap free regime as shown in ref. [88].

doped samples, the following relationship can be written:

$$[d^+] + [\mathrm{DX}_1^-] + [\mathrm{DX}_2^-] > [N_A^+] > [d^+] + [\mathrm{DX}_1^-] \tag{4.11}$$

A simplified representation of such case is shown in figure 4.13. The large amount of depleted states is indeed in agreement with the low mobility values previously discussed, regardless of the sample.

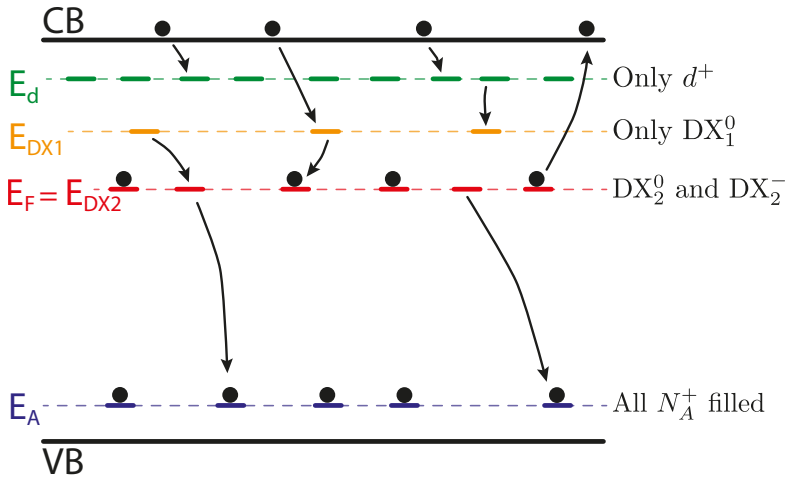

Figure 4.13: Schematic representation of the band structure with one acceptor and three donor levels. Black circle represents electron while colored dashes represent states. Fermi level E_F is assumed to be aligned with the DX_2 level E_{DX2}.

Literature hindsight

Transition level energies of Si in AlN from this study and literature are gathered and plotted as function of silicon concentration in figure 4.14. In contrast to the present study, all samples were bulk AlN grown by different techniques on various substrate materials. Large discrepancies exist depending on measurement techniques. These energies also vary as function of the growth technique (Figure D.1a) and of the substrate (Figure D.1b), indicating no specificity of the transition level energy with any of these two parameters. Three distinct families of ionization energies emerge corresponding to the ones reported in the present study: 75, 150, and 270 meV. As these three levels are only observed in the AlN NWs, it suggests that their relative population could depend on both the doping level and growth technique. It further suggests that NW morphology and peculiar strain relaxation mechanisms could favor the formation of a full set of possible Si-related DX centers. Especially, a level at $\sim$ 160 meV below CB was predicted by several computational studies [193, 195, 197] but not often measured experimentally.

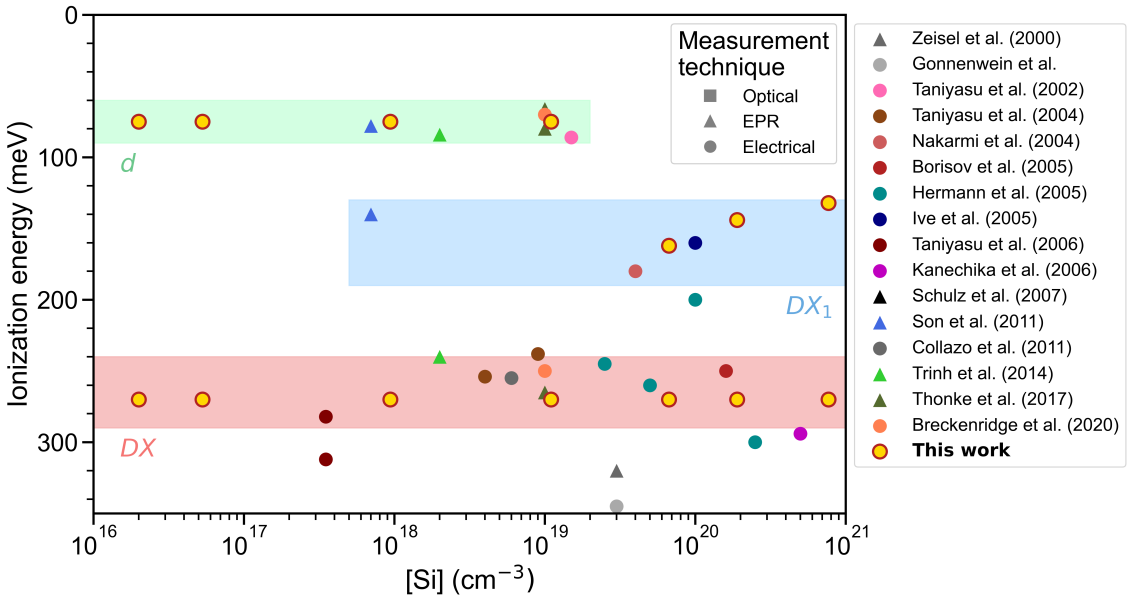

Figure 4.14: Review of transition level energies of silicon in AlN reported in the literature as a function of the silicon concentration [11, 76, 80, 172–183]. Optical refers to photoluminescence techniques, EPR to electron paramagnetic resonance and electrical refers to either Hall or conductivity measurements. Green, blue, and red regions are indicative.

It must be noticed that because the substitutional d level is quite shallow and its ionization energy is well described by the hydrogenic model, one can evaluate the metal nonmetal transition to be in the range of 10^{19} cm^{-3}, as observed for other wide bandgap semiconductors (10^{19} cm^{-3} in N-doped 4H-SiC [212], 4.10^{20} cm^{-3} in B-doped Diamond [213] or 10^{18} cm^{-3} in Si-doped GaN [78]). However, in figure 4.14, no ionization energy decrease versus Si-doping concentration is observed at around 10^{19} cm^{-3}. Instead, the abrupt appearance of the DX $_1$ level and the simultaneous disappearance of the d level are put in evidence, without an understanding of whether its is pure coincidence or a correlation induced by a physical effect.

4.5 Summary of Chapter 4

4.5.1 Conclusion on Si-doping of AlN NWs

To conclude this chapter, fifteen samples were investigated over a wide range of doping up to almost 1% Si in AlN. Structural study shows a change in growth mechanisms above an effusion cell temperature of 1100°C corresponding to a doping level of around 10^{19} Si/cm^3. It was assessed that solubility limit was not reached in our samples without strain building-up, although exhibiting large inhomogeneities at largest flux. I-V characterizations were carried out and showed the presence of an Ohmic regime at low bias followed by SCLC

regime at larger bias.

Ohmic regime study allowed to confirm the presence of compensation effect with an optimized conductance at around 10^{17} Si/cm^3 in agreement with *Harris* et al. [186]. By the mean of temperature study, both shallow donors and deep DX states were found to be contributing depending on the NW doping level.

From the study of SCLC regime, we could understand the differences in electrical transport based on a theoretical modeling from 1956 [88]. Especially, the influence of trap is strong in the most doped samples where only DX signature have been seen. An increased concentration of identified traps was observed as function of doping level. Its energy level points towards another state of Si in a DX center as it was suggested by theoretical computations and sometimes experimental data.

4.5.2 To go further

To go further, AlN NWs showed an alternative in order to incorporate Si in pure substitutional state and benefit from its low ionization energy. Between donor ionization energy of 270 meV and 75 meV, the increase in free electron concentration is significant at room temperature and would allow the realization of highly conductive n-AlN. However, we demonstrated that self-compensation effect starts relatively early and DX states are still the majority. It reduces the performances and further study need to be addressed in order to control the amount of compensating centers. To my opinion, this system is still full of surprises and requires more in-depth research on both thin films and NWs although facing intrinsic limits. The question is to know if these will be acceptable for the realization of a device.

Two questions are still open in our system. The first one is an experimental proof of a DX center behavior following the definition of *Zeisel* [174]. To confirm this, persistent photocurrent at low temperature is the must to exhibit trapping behavior and identify the DX through hysteresis in conductivity. The second one is about the spatial distribution of Si atoms. If for low Si doping, a uniform repartition of dopant seems intuitive (but still needs to be assessed), for higher Si flux, we can only make the assumption that it is the case. As seen in GaN nanowires, dopants can be incorporated preferentially in the periphery of the wire, leading non-uniform electrical conductivity [214]. Despite all my efforts, I could not access to a technical solution to prepare plane-view of the NWs for further TEM study.

Moreover, surface states appeared to have a drastic effect on the electrical properties. Surface passivation could be studied in order to clarify the discussion in paragraph 4.3.3 and seen as a way to improve the total electron density especially as nanowires are thin.

Research projects could also explore different donor atoms. Ge, which is as efficient or even better than Si in realizing n-type GaN, is known to undergo DX transition as well [215]

and have a solubility limit lower than Si in AlN [216]. The story is similar for O in AlGaN. Theoretical computations indicates that S could remain stable in AlN [217]. Although nobody reported any experimental facts on AlN:S and our attempts on S-implanted AlN thin film were not conclusive.

CHAPTER 5

AlN Nanowires pn-junction: Doping and contact optimization

In this chapter, the study of AlN NW pn-junctions is carried out. Electrical behavior is investigated for different designs and doping of both n-type and p-type sections. Optimal doping was found in order to get a good balance between the two sides and ensure an optimal injection of carriers in the active area.

Contents

5.1 Do AlN pn-junctions exist? 106

5.2 Influence of dopants and their concentration 107

5.2.1 Mg/In codoping of p-AlN 107

5.2.2 Balance between n and p sides 111

5.3 Top interface and hole injection issue 116

5.3.1 Fowler-Nordheim tunneling 116

5.3.2 On the identification 118

5.3.3 Influence of p-GaN cap 119

5.4 Summary of Chapter 5 121

5.4.1 Conclusion on AlN NWs pn-junctions 121

5.4.2 To go further 121

5.1 Do AlN pn-junctions exist?

After three years as a PhD student, general feeling I have is that most AlGaN researchers do not believe AlN can be doped and able to let current flow in a decent manner. AlGaN is indeed good enough for most of the applications and better than pure AlN from an electrical point of view. Reasons for this belief are numerous, one being that n-type doping is much more difficult because of ionization energy of Si in AlGaN drastically increasing for Al content greater than $\sim$ 70%. The topic has been already discussed in Chapter 4. A second reason is that electrical conduction in p-AlN is impossible to achieve because Mg acceptors are more than 500 meV above valence band and are highly compensated by native n-type impurities. Despite the lack of motivation for this field, progress have been made.

Highly Mg-doped AlN NWs were demonstrated and exhibit good conduction properties in a single NW configuration. Noticeably, *Tang* et al. [218] reported free hole concentration up to 5.10^{19} /cm^{-3} with 20 Ω^{-1}.cm^{-1} in AlN NWs grown by chloride-CVD. *Tran* et al. [219] reported free hole concentrations of a few 10^{17} cm^{-3} in MBE-grown AlN NWs and attributed conduction mechanisms to hole hopping. Magnesium is the main p-type dopant investigated as carbon and beryllium are predicted to suffer from interstitial incorporations [220, 221]. However, one group from Georgia Tech has achieved efficient p-type doping of GaN and AlN layers using Be as dopant. Free hole concentrations up to 10^{19} cm^{-3} and 8.10^{17} cm^{-3} were reported in GaN and AlN respectively [222, 223]. Moreover, they reported the realization of devices which take advantage of Be doping, presenting good properties in forward bias despite large leakage current and premature breakdown, probably sign of degraded crystal quality [224].

However, studies on the electrical properties of pn-junctions themselves are somewhat lacking, with reports presenting simplistic IV curves without attempting to investigating limiting factors and possible improvements.

Therefore, the aim of this chapter is to give answers to several questions within the scope of doping and electrical transport in AlN NW pn-junctions. How do Mg and Si concentrations influence the pn-junction electrostatics and which design is the optimal for light emission? Which mechanisms are limiting the current flow in such structure?

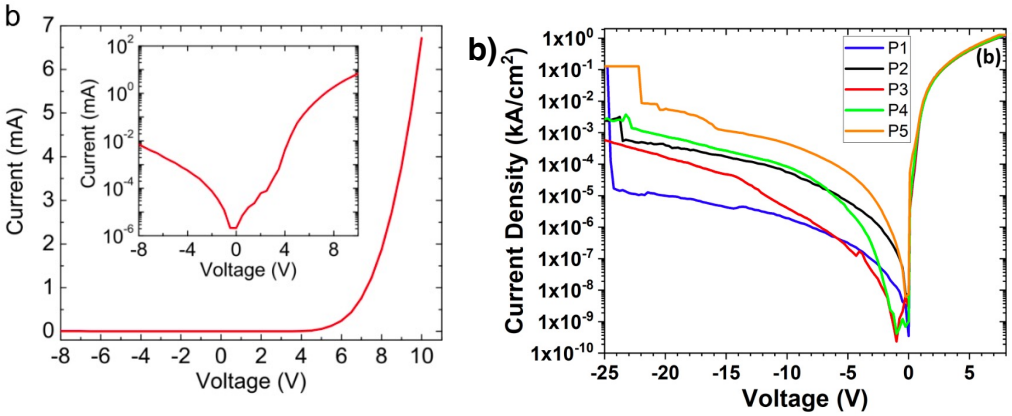

Figure 5.1: (a) I-V characteristics of AlGaN NWs pin junctions from [168]. (b) I-V characteristics of p-AlN:Be / i-GaN:Be / n-GaN:Ge pin-diode from [224].

5.2 Influence of dopants and their concentration

5.2.1 Mg/In codoping of p-AlN

To begin with, a focus is given on Mg/In codoping of AlN for improved p-type doping. If *A.M. Siladie* showed that In incorporation in AlN gives rise to an increased Mg incorporation [105], its impact on transport properties of pn-junctions has not been completely understood. Especially, an irradiation step, demonstrated as necessary in her work, was not required for the following structures that were grown during my PhD.

The two first pn-junctions are presented here. Their growths were achieved on n-type (111)-Si wafers as for the study on n-type AlN NWs. Firstly, a n-GaN stem was grown at around 820°C and with a Ga/N ratio of 0.3 prior to grow n-AlN and p-AlN sections at 900°C and 800°C, respectively. The Si cell temperature was kept at 900°C for n-AlN section since it was found to be the optimal point (Chapter 4). The p-type AlN section was doped with a Mg cell temperature of 300°C based on ref [105]. The only difference was the presence of an In flux in N3831 compared to N3830 (table 5.1). A schematic is given in figure 5.2 (a). Samples were processed with a metal stack consisting of Pt/Pd/Au (10 nm/10 nm/50 nm) in order to make 100 × 100 μm^2 square pads and perform IV characteristics. The results are shown in figure 5.2.

Table 5.1: Number, and dopant cell temperatures of the different sections of the studied samples.

Sample number	n-GaN T_{Si} (°C)	n-AlN T_{Si} (°C)	p-AlN T_{Mg} / T_{In} (°C)	p-GaN T_{Mg}
N3830	920	900	300 / —	**no p-GaN**
N3831	920	900	300 / **800**	**no p-GaN**
N3838	920	900	300 / **800**	**280**

Both samples are rectifying when applying a positive bias on the p-side (i.e. forward biased), meaning that the pn-junction is effectively playing its role of diode. The strongest differences are exhibited in forward bias. While N3831 with In shows a reasonable ideality factor of 23, sample N3830 without In shows a large ideality factor of 110 which describes the poor rectifying behavior of the sample. Such a high value cannot be caused by thermoionic effect describing the lowering of the pn-junction potential barrier. Instead, Poole-Frenkel model is more adequate to describe this behavior. This model describes carrier flow by trap assisted tunneling and is usually used to in reverse biased Schottky contacts and diodes [225]. The equation ruling the current in this model is:

$$I \propto V \cdot \exp\left(\frac{q\sqrt{\frac{qV}{4\pi\varepsilon_r\varepsilon_0 w}} - q\Phi_t}{kT}\right) \tag{5.1}$$

where $\varepsilon_r = 9$ is the relative dielectric constant of AlN [208], w the length of tunneling and Φ_t the trap energy level. The linear dependence of $\ln(I/V)$ vs $\sqrt{V}$ shown in figure 5.2 (c) clearly indicates that N3830 follows this model. Moreover, a fitting of the data allows to extract the value of w which is found here to be of 70 nm. This value is quite large for a tunnel process but may be biased by a competition between several conduction mechanisms as a large number of NWs is probed.

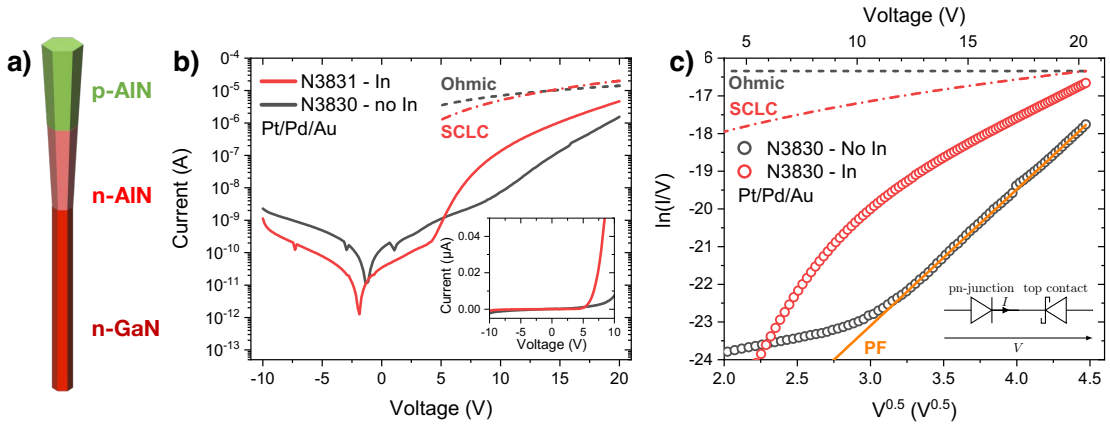

Figure 5.2: (a) Schematics of the NW structure. (b) I-V characteristics in semi-log scale. Inset: lin-lin scale. (c) Same data plotted in a Poole-Frenkel plot. Dots represents experimental data. Lines represent different model used: SCLC stands for Space charge limited current, PF stands for Poole-Frenkel. Inset: equivalent circuit proposed to explain the I-V behavior of N3830 — without In.

The explanation to account for this difference between N3830 and N3831 is the formation of Schottky contact at the p-AlN / metal interface induced by a low Mg concentration when no In is added during the growth. This Schottky barrier is opposite to the pn-junction (inset of figure 5.2 (c)) and the current is limited primarily by the leakage of the contact. When In is added, the increased Mg concentration diminishes the barrier and

the pn-junction becomes the main limitation to current flow. Nevertheless, as seen in figure 5.2 (b-c), neither Ohmic nor SCLC conduction models fits experimental data of N3831 at high voltage, indicating that another barrier must be at play.

Changing the metal stack to Ni/Au (30 nm/50 nm) gives a rectifying behavior being mainly thermoionic in both samples with ideality factor of 31 without In and 20 with In (figure 5.3). It points toward the importance of metal as the work function of Pt and Ni are different and assess the difficulty of having a good metal — p-AlN contact.
On the basis of N3831, a third sample was grown on which was added a 10 nm p-GaN cap (table 5.1). Its current-voltage characteristic was measured using Ni/Au metal stack and compared to the others in figure 5.4. If the current level and behavior don't change at high bias with respect to N3831, it exhibits a low ideality factor of 15 and less leakage current. At this stage, the reason for this improvement is tentatively attributed to a better hole injection thanks to the thin p-GaN capping.

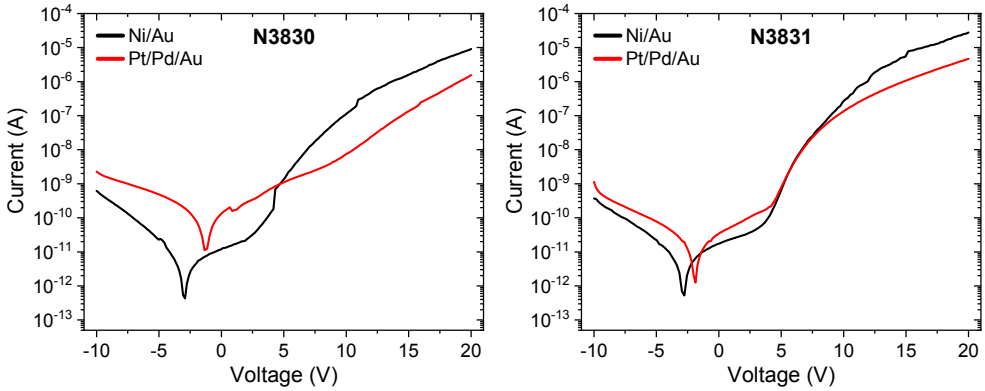

Figure 5.3: I-V characteristics in semi-log scale of N3830 (a) and N3831 (b) for the two different contact metal.

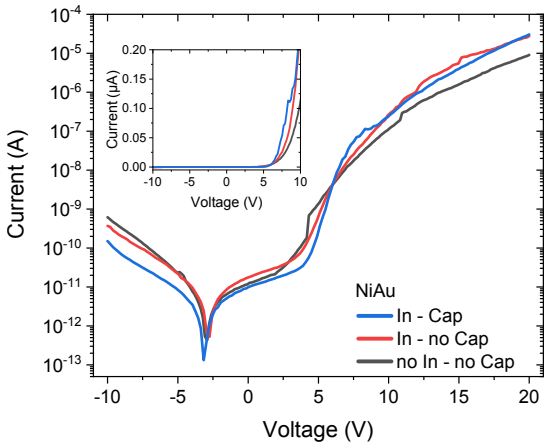

Figure 5.4: I-V characteristics in semi-log scale of samples with Ni/Au metal stack. Inset: lin-lin scale.

Table 5.2: Summary of ideality factors, tunneling energies and main transport mechanisms in forward regime of N3830, N3831 and N3838.

Sample	Features	Metal stack	η (best)	E_T (meV)	Transport mechanism
N3830	No In — No p-GaN	Pt/Pd/Au	110	—	Poole-Frenkel
N3831	In — No p-GaN	Pt/Pd/Au	23	591	TAT
N3838	In — p-GaN	Pt/Pd/Au	27	690	TAT
N3830	No In — No p-GaN	Ni/Au	31	797	TAT
N3831	In — No p-GaN	Ni/Au	20	514	TAT
N3838	In — p-GaN	Ni/Au	15	385	TAT

Large ideality factor and tunneling

Because of the rather large ideality factor between 10 to 30, it is unlikely that pure thermoionic effect is at play at the pn-junction as described in Schokley equation 2.8. Several studies have tried to identify the origin of such large ideality factors found in wide-bandgap semiconductor based diodes [93, 94, 226–228]. In particular, the work of *Lee et al.* gives an understanding as they relate it to material properties and trap-assisted tunneling (TAT) mechanism [227]. Indeed, in this model, electrons and hole can recombine thanks to deep-level traps lying in the band gap at the pn-junction as depicted in figure 5.5. This tunneling current can be written as follows:

$$I \propto \exp(\frac{qV}{E_T}) \tag{5.2}$$

where E_T is a characteristic tunneling energy given by the following expression:

$$E_T = \frac{4h}{\pi}\sqrt{\frac{N_i}{m^*\varepsilon_r\varepsilon_0}} \tag{5.3}$$

with m^* the effective mass of the tunneling entity and N_i the density of impurities. Taking N3830 with Ni/Au electrode as example, the slope of the $\ln(I)$ vs V can lead to an ideality factor of 31 or equivalently a tunneling energy of 797 meV. depending if one takes into account only electrons with $m_e^* = 0.33$ or only holes with $m_h^* = 4$ [229], N_i can be comprised between 2.10^{17} cm^{-3} and 3.10^{18} cm^{-3}. Because of the intricacy, no further analysis will be carried in this chapter. Nevertheless, it highlights the role of impurities in the electrical transport, which seems to limit the current in a pure thermoionic behavior and a rather low bias ($V < 6$ V).

To conclude this part on the relevance of In/Mg codoping in p-AlN, table 5.2 provides a summary of the measured samples, their features and electrical characteristics. It is chosen for the following study to use N3838 as base structure and work with In/Mg codoping, a p-GaN cap and Ni/Au cap.

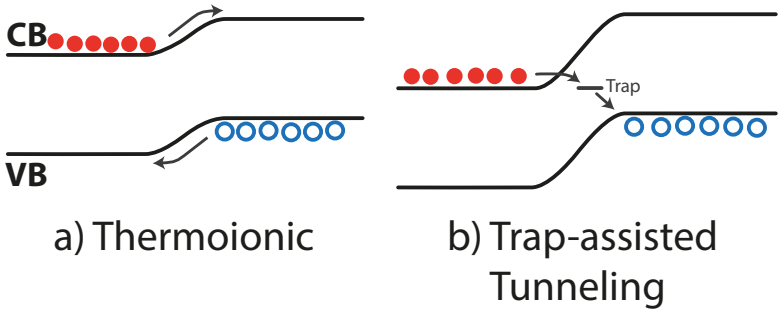

Figure 5.5: Schematic representation of a) pure thermoionic and b)trap assisted tunneling mechanisms at a pn-junction.

5.2.2 Balance between n and p sides

In a second part, the focus is put onto the doping levels of AlN sections. To do so, three samples were grown. The structure consists of a 400 nm n-type GaN stem, a 300 nm n-AlN section, a nid-GaN layer of a few nm, a 300 nm p-AlN section and a 10 nm p-GaN cap. AlN sections were grown at 870°C while n-GaN was grown at around 810°C, nid-GaN QW at 780°C and p-GaN cap at 750°C in Ga-rich conditions to promote NWs enlargement and reduce Mg desorption. SEM images of one of the samples as well as its sketched structure are displayed on figure 5.6. Differences only lie in doping of AlN sections, specifically in the temperature of Si and Mg cells during the growth of n and p sides respectively. Cell temperatures have been chosen in the light of previous studies and are reported on table 5.3. The Mg and In cell temperatures have been chosen according to *Siladie et al.* [105] and to the previous subsection. Si cell temperature has been chosen in regards of the results from part 4. $T_{Si} = 900$°C was the maximum of the conductance curve while a $T_{Si} = 1050$°C degrades the electrical properties although without affecting the NWs morphology (see figures 4.4 and 4.7). These samples were further contacted using $100 \times 100\ \mu m^2$ Ni/Au (30 nm/50 nm) and Pt/Pd/Au (10 nm/10 nm/50 nm) in a second time.

Table 5.3: Number, name and dopant cell temperatures of the different section of the studied samples.

Sample number	Sample name	n-GaN T_{Si} (°C)	n-AlN T_{Si} (°C)	p-AlN T_{Mg} / T_{In} (°C)	p-GaN T_{Mg} (°C)
N3735	Si9-Mg2	930	**900**	**280** / 800	280
N3736	Si10-Mg2	930	**1050**	**280** / 800	280
N3737	Si9-Mg3	930	**900**	**300** / 800	280

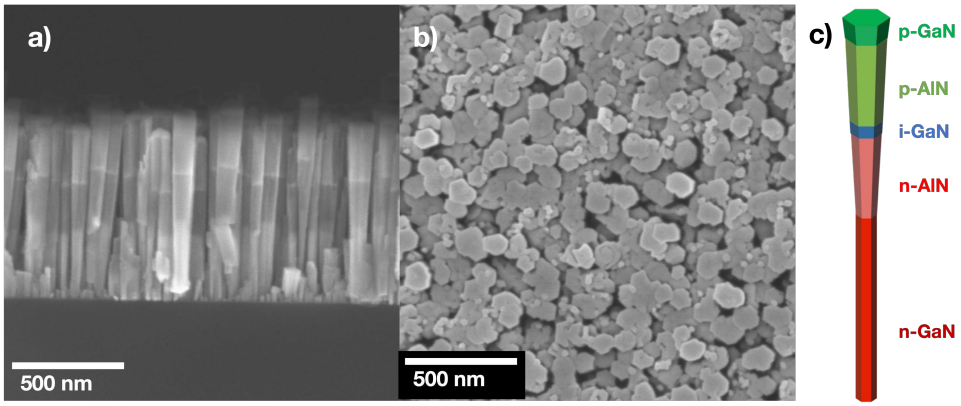

Figure 5.6: Top (a) and cross sectional (b) SE image of one of the three samples of the study. (c) Sketch of the NW structure.

Electrical current conduction

Figure 5.7 presents IV characteristics of the four devices. Once again good rectifying behavior is observed in all samples with leakage current levels slightly increased with respect to previous ones (10^{-9} vs 10^{-10} A). The reverse current behavior remains constant and indicating no effect of the changes in pn-junctions on it thus, it will not be further analyzed in this section. Influence of leakage can be observed on the first few volts in forward bias, hiding the exponential part, especially for Si9-Mg2 and Si10-Mg2. Si9-Mg2 presents the lowest current level on the whole characteristics followed with Si10-Mg2. Si9-Mg3 is always higher than the two others samples but shows an increased current with Pt/Pd/Au metal stack compared to a Ni/Au one.

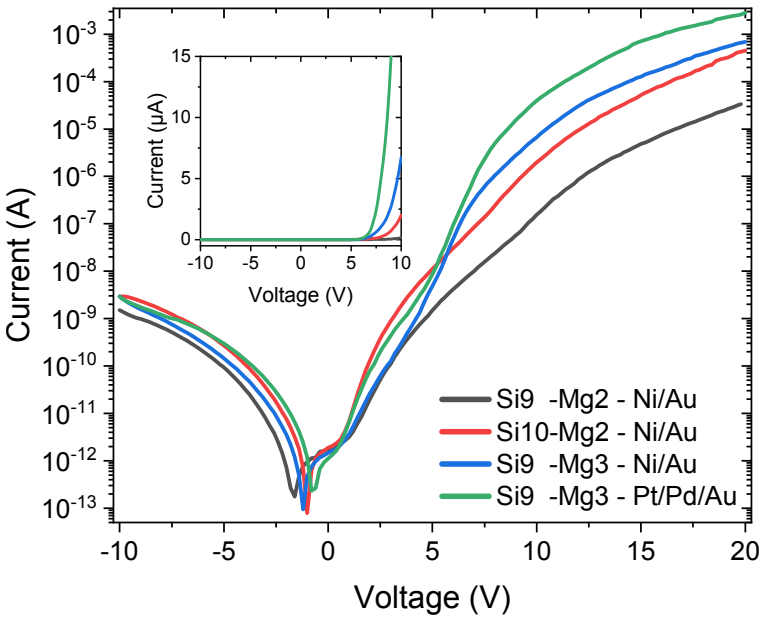

Figure 5.7: IV-characteristics of the four samples presented in table 5.3.

On the one hand, the comparison between Si9-Mg2 and Si10-Mg2 highlights a higher current value for a higher Si cell temperature in contradiction with previous results. On the other hand, Si9-Mg3 exhibits a larger current than Si9-Mg2 by one order of magnitude and a clearer exponential part at $\sim$ 6 V. Mg2 corresponding to a lower Mg concentration than Mg3 ($\sim 10^{19}$ Mg.cm^{-3} vs $\sim 10^{20}$ Mg.cm^{-3}) [105], this change in behavior is attributed to an increased free hole concentration in the p-AlN. It would also mean that self-compensation is not reached or mitigated by opening of a Mg-band within the forbidden gap, reducing the effective ionization energy [100, 219]. If n-AlN was limiting the current, no changes would have been seen in this case. Moreover, the fact that changing the metal contact changes the current level at high bias emphasizes, yet again, the importance of the top contact in electrical transport.

Electron beam induced current

EBIC was performed to get experimental information about the devices electrostatics. Results are plotted on figure 5.8. The focus is put on the n-doped AlN first where donor concentration N_D is supposed to be equivalent to $[Si]$ and eventual compensators will be referred to as N_A. Si9-Mg2 exhibits an EBIC peak in the p-AlN section while, in the case of Si10-Mg2, it is closer to the n / p interface, indicating a shift in the effective pn-junction location which is attributed to a lower effective doping in the latter. The interpretation is the following: for higher Si concentration, $N_D - N_A$ is smaller with N_D increasing. Therefore, N_A has increased more than N_D, in other words, donors have been self-compensated (supposedly by the appearance of DX centers or other complexes). This is consistent with the expected behavior reported in Chapter 4.

In a second time, we focus on the EBIC behavior when doping in the p-AlN section is varied, looking at the differences between Si9-Mg2 and Si9-Mg3. Increasing Mg flux is expected to increase Mg concentration and the net acceptor density. This would results in a shift of the electric field maximum and, consequently, of the EBIC signal towards the n-AlN section. This is experimentally verified even if a rather low collection of carriers is recorded. The presence of an additionnal contribution closer to the metal contact may be responsible for this, exhibiting once again issues in hole injection.

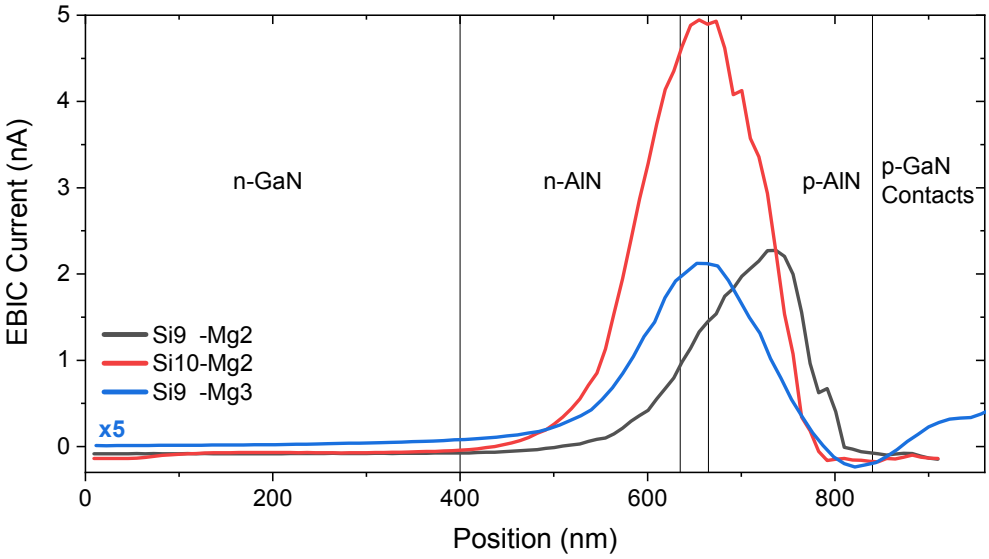

Figure 5.8: EBIC linescan along the NW of the three samples presented in table 5.3. Acceleration voltage was 5 kV and beam current of the order of 0.1 nA. EBIC signal was multiplied by 5 for Si9-Mg3.

Electroluminescence

Finally, EL spectra were acquired under a continuous DC bias using special pads, shown on figure 5.9. They consist in square pads with circular openings in the metal in order to let photons escape while preserving as much as possible electrical injection. This is done to overcome the lack of transparent electrode in the UV-C region, even if in this case, ITO would have worked perfectly considering the emission wavelength.

Figure 5.10 (a) shows the EL signal of Si9-Mg3 - Pt/Pd/Au as function of the applied bias while figure 5.10 (b) compares the EL spectra at +10 V of all four samples. From the first plot, as the voltage and current increase, light is being emitted and collected by the CCD camera at a wavelength around 325 nm. It is assigned to the GaN section inserted in the pn-junction.

When it comes to compare EL spectrum of the four samples, Si9-Mg2 and Si10-Mg2 are showing a broad EL peak in the blue band attributed to radiative recombinations of carriers on deep defects of AlN. As EBIC showed, space charge region of Si10-Mg2 is located mainly into the p-AlN side and therefore electrons and holes meet and recombine on present defects. As concerns Si9-Mg2, its EBIC signal exhibited better features which is not in agreement with EL signal, with a main contribution arising from defects and a smaller one from GaN well at 345 nm.

Contrarily to them, luminescence from Si9-Mg3 is comprised between 325 nm and 355 nm corresponding to nid-GaN region, whatever the metal stack used. To account for the variations in emission wavelength between the two Si9-Mg3 devices, let start by

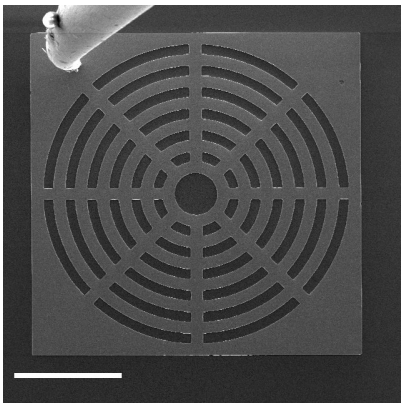

Figure 5.9: SE image of a contacted metal pad for EL measurements. Scale bar is 100 µm.

noticing that their spectra are composed by several peaks which is a sign of QW thickness fluctuations from NWs to NWs. Especially, because of current spread on the top layer and dopant inhomogeneities from wires to wires and perhaps, only few hundreds of wires are contributing to the EL signal which exacerbates variations in active area. This is further confirmed by measuring EL of different LEDs. Slight variations in peaks emission wavelength were observed (not shown here).

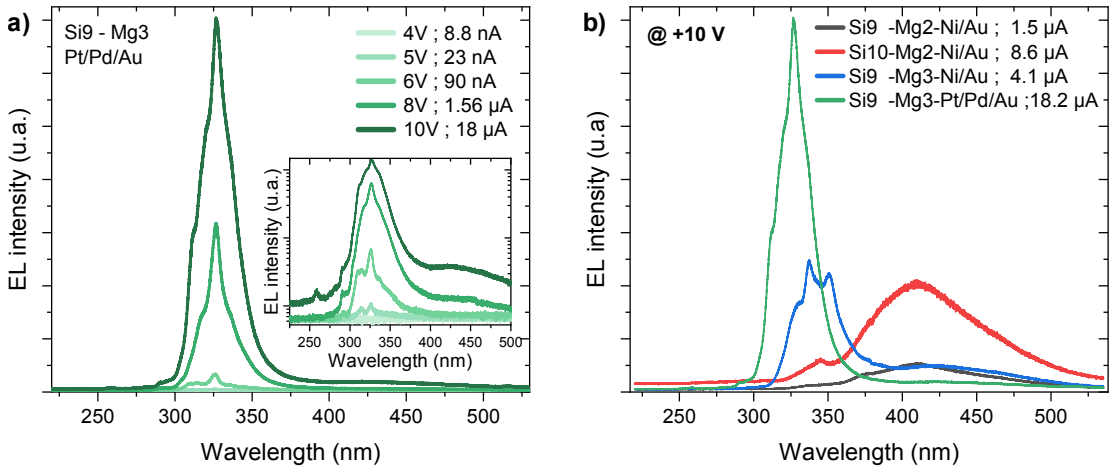

Figure 5.10: (a) EL spectra as function of the applied bias of Si9-Mg3-Pt/Pd/Au. Inset: EL measurements plotted on a semi-logarithmic scale. (b) Comparison of EL of the four different samples.

In the end, the results from this last experiment consolidates IV and EBIC results. Only Si9-Mg3 with $T_{\mathrm{Si}} = 900°\mathrm{C}$ and $T_{\mathrm{Mg}} = 300°\mathrm{C}$ is optimized in order to achieve sufficient carrier injection at the metallurgic junction where the active area is located. Still, the issue of contacts, as pointed by EBIC and differences with metal stack, has to be tackled and will be in the coming section.

5.3 Top interface and hole injection issue

5.3.1 Fowler-Nordheim tunneling

As emphasized in this chapter, top section of the NW structure has a particular influence on transport mechanisms, limiting the pn-junction performances and resulting in high ideality factors. Moreover as pointed out in figure 5.2 (b), current flow is not following neither an Ohmic nor SCLC model after the junction is fully lowered (i.e. at bias larger than $6 \sim 7$ V). However, figure 5.2 (c) shows that electrical transport behavior is close to a Poole-Frenkel model, although not fitting well enough IV data except for the special case without In codoping.

Looking a the literature, another similar model seems to be better suited to the experiment. The so-called Fowler-Nordheim model is used to describe tunneling through a triangular potential barrier. Contrary to direct tunneling, charge carriers tunnel only partly and do not cross all the dielectric as depicted on figure 5.11 [230]. In this case, current flow is given by the following equation:

$$I = \frac{qSE^2}{16\pi\hbar\phi_B} \exp\left(- \frac{4\sqrt{2m^*}(q\phi_B)^{3/2}}{3\hbar q\varepsilon_r E} \right) \tag{5.4}$$

with, m^* the effective mass of the particle, $\hbar$ the reduced Planck's constant, S the contact surface area, E the electric field and ϕ_B the barrier height. Plotting $\ln(I/E^2)$ vs $1/E$ gives a so-called Fowler-Nordheim plot and if one assumes a linear dependence of the voltage with the electric field, FN plot can be rewritten as $\ln(I/V^2)$ vs $1/V$. Few articles report this transport mechanism in wide bandgap pn-junctions. Often, it is observed in metal — (insulator) — semiconductor junctions in silicon, nitrides or diamond [230–235].

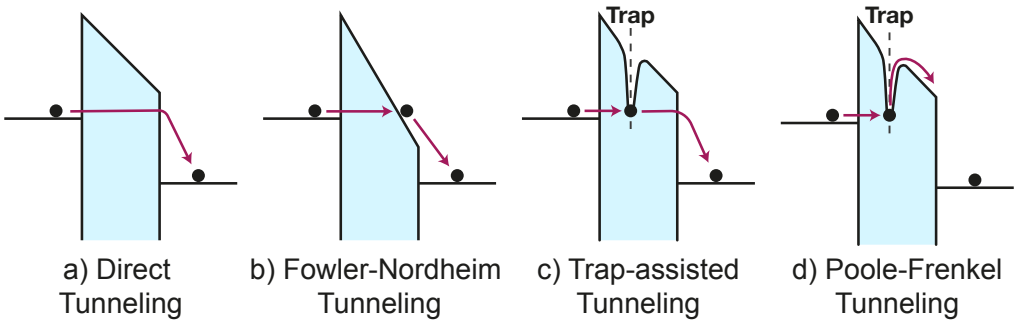

Figure 5.11: Cartoon of four kinds of tunneling model.

Figure 5.12 shows the same data as on figure 5.7 on a FN plot. The linear behavior at lower 1/V (higher bias) indicates that FN tunneling is at play and limits the current flow. Interestingly, it appears at voltages above 7 V when the pn-junction is fully lowered.

The physical mechanisms being revealed, the following questions are: *which interface*

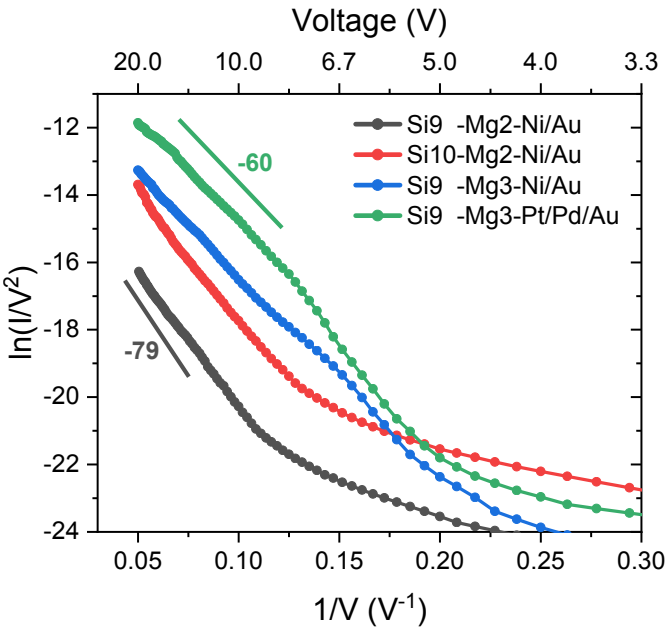

Figure 5.12: FN plots of samples N3735, N3736 and N3737.

is in cause ? and *how to improve it ?*. Several interfaces are present and could lead to the kind of band bending represented in figure 5.11. They are enumerated below and indicated on the band diagram in figure 5.13.

1. n-Si — n-GaN: Plotting IV characteristics of samples presented in Chapter 4 in which the structure was n-Si / n-GaN / n-AlN / n-GaN do not exhibit FN behavior. In addition, EBIC never exhibited any signal which could be attributed to the presence of an internal electric field. Therefore, this interface is excluded.

2. n-GaN — n-AlN: Excluded for the same argument as for the n-Si / n-GaN interface despite the clear discontinuities because of band offsets and polarization effects.

3. n-AlN — p-AlN: Already observed in pin-Schottky diamond device [235], FN tunneling can be present at a pn-junction due to uneven carrier density in n and p sections leading to an unbalanced band bending between neutral zones. It cannot be discarded although the reduced conductivities and similar dopants levels make it less probable.

4. p-AlN — p-GaN: Due to the ~ 1 eV discontinuities between VB of GaN and AlN [236, 237], it cannot be discarded either.

5. p-GaN — metal: A large band offset between metal and p-GaN can lead to the same situation as the previous interface.

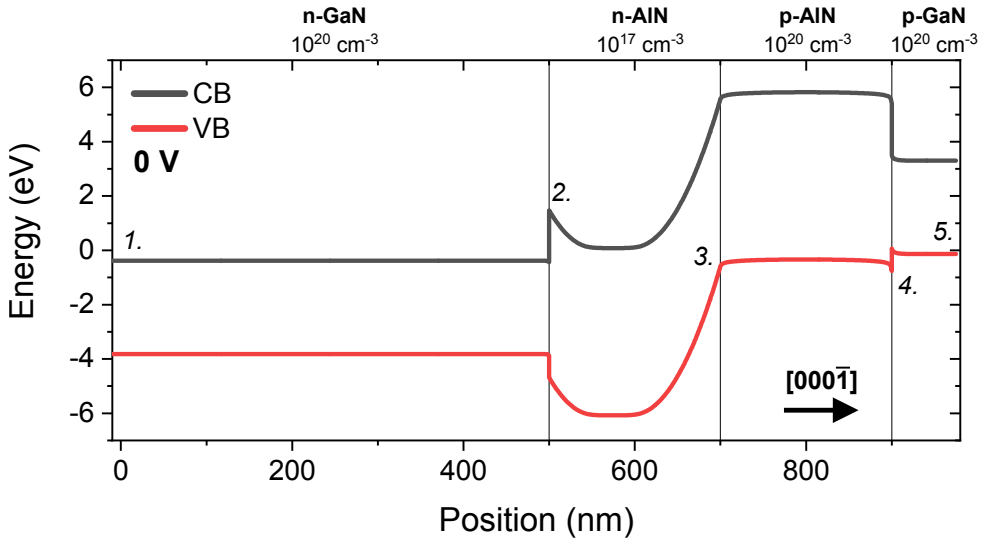

Figure 5.13: Band structure of the overall NW pn-junction at zero bias. Numbers refer to the different interfaces. Fermi level is at 0 eV. n-Si / n-GaN and p-GaN / metal contacts are not simulated. Doping level in the p-AlN is probably overestimated. Indeed, it is assumed that all dopant atoms are in site, active, and not compensated, which is an ideal case scenario.

5.3.2 On the identification

Looking at figure 5.12, several slopes can be extracted from the linear part which is directly linked to the energy barrier. From equation 5.4 rewritten with $E = V/d$, the slope α of the FN plot is given by:

$$\alpha = \frac{4dq^{3/2}\sqrt{2m^*}}{3\hbar q\varepsilon_r}\phi_B^{3/2} \tag{5.5}$$

However, two unknowns are present —d and ϕ_B— and cannot be extracted at once. Direct comparison of the slopes remains relevant. On these samples, two values for α emerge: -79 V for Si9-Mg2 and Si10-Mg2 and -60 V for Si9-Mg3 with both Ni/Au and Pt/Pd/Au metal contacts. Changing Si doping does not change the value of the slope from which is inferred that n-interfaces is not the cause (as previously assumed). The same conclusion is obtained about the top metal contact. However, increasing Mg concentration led to a smaller slope pointing towards the importance of p-AlN doping.

This clue is further supported by *NextNano* simulations performed under different bias. For this purpose, only the AlN pn-junction is simulated with a p-GaN capping, assuming no strain and no impact of n-GaN. p-GaN / metal contact was too difficult to simulate with the few information available to me (value of the work function and hole concentration are missing). Figure 5.14 (a) presents the band structure at 0 V, +6 V and +9 V. If the bands are flat at 6 V as expected from the pn-junction barrier lowering, at 9 V the potential drop occurs at the p-AlN / p-GaN interface instead of in neutral zones. It is

further emphasized on the zoom in figure 5.14 (b), in which valence bands are normalized with respect to its level in the p-GaN zone. For a bias of $\sim$ 6 V, one can notice the shape of the VB approximate very well a triangle such as in FN tunneling model. Thus, te hypothesis of the electric field being linearly proportional to the voltage is confirmed in first approximation.

From this simulation a tunneling distance d of around 1.5 nm is extracted. Associated with the slopes of FN plots and equation 5.4, barrier heights of 16 eV and 19 eV are found which are unreasonably large. One explanation for this would be that the potential drop is not only at the FNbarrier but rather share with another interface such as the pn-junction or the p-GaN / metal interface.

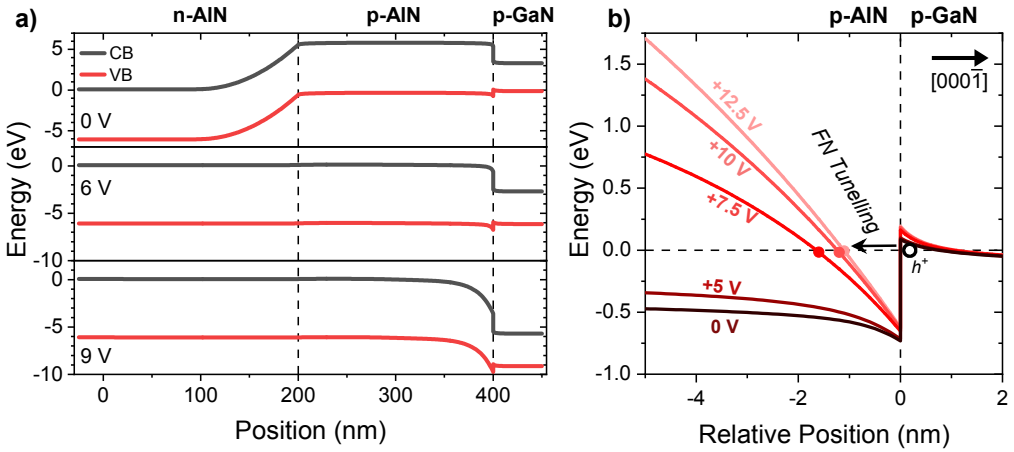

Figure 5.14: (a) Simulated band diagram of the n-AlN / p-AlN / p-GaN sections at 0 V, 6 V and 9 V. (b) Focus at the Valence band a the interface p-AlN / p-GaN for applied bias between 0 V and 15 V. Normalized with respect to the VB in p-GaN.

5.3.3 Influence of p-GaN cap

Removing the p-GaN cap is also a way to assess the influence of the interface. As discussed in Section 5.2.1, such samples exist (see table 5.1). N3838 and N3831 are respectively with and without p-GaN and in both cases exhibit FN-limited regime at high bias. Their ideality factor are recalled in table 5.4 and the extracted slopes of FN plots α are added. Contrary to previous samples, slopes greatly depend on the metal stack more than on the presence or absence of the p-GaN layer.

All the discrepancies found in between the two groups of samples rather indicate that the quality of the interface matters at least as much as the materials it is composed of. Looking at the morphology of the top of the NWs, they can be quite different depending on the recipe used. Even if the growth parameters were approximately the same, some variations can be observed between samples.

Table 5.4: Ideality factor η extracted from IV plots and slopes α extracted from FN plots of samples from Section 5.2.1.

Sample	Features	Metal stack	η	α
N3831	In — No p-GaN	Pt/Pd/Au	23	-37
N3838	In — p-GaN	Pt/Pd/Au	27	-43
N3830	No In — No p-GaN	Ni/Au	31	-70
N3831	In — No p-GaN	Ni/Au	20	-65
N3838	In — p-GaN	Ni/Au	15	-70

As shown in figure 5.15, N3735 (Si9-Mg2) is not as coalesced as N3838 which doesn't exhibit NW morphology at the very top. It may have an impact on dopant incorporation and on the quality of the metal deposited. It has been also measured that samples with a top p-GaN thicker than 30 nm exhibit leakages with current bypassing the diode (not shown).

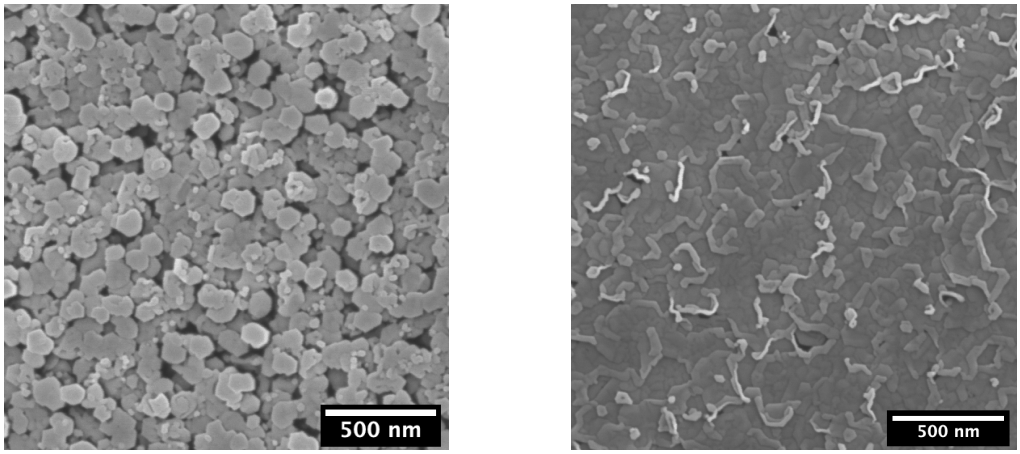

Figure 5.15: SE image in top view of (a) N3735 (Si9-Mg2) and N3838 (b).

5.4 Summary of Chapter 5

5.4.1 Conclusion on AlN NWs pn-junctions

To conclude this chapter, electrical properties of 6 carefully chosen samples were investigated by the mean of various techniques. A first part allowed to confirm the advantage of In codoping for an improved p-type conductivity in AlN NWs. The use of a thin GaN cap was also motivated by the increase in hole injection.

In a second part, an in-depth study of samples grown with various pn-junction characteristics has been realized. Current-voltage, electron-beam induced current and electroluminescence measurements have been correlated and agreed on the best doping levels in order to optimize charge carriers injection and achieve an efficient light emission.

An investigation of the mechanism limiting the current at high bias was done in a third part. Fowler-Nordheim tunneling regime was found to limit the current by limiting hole injection from the metal into the p-type NW section. Several experimental and simulation facts pointed towards the p-AlN / p-GaN and the p-AlN / metal to be responsible. However, discrepancies were also reported. The role of surface morphology might play an important role, more than anticipated.

Finally, this chapter allows to continue as the choice of the optimized set of parameters for the pn-junction is achieved.

5.4.2 To go further

The work in order to improve the diode electrical properties remains vast. If the limiting factor is found to be the top contact, several ways of improvements are suggested here.

- The growth of a graded p-AlGaN section could be implemented in order to suppress the abrupt p-AlN / p-GaN interface. As stated in Chapter 3, the growth of AlGaN NWs is difficult and the realization of a controlled gradient is a challenge in itself.
- Investigation of the role of NWs morphology is of importance too. The use of patterned substrate could be beneficial in order to control the density while playing on the growth parameters of the top section with a greater freedom. Filling of the space between NWs could be also of good use in order to planarize the top surface prior to metal deposition. The idea of hole injection by the side-walls instead of the c-plane (in a contact-all-around fashion) could be interesting as Mg tends to segregate on NWs periphery [199].
- The idea of beryllium doping of AlN NWs for p-type doping, in the light of the approach of *Doolittle*'s group would also be a benefit if the results are confirmed.
- As a last suggestion, the exploration of new materials for p-type contact is relevant as the one used here are shown to insufficiently promote hole injection and are opaque to UV. In all these respects, graphene [238], h-BN [239] and diamond should be considered.

CHAPTER 6

UV light emitting diodes from AlN nanowires

In this chapter, properties of AlN nanowire based light emitting diode are investigated. After reviewing the state-of-the-art of UV LED and describing the studied sample, optical properties are briefly recalled as they were already discussed extensively in Chapter 3. In the light of Chapter 5, electrical properties of the device are detailed. It further exhibits promising electro-luminescence behavior, emitting at 285 nm and in agreement with the correlated CL and EBIC electro-optical measurements. Finally, a discussion on the efficiency is conducted.

Contents

6.1 Insight about deep UV LEDs . . . 124
6.1.1 State of the art in thin films . . . 124
6.1.2 Reports on NW based UV LEDs . . . 125
6.2 Design of the device . . . 126
6.3 Device characterizations . . . 127
6.3.1 Optical characterization . . . 127
6.3.2 Electrical characterization . . . 128
6.3.3 Electro-optical characterization . . . 130
6.4 Light emission behavior . . . 132
6.4.1 Electroluminescence . . . 132
6.4.2 About efficiency . . . 133
6.5 Summary of chapter 6 . . . 135
6.5.1 Conclusion on AlN NWs LED . . . 135
6.5.2 To go further . . . 135

6.1 Insight about deep UV LEDs

To begin with, a brief review of UV-LEDs realization in thin films and nanowires is done in order to give the reader more insight of what is currently achieved in the community.

6.1.1 State of the art in thin films

In current state-of-the-art of deep UV LEDs, few features have now became inevitable in order to tackle bottlenecks.

Because light extraction efficiency is diminished as the emission wavelength reduces, solutions to improve this aspect have been developed. The use of patterned AlN or sapphire substrate combined with reflective electrodes is now a must-have to reach high external quantum efficiency (EQE) DUV LEDs. Noticeably, the world record EQE is, at this moment, held by *Takano et al.* with 20% at 275 nm [111] (Figure 6.1a). Such high value was achieved thanks to three points. They used a patterned sapphire substrate in addition to an encapsulation with a UV-transparent resin, both allowing more light to escape the device. The p-type AlGaN layer was also realized with high enough Al content to be transparent to the UV radiation, while a good electrical conductivity. Finally, the use of a Rh mirror p-type contact enabled the reflection of part of the UV usually lost at the rear face.

Another path which is followed, relies on the improvement of the internal quantum efficiency (IQE) by reducing the amount of dislocations in the grown layer. To do so, epitaxial lateral overgrown (ELO) AlN layer is widely used. Etching AlN strips and promoting lateral growth of the subsequent AlN layer, dislocations are able to bend and annihilate (Figure 6.1b). The resulting amount of threading dislocation density (TDD) can be reduced from a few 10^9 cm^{-2} down to a few 10^8 cm^{-2} [240]. However, the resulting increase in IQE is at the expense of a costly and complex fabrication step. Recently, *Susilo et al.* have shown equivalent performances of ELO AlN substrate and sputtered and annealed AlN on sapphire [241]. This fabrication being much simpler than ELO, it opens a way for further improvement on large scale DUV-LEDs, while reducing their cost.
The technique of NH_3 pulse-flow multilayer is also quite popular in MOCVD grown AlN buffers [242, 243]. It consists of the alternating of pulsed and continuous supply of NH_3 during the growth in order to enhance the Al adatom diffusion length and allows to reach TDD as low as in ELO.

Along with p-type AlGaN superlattices for improved hole concentration, these are the main advances of the recent years, which have allowed to reach such high efficiencies.

On MBE side, at this stage, only very few reports on DUV-LED displays EQE, probably because of their low efficiencies. To be noted, the work of *Brault et al.* who grew AlGaN/AlGaN quantum dots LED with efficiency of 0.15% at 300 nm [116] and of *Mous-*

takas et al., whose LEDs based on MBE grown AlGaN/AlGaN QWs reached an EQE of 0.4% at 273 nm [244]. Both EQE values are indeed one order of magnitude lower than their MOCVD competitors.

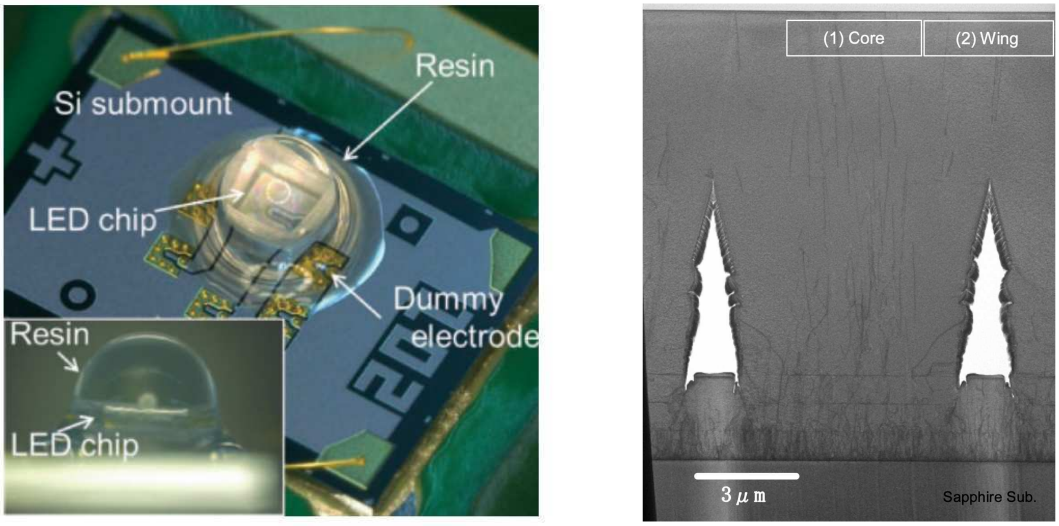

(a) (b)

Figure 6.1: a) Image of the 275 nm LED with its package from [111]. b) Cross-sectional ABF-STEM image of an ELO substrate from [240]. Black lines are dislocations.

6.1.2 Reports on NW based UV LEDs

Away from the active research on thin film DUV-LEDs, nanowire systems are also studied. However, reports on UV electroluminescence from such devices are not abundant, even if some can be highlighted. In our group, *Durand* and coworkers aim at developing core-shell AlGaN micro-wires grown by MOCVD for UV emission [245]. If they demonstrated EL in the UV-B range, strain relaxation issues due to the bulky GaN core, limits either the layers quality or the minimal achievable wavelength. Also in UV-B region, *Velpula et al.* [246], have used AlInN NWs in order to emit light at 295 nm. Deeper in the UV, the work of *Zhao et al.* [168] reports electroluminescence spectra from AlGaN NWs between 280 nm and 230 nm in a p-i-n LED structure. They claim the reduced nitrogen flux at 0.4 sccm to be responsible for the AlGaN alloy uniformity contrary to the disordered alloy in AlGaN NWs when grown with 1.0 sccm. The emission wavelength was adjusted by increasing the temperature which effect is to lower Ga resident time and its incorporation. No significant discussion on the electrical properties is done. Especially, as the Al content increases, the increase in ionization energy of both p-type and n-type dopants should lead into a more difficult injection of carriers into the active area.

In parallel, and to reach deeper wavelength, the use of h-BN as replacement for p-AlN has been investigated in *Laleyan et al.* [239]. The heterostructure is composed of an n-

AlN and i-AlN section on which h-BN is deposited. This AlN/h-BN LED exhibits an EL signal at 210 nm without parasitic luminescence, in a narrow window ranging from 200 to 230 nm. Electrical properties of this UV-transparent contact was limited to a simple I-V characteristics. However the use of h-BN, directly evaporated in the MBE chamber is interesting to get access to a transparent and potentially highly conductive top layer.

6.2 Design of the device

The hereafter presented AlN NWs LED sample, named N3784, was grown by plasma-assisted MBE on highly conductive n-type (111)-Si substrate. Figure 6.2 shows a sketch of the sample structure and SEM images from top and cross-sectional view. The design has been chosen in the light of the results from the previous chapter 5. The heterostructure consists of a 500 nm long highly conductive n-GaN stem, followed by 150 nm n-type AlN section, an AlN:Ga active area, a 150 nm long p-type AlN section and a 15 nm p-type GaN cap. GaN stem was grown at a substrate temperature of ∼815°C and a metal/nitrogen ratio of 0.3 whereas n-type and p-type AlN sections were grown at 900°C and 800°C respectively with the same metal/nitrogen ratio. n-type doping was achieved using silicon while p-type doping was obtained using magnesium / indium co-doping. The Si concentration in the n-type AlN section was around 10^{17} Si/cm^{-3} [169]. In the p-type AlN section, the concentration of Mg and In was around 10^{20} and 5.10^{18} cm^{-3}, respectively [105]. Doping level of around 10^{20} Si/cm^{-3} was used in the GaN stems to ensure a high conductivity and metallic behavior of this section [77]. The AlN:Ga section was grown at 800°C by alternating the metal and nitrogen fluxes as presented in Section 3.3.1.

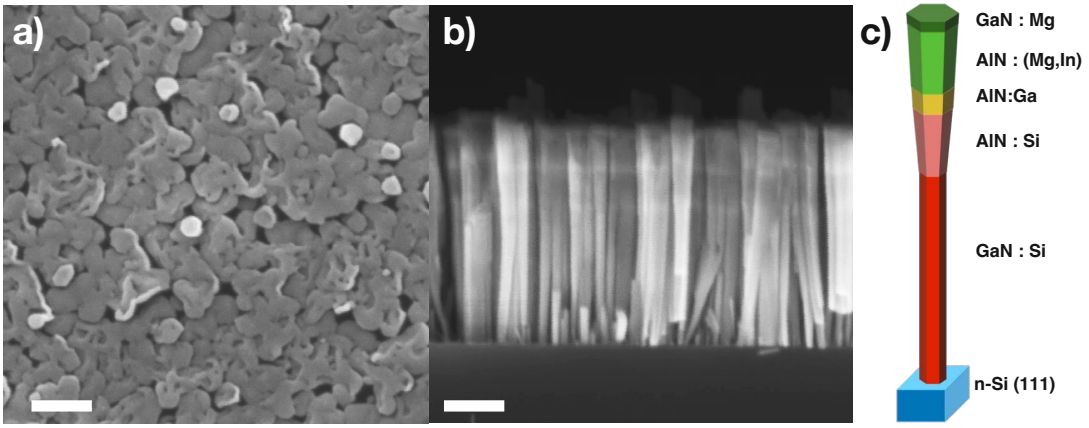

Figure 6.2: SEM image from top view (a) and cross-sectional view (b) of AlN NW sample. Scale bars are of 200 nm for both images. (c) Schematic of the sample structure.

6.3 Device characterizations

6.3.1 Optical characterization

The majority of the optical properties of this sample were already discussed in Chapter 3, Section 3.3.1. CL spectra revealed the presence of recombination centers emitting at around 285 nm and which behaved as quantum dots. The luminescence was attributed to the presence of AlGaN clusters in the active area where excitons can be strongly localized. In complement to the previous results, temperature dependent CL measurements were also performed and are shown in the inset of figure 6.3. Figure 6.3 shows the integrated CL intensity as function of the temperature. A good ratio of CL intensity between room temperature and low temperature of around 20% is measured, which is attributed to the high degree of localization of the exciton in the AlGaN clusters.

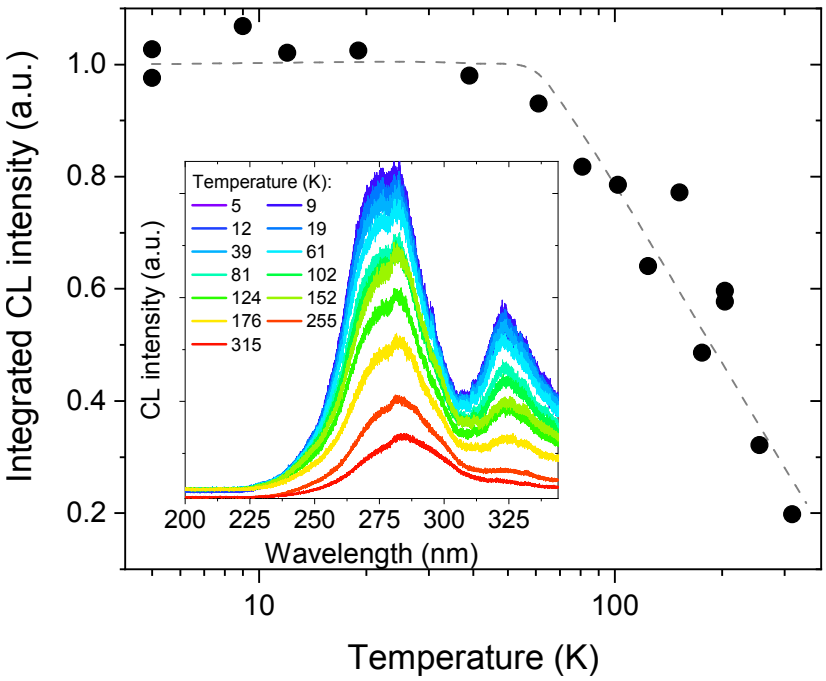

Figure 6.3: Integrated CL intensity between 200 and 305 nm as function of the temperature and normalized with respect to the measurements at low temperature. Dashed grey line is a guide to the eye. Inset CL spectrum as function of the temperature.

6.3.2 Electrical characterization

Moving on to electrical characterizations, I-V characteristics of ten diodes are plotted in a semi-logarithmic scale in figure 6.4 (a). The sample exhibits a rectifying behavior with five orders of magnitude difference between −10 V and +10 V. Good reproducibility from diodes to diodes is observed up to at least +/−30 V while keeping the same ON/OFF ratio, as shown in figure 6.4 (b). Several models were considered to account for the transport mechanisms involved in the AlN pn-junction, as some are shown in the latter figure.

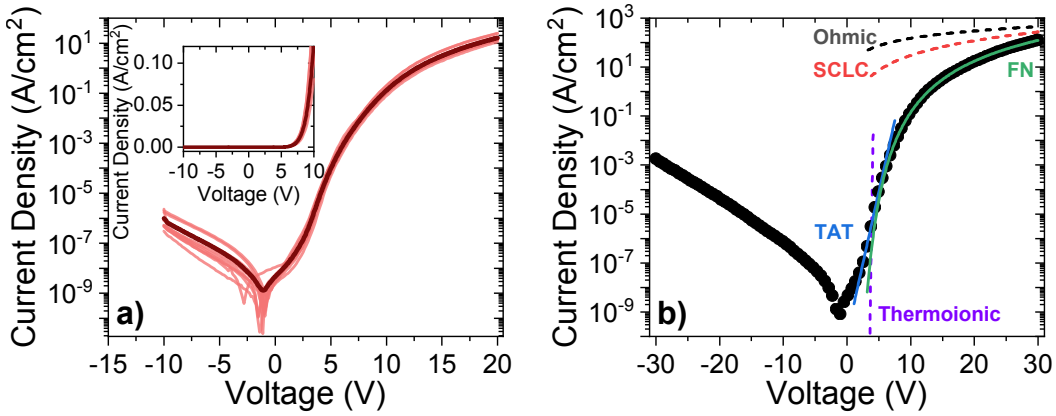

Figure 6.4: (a) Current-voltage (J-V) characteristics of ten AlN NWs LEDs. Dark red curve is the averaged curve. Upper left inset: J-V characteristics in a lin-lin scale. Lower right inset: SE image of a contacted device. (b) J-V characteristics of one diode between -30 V and +30 V (full circles) with fits of trap-assisted tunneling (TAT, $J \propto \exp(V)$) and Fowler-Nordheim (FN, $J \propto V^2 \exp(1/V)$ (straight lines). The expected dependencies according to ohmic ($J = 15 \cdot V$), space charge limited current (SCLC, $J = 0.3 \cdot V^2$) and thermoionic ($J = 10^{-70} \cdot \exp(qV/kT)$) models are also shown, represented with dashed lines. Detection limit is of 10^{-9}A/cm^2.

Firstly, at low positive bias, lowering of the pn-junction barrier results in an exponentially increasing current with voltage. Following Schokley equation 2.8, an ideality factor comprised between 13 and 16 is extracted from the exponential part of the characteristic, revealing once again a non-ideal diode, yet in agreement with the best samples studied in Chapter 5. Using trap-assisted tunneling (TAT) model as stated in section 5.2.1, a characteristic energy E_T of 340 meV is found. In order to use equation 5.3 to get access to the density of ionized impurity N_i, the choice of the adequate effective mass is of importance. By taking into account only electrons with $m_e^* = 0.33$ or only holes with $m_h^* = 4$ [229], N_i takes the values 4.10^{16} cm^{-3} or 5.10^{17} cm^{-3}, respectively. The tunneling occurring in a non-intentionally doped active area, the favored scenario is a tunneling of electrons on residual impurities present at a concentration of 4.10^{16} cm^{-3}. This is tentatively assigned to ionized oxygen dopants in the light of results of chapter 4.

Secondly, at high positive bias, neither ohmic conduction nor space-charge limited current conduction mechanisms are limiting the current once the pn-junction is lowered

(i.e. for $V \gtrsim 6$ V). Instead, I-V measurements fit once again well to a Fowler-Nordheim (FN) tunneling model, which is described by equation 5.4. By assuming that the potential is fully applied on a triangular shaped barrier, FN plot is again plotted as $\ln(J/V^2)$ vs $1/V$. This hypothesis was already validated by simulations as shown in figure 5.14 (b), which illustrates the evolution of valence band at the p-AlN / p-GaN interface under different applied bias. Figure 6.5 (a) shows I-V characteristics of the sample in a FN plot for different temperature between 6 K and 300 K. The linear part at bias higher than ~ 6 V clearly supports that this electrical transport mechanism is at play. In addition, the rather early onset of FN tunneling may signify that this barrier is competing with pn-junction lowering and may account for the rather large ideality factor identified. At voltages below 6 V, as the temperature decreases, TAT current is reduced, in agreement with freezing of carriers. At the same time, the slope in the FN regime increases from 60 to 110, which can only be due to a change in the electric field in the barrier, while the applied voltage on the whole structure remains constant. This fact, in addition to the early onset of FN tunneling, indicates that the potential is not only applied on either the pn-junction or the triangular barrier, but is rather distributed between them.

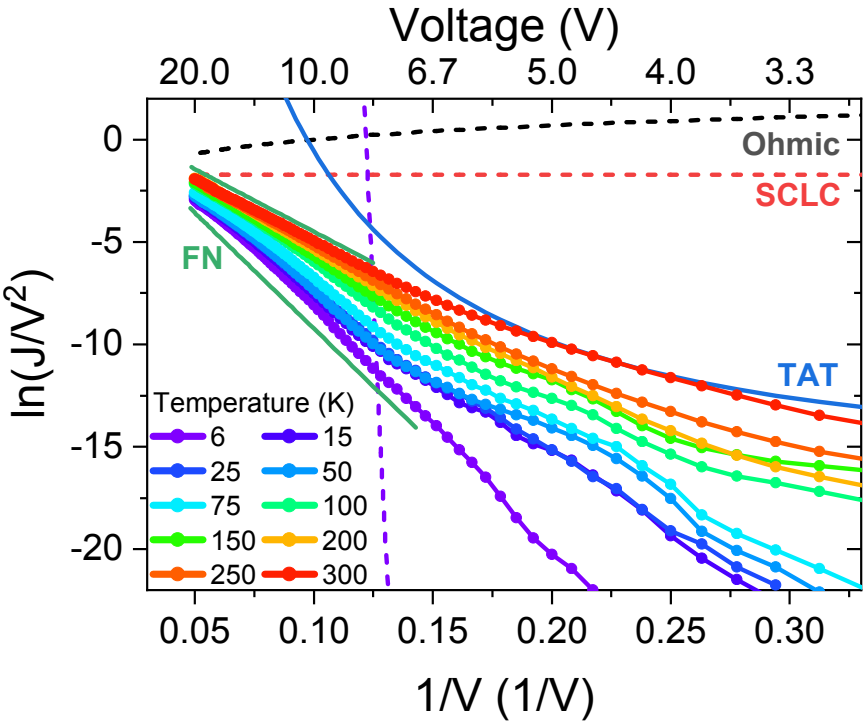

Figure 6.5: Fowler-Nordheim (FN) plot of the J-V characteristics as function of temperature. Solid lines represent FN (green) and TAT (blue) based on fits. Ohmic (grey), SCLC (red) and thermoionic (purple) conduction models are added with dashed lines taking the same parameters as in figure 6.4.

As already discussed in the previous chapter, the barrier responsible for this tunneling process is assumed to be located at the p-AlN / p-GaN interface. On this particular sample, changing the metal from Ni/Au to Pt/Pd/Au had no conclusive effect on the electrical properties.

Surprisingly, current is flowing even at temperature as low as 6 K at which all carriers should be frozen in regard of the ionization energies of the shallowest Si donor of 75 meV (Chapter 4) and Mg of 550 meV [101] in AlN and supported by theoretical calculations in Appendix B. To explain this fact, a scenario involving direct injection of carriers into their respective bands is put forward. On the one hand, holes can be provided to VB by FN tunneling from p-GaN section. Especially, figure 5.14 displaying the simulated band diagram of the structure, shows that holes are accumulating at the p-GaN / p-AlN interface. Direct injection of holes in p-GaN from the contact by SCLC is also plausible especially due to the reduced size of the p-GaN layer of only 15 - 20 nm. On the other hand, electrons are provided by the metallic n-GaN stem and are directly injected into the n-AlN CB by SCLC as reported in Chapter 4. Once injected in the bands, the electric field is enough to make both charge carriers drift to the active region.

6.3.3 Electro-optical characterization

In a second time, electro-optical characterizations were carried out. In order to perform EBIC characterizations, the sample was cleaved to access the NWs array from the side. In this configuration, EBIC at 0 V and CL signals were recorded under a 5 keV electron beam excitation. It is worth noting that these two signals were not acquired at the same location. Since EBIC implies the collection of injected charges, their separation by the internal electric field would result in the absence of recombination in this area, thus, the absence of CL signal. To cope with this issue, CL was acquired on contact-free NWs in the vicinity of the contacted ones investigated by EBIC.

On the first hand, zero bias EBIC and CL linescans are displayed in figure 6.6 (a) and (b). From EBIC signal, the pn-junction can clearly be located at the middle of the AlN section, with the electric field reaching a plateau corresponding to the space charge region, which width is found to be around 100 nm. In the case of an abrupt pn-junction, this width w is expressed as:

$$w = \sqrt{\frac{2\varepsilon(V_{\text{bi}} - V)}{qN_{\text{eff}}}} \tag{6.1}$$

with $N_{\text{eff}} = (1/N_D + 1/N_A)^{-1}$, $N_{D,A}$ the donor and acceptor concentrations and V_{bi} the built-in voltage taken as equal to 5.5 V, to account for ionization energy of dopants. With a depletion width of 100 nm, the equivalent N_{eff} is 5.10^{17} cm^{-3}. This result gives a lower limit for the dopant concentration, assigned to the n-type one and assesses a significant effective p-type doping of the AlN section.

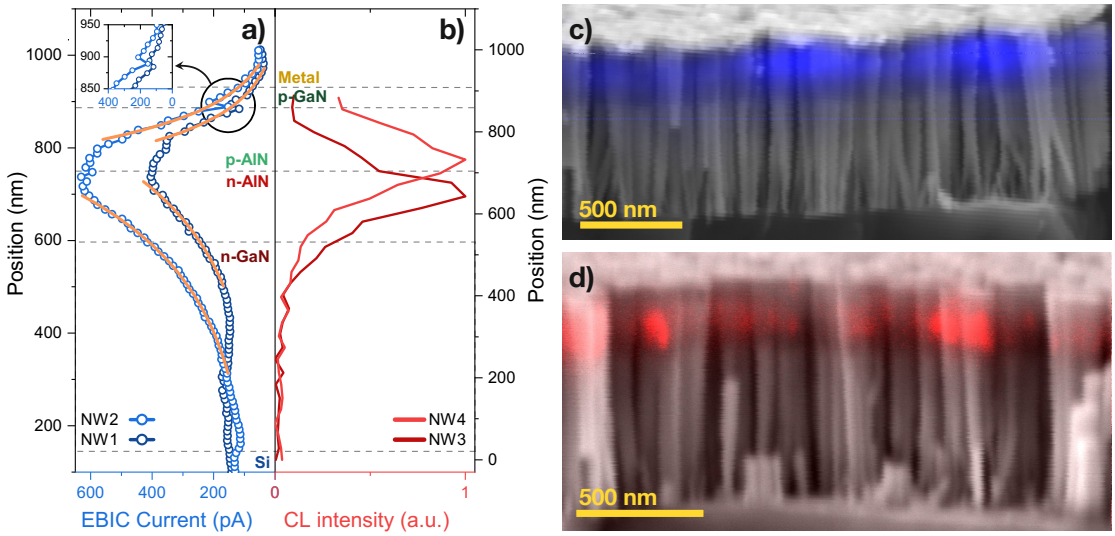

Figure 6.6: (a) Quantitative EBIC signal at zero bias in blue along with exponential fits in orange solid lines and (b) CL signal recorded along four NWs. Inset in (a) is a zoom showing the EBIC shift at the p-AlN / p-GAN interface. (c) Zero bias EBIC mapping. (d) CL mapping at 285 ± 3 nm.

Following the above equation, one can measure w at various bias until the pn-junction is fully lowered. However, this did not give conclusive results,probably because of the presence of the different barrier and the low collection of generated carrier.

Away from the depletion region, EBIC signal scales as:

$$I_{\mathrm{EBIC}} \propto \exp\left(-\frac{x}{L_{n,p}}\right) \tag{6.2}$$

where $L_{n,p}$ is the minority carrier diffusion length. Accordingly, fits were performed and are plotted as orange lines in figure 6.6 (a). Diffusion lengths of 80 ± 10 nm for electrons in p-AlN and 205 ± 15 nm for holes in n-AlN are found which are close to the ones found in other (Al)GaN systems [204, 247, 248]. A slight shift of EBIC at the p-AlN / p-GaN section is measured. Its presence might reveal the tunnel barrier previously mentioned. From CL linescan centered on 285 nm (± 3 nm), the maximum intensity is aligned with the maximum of EBIC signal which indicates the good overlap of both active region and space-charge region. On the other hand, figure 6.6 (c) and (d) show signals acquired as the electron beam was scanning the sample. It highlights the good homogeneity from wires to wires of both CL and EBIC signals. This situation is favorable to the injection of charge carriers in the active area in order to make them recombine as efficient as possible and emit photons at the desired wavelength.

6.4 Light emission behavior

6.4.1 Electroluminescence

Electroluminescence of the LED was recorded by applying a DC voltage on circular pads as displayed on figure 5.9 in order to collect light from the top. Figure 6.7 (a) shows electroluminescence spectra as a function of the applied bias. One single peak at 285 nm can be seen, which increases with voltage and current. Furthermore, the onset of the EL signal starting at 6 V (inset of figure 6.7 (a)) is consistent with the bandgap of AlN and the LED band structure. CL spectrum acquired from top view with a 15 kV acceleration voltage on a 10 × 10 µm^2 region at the center of the pad, and EL spectrum at +20 V are compared on figure 6.7 (c). Besides a good agreement of the main peak wavelength position, no significant contribution of GaN or defect related luminescence at higher wavelength is present in EL with respect to CL. This feature points toward recombination of carriers mainly in the active area, even at bias as high as 20 V.

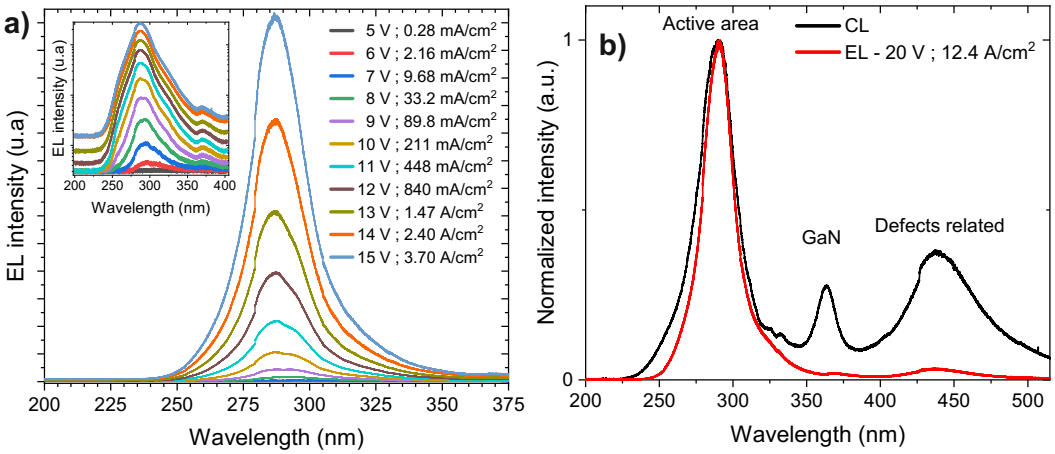

Figure 6.7: (a) Electroluminescence spectra peaking at 285 nm. Inset: same data plotted in a semi-logarithmic scale. (b) Comparison between normalized EL and CL spectra.

The expression of the external quantum efficiency is recalled:

$$\mathrm{EQE} = \frac{qP_{\mathrm{opt}}}{h\nu I} \tag{6.3}$$

with q the elementary charge, P_{opt} the optical output power, h Planck's constant, ν the photon frequency and I the current flowing in the device. This equation can be also rewritten as:

$$P_{\mathrm{opt}} = \frac{h\nu}{q} \cdot \mathrm{EQE} \cdot I \tag{6.4}$$

which state that optical power is linearly proportional to the injected current, in a standard

LED behavior. In order to know if we are in such case, EL intensities were integrated to get access to the optical power. However, in this setup, this quantity could not be measured quantitatively but it allows to plot P_{opt}/I vs I in figure 6.8. A plateau for current density lower than 0.2 A/cm^2 is observed, meaning that the above equation is followed.

However, at current injection higher than 0.2 A/cm^2, a drop is measured indicating the apparition of losses. Indeed, several factors can account for these, as depicted in figure 2.7. Among all charge carriers injected in the LED, some can be lost by Joule effect, due to high access resistances of p-type and n-type sections, some can overflow in neutral regions and exit the active area, some can recombine non-radiatively in the active area. In addition, it is much likely that only a fraction of the NWs contributes effectively to the light emission and therefore the effective area of conduction would be smaller, pushing the plateau towards higher current densities. Which of these is the predominant factor remains an open question.

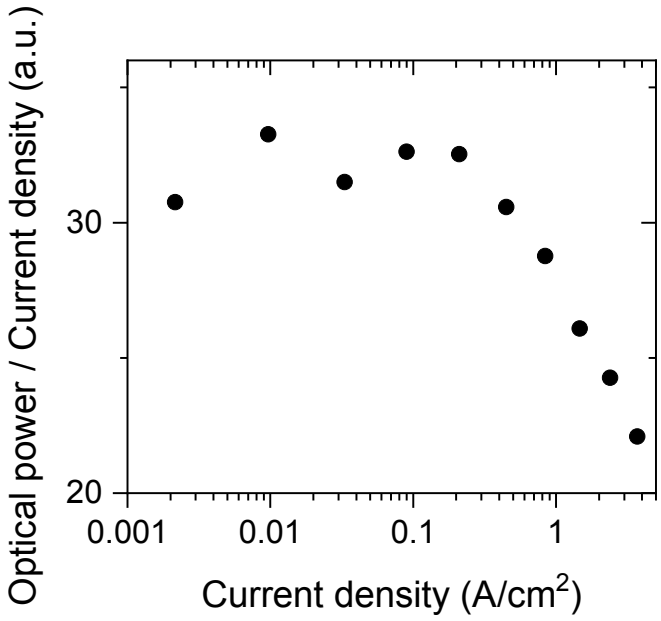

Figure 6.8: Ratio of optical power over current density as a function of current density.

6.4.2 About efficiency

In the aim of measuring the EQE and the optical power, a new contact design has been tested. A large 0.7 × 0.7 mm^2 contact made of Pt/Pd/Au (5 nm thick each) was deposited on top of the NW array. Due to its reduced thickness, this layer is behaving as semi-transparent. CL measurements on the pad and away from the pad allows to give a rough estimation of the UV light transmitted through the metal layer, which is found to be around 40%. A second lithography step was realized in order to deposit an additionnal 100×100 µm^2 square pad on top of the first one and is composed by 80 nm of gold. An optical microscope image of the pad is shown on figure 6.9 (a). Figure 6.9 (b) shows a

picture of the sample when one LED is contacted. The square pad can be clearly seen in blue indicating an homogenous current spreading, at this rather large scale. This emission color is the electroluminescence of defects in the blue band. Although it is visible with naked eyes, EL spectrum shows that this peak is around 20 times smaller than the main peak at 285 nm, as observed in figure 6.7 and confirmed by a EL measurement on this very LED, shown in figure 6.7 (c).

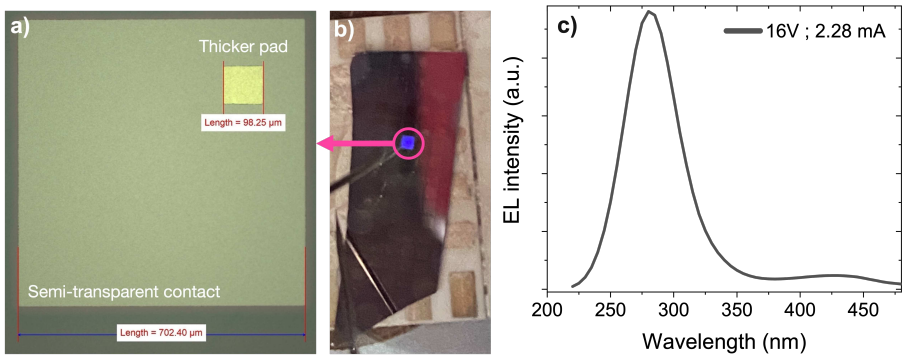

Figure 6.9: a) Optical microscope image of the semi-transparent metal contact deposited on top of N3784. b) Picture of the processed sample. One LED, designated by the pink circle, is connected and a 12 V bias is applied. c) Recorded EL spectra of the LED shown on (b).

In this configuration, generation of photons is increased thanks to the larger contact surface. However, current level was of the same order of magnitude as in the previous contact design which was 5 times smaller, indicating a high access resistance probably due to the high resistance of the thin contact layer, or a fewer number of NWs connected. In the end, improving the collection of light led to a decrease in injection efficiency.

Nevertheless, an optical power of few 10^{-8} W was measured. Taking into account the distance between the sample and the power meter and its small solid angle on which it is actually collecting the light, an EQE $\sim 5.10^{-3}$ % is inferred. It is the first measured efficiency from an AlN NWs LEDs emitting at these wavelengths achieved in our team and, to my knowledge, ever reported.

Still, the value in itself is quite low. From temperature dependant CL measurements (Figure 6.3), one can assume, in first approximation, that IQE $= \frac{\text{CL(300 K)}}{\text{CL(5 K)}} \sim 20\%$. This high value of IQE cannot account for the low EQE value which means that injection and light extraction efficiencies are indeed responsible for the majority of the losses. If lots of effort were put on the investigation of the pn-junction and therefore current injection, a lot of work is still to be done in order to increase at both at the same times. Therefore even with this design adapted to EQE measurements, p-side contact remains the main limiting factor.

6.5 Summary of chapter 6

6.5.1 Conclusion on AlN NWs LED

To summarize, the realization of an AlN LED emitting at 285 nm grown by MBE was presented. Optical characterizations were recalled and complemented as they were substantially presented in Chapter 3. The nature of localization centers in the Ga-doped AlN active area is different from standard AlGaN alloy emitting in the same spectral range. The random distribution of small AlGaN clusters in the AlN matrix is actually leading to a similar QD-like behavior at the scale probed by the exciton. A ratio between CL at room temperature and low temperature of 20% is measured, pointing towards high recombination efficiency due to the large confinement of the exciton on the AlGaN clusters.

Electrical characterizations were performed in the light of the results presented in Chapter 5. A high ratio of $\sim 10^5$ between ON state and OFF state is measured, describing the good rectifying behavior of the diode. The devices show good reproducibility and current level although it is limited by the presence of a tunnel barrier assumed to be at the p-AlN / p-GaN interface.

CL and EBIC experiments allowed to locate the space charge region and the active area. Their overlap is observed, which is beneficial to promote radiative recombinations of electron-hole pairs with the desired energy. By modeling of I-V and EBIC, a high effective doping of 5×10^{17} cm^{-3} was extracted as well as diffusion lengths of around 80 nm and 200 nm for electrons and holes in p-AlN and n-AlN respectively.

Electroluminescence was successfully obtained, consistent with optical measurements and device behavior is in line with standard LEDs. A linear relationship between optical power and current is observed followed by the apparition of losses in a high injection regime. EQE of the device is estimated to around 5.10^{-3} %.

6.5.2 To go further

As this chapter is the last of my work, it has presented a functioning LED. The realization of such device requires the combination of several parts that have been studied in the three previous chapters and therefore, its improvements goes through the improvements of all the sections. Naturally, my first direction to go further and guide future work is to read the other *'To go further'* sections in the previous chapters.

Nevertheless, I would like to highlight some here:

- The NWs homogeneity is also a key point as it governs NW doping homogeneity and therefore current spreading homogeneity. Moreover, increasing it would allow a better control and homogeneity of the emission wavelength as well as potentially delaying the onset of the efficiency drop towards higher current.

- The search for a better p-type electrode is necessary as the compromise between light extraction and hole injection is the main limiting factor in the LEDs presented in this work.
- Opportunity to remove the substrate and transfer the NWs LED onto a UV-reflective layer could be investigated to further increase the number of collected photons.

General Conclusion

To finally end this PhD thesis, an overall conclusion is now offered.

A lot of research is currently carried out worldwide in order to address the increasing needs for solid state UV-C emitters and replace mercury-based lamps in sanitation applications. Being part of this effort, this work has explored the realization of LEDs emitting in the UV-C based on an alternative structure compared to the state-of-the-art. The use of pure AlN in a nanowire (NW) structure is advantageous and promising in term of dopant incorporation and light extraction. At the same time, challenges appear as for instance, electrical conductivity, control of the light emission or technological development. Especially, by the time of my PhD beginning, underlying physical mechanisms at play in these nanostructures lacked clear understanding limiting further development.

Therefore, scientific questions were stated at the beginning of this manuscript, which my work contributed to answer to.

1. How can efficient UV emission be achieved from AlGaN nanowires?

Ways to achieve light emission in the UV-C range were firstly investigated in **Chapter 3** mainly through cathodoluminescence (CL) measurements. The use of pure binary compounds as constituents was motivated by previous results in the literature, highlighting the difficult control of AlGaN nanowire composition and optical properties. Using binary AlN/GaN heterostructures, the growth of mono-layer thin GaN quantum wells was demonstrated, with luminescence from 239 nm up to 304 nm depending on the number of GaN mono-layers. To achieve such difficult growth, diffusion properties of Ga adatoms and self-limiting processes were used to our advantage.

Secondly, my work led to the study of AlGaN nanowire with extremely low Ga content (below 1%). This system revealed interesting properties with light emission in the UV-C range, being drastically different than standard III-N alloys. Optical properties were attributed to AlGaN clusters able to localize and strongly confine the exciton in a quantum dot manner. In both cases, the structures showed good thermal stability with room temperature luminescence intensity between 15 to 30% of the one at low temperature.

2. How does Si incorporation change AlN nanowires structural and electrical properties?

Silicon doping of AlN NWs was also investigated with the aim of improving electrical conductivity of future devices. A wide range of doping was studied up to 10^{21} Si/cm^3. It was inferred from Raman spectroscopy and electron microscopy that solubility limit was not reached. A change of morphology was observed and attributed to a change in growth mechanisms.

Current-voltage (I-V) characterizations were carried out and showed the presence of an Ohmic regime for bias below 0.1 V, followed by a space charge limited (SCLC) regime at larger bias. Study of the Ohmic regime confirmed the apparition of self-compensation effect with a maximal conductance reached for 10^{17} Si/cm^3, in agreement with previous reports from literature.

3. In which state are Si donors in AlN nanowires?

Temperature dependent I-V measurements were performed in order to measure activation energy of the dopants. Contrary to commonly found DX state exhibiting an energy of 270 meV, shallow Si donors remained active at room temperature in the lowest doping regime, exhibiting an activation energy of 75 meV. Deep DX state was however found to be the only active at higher doping regime and in the range of temperature investigated. SCLC regime study allowed to identify a third Si-related level at ∼160 meV only acting as an electron trap in the highest doped samples. The presence of these three levels corresponds to three Si configurations: the pure substitutional Si_{Al} and two DX states reconciling results from literature.

With its reduced ionization energy, shallow Si donor is an asset in order to increase free electron density and conductivity of AlN:Si. Reasons for this stabilization are still unclear but are assumed to be arising from strain relaxation at NWs sidewalls.

4. What are the electric transport mechanisms at play in AlN nanowires pn-junction?

Through I-V and electron beam induced current (EBIC) experiments, AlN pn-junction electrical transport was probed in **Chapter 5**. Devices showed good rectifying behavior and ideality factors between 10 and 100. The latter corresponds to the case when no In-codoping was used for the p-AlN section. The presence of a Schottky contact at the p-type interface was evidenced leading to a limited ON-State current. Fowler-Nordheim regime is found to be the main mechanism limiting current flow in forward bias. It is assigned to the presence of a barrier through which holes tunnel prior to flow in the p-AlN

section. Identification of the barrier points toward either the p-AlN/p-GaN or p-AlN / metal interface.

5. Is the realization of an AlN nanowires LED possible? With which performances?

Optimization of the AlN pn-junction was realized in **Chapter 5** using I-V, EBIC and electroluminescence (EL). It allowed to choose the adequate design in which was inserted an emitting region. The overall properties of the device were presented in **Chapter 6**. A large 10^5 ratio between ON and OFF states is measured. Diffusion lengths of minority carriers could be extracted from EBIC measurements which are of around 80 mn for electrons in p-AlN and 200 nm for holes in n-AlN.

The device exhibited EL at 285 nm in agreement with CL spectra. The optical output power and current density were found to be linearly dependant at low injection regime as excepted from standard LED physics. External quantum efficiency of around 4.10^{-3} % was estimated, mainly limited by the lack of transparent electrode reducing drastically the light extraction.

Prospects

I. Luminescence properties

Regarding the optical properties, both ultra-thin GaN quantum wells and Ga-doped AlN NWs have shown great results. The emission wavelength being controlled, a deeper investigation of properties is needed in order to precisely assess and further improve radiative efficiency. Notably, questions are *which points defects are present in AlN NWs?*, *Are they detrimental to the generation of light?*, *If yes, how to reduce their density?*, *What is the role of surfaces?*

Ensuing Ga-doped AlN NWs intriguing optical properties, a large panel of experiments could be done in order to understand and control the formation of the AlGaN clusters. Will it be possible to reduce the density of clusters and measure intrinsic properties of such single-photon emitters?

Is this system favorable for light emission in LEDs? In this regards, QW structures were favored in blue LEDs thanks to their large density of states compared to QD, allowing for more photons to be produced.

II. Doping and electrical transport in AlN nanowires

As concerns doping of AlN NWs, the study of Si-doped AlN highlights the specific incorporation of Si in a NW geometry with respect to bulk. However, the reason for this specificity is still unclear and need to be addressed. *Is it possible to stabilize Si in shallow state and reach Mott transition? What is the role of surface states, growth condition diameter? How are Si atoms spatially distributed? Can other dopants be used to achieve a high n-type conductivity?*

Along my PhD work, I chose not to dive into the study of electrical properties of Mg-doped GaN and AlN NWs. However transport properties in such materials can be quite different from what we know in bulk. The same kind of study as for AlN:Si NWs should be carried out in order to optimize free hole concentration of these materials. In p-GaN especially, although a large amount of acceptors can be introduced, there is a lack of conductivity measurements in NWs and non have been performed in my thesis work.

Hole injection being a major issue the use of new materials as top electrodes are to be seriously considered. Diamond, h-BN, graphene solutions might be easy to realize or at least to test.

III. Technological developments

TEM studies are convenient with nanowires since they can be dispersed on a TEM grid with a relative ease. However, this preparation reaches its limits when it comes to detailed analysis and not only imaging. Having NWs on a proper lamella would have allowed much deeper insight on, for instance, dopant spatial distribution, better measurements of dopant concentration and cleaner imaging. One technological development that could be of particular interest is the use of tools for TEM lamella preparation such as ultramicrotomy and FIB processes.

As many times stated in this thesis, nanowire morphology is a key parameter as it rules several aspects such as, active area dimensions, doping and conductivity or processing and contacting. The use of patterned substrates would suppress all these considerations. Having access to a uniform distribution of NWs morphology would therefore give access to differences in physical properties which are difficult to disentangle in the case of self-nucleated wires. Therefore, developing e-beam or nano-imprint lithography techniques would be largely valuable for device fabrication as well as for providing material seized to perform experiments and bring understanding of physical mechanisms.

I hope you have appreciated this manuscript.
Thank you for reading.

Scientific Communication

Publications

Comprehensive Electro-Optical Investigation of a Ga-doped AlN Nanowire LED. Rémy Vermeersch, Eric Robin, Gwénolé Jacopin, Bruno Gayral, Julien Pernot, Bruno Daudin. *Under review.*

Ultrathin GaN quantum wells in AlN nanowire for UV-C emission. Rémy Vermeersch, Gwénolé Jacopin, F. Castioni, J. L. Rouvière, A. García-Cristóbal, A. Cros, Julien Pernot, Bruno Daudin. In: *Nanotechnology*, In press. DOI: 10.1088/1361-6528/accaeb

Optical properties of Ga-doped AlN nanowires. Rémy Vermeersch, Gwénolé Jacopin, Eric Robin, Julien Pernot, Bruno Gayral, Bruno Daudin. In: *Applied Physics Letters* 122.9 (February 2023), p. 091106. DOI: 10.1063/5.0137424

Patent: **Diode éléctroluminescente comportant une région emissive à base d'AlN comportant des atomes de gallium et/ou d'indium.** Rémy Vermeersch, Bruno Daudin. (July 2022) *Deposited*

DX center formation in highly Si doped AlN nanowires revealed by trap assisted space-charge limited current. Rémy Vermeersch, Gwénolé Jacopin, Bruno Daudin, Julien Pernot. In: *Applied Physics Letter* 120.16 (April 2022), p. 162104. DOI: 10.1063/5.0087789

Nanoscale imaging of dopant incorporation in n-type and p-type GaN nanowires by scanning spreading resistance microscopy. Ece N. Aybeke, Alexandra-Madalina Siladie, Rémy Vermeersch, Eric Robin, Oleksandr Synhaivskyi, Bruno Gayral, Julien Pernot, Georges Brémond, and Bruno Daudin. In: *Journal of Applied Physics* 131.7 (February 2022), p. 075701. DOI: 10.1063/5.0080713

Europium-Implanted AlN Nanowires for Red Light-Emitting Diodes. José P. S. Cardoso, Maria Rosario Correia, Rémy Vermeersch, Dirkjan Verheij, Gwenole Jacopin, Julien Pernot, Teresa Monteiro, Susana Cardoso, Katharina Lorenz, Bruno Daudin, Nabiha Ben Sedrine. In: *ACS Applied Nano Materials* 131.7 (January 2022), p. 075701. DOI: 10.1021/acsanm.1c03654

Shallow donor and DX state in Si doped AlN nanowires grown by molecular beam epitaxy. Rémy Vermeersch, Eric Robin, Ana Cros, Gwénolé Jacopin, Bruno Daudin, Julien Pernot. In: *Applied Physics Letter* 119.26 (December 2021), p. 262105. DOI: 10.1063/5.0074454

Growth of zinc-blende GaN on muscovite mica by molecular beam epitaxy. Bruno Daudin, Fabrice Donatini, Catherine Bougerol, Bruno Gayral, Edith Bellet-Amalric, Rémy Vermeersch, Nathaniel Feldberg, Jean-Luc Rouvière, Maria-José Recio Carretero, Nuria Garro, Saul Garcia-Orrit, Ana Cros In: *Nanotechnology* 120.16 (January 2021), p. 025601. DOI: 10.1088/1361-6528/abb6a5

Conferences

Shallow donors and DX states in AlN nanowires.
Rémy Vermeersch, E. Robin, A. Cros, G. Jacopin, B. Daudin, J. Pernot. **Oral** presentation at IWN, Berlin, October 2022.

A 285 nm AlN nanowire-based light emitting diode.
Rémy Vermeersch, G. Jacopin, J. Pernot, B. Daudin. **Poster** presentation at IWN, Berlin, October 2022.

Intrinsic heterogeneous distribution of electrical dopants in GaN nanowires
B. Daudin, E. N. Aybeke, A. M. Siladie, Rémy Vermeersch, O. Synhaivskyi, E. Robin, B. Gayral, J. Pernot, G. Brémond, N. Garro, A. Cros. **Oral** presentation at IWN, Berlin, October 2022.

Europium-implanted AlN p-n junction nanowires – towards the realization of red light-emitting devices.
J. Cardoso, Rémy Vermeersch, Dirkjan Verheij, G. Jacopin, J. Pernot, T. Monteiro, S. Cardoso, K. Lorenz, B. Daudin, N. Ben Sedrine, R. Correia. **Poster** presentation at IWN, Berlin, October 2022.

Strain relaxation of GaN grown on Mica through the formation of telephone cord buckles.
A. Cros, S. Garcia-Orrit, N. Garro, M. J. Recio-Carretero, F. Donatini, C. Bougerol, B. Gayral, E. Bellet-Amalric, J.-L. Rouviere, R. Vermeersch, N. Feldberg, B. Daudin. **Poster** presentation at IWN, Berlin, October 2022.

AlN/GaN nanowire heterostructures for UV-C light emitting devices.
Rémy Vermeersch, G. Jacopin, B. Gayral, J. Pernot, **B. Daudin**. **Invited Oral** presentation at E-MRS, Warsaw, October 2022.

Demonstration of red light-emitting devices based on europium-implanted AlN p-n junction nanowires.
J. P. S. Cardoso, M. R. Correia, Rémy Vermeersch, D. Verheij, G. Jacopin, J. Pernot, T. Monteiro, K. Lorenz, B. Daudin, and N. Ben Sedrine. **Oral** presentation at IBMM, Lisbon, July 2022.

Shallow donors and DX states in Si doped AlN nanowires.
Rémy Vermeersch, E. Robin, A. Cros, G. Jacopin, J. Pernot, B. Daudin. **Oral** presentation at MRS, Honolulu, May 2022.

UV-C emission in the 230 — 280 nm range from AlN based light emitting diode.
Rémy Vermeersch, G. Jacopin, J. Pernot, B. Daudin. **Oral** presentation at Nanowire Week Chamonix, April 2022.

Towards a better understanding of electronic transport in Si doped AlN nanowires.
Rémy Vermeersch, E. Robin, A. Cros, G. Jacopin, B. Daudin, J. Pernot. **Oral** presentation at MRS, Boston, November 2021

AlN nanowire pn heterojunctions: a new paradigm towards UV-C LEDs
Rémy Vermeersch, A-M Siladie, G. Jacopin, A. Cros, N. Garro, E. Robin, D. Calliste, P. Pochet, F. Donatini, J. Pernot, **B. Daudin Invited Oral** presentation at MRS, Boston, November 2021

Quasi-strain-free GaN on van der Waals substrates: the case of graphene and muscovite mica.
A. Cros, S. Garcia-Orrit, N. Garro, O. Klymov, M. J. Recio-Carretero, M. Gruart, Rémy Vermeersch, F. Donatini, C. Bougerol, B. Gayal, S. Pouget, E. Bellet-Amalric, N. Mollard, H. Okuno, J. L. Rouviere, N. Feldberg, and B. Daudin. **Oral** presentation at SPIE Nanoscience and Engineering, San Diego, August 2021

Highly doped AlN nanowire pn junction: a step towards a new generation of UV-C LEDs
Rémy Vermeersch, A.-M. Siladie, G. Jacopin, A. Cros, N. Garro, E. Robin, D. Caliste, P. Pochet, F. Donatini, J. Pernot, and **B. Daudin**. **Oral** presentation at SPIE Photonic West, San Francisco.*Online*, March 2021

Bibliography

[1] Michael Kneissl and Jens Rass. *III-Nitride Ultraviolet Emitters*. Ed. by Michael Kneissl and Jens Rass. Vol. 227. Springer Series in Materials Science. Cham: Springer International Publishing, 2016. DOI: 10.1007/978-3-319-24100-5 (cit. on pp. 2, 21, 58).

[2] Ernest R Blatchley, David J Brenner, Holger Claus, Troy E Cowan, Karl G. Linden, Yijing Liu, Ted Mao, Sung-jin Park, Patrick J Piper, Richard M Simons, and David H Sliney. "Far UV-C radiation: An emerging tool for pandemic control". In: *Critical Reviews in Environmental Science and Technology* 0.0 (June 2022), pp. 1–21. DOI: 10.1080/10643389.2022.2084315 (cit. on pp. 3, 4).

[3] Wladyslaw Kowalski. *Ultraviolet Germical Irradiation*. Vol. 53. 9. 2009, pp. 1689–1699 (cit. on p. 3).

[4] Yole Developpement. *UV LEDs and UV lamps – Market and technology trends*. 2021. URL: https://www.i-micronews.com/products/uv-leds-and-uv-lamps-market-and-technology-trends-2021/ (visited on August 22, 2022) (cit. on p. 4).

[5] Allied Market Research. *Global UV LED Market Outlook - 2027*. 2022. URL: https://www.alliedmarketresearch.com/uv-led-market (visited on August 22, 2022) (cit. on p. 4).

[6] Global Industry Analysts. *Global Ultraviolet (UV) Disinfection Industry*. 2022. URL: https://www.reportlinker.com/p06033190/Global-Ultraviolet-UV-Disinfection-Equipment-Industry.html?utm%7B%5C_%7Dsource=GNW (visited on August 22, 2022) (cit. on p. 4).

[7] Piséo. *COVID-19, un cas parfait d'utilisation des technologies d'éclairage UV*. URL: https://piseo.fr/non-classifiee/uv-led-lighting-technologies/ (visited on August 22, 2022) (cit. on p. 4).

[8] Michael Kneissl. *UV LEDs efficiencies*. URL: https://www.ifkp.tu-berlin.de/fileadmin/i1/Kneissl/EQE%7B%5C_%7D20181120.pdf (visited on August 24, 2022) (cit. on p. 8).

[9] J. Li, T. N. Oder, M. L. Nakarmi, J. Y. Lin, and H. X. Jiang. "Optical and electrical properties of Mg-doped p-type AlxGa 1-xN". In: *Applied Physics Letters* 80.7 (2002), pp. 1210–1212. DOI: 10.1063/1.1450038 (cit. on p. 9).

[10] S. R. Jeon, Z. Ren, G. Cui, J. Su, M. Gherasimova, J. Han, H. K. Cho, and L. Zhou. "Investigation of Mg doping in high-Al content p -type Alx Ga1-x N (0.3<x<0.5)". In: *Applied Physics Letters* 86.8 (2005), pp. 1–3. DOI: 10.1063/1.1867565 (cit. on p. 9).

[11] Ramón Collazo, Seiji Mita, Jinqiao Xie, Anthony Rice, James Tweedie, Rafael Dalmau, and Zlatko Sitar. "Progress on n-type doping of AlGaN alloys on AlN single crystal substrates for UV optoelectronic applications". In: *physica status solidi (c)* 8.7-8 (July 2011), pp. 2031–2033. DOI: 10.1002/pssc.201000964 (cit. on pp. 9, 82, 83, 100).

[12] Frank Mehnke, Xuan Thang Trinh, Harald Pingel, Tim Wernicke, Erik Janzén, Nguyen Tien Son, and Michael Kneissl. "Electronic properties of Si-doped Alx Ga 1 - X N with aluminum mole fractions above 80%". In: *Journal of Applied Physics* 120.14 (2016), pp. 1–10. DOI: 10.1063/1.4964442 (cit. on pp. 9, 82).

[13] Hideki Hirayama, Norimichi Noguchi, Tohru Yatabe, and Norihiko Kamata. "227 nm AlGaN light-emitting diode with 0.15 mW output power realized using a thin quantum well and AIN buffer with reduced threading dislocation density". In: *Applied Physics Express* 1.5 (2008), pp. 0511011–0511013. DOI: 10.1143/APEX.1.051101 (cit. on p. 9).

[14] Hideki Hirayama, Sachie Fujikawa, Norimichi Noguchi, Jun Norimatsu, Takayoshi Takano, Kenji Tsubaki, and Norihiko Kamata. "222-282 nm AlGaN and InAlGaN-based deep-UV LEDs fabricated on high-quality AlN on sapphire". In: *Physica Status Solidi (A) Applications and Materials Science* 206.6 (2009), pp. 1176–1182. DOI: 10.1002/pssa.200880961 (cit. on p. 9).

[15] Kazuhito Ban, Jun-ichi Ichi Yamamoto, Kenichiro Takeda, Kimiyasu Ide, Motoaki Iwaya, Tetsuya Takeuchi, Satoshi Kamiyama, Isamu Akasaki, and Hiroshi Amano. "Internal Quantum Efficiency of Whole-Composition-Range AlGaN Multiquantum Wells". In: *Applied Physics Express* 4.5 (May 2011), p. 52101. DOI: 10.1143/apex.4.052101 (cit. on p. 9).

[16] Jan Ruschel, Johannes Glaab, Norman Susilo, Sylvia Hagedorn, Sebastian Walde, Eviathar Ziffer, Hyun Kyong Cho, Neysha Lobo Ploch, Tim Wernicke, Markus Weyers, Sven Einfeldt, and Michael Kneissl. "Reliability of UVC LEDs fabricated on AlN/sapphire templates with different threading dislocation densities". In: *Applied Physics Letters* 117.24 (2020), p. 241104. DOI: 10.1063/5.0027769 (cit. on p. 9).

[17] D. E. Lacklison, J. W. Orton, I. Harrison, T. S. Cheng, L. C. Jenkins, C. T. Foxon, and S. E. Hooper. "Band gap of GaN films grown by molecular-beam epitaxy on GaAs and GaP substrates". In: *Journal of Applied Physics* 78.3 (August 1995), pp. 1838–1842. DOI: 10.1063/1.360217 (cit. on p. 17).

[18] S. Miyoshi, K. Onabe, N. Ohkouchi, H. Yaguchi, R. Ito, S. Fukatsu, and Y. Shiraki. "MOVPE growth of cubic GaN on GaAs using dimethylhydrazine". In: *Journal of Crystal Growth* 124.1-4 (November 1992), pp. 439–442. DOI: 10.1016/0022-0248(92)90497-7 (cit. on p. 17).

[19] H. Jiang, G. Y. Zhao, H. Ishikawa, T. Egawa, T. Jimbo, and M. Umeno. "Determination of exciton transition energy and bowing parameter of AlGaN alloys in AlGaN/GaN heterostructure by means of reflectance measurement". In: *Journal of Applied Physics* 89.2 (2001), pp. 1046–1052. DOI: 10.1063/1.1334923 (cit. on pp. 17, 19).

[20] H. Okumura, K. Ohta, G. Feuillet, K. Balakrishnan, S. Chichibu, H. Hamaguchi, P. Hacke, and S. Yoshida. "Growth and characterization of cubic GaN". In: *Journal of Crystal Growth* 178.1-2 (June 1997), pp. 113–133. DOI: 10.1016/S0022-0248(97)00084-5 (cit. on p. 17).

[21] B Daudin, G Feuillet, J Hübner, Y Samson, F Widmann, A Philippe, C Bru-Chevallier, G Guillot, E Bustarret, G Bentoumi, and A Deneuville. "How to grow cubic GaN with low hexagonal phase content on (001) SiC by molecular beam epitaxy". en. In: *Journal of Applied Physics* 84.4 (November 1998), pp. 2295–2300. DOI: 10/bcmfnx (cit. on p. 17).

[22] I. Vurgaftman and J. R. Meyer. "Band parameters for nitrogen-containing semiconductors". en. In: *Journal of Applied Physics* 94.6 (September 2003), pp. 3675–3696. DOI: 10.1063/1.1600519 (cit. on pp. 18, 20, 22).

[23] B. Daudin, J.L. Rouvière, and M. Arlery. "The key role of polarity in the growth process of (0001) nitrides". In: *Materials Science and Engineering: B* 43.1-3 (January 1997), pp. 157–160. DOI: 10.1016/S0921-5107(96)01854-5 (cit. on p. 18).

[24] M. Sumiya, K. Yoshimura, K. Ohtsuka, and S. Fuke. "Dependence of impurity incorporation on the polar direction of GaN film growth". In: *Applied Physics Letters* 76.15 (April 2000), pp. 2098–2100. DOI: 10.1063/1.126267 (cit. on p. 18).

[25] N.A. Fichtenbaum, T.E. Mates, S. Keller, S.P. DenBaars, and U.K. Mishra. "Impurity incorporation in heteroepitaxial N-face and Ga-face GaN films grown by metalorganic chemical vapor deposition". In: *Journal of Crystal Growth* 310.6 (March 2008), pp. 1124–1131. DOI: 10.1016/j.jcrysgro.2007.12.051 (cit. on p. 18).

[26] A. J. Ptak, T. H. Myers, L. T. Romano, C. G. Van de Walle, and J. E. Northrup. "Magnesium incorporation in GaN grown by molecular-beam epitaxy". In: *Applied Physics Letters* 78.3 (January 2001), pp. 285–287. DOI: 10.1063/1.1339255 (cit. on p. 18).

[27] S. F. Chichibu, A. Setoguchi, A. Uedono, K. Yoshimura, and M. Sumiya. "Impact of growth polar direction on the optical properties of GaN grown by metalorganic vapor phase epitaxy". In: *Applied Physics Letters* 78.1 (January 2001), pp. 28–30. DOI: 10.1063/1.1337641 (cit. on p. 18).

[28] M. I. den Hertog, F. González-Posada, R. Songmuang, J. L. Rouviere, T. Fournier, B. Fernandez, and E. Monroy. "Correlation of Polarity and Crystal Structure with Optoelectronic and Transport Properties of GaN/AlN/GaN Nanowire Sensors". In: *Nano Letters* 12.11 (November 2012), pp. 5691–5696. DOI: 10.1021/nl302890f (cit. on p. 18).

[29] Karine Hestroffer, Cédric Leclere, Catherine Bougerol, Hubert Renevier, and Bruno Daudin. "Polarity of GaN nanowires grown by plasma-assisted molecular beam epitaxy on Si(111)". In: *Physical Review B* 84.24 (December 2011), p. 245302. DOI: 10.1103/PhysRevB.84.245302 (cit. on pp. 18, 25).

[30] A. Minj, A. Cros, N. Garro, J. Colchero, T. Auzelle, and B. Daudin. "Assessment of Polarity in GaN Self-Assembled Nanowires by Electrical Force Microscopy". In: *Nano Letters* 15.10 (October 2015), pp. 6770–6776. DOI: 10.1021/acs.nanolett.5b02607 (cit. on p. 18).

[31] J. L. Rouviere, J. L. Weyher, M. Seelmann-Eggebert, and S. Porowski. "Polarity determination for GaN films grown on (0001) sapphire and high-pressure-grown GaN single crystals". In: *Applied Physics Letters* 73.5 (August 1998), pp. 668–670. DOI: 10.1063/1.121942 (cit. on p. 18).

[32] Ludovic Largeau, Elisabeth Galopin, Noelle Gogneau, Laurent Travers, Frank Glas, and Jean-Christophe Harmand. "N-Polar GaN Nanowires Seeded by Al Droplets on Si(111)". In: *Crystal Growth & Design* 12.6 (June 2012), pp. 2724–2729. DOI: 10.1021/cg300212d (cit. on p. 18).

[33] G. Naresh-Kumar, J. Bruckbauer, A. Winkelmann, X. Yu, B. Hourahine, P. R. Edwards, T. Wang, C. Trager-Cowan, and R. W. Martin. "Determining GaN Nanowire Polarity and its Influence on Light Emission in the Scanning Electron Microscope". In: *Nano Letters* 19.6 (June 2019), pp. 3863–3870. DOI: 10.1021/acs.nanolett.9b01054 (cit. on p. 18).

[34] Christophe Durand, Catherine Bougerol, Jean François Carlin, Georg Rossbach, Florian Godel, Joël Eymery, Pierre Henri Jouneau, Anna Mukhtarova, Raphaël Butté, and Nicolas Grandjean. "M-Plane GaN/InAlN Multiple Quantum Wells in Core-Shell Wire Structure for UV Emission". In: *ACS Photonics* 1.1 (2014), pp. 38–46. DOI: 10.1021/ph400031x (cit. on p. 18).

[35] Vincent Grenier, Sylvain Finot, Gwénolé Jacopin, Catherine Bougerol, Eric Robin, Nicolas Mollard, Bruno Gayral, Eva Monroy, Joël Eymery, and Christophe Durand. "UV Emission from GaN Wires with m-Plane Core-Shell GaN/AlGaN Multiple Quantum Wells". In: *ACS Applied Materials and Interfaces* 12.39 (2020), pp. 44007–44016. DOI: 10.1021/acsami.0c08765 (cit. on p. 18).

[36] Arpan Chakraborty, Benjamin A. Haskell, Stacia Keller, James S. Speck, Steven P. Denbaars, Shuji Nakamura, and Umesh K. Mishra. "Demonstration of nonpolar m-plane InGaN/GaN light-emitting diodes on free-standing m-plane GaN substrates". In: *Japanese Journal of Applied Physics, Part 2: Letters* 44.1-7 (2005), pp. 118–121. DOI: 10.1143/JJAP.44.L173 (cit. on p. 18).

[37] W. M. Yim, E. J. Stofko, P. J. Zanzucchi, J. I. Pankove, M. Ettenberg, and S. L. Gilbert. "Epitaxially grown AlN and its optical band gap". In: *Journal of Applied Physics* 44.1 (January 1973), pp. 292–296. DOI: 10.1063/1.1661876 (cit. on p. 19).

[38] P. B. Perry and R. F. Rutz. "The optical absorption edge of single-crystal AlN prepared by a close-spaced vapor process". In: *Applied Physics Letters* 33.4 (August 1978), pp. 319–321. DOI: 10.1063/1.90354 (cit. on p. 19).

[39] R. Dingle, D. D. Sell, S. E. Stokowski, and M. Ilegems. "Absorption, Reflectance, and Luminescence of GaN Epitaxial Layers". In: *Physical Review B* 4.4 (August 1971), pp. 1211–1218. DOI: 10.1103/PhysRevB.4.1211 (cit. on p. 19).

[40] M. Ilegems, R. Dingle, and R. A. Logan. "Luminescence of Zn- and Cd-doped GaN". In: *Journal of Applied Physics* 43.9 (September 1972), pp. 3797–3800. DOI: 10.1063/1.1661813 (cit. on p. 19).

[41] Caro Ángel Miguel Bayo. "Miguel Angel Caro Bayo". PhD thesis. University of Cork, 2013 (cit. on p. 20).

[42] S. R. Lee, A. F. Wright, M. H. Crawford, G. A. Peterson, J. Han, and R. M. Biefeld. "The band-gap bowing of alloys". In: *Applied Physics Letters* 3344.April 1999 (2003), pp. 10–13 (cit. on p. 19).

[43] Feng Yun, Michael A. Reshchikov, Lei He, Thomas King, Hadis Morkoç, Steve W. Novak, and Luncun Wei. "Energy band bowing parameter in Al xGa 1-xN alloys". In: *Journal of Applied Physics* 92.8 (2002), pp. 4837–4839. DOI: 10.1063/1.1508420 (cit. on p. 19).

[44] H. Angerer, D. Brunner, F. Freudenberg, O. Ambacher, M. Stutzmann, R. Höpler, T. Metzger, E. Born, G. Dollinger, A. Bergmaier, S. Karsch, and H. J. Körner. "Determination of the Al mole fraction and the band gap bowing of epitaxial AlxGa1-xN films". In: *Applied Physics Letters* 71.11 (September 1997), pp. 1504–1506. DOI: 10.1063/1.119949 (cit. on p. 19).

[45] A. Sedhain, J. Y. Lin, and H. X. Jiang. "Valence band structure of AlN probed by photoluminescence". In: *Applied Physics Letters* 92.4 (January 2008), p. 041114. DOI: 10.1063/1.2840176 (cit. on p. 21).

[46] K. B. Nam, J. Li, M. L. Nakarmi, J. Y. Lin, and H. X. Jiang. "Unique optical properties of AlGaN alloys and related ultraviolet emitters". In: *Applied Physics Letters* 84.25 (June 2004), pp. 5264–5266. DOI: 10.1063/1.1765208 (cit. on p. 21).

[47] Tim Kolbe, Arne Knauer, Chris Chua, Zhihong Yang, Sven Einfeldt, Patrick Vogt, Noble M. Johnson, Markus Weyers, and Michael Kneissl. "Optical polarization characteristics of ultraviolet (In)(Al)GaN multiple quantum well light emitting diodes". In: *Applied Physics Letters* 97.17 (October 2010), p. 171105. DOI: 10.1063/1.3506585 (cit. on p. 21).

[48] R. G. Banal, M. Funato, and Y. Kawakami. "Optical anisotropy in [0001]-oriented AlGaN/AlN Quantum wells". In: *Physical Review B* 79.12 (March 2009), p. 121308. DOI: 10.1103/PhysRevB.79.121308 (cit. on p. 21).

[49] Hideo Kawanishi, Masanori Senuma, and Takeaki Nukui. "Anisotropic polarization characteristics of lasing and spontaneous surface and edge emissions from deep-ultraviolet (λ=240nm) AlGaN multiple-quantum-well lasers". In: *Applied Physics Letters* 89.4 (July 2006), p. 041126. DOI: 10.1063/1.2236792 (cit. on p. 21).

[50] T. K. Sharma, D. Naveh, and E. Towe. "Strain-driven light-polarization switching in deep ultraviolet nitride emitters". In: *Physical Review B* 84.3 (July 2011), p. 035305. DOI: 10.1103/PhysRevB.84.035305 (cit. on p. 21).

[51] Fabio Bernardini, Vincenzo Fiorentini, and David Vanderbilt. "Spontaneous polarization and piezoelectric constants of III-V nitrides". In: *Physical Review B* 56.16 (October 1997), R10024–R10027. DOI: 10.1103/PhysRevB.56.R10024 (cit. on p. 22).

[52] Mitsuru Funato, Ryan G. Banal, and Yoichi Kawakami. "Screw dislocation-induced growth spirals as emissive exciton localization centers in Al-rich AlGaN/AlN quantum wells". In: *AIP Advances* 5.11 (2015). DOI: 10.1063/1.4935567 (cit. on p. 24).

[53] Stacia Keller, Haoran Li, Matthew Laurent, Yanling Hu, Nathan Pfaff, Jing Lu, David F. Brown, Nicholas A. Fichtenbaum, James S. Speck, Steven P. Denbaars, and Umesh K. Mishra. "Recent progress in metal-organic chemical vapor deposition

of (0001¯) N-polar group-III nitrides". In: *Semiconductor Science and Technology* 29.11 (2014). DOI: 10.1088/0268-1242/29/11/113001 (cit. on p. 24).

[54] Hadis Morkoç. *Handbook of Nitride Semiconductors and Devices*. Wiley, June 2008. DOI: 10.1002/9783527628414 (cit. on p. 25).

[55] D. G. Zhao, S. J. Xu, M. H. Xie, S. Y. Tong, and Hui Yang. "Stress and its effect on optical properties of GaN epilayers grown on Si(111), 6H-SiC(0001), and c - plane sapphire". In: *Applied Physics Letters* 83.4 (July 2003), pp. 677–679. DOI: 10.1063/1.1592306 (cit. on p. 25).

[56] Hiroto Sekiguchi, Katsumi Kishino, and Akihiko Kikuchi. "Ti-mask selective-area growth of GaN by RF-plasma-assisted molecular-beam epitaxy for fabricating regularly arranged InGaN/GaN nanocolumns". In: *Applied Physics Express* 1.12 (2008), pp. 1240021–1240023. DOI: 10.1143/APEX.1.124002 (cit. on pp. 25, XLIII).

[57] K. Hestroffer, C. Leclere, V. Cantelli, C. Bougerol, H. Renevier, and B. Daudin. "In situ study of self-assembled GaN nanowires nucleation on Si(111) by plasma-assisted molecular beam epitaxy". In: *Applied Physics Letters* 100.21 (2012). DOI: 10.1063/1.4721521 (cit. on p. 25).

[58] Thomas Auzelle, Benedikt Haas, Albert Minj, Catherine Bougerol, Jean-Luc Rouvière, Ana Cros, Jaime Colchero, and Bruno Daudin. "The influence of AlN buffer over the polarity and the nucleation of self-organized GaN nanowires". en. In: *Journal of Applied Physics* 117.24 (June 2015), p. 245303. DOI: 10.1063/1.4923024 (cit. on p. 25).

[59] Thomas Auzelle, Mani Azadmand, Timur Flissikowski, Manfred Ramsteiner, Katrin Morgenroth, Carsten Stemmler, Sergio Fernández-Garrido, Stefano Sanguinetti, Holger T. Grahn, Lutz Geelhaar, and Oliver Brandt. "Enhanced Radiative Efficiency in GaN Nanowires Grown on Sputtered TiN x : Effects of Surface Electric Fields". In: *ACS Photonics* 8.6 (June 2021), pp. 1718–1725. DOI: 10.1021/acsphotonics.1c00224 (cit. on p. 25).

[60] Johannes K. Zettler, Christian Hauswald, Pierre Corfdir, Mattia Musolino, Lutz Geelhaar, Henning Riechert, Oliver Brandt, and Sergio Fernández-Garrido. "High-Temperature Growth of GaN Nanowires by Molecular Beam Epitaxy: Toward the Material Quality of Bulk GaN". In: *Crystal Growth and Design* 15.8 (2015), pp. 4104–4109. DOI: 10.1021/acs.cgd.5b00690 (cit. on p. 25).

[61] Sergio Fernández-Garrido, Vladimir M Kaganer, Karl K Sabelfeld, Tobias Gotschke, Javier Grandal, Enrique Calleja, Lutz Geelhaar, and Oliver Brandt. "Self-Regulated Radius of Spontaneously Formed GaN Nanowires in Molecular Beam Epitaxy". en. In: *Nano Letters* 13.7 (November 2013), pp. 3274–3280. DOI: 10/f445g4 (cit. on p. 25).

[62] Vladimir M. Kaganer, Sergio Fernández-Garrido, Pinar Dogan, Karl K. Sabelfeld, and Oliver Brandt. "Nucleation, growth, and bundling of GaN nanowires in molecular beam epitaxy: Disentangling the origin of nanowire coalescence". In: *Nano Letters* 16.6 (2016), pp. 3717–3725. DOI: 10.1021/acs.nanolett.6b01044 (cit. on p. 25).

[63] S. Fernández-Garrido, J. Grandal, E. Calleja, M. A. Sánchez-García, and D. López-Romero. "A growth diagram for plasma-assisted molecular beam epitaxy of GaN nanocolumns on Si(111)". en. In: *Journal of Applied Physics* 106.12 (October 2009), p. 126102. DOI: 10/b8j87z (cit. on pp. 25, 26).

[64] Raffaeila Calarco, Ralph J. Meijers, Ratan K. Debnath, Toma Stoical, Eli Sutter, and Hans Lüth. "Nucleation and growth of GaN nanowires on Si(111) performed by molecular beam epitaxy". In: *Nano Letters* 7.8 (August 2007), pp. 2248–2251. DOI: 10.1021/nl0707398 (cit. on p. 25).

[65] E. Bellet-Amalric, M. Elouneg-Jamroz, C. Bougerol, M. Den Hertog, Y. Genuist, S. Bounouar, J. P. Poizat, K. Kheng, R. André, and S. Tatarenko. "Epitaxial growth of ZnSe and ZnSe/CdSe nanowires on ZnSe". In: *Physica Status Solidi (C) Current Topics in Solid State Physics* 7.6 (2010), pp. 1526–1529. DOI: 10.1002/pssc.200983254 (cit. on p. 25).

[66] O. Landré, C. Bougerol, H. Renevier, and B. Daudin. "Nucleation mechanism of GaN nanowires grown on (111) Si by molecular beam epitaxy". en. In: *Nanotechnology* 20.41 (December 2009), p. 415602. DOI: 10/cb7r6s (cit. on p. 26).

[67] Mani Azadmand, Thomas Auzelle, Jonas Lähnemann, Guanhui Gao, Lars Nicolai, Manfred Ramsteiner, Achim Trampert, Stefano Sanguinetti, Oliver Brandt, and Lutz Geelhaar. "Self-Assembly of Well-Separated AlN Nanowires Directly on Sputtered Metallic TiN Films". In: *Physica Status Solidi - Rapid Research Letters* 14.3 (March 2020), p. 1900615. DOI: 10.1002/pssr.201900615 (cit. on p. 26).

[68] Takanori Suzuki and Yusuke Hirabayashi. "First observation of the si(Lll)-7 x 7<->l x 1 phase transition by the optical second harmonic generation". In: *Japanese Journal of Applied Physics* 32.4 B (1993), pp. L610–L613. DOI: 10.1143/JJAP.32.L610 (cit. on pp. 30, XXXIII).

[69] University of Cambridge. *Engineering atoms*. 2022. URL: https://www.eng-atoms.msm.cam.ac.uk/RoyalSocDemos/SEM (cit. on p. 33).

[70] Stephen Hutcheon and Alex Palmer. *Fighting the invisible enemy*. 2020 (cit. on p. 33).

[71] Pierre Tchoulfian. "Electrical, optical, and electro-optical properties of GaN microwires for the fabrication of LEDs". PhD thesis. Université Grenoble Alpes, 2015 (cit. on p. 38).

[72] S. Hautakangas, J. Oila, M. Alatalo, K. Saarinen, L. Liszkay, D. Seghier, and H. P. Gislason. "Vacancy Defects as Compensating Centers in Mg-Doped GaN". In: *Physical Review Letters* 90.13 (2003), p. 4. DOI: 10.1103/PhysRevLett.90.137402 (cit. on p. 39).

[73] I. Prozheev, F. Mehnke, T. Wernicke, M. Kneissl, and F. Tuomisto. "Electrical compensation and cation vacancies in Al rich Si-doped AlGaN". In: *Applied Physics Letters* 117.14 (2020). DOI: 10.1063/5.0016494 (cit. on p. 39).

[74] K. Laaksonen, M. G. Ganchenkova, and R. M. Nieminen. "Vacancies in wurtzite GaN and AlN". In: *Journal of Physics Condensed Matter* 21.1 (2009). DOI: 10.1088/0953-8984/21/1/015803 (cit. on p. 39).

[75] David C Look. *Electrical characterization of GaAs materials and devices*. Ed. by Wiley. 1989 (cit. on pp. 39, XXXV).

[76] Yoshitaka Taniyasu, Makoto Kasu, and Toshiki Makimoto. "Electrical conduction properties of n-type Si-doped AlN with high electron mobility (>100cm2V-1s-1)". en. In: *Applied Physics Letters* 85.20 (November 2004), pp. 4672–4674. DOI: 10.1063/1.1824181 (cit. on pp. 40, 82, 83, 93, 95, 100).

[77] Zhihua Fang, Eric Robin, Elena Rozas-Jiménez, Ana Cros, Fabrice Donatini, Nicolas Mollard, Julien Pernot, and Bruno Daudin. "Si Donor Incorporation in GaN Nanowires". In: *Nano Letters* 15.10 (2015), pp. 6794–6801. DOI: 10.1021/acs.nanolett.5b02634 (cit. on pp. 40, 84, 85, 88, 126).

[78] A. Wolos, Z. Wilamowski, M. Piersa, W. Strupinski, B. Lucznik, I. Grzegory, and S. Porowski. "Properties of metal-insulator transition and electron spin relaxation in GaN:Si". In: *Physical Review B - Condensed Matter and Materials Physics* 83.16 (2011), pp. 1–8. DOI: 10.1103/PhysRevB.83.165206 (cit. on pp. 40, 82, 89, 100, XXXVII).

[79] P. Tchoulfian, F. Donatini, F. Levy, B. Amstatt, A. Dussaigne, P. Ferret, E. Bustarret, and J. Pernot. "Thermoelectric and micro-Raman measurements of carrier density and mobility in heavily Si-doped GaN wires". In: *Applied Physics Letters* 103.20 (2013). DOI: 10.1063/1.4829857 (cit. on p. 40).

[80] Yoshitaka Taniyasu, Makoto Kasu, and Toshiki Makimoto. "Increased electron mobility in n -type Si-doped AlN by reducing dislocation density". In: *Applied Physics Letters* 89.18 (2006), pp. 9–11. DOI: 10.1063/1.2378726 (cit. on pp. 40, 82, 83, 93, 97, 100).

[81] Nevill Francis Mott. "Conduction in Non-crystalline Materials III. Localized States in a Pseudogap and Near Extremities of Conduction and Valence Bands". In: *Philosophical Magazine* (August 1968). DOI: 10.1142/9789812794086_0027 (cit. on p. 40).

[82] R. M. Hill. "Variable-range hopping". In: *Physica Status Solidi (a)* 34.2 (April 1976), pp. 601–613. DOI: 10.1002/pssa.2210340223 (cit. on p. 40).

[83] A L Efros and B I Shklovskii. "Coulomb gap and low temperature conductivity of disordered systems". In: *Journal of Physics C: Solid State Physics* 8.4 (February 1975), pp. L49–L51. DOI: 10.1088/0022-3719/8/4/003 (cit. on p. 40).

[84] T. Adam, J. Kolodzey, C. P. Swann, M. W. Tsao, and J. F. Rabolt. "The electrical properties of MIS capacitors with ALN gate dielectrics". In: *Applied Surface Science* 175-176 (2001), pp. 428–435. DOI: 10.1016/S0169-4332(01)00091-5 (cit. on p. 41).

[85] Sergey L. Rumyantsev, Michael S. Shur, and Michael E. Levinshtein. "Material Properties of Nitrides: Summary". en. In: *International Journal of High Speed Electronics and Systems* 14.01 (March 2004), pp. 1–19. DOI: 10.1142/S012915640400220X (cit. on p. 41).

[86] M. Borga, M. Meneghini, D. Benazzi, E. Canato, R. Püsche, J. Derluyn, I. Abid, F. Medjdoub, G. Meneghesso, and E. Zanoni. "Buffer breakdown in GaN-on-Si HEMTs: A comprehensive study based on a sequential growth experiment". In: *Microelectronics Reliability* 100-101.July (September 2019). DOI: 10.1016/j.microrel.2019.113461 (cit. on p. 41).

[87] Atsushi Hiraiwa and Hiroshi Kawarada. "Figure of merit of diamond power devices based on accurately estimated impact ionization processes". In: *Journal of Applied Physics* 114.3 (2013). DOI: 10.1063/1.4816312 (cit. on p. 41).

[88] Murray A. Lampert. "Simplified theory of space-charge-limited currents in an insulator with traps". In: *Physical Review* 103.6 (1956), pp. 1648–1656. DOI: 10.1103/PhysRev.103.1648 (cit. on pp. 41, 88, 94, 95, 98, 101).

[89] A Rose. "Space-Charge-Limited Currents in Solids". en. In: *Physical Review* 97.6 (October 1955), pp. 1538–1544. DOI: 10.1103/PhysRev.97.1538 (cit. on pp. 41, 88, 94).

[90] E. Fred Schubert. *Light-Emitting Diodes*. Cambridge: Cambridge University Press, 2006. DOI: 10.1017/CBO9780511790546 (cit. on p. 44).

[91] Zongyang Hu, Kazuki Nomoto, Bo Song, Mingda Zhu, Meng Qi, Ming Pan, Xiang Gao, Vladimir Protasenko, Debdeep Jena, and Huili Grace Xing. "Near unity ideality factor and Shockley-Read-Hall lifetime in GaN-on-GaN p-n diodes with avalanche breakdown". In: *Applied Physics Letters* 107.24 (2015), pp. 1–7. DOI: 10.1063/1.4937436 (cit. on p. 44).

[92] Matt D. Brubaker, Paul T. Blanchard, John B. Schlager, Aric W. Sanders, Andrew M. Herrero, Alexana Roshko, Shannon M. Duff, Todd E. Harvey, Victor M. Bright, Norman A. Sanford, and Kris A. Bertness. "Toward discrete axial p-n junction nanowire light-emitting diodes grown by plasma-assisted molecular beam epitaxy". In: *Journal of Electronic Materials* 42.5 (May 2013), pp. 868–874. DOI: 10.1007/s11664-013-2498-y (cit. on p. 44).

[93] Jay M. Shah, Y. L. Li, Th Gessmann, and E. F. Schubert. "Experimental analysis and theoretical model for anomalously high ideality factors (n>2.0) in AlGaN/GaN p-n junction diodes". In: *Journal of Applied Physics* 94.4 (2003), pp. 2627–2630. DOI: 10.1063/1.1593218 (cit. on pp. 44, 110).

[94] Di Zhu, Jiuru Xu, Ahmed N. Noemaun, Jong Kyu Kim, E. Fred Schubert, Mary H. Crawford, and Daniel D. Koleske. "The origin of the high diode-ideality factors in GaInN/GaN multiple quantum well light-emitting diodes". In: *Applied Physics Letters* 94.8 (2009), pp. 1–4. DOI: 10.1063/1.3089687 (cit. on pp. 44, 110).

[95] W. Shan, B. Little, A. Fischer, J. Song, and B. Goldenberg. "Binding energy for the intrinsic excitons in wurtzite GaN". In: *Physical Review B - Condensed Matter and Materials Physics* 54.23 (1996), pp. 16369–16372. DOI: 10.1103/PhysRevB.54.16369 (cit. on p. 45).

[96] Ryota Ishii, Mitsuru Funato, and Yoichi Kawakami. "Huge electron-hole exchange interaction in aluminum nitride". In: *Physical Review B - Condensed Matter and Materials Physics* 87.16 (2013). DOI: 10.1103/PhysRevB.87.161204 (cit. on p. 45).

[97] W. Shockley and W. T. Read. "Statistics of the recombinations of holes and electrons". In: *Physical Review* 87.5 (1952), pp. 835–842. DOI: 10.1103/PhysRev.87.835 (cit. on p. 46).

[98] Pengwei Du, Ying'er Zhang, Lei Rao, Yang Liu, and Zhiyuan Cheng. "Enhancing the light extraction efficiency of AlGaN LED with nanowire photonic crystal and graphene transparent electrode". In: *Superlattices and Microstructures* 133 (September 2019), p. 106216. DOI: 10.1016/j.spmi.2019.106216 (cit. on p. 47).

[99] Martin Guttmann, Anna Susilo, Luca Sulmoni, Norman Susilo, Eviathar Ziffer, Tim Wernicke, and Michael Kneissl. "Light extraction efficiency and internal quantum efficiency of fully UVC-transparent AlGaN based LEDs". In: *Journal of Physics D: Applied Physics* 54.33 (2021). DOI: 10.1088/1361-6463/ac021a (cit. on pp. 47, 49).

[100] Stéphane Brochen, Julien Brault, Sébastien Chenot, Amélie Dussaigne, Mathieu Leroux, and Benjamin Damilano. "Dependence of the Mg-related acceptor ionization energy with the acceptor concentration in p-type GaN layers grown by

molecular beam epitaxy". In: *Applied Physics Letters* 103.3 (2013), pp. 1–5. DOI: 10.1063/1.4813598 (cit. on pp. 47, 113, XXXVII).

[101] K B Nam, M L Nakarmi, J Li, J Y Lin, and H X Jiang. "Mg acceptor level in AlN probed by deep ultraviolet photoluminescence". en. In: *Applied Physics Letters* 83.5 (November 2003), pp. 878–880. DOI: 10/cqz23q (cit. on pp. 47, 130).

[102] Chuan-Zhen Zhao, Tong Wei, Li-Ying Chen, Sha-Sha Wang, and Jun Wang. "The activation energy for Mg acceptor in AlxGa1-xN alloys in the whole composition range". In: *Superlattices and Microstructures* 109 (September 2017), pp. 758–762. DOI: 10.1016/j.spmi.2017.06.006 (cit. on p. 47).

[103] Kazuaki Ebata, Junichi Nishinaka, Yoshitaka Taniyasu, and Kazuhide Kumakura. "High hole concentration in Mg-doped AlN/AlGaN superlattices with high Al content". In: *Japanese Journal of Applied Physics* 57.4 (2018), pp. 4–7. DOI: 10.7567/JJAP.57.04FH09 (cit. on p. 48).

[104] Christian Kuhn, Luca Sulmoni, Martin Guttmann, Johannes Glaab, Norman Susilo, Tim Wernicke, Markus Weyers, and Michael Kneissl. "MOVPE-grown AlGaN-based tunnel heterojunctions enabling fully transparent UVC LEDs". In: *Photonics Research* 7.5 (2019), B7. DOI: 10.1364/prj.7.0000b7 (cit. on p. 48).

[105] Alexandra-Madalina Siladie, Gwénolé Jacopin, Ana Cros, Nuria Garro, Eric Robin, Damien Caliste, Pascal Pochet, Fabrice Donatini, Julien Pernot, and Bruno Daudin. "Mg and In Codoped p-type AlN Nanowires for pn Junction Realization". en. In: *Nano Letters* 19.12 (December 2019), pp. 8357–8364. DOI: 10.1021/acs.nanolett.9b01394 (cit. on pp. 48, 107, 111, 113, 126).

[106] Frank Mehnke, Christian Kuhn, Martin Guttmann, Christoph Reich, Tim Kolbe, Viola Kueller, Arne Knauer, Mickael Lapeyrade, Sven Einfeldt, Jens Rass, Tim Wernicke, Markus Weyers, and Michael Kneissl. "Efficient charge carrier injection into sub-250 nm AlGaN multiple quantum well light emitting diodes". In: *Applied Physics Letters* 105.5 (2014), pp. 1–5. DOI: 10.1063/1.4892883 (cit. on p. 48).

[107] Hideki Hirayama, Tohru Yatabe, Norimichi Noguchi, Tomoaki Ohashi, and Norihiko Kamata. "231-261 nm AlGaN deep-ultraviolet light-emitting diodes fabricated on AlN multilayer buffers grown by ammonia pulse-flow method on sapphire". In: *Applied Physics Letters* 91.7 (2007), pp. 1–4. DOI: 10.1063/1.2770662 (cit. on p. 48).

[108] Sang Heon Han, Dong Yul Lee, Sang Jun Lee, Chu Young Cho, Min Ki Kwon, S. P. Lee, D. Y. Noh, Dong Joon Kim, Yong Chun Kim, and Seong Ju Park. "Effect of electron blocking layer on efficiency droop in InGaN/GaN multiple quantum well light-emitting diodes". In: *Applied Physics Letters* 94.23 (2009), pp. 1–4. DOI: 10.1063/1.3153508 (cit. on p. 48).

[109] C. H. Wang, C. C. Ke, C. Y. Lee, S. P. Chang, W. T. Chang, J. C. Li, Z. Y. Li, H. C. Yang, H. C. Kuo, T. C. Lu, and S. C. Wang. "Hole injection and efficiency droop improvement in InGaN/GaN light-emitting diodes by band-engineered electron blocking layer". In: *Applied Physics Letters* 97.26 (2010), pp. 1–4. DOI: 10.1063/1.3531753 (cit. on p. 48).

[110] Hideki Hirayama, Noritoshi Maeda, Sachie Fujikawa, Shiro Toyoda, and Norihiko Kamata. "Recent progress and future prospects of AlGaN-based high-ef fi ciency deep-ultraviolet light-emitting diodes". In: *Japanese Journal of Applied Physics* (2014) (cit. on p. 49).

[111] Takayoshi Takano, Takuya Mino, Jun Sakai, Norimichi Noguchi, Kenji Tsubaki, and Hideki Hirayama. "Deep-ultraviolet light-emitting diodes with external quantum efficiency higher than 20% at 275 nm achieved by improving light-extraction efficiency". In: *Applied Physics Express* 10.3 (2017). DOI: 10.7567/APEX.10.031002 (cit. on pp. 49, 124, 125).

[112] Yukio Kashima, Noritoshi Maeda, Eriko Matsuura, Masafumi Jo, Takeshi Iwai, Toshiro Morita, Mitsunori Kokubo, Takaharu Tashiro, Ryuichiro Kamimura, Yamato Osada, Hideki Takagi, and Hideki Hirayama. "High external quantum efficiency (10%) AlGaN-based deep-ultraviolet light-emitting diodes achieved by using highly reflective photonic crystal on p-AlGaN contact layer". In: *Applied Physics Express* 11.1 (January 2018), p. 012101. DOI: 10.7567/APEX.11.012101 (cit. on p. 49).

[113] Stefan Schulz, Miguel A. Caro, Lay Theng Tan, Peter J. Parbrook, Robert W. Martin, and Eoin P. O'Reilly. "Composition-dependent band gap and band-edge bowing in AIInN: A combined theoretical and experimental study". In: *Applied Physics Express* 6.12 (2013), pp. 1–5. DOI: 10.7567/APEX.6.121001 (cit. on p. 58).

[114] E. Kuokstis, W. H. Sun, M. Shatalov, J. W. Yang, and M. Asif Khan. "Role of alloy fluctuations in photoluminescence dynamics of AlGaN epilayers". In: *Applied Physics Letters* 88.26 (2006), pp. 1–4. DOI: 10.1063/1.2218275 (cit. on p. 58).

[115] Hideki Hirayama, Tohru Yatabe, Norimichi Noguchi, and Norihiko Kamata. "Development of 230-270 nm AlGaN-based deep-UV LEDs". In: *Electronics and Communications in Japan* 93.3 (2010), pp. 24–33. DOI: 10.1002/ecj.10197 (cit. on p. 58).

[116] J. Brault, S. Matta, T. H. Ngo, M. Al Khalfioui, P. Valvin, M. Leroux, B. Damilano, M. Korytov, V. Brändli, P. Vennéguès, J. Massies, and B. Gil. "Internal quantum efficiencies of AlGaN quantum dots grown by molecular beam epitaxy and emitting in the UVA to UVC ranges". In: *Journal of Applied Physics* 126.20 (2019), p. 10. DOI: 10.1063/1.5115593 (cit. on pp. 58, 124).

[117] C. Himwas, M. Den Hertog, E. Bellet-Amalric, R. Songmuang, F. Donatini, Le Si Dang, and E. Monroy. "Enhanced room-temperature mid-ultraviolet emission from AlGaN/AlN Stranski-Krastanov quantum dots". In: *Journal of Applied Physics* 116.2 (2014). DOI: 10.1063/1.4887140 (cit. on p. 58).

[118] A. Harikumar, F. Donatini, C. Bougerol, E. Bellet-Amalric, Q. M. Thai, C. Dujardin, I. Dimkou, S. T. Purcell, and E. Monroy. "Internal quantum efficiency of AlGaN/AlN quantum dot superlattices for electron-pumped ultraviolet sources". In: *Nanotechnology* 31.50 (2020), pp. 1–34. DOI: 10.1088/1361-6528/aba86c (cit. on p. 58).

[119] A. Pierret, C. Bougerol, S. Murcia-Mascaros, A. Cros, H. Renevier, B. Gayral, and B. Daudin. "Growth, structural and optical properties of AlGaN nanowires in the whole composition range". In: *Nanotechnology* 24.11 (2013). DOI: 10.1088/0957-4484/24/11/115704 (cit. on pp. 59, 76).

[120] C Sinito, P Corfdir, C Pfüller, G Gao, J Bartolomé, S Kölling, A Rodil Doblado, U Jahn, J Lähnemann, T Auzelle, J K Zettler, T Flissikowski, P Koenraad, H T Grahn, L Geelhaar, S Fernández-Garrido, and O Brandt. "Absence of Quantum-Confined Stark Effect in GaN Quantum Disks Embedded in (Al,Ga)N Nanowires Grown by Molecular Beam Epitaxy". en. In: *Nano Letters* 19.9 (January 2019), pp. 5938–5948. DOI: 10.1021/acs.nanolett.9b01521 (cit. on p. 59).

[121] M. Belloeil, M. G. Proietti, Hubert Renevier, and Bruno Daudin. "Nanoscale x-ray investigation of composition fluctuations in AlGaN nanowires". In: *Nanotechnology* 31.37 (September 2020), p. 375709. DOI: 10.1088/1361-6528/ab94e1 (cit. on pp. 59, 76).

[122] Bruno Daudin, Alexandra Madalina Siladie, Marion Gruart, Martien Den Hertog, Catherine Bougerol, Benedikt Haas, Jean Luc Rouvi re, Eric Robin, Maria José Recio-Carretero, Núria Garro, and Ana Cros. "The role of surface diffusion in the growth mechanism of III-nitride nanowires and nanotubes". In: *Nanotechnology* 32.8 (2021). DOI: 10.1088/1361-6528/abc780 (cit. on pp. 59, 60).

[123] Xianhe Liu, Ayush Pandey, and Zetian Mi. "Nanoscale and quantum engineering of III-nitride heterostructures for high efficiency UV-C and far UV-C optoelectronics". In: *Japanese Journal of Applied Physics* 60.11 (2021). DOI: 10.35848/1347-4065/ac2918 (cit. on pp. 59, 60).

[124] Sonachand Adhikari, Olivier Lee Cheong Lem, Felipe Kremer, Kaushal Vora, Frank Brink, Mykhaylo Lysevych, Hark Hoe Tan, and Chennupati Jagadish. "Nonpolar AlxGa1-xN/AlyGa1-yN multiple quantum wells on GaN nanowire for UV emission". In: *Nano Research* 15.8 (August 2022), pp. 7670–7680. DOI: 10.1007/s12274-022-4403-6 (cit. on p. 59).

[125] M. Belloeil, B. Gayral, and B. Daudin. "Quantum Dot-Like Behavior of Compositional Fluctuations in AlGaN Nanowires". In: *Nano Letters* 16.2 (2016), pp. 960–966. DOI: 10.1021/acs.nanolett.5b03904 (cit. on pp. 59, 76).

[126] Hirotsugu Kobayashi, Shuhei Ichikawa, Mitsuru Funato, and Yoichi Kawakami. "Self-Limiting Growth of Ultrathin GaN/AlN Quantum Wells for Highly Efficient Deep Ultraviolet Emitters". In: *Advanced Optical Materials* 7.21 (2019), pp. 1–7. DOI: 10.1002/adom.201900860 (cit. on pp. 59, 68).

[127] Yoshitaka Taniyasu and Makoto Kasu. "Polarization property of deep-ultraviolet light emission from C-plane AlN/GaN short-period superlattices". In: *Applied Physics Letters* 99.25 (2011), pp. 7–11. DOI: 10.1063/1.3671668 (cit. on pp. 59, 68).

[128] S. M. Islam, Vladimir Protasenko, Kevin Lee, Sergei Rouvimov, Jai Verma, Huili Xing, and Debdeep Jena. "Deep-UV emission at 219 nm from ultrathin MBE GaN/AlN quantum heterostructures". In: *Applied Physics Letters* 111.9 (2017), pp. 3–7. DOI: 10.1063/1.5000844 (cit. on pp. 59, 68).

[129] S. M. Islam, Kevin Lee, Jai Verma, Vladimir Protasenko, Sergei Rouvimov, Shyam Bharadwaj, Huili Xing, and Debdeep Jena. "MBE-grown 232-270 nm deep-UV LEDs using monolayer thin binary GaN/AlN quantum heterostructures". In: *Applied Physics Letters* 110.4 (2017). DOI: 10.1063/1.4975068 (cit. on pp. 59, 60, 68).

[130] Anthony Aiello, Yuanpeng Wu, Ayush Pandey, Ping Wang, Woncheol Lee, Dylan Bayerl, Nocona Sanders, Zihao Deng, Jiseok Gim, Kai Sun, Robert Hovden, Emmanouil Kioupakis, Zetian Mi, and Pallab Bhattacharya. "Deep Ultraviolet Luminescence Due to Extreme Confinement in Monolayer GaN/Al(Ga)N Nanowire and Planar Heterostructures". en. In: *Nano Letters* 19.11 (January 2019), pp. 7852–7858. DOI: 10.1021/acs.nanolett.9b02847 (cit. on pp. 60, 68).

[131] Marion Gruart, Gwénolé Jacopin, and Bruno Daudin. "Role of Ga Surface Diffusion in the Elongation Mechanism and Optical Properties of Catalyst-Free GaN Nanowires Grown by Molecular Beam Epitaxy". en. In: *Nano Letters* 19.7 (October 2019), pp. 4250–4256. DOI: 10/ggb393 (cit. on pp. 62, 63, 78).

[132] C. Adelmann, J. Brault, D. Jalabert, P. Gentile, H. Mariette, Guido Mula, and B. Daudin. "Dynamically stable gallium surface coverages during plasma-assisted molecular-beam epitaxy of (0001) GaN". In: *Journal of Applied Physics* 91.12 (2002), pp. 9638–9645. DOI: 10.1063/1.1471923 (cit. on p. 63).

[133] Christoph Adelmann, Julien Brault, Guido Mula, Bruno Daudin, Liverios Lymperakis, and Jörg Neugebauer. "Gallium adsorption on (0001) GaN surfaces". In: *Physical Review B - Condensed Matter and Materials Physics* 67.16 (April 2003), pp. 1–9. DOI: 10.1103/PhysRevB.67.165419 (cit. on p. 63).

[134] B. Daudin, Guido Mula, C. Adelmann, J. Oullier, and S. Moehl. "Surfactant effect of gallium during molecular-beam epitaxy of GaN on AlN (0001)". In: *Physical Review B - Condensed Matter and Materials Physics* 64.19 (2001), pp. 1–12. DOI: 10.1103/PhysRevB.64.195406 (cit. on p. 63).

[135] N. Gogneau, E. Sarigiannidou, E. Monroy, S. Monnoye, H. Mank, and B. Daudin. "Surfactant effect of gallium during the growth of GaN on AlN(000-1) by plasma-assisted molecular beam epitaxy". In: *Applied Physics Letters* 85.8 (2004), pp. 1421–1423. DOI: 10.1063/1.1782264 (cit. on p. 63).

[136] Ryan G. Banal, Mitsuru Funato, and Yoichi Kawakami. "Growth characteristics of AlN on sapphire substrates by modified migration-enhanced epitaxy". In: *Journal of Crystal Growth* 311.10 (2009), pp. 2834–2836. DOI: 10.1016/j.jcrysgro.2009.01.023 (cit. on p. 63).

[137] Yoshiji Horikoshi, Minoru Kawashima, and Hiroshi Yamaguchi. "Migration-enhanced epitaxy of GaAs and AlGaAs". In: *Japanese Journal of Applied Physics* 27.2R (1988), pp. 169–179. DOI: 10.1143/JJAP.27.169 (cit. on p. 63).

[138] Karine Hestroffer. "Croissance et caractérisation de nanofils de GaN et d'hétérostructures filaires de GaN/AlN". fr. PhD thesis. Grenoble, 2013, p. 211 (cit. on p. 65).

[139] B. Daudin, F. Widmann, G. Feuillet, Y. Samson, M. Arlery, and J. Rouvière. "Stranski-Krastanov growth mode during the molecular beam epitaxy of highly strained GaN". In: *Physical Review B - Condensed Matter and Materials Physics* 56.12 (1997), R7069–R7072. DOI: 10.1103/PhysRevB.56.R7069 (cit. on p. 67).

[140] P. Sohi, D. Martin, and N. Grandjean. "Critical thickness of GaN on AlN: Impact of growth temperature and dislocation density". In: *Semiconductor Science and Technology* 32.7 (2017). DOI: 10.1088/1361-6641/aa7248 (cit. on p. 67).

[141] C. Bougerol, R. Songmuang, D. Camacho, Y. M. Niquet, R. Mata, A. Cros, and B. Daudin. "The structural properties of GaN insertions in GaN/AlN nanocolumn heterostructures". In: *Nanotechnology* 20.29 (2009). DOI: 10.1088/0957-4484/20/29/295706 (cit. on p. 67).

[142] L. Rigutti, G. Jacopin, L. Largeau, E. Galopin, A. De Luna Bugallo, F. H. Julien, J.-C. Harmand, F. Glas, and M. Tchernycheva. "Correlation of optical and structural properties of GaN/AlN core-shell nanowires". In: *Physical Review B* 83.15 (April 2011), p. 155320. DOI: 10.1103/PhysRevB.83.155320 (cit. on p. 68).

[143] Katsumasa Kamiya, Yasuhiro Ebihara, Kenji Shiraishi, and Makoto Kasu. "Structural design of AlN/GaN superlattices for deep-ultraviolet light-emitting diodes with high emission efficiency". In: *Applied Physics Letters* 99.15 (2011), pp. 1–4. DOI: 10.1063/1.3651335 (cit. on p. 68).

[144] Wei Sun, Chee Keong Tan, and Nelson Tansu. "AlN/GaN Digital Alloy for Mid- and Deep-Ultraviolet Optoelectronics". In: *Scientific Reports* 7.1 (2017), pp. 1–8. DOI: 10.1038/s41598-017-12125-9 (cit. on p. 68).

[145] I. Gorczyca, T. Suski, N. E. Christensen, and A. Svane. "Theoretical study of nitride short period superlattices". In: *Journal of Physics Condensed Matter* 30.6 (2018). DOI: 10.1088/1361-648X/aaa2ae (cit. on p. 68).

[146] M. F. MacMillan, L. L. Clemen, R. P. Devaty, W. J. Choyke, M. Asif Khan, J. N. Kuznia, and S. Krishnankutty. "Cathodoluminescence of AlN–GaN short period superlattices". en. In: *Journal of Applied Physics* 80.4 (January 1996), pp. 2378–2382. DOI: 10.1063/1.363726 (cit. on p. 68).

[147] Sergey A. Nikishin, Mark Holtz, and Henryk Temkin. "Digital alloys of AlN/AlGaN for deep UV light emitting diodes". In: *Japanese Journal of Applied Physics, Part 1: Regular Papers and Short Notes and Review Papers* 44.10 (2005), pp. 7221–7226. DOI: 10.1143/JJAP.44.7221 (cit. on p. 68).

[148] Dylan Bayerl, Sm Islam, Christina M. Jones, Vladimir Protasenko, Debdeep Jena, and Emmanouil Kioupakis. "Deep ultraviolet emission from ultra-thin GaN/AlN heterostructures". In: *Applied Physics Letters* 109.24 (2016). DOI: 10.1063/1.4971968 (cit. on p. 68).

[149] Cheng Liu, Yu Kee Ooi, S. M. Islam, Jai Verma, Huili Xing, Debdeep Jena, and Jing Zhang. "Physics and polarization characteristics of 298 nm AlN-delta-GaN quantum well ultraviolet light-emitting diodes". In: *Applied Physics Letters* 110.7 (2017). DOI: 10.1063/1.4976203 (cit. on p. 68).

[150] Jian Liu and Sokrates T. Pantelides. "Mechanisms of Pyroelectricity in Three- and Two-Dimensional Materials". In: *Physical Review Letters* 120.20 (2018). DOI: 10.1103/PhysRevLett.120.207602 (cit. on p. 68).

[151] O. A. Koshelev, D. V. Nechaev, P. N. Brunkov, K. N. Orekhova, S. I. Troshkov, S. V. Ivanov, and V. N. Jmerik. "Suppression of Stark effect in ultra-thin stress-free GaN/AlN multiple quantum well structures grown by plasma-assisted molecular beam epitaxy". In: *Journal of Physics: Conference Series*. Vol. 1410. 1. 2019. DOI: 10.1088/1742-6596/1410/1/012032 (cit. on p. 68).

[152] Na Gao, Xiang Feng, Shiqiang Lu, Wei Lin, Qinqin Zhuang, Hangyang Chen, Kai Huang, Shuping Li, and Junyong Kang. "Integral Monolayer-Scale Featured Digital-Alloyed AlN/GaN Superlattices Using Hierarchical Growth Units". In: *Crystal Growth and Design* 19.3 (2019), pp. 1720–1727. DOI: 10.1021/acs.cgd.8b01677 (cit. on p. 68).

[153] Yixin Wang, Xin Rong, Sergey Ivanov, Valentin Jmerik, Zhaoying Chen, Hui Wang, Tao Wang, Ping Wang, Peng Jin, Yanan Chen, Vladimir Kozlovsky, Dmitry Sviridov, Michail Zverev, Elena Zhdanova, Nikita Gamov, Valentin Studenov, Hideto Miyake, Hongwei Li, Shiping Guo, Xuelin Yang, Fujun Xu, Tongjun Yu, Zhixin Qin, Weikun Ge, Bo Shen, and Xinqiang Wang. "Deep Ultraviolet Light Source from Ultrathin GaN/AlN MQW Structures with Output Power Over 2 Watt". In: *Advanced Optical Materials* 7.10 (2019). DOI: 10.1002/adom.201801763 (cit. on p. 68).

[154] Valentin Jmerik, Dmitrii Nechaev, Kseniya Orekhova, Nikita Prasolov, Vladimir Kozlovsky, Dmitry Sviridov, Mikhail Zverev, Nikita Gamov, Lars Grieger, Yixin Wang, Tao Wang, Xinqiang Wang, and Sergey Ivanov. "Monolayer-scale gan/aln multiple quantum wells for high power e-beam pumped uv-emitters in the 240–270 nm spectral range". In: *Nanomaterials* 11.10 (2021). DOI: 10.3390/nano11102553 (cit. on p. 68).

[155] Yuanpeng Wu, David A Laleyan, Zihao Deng, Chihyo Ahn, Anthony F Aiello, Ayush Pandey, Xianhe Liu, Ping Wang, Kai Sun, Elaheh Ahmadi, Yi Sun, Mackillo Kira, Pallab K Bhattacharya, Emmanouil Kioupakis, and Zetian Mi. "Controlling Defect Formation of Nanoscale AlN: Toward Efficient Current Conduction of Ultrawide-Bandgap Semiconductors". In: *Advanced Electronic Materials* 6.9 (2020), pp. 1–7. DOI: 10.1002/aelm.202000337 (cit. on p. 68).

[156] N. Gogneau, D. Jalabert, E. Monroy, E. Sarigiannidou, J. L. Rouvière, T. Shibata, M. Tanaka, J. M. Gerard, and B. Daudin. "Influence of AlN overgrowth on structural properties of GaN quantum wells and quantum dots grown by plasma-assisted molecular beam epitaxy". In: *Journal of Applied Physics* 96.2 (2004), pp. 1104–1110. DOI: 10.1063/1.1759785 (cit. on p. 71).

[157] G. Callsen, R. Butté, and N. Grandjean. "Probing Alloy Formation Using Different Excitonic Species: The Particular Case of InGaN". In: *Physical Review X* 9.3 (2019). DOI: 10.1103/PhysRevX.9.031030 (cit. on p. 76).

[158] Yong Zhang, B. Fluegel, A. Mascarenhas, H. Xin, and C. Tu. "Optical transitions in the isoelectronically doped semiconductor GaP:N: An evolution from isolated centers, pairs, and clusters to an impurity band". In: *Physical Review B - Condensed Matter and Materials Physics* 62.7 (2000), pp. 4493–4500. DOI: 10.1103/PhysRevB.62.4493 (cit. on p. 76).

[159] H Mariette, J. Chevallier, and P. Leroux-Hugon. "Local-environment effect on the nitrogen bound state in GaPAs alloys: Experiments and coherent-potential approximation theory". In: *Physical Review B* 21.12 (June 1980), pp. 5706–5716. DOI: 10.1103/PhysRevB.21.5706 (cit. on p. 76).

[160] T. S. Kim, T. V. Cuong, C. S. Park, J. Y. Park, H. J. Lee, E. K. Suh, and C. H. Hong. "Composition Dependence of the Band-Gap Energy of GaAsN Alloys". In: *Journal of the Korean Physical Society* 43.2 (2003), pp. 273–276 (cit. on p. 76).

[161] J. L. Merz. "Isoelectronic oxygen trap in ZnTe". In: *Physical Review* 176.3 (1968), pp. 961–968. DOI: 10.1103/PhysRev.176.961 (cit. on p. 76).

[162] T. Mattila and Alex Zunger. "P-P and As-As isovalent impurity pairs in GaN: Interaction of deep t2 levels". In: *Physical Review B - Condensed Matter and Materials Physics* 59.15 (1999), pp. 9943–9953. DOI: 10.1103/PhysRevB.59.9943 (cit. on p. 76).

[163] S. Filippov, M. Jansson, J. E. Stehr, J. Palisaitis, P. O.A. Persson, F. Ishikawa, W. M. Chen, and I. A. Buyanova. "Strongly polarized quantum-dot-like light emitters embedded in GaAs/GaNAs core/shell nanowires". In: *Nanoscale* 8.35 (2016), pp. 15939–15947. DOI: 10.1039/c6nr05168e (cit. on p. 76).

[164] Mattias Jansson, Shula Chen, Rui La, Jan E. Stehr, Charles W. Tu, Weimin M. Chen, and Irina A. Buyanova. "Effects of Nitrogen Incorporation on Structural and Optical Properties of GaNAsP Nanowires". In: *Journal of Physical Chemistry C* 121.12 (2017), pp. 7047–7055. DOI: 10.1021/acs.jpcc.7b00985 (cit. on p. 76).

[165] T. Onuma, S. F. Chichibu, T. Sota, K. Asai, S. Sumiya, T. Shibata, and M. Tanaka. "Exciton spectra of an AlN epitaxial film on (0001) sapphire substrate grown by low-pressure metalorganic vapor phase epitaxy". In: *Applied Physics Letters* 81.4 (2002), pp. 652–654. DOI: 10.1063/1.1493666 (cit. on p. 76).

[166] C. J. Collins, A. V. Sampath, G. A. Garrett, W. L. Sarney, H. Shen, M. Wraback, A. Yu Nikiforov, G. S. Cargill, and V. Dierolf. "Enhanced room-temperature luminescence efficiency through carrier localization in Alx Ga1-x N alloys". In: *Applied Physics Letters* 86.3 (2005), pp. 1–3. DOI: 10.1063/1.1856702 (cit. on p. 76).

[167] M. Gao, Y. Lin, S. T. Bradley, S. A. Ringel, J. Hwang, W. J. Schaff, and L. J. Brillson. "Spontaneous compositional superlattice and band-gap reduction in Si-doped Al xGa 1-xN epilayers". In: *Applied Physics Letters* 87.19 (2005), pp. 1–3. DOI: 10.1063/1.2126127 (cit. on p. 76).

[168] S. Zhao, S. Y. Woo, S. M. Sadaf, Y. Wu, A. Pofelski, D. A. Laleyan, R. T. Rashid, Y. Wang, G. A. Botton, and Z. Mi. "Molecular beam epitaxy growth of Al-rich AlGaN nanowires for deep ultraviolet optoelectronics". In: *APL Materials* 4.8 (2016). DOI: 10.1063/1.4961680 (cit. on pp. 76, 107, 125).

[169] Rémy Vermeersch, Eric Robin, Ana Cros, Gwénolé Jacopin, Bruno Daudin, and Julien Pernot. "Shallow donor and DX state in Si doped AlN nanowires grown by molecular beam epitaxy". In: *Applied Physics Letters* 119.26 (December 2021), p. 262105. DOI: 10.1063/5.0074454 (cit. on pp. 82, 126).

[170] Rémy Vermeersch, Gwénolé Jacopin, Bruno Daudin, and Julien Pernot. "DX center formation in highly Si doped AlN nanowires revealed by trap assisted space-charge limited current". In: *Applied Physics Letters* 120.16 (April 2022), p. 162104. DOI: 10.1063/5.0087789 (cit. on p. 82).

[171] A. Y. Polyakov, N. B. Smirnov, A. V. Govorkov, M. G. Mil'vidskii, J. M. Redwing, M. Shin, M. Skowronski, D. W. Greve, and R. G. Wilson. "Properties of Si donors and persistent photoconductivity in AlGaN". In: *Solid-State Electronics* 42.4 (1998), pp. 627–635. DOI: 10.1016/S0038-1101(97)00277-3 (cit. on p. 82).

[172] M. L. Nakarmi, K. H. Kim, K. Zhu, J. Y. Lin, and H. X. Jiang. "Transport properties of highly conductive n-type Al-rich AlxGa1-xN(x>0.7)". In: *Applied Physics Letters* 85.17 (October 2004), pp. 3769–3771. DOI: 10.1063/1.1809272 (cit. on pp. 82, 83, 100).

[173] Yoshitaka Taniyasu, Makoto Kasu, and Naoki Kobayashi. "Intentional control of n -type conduction for Si-doped AlN and AlXGa1-XN (0.42<x<1)". In: *Applied Physics Letters* 81.7 (August 2002), pp. 1255–1257. DOI: 10.1063/1.1499738 (cit. on pp. 82, 83, 89, 100).

[174] R. Zeisel, M. Bayerl, S. Goennenwein, R. Dimitrov, O. Ambacher, M. Brandt, and M. Stutzmann. "DX behavior of Si in AlN". In: *Physical Review B - Condensed Matter and Materials Physics* 61.24 (2000), R16283–R16286. DOI: 10.1103/PhysRevB.61.R16283 (cit. on pp. 82, 83, 88, 90, 96, 100, 101).

[175] M. Hermann, F. Furtmayr, A. Bergmaier, G. Dollinger, M. Stutzmann, and M. Eickhoff. "Highly Si-doped AlN grown by plasma-assisted molecular-beam epitaxy". In: *Applied Physics Letters* 86.19 (2005), pp. 1–3. DOI: 10.1063/1.1923180 (cit. on pp. 82, 83, 87, 89, 100).

[176] S. T.B. Goennenwein, R. Zeisel, O. Ambacher, M. S. Brandt, M. Stutzmann, and S. Baldovino. "Generation-recombination noise of DX centers in AlN:Si". In: *Applied Physics Letters* 79.15 (2001), pp. 2396–2398. DOI: 10.1063/1.1405426 (cit. on pp. 82, 83, 88, 96, 100).

[177] Tommy Ive, Oliver Brandt, Helmar Kostial, Klaus J. Friedland, Lutz Däweritz, and Klaus H. Ploog. "Controlled n -type doping of AlN:Si films grown on 6H-SiC(0001) by plasma-assisted molecular beam epitaxy". In: *Applied Physics Letters* 86.2 (2005), pp. 1–4. DOI: 10.1063/1.1850183 (cit. on pp. 83, 100).

[178] B. Borisov, V. Kuryatkov, Yu Kudryavtsev, R. Asomoza, S. Nikishin, D. Y. Song, M. Holtz, and H. Temkin. "Si-doped Al xGa 1-xN (0.56<×<1) layers grown by molecular beam epitaxy with ammonia". In: *Applied Physics Letters* 87.13 (September 2005), pp. 1–3. DOI: 10.1063/1.2061856 (cit. on pp. 83, 100).

[179] Masakazu Kanechika and Tetsu Kachi. "N -type AlN layer by Si ion implantation". In: *Applied Physics Letters* 88.20 (2006), pp. 2004–2006. DOI: 10.1063/1.2204656 (cit. on pp. 83, 100).

[180] N. T. Son, M. Bickermann, and E. Janzén. "Shallow donor and DX states of Si in AlN". In: *Applied Physics Letters* 98.9 (2011). DOI: 10.1063/1.3559914 (cit. on pp. 83, 100).

[181] Xuan Thang Trinh, Daniel Nilsson, Ivan G. Ivanov, Erik Janzén, Anelia Kakanakova-Georgieva, and Nguyen Tien Son. "Stable and metastable Si negative-U centers in AlGaN and AlN". In: *Applied Physics Letters* 105.16 (2014). DOI: 10.1063/1.4900409 (cit. on pp. 83, 88, 90, 100).

[182] Klaus Thonke, Matthias Lamprecht, Ramon Collazo, and Zlatko Sitar. "Optical signatures of silicon and oxygen related DX centers in AlN". In: *Physica Status Solidi (A) Applications and Materials Science* 214.9 (2017). DOI: 10.1002/pssa.201600749 (cit. on pp. 83, 88, 100).

[183] M. Hayden Breckenridge, Qiang Guo, Andrew Klump, Biplab Sarkar, Yan Guan, James Tweedie, Ronny Kirste, Seiji Mita, Pramod Reddy, Ramón Collazo, and Zlatko Sitar. "Shallow Si donor in ion-implanted homoepitaxial AlN". In: *Applied Physics Letters* 116.17 (2020), p. 172103. DOI: 10.1063/1.5144080 (cit. on pp. 83, 88, 90, 93, 100).

[184] T. Mattila and R. Nieminen. "Point-defect complexes and broadband luminescence in GaN and AlN". In: *Physical Review B - Condensed Matter and Materials Physics* 55.15 (1997), pp. 9571–9576. DOI: 10.1103/PhysRevB.55.9571 (cit. on p. 82).

[185] Chris G. Van de Walle and Jörg Neugebauer. "First-principles calculations for defects and impurities: Applications to III-nitrides". In: *Journal of Applied Physics* 95.8 (April 2004), pp. 3851–3879. DOI: 10.1063/1.1682673 (cit. on p. 82).

[186] Joshua S. Harris, Jonathon N. Baker, Benjamin E. Gaddy, Isaac Bryan, Zachary Bryan, Kelsey J. Mirrielees, Pramod Reddy, Ramón Collazo, Zlatko Sitar, and Douglas L. Irving. "On compensation in Si-doped AlN". In: *Applied Physics Letters* 112.15 (2018). DOI: 10.1063/1.5022794 (cit. on pp. 82, 88, 93, 98, 101).

[187] D. V. Lang, R. A. Logan, and M. Jaros. "Trapping characteristics and a donor-complex (DX) model for the persistent-photoconductivity trapping center in Te-doped AlxGa1-xAs". In: *Physical Review B* 19.2 (1979), pp. 1015–1030. DOI: 10.1103/PhysRevB.19.1015 (cit. on pp. 82, 83, 90).

[188] D. J. Chadi and K. J. Chang. "Theory of the atomic and electronic structure of DX centers in GaAs and AlxGa1-xAs alloys". In: *Physical Review Letters* 61.7 (1988), pp. 873–876. DOI: 10.1103/PhysRevLett.61.873 (cit. on pp. 82, 84).

[189] P. M. Mooney. "Deep donor levels (DX centers) in III-V semiconductors". In: *Journal of Applied Physics* 67.3 (1990), R1–R26. DOI: 10.1063/1.345628 (cit. on pp. 82, 90).

[190] M. G. Craford, G. E. Stillman, J. A. Rossi, and N. Holonyak. "Effect of Te and S Donor Levels in the Properties of GaAs_{1-x}P_x". In: *Physical Review* 168.3 (1968), pp. 867–882 (cit. on p. 82).

[191] P Bogusławski and J Bernholc. "Doping properties of C, Si, and Ge impurities in GaN and AlN". en. In: *Physical Review B* 56.15 (January 1997), pp. 9496–9505. DOI: 10.1103/PhysRevB.56.9496 (cit. on pp. 83, 98).

[192] C. Park and D. Chadi. "Stability of deep donor and acceptor centers in GaN, AlN, and BN". In: *Physical Review B - Condensed Matter and Materials Physics* 55.19 (1997), pp. 12995–13001. DOI: 10.1103/PhysRevB.55.12995 (cit. on p. 83).

[193] L. Gordon, J. L. Lyons, A. Janotti, and C. G. Van De Walle. "Hybrid functional calculations of D X centers in AlN and GaN". In: *Physical Review B - Condensed Matter and Materials Physics* 89.8 (2014), pp. 1–6. DOI: 10.1103/PhysRevB.89.085204 (cit. on pp. 83, 89, 90, 98, 99).

[194] Leonardo Silvestri, Kerry Dunn, Steven Prawer, and Franois Ladouceur. "Hybrid functional study of Si and O donors in wurtzite AlN". In: *Applied Physics Letters* 99.12 (2011). DOI: 10.1063/1.3641861 (cit. on pp. 83, 98).

[195] Leonardo Silvestri, Kerry Dunn, Steven Prawer, and François Ladouceur. "Concentration of point defects in wurtzite AlN: A hybrid functional study". In: *Epl* 98.3 (2012). DOI: 10.1209/0295-5075/98/36003 (cit. on pp. 83, 99).

[196] Chris G. Van de Walle. "DX-Center formation in wurtzite and zinc-blende AlGaN". In: *Physical Review B - Condensed Matter and Materials Physics* 57.4 (1998), R2033–R2036. DOI: 10.1103/PhysRevB.57.R2033 (cit. on pp. 83, 87).

[197] Ivan A. Aleksandrov and Konstantin S. Zhuravlev. "Luminescence line shapes of band to deep centre and donor-acceptor transitions in AlN". In: *Journal of Physics Condensed Matter* 32.43 (2020). DOI: 10.1088/1361-648X/aba295 (cit. on pp. 83, 98, 99).

[198] Florian Furtmayr, Martin Vielemeyer, Martin Stutzmann, Jordi Arbiol, Snia Estrad, Francesca Peir, Joan Ramon Morante, and Martin Eickhoff. "Nucleation and growth of GaN nanorods on Si (111) surfaces by plasma-assisted molecular beam epitaxy - The influence of Si- and Mg-doping". In: *Journal of Applied Physics* 104.3 (2008). DOI: 10.1063/1.2953087 (cit. on pp. 84, 88).

[199] Alexandra-Madalina Siladie, Lynda Amichi, Nicolas Mollard, Isabelle Mouton, Bastien Bonef, Catherine Bougerol, Adeline Grenier, Eric Robin, Pierre-Henri Jouneau, Nuria Garro, Ana Cros, and Bruno Daudin. "Dopant radial inhomogeneity in Mg-doped GaN nanowires". en. In: *Nanotechnology* 29.25 (October 2018), p. 255706. DOI: 10/gf9rkh (cit. on pp. 84, 121).

[200] Nevill Francis Mott and Ronald Wilfrid Gurney. *Electronic processes in non-crystalline materials*. Oxford university press, 1940 (cit. on p. 88).

[201] A. Alec Talin, B. S. Swartzentruber, François Léonard, X. Wang, and Stephen D. Hersee. "Electrical transport in GaN nanowires grown by selective epitaxy". In: *Journal of Vacuum Science & Technology B: Microelectronics and Nanometer Structures* 27.4 (2009), p. 2040. DOI: 10.1116/1.3123302 (cit. on pp. 88, 94).

[202] V. Lebedev, G. Cherkashinin, G. Ecke, I. Cimalla, and O. Ambacher. "Space charge limited electron transport in AlGaN photoconductors". In: *Journal of Applied Physics* 101.3 (2007). DOI: 10.1063/1.2433139 (cit. on p. 88).

[203] Raffaella Calarco, Toma Stoica, Oliver Brandt, and Lutz Geelhaar. "Surface-induced effects in GaN nanowires". In: *Journal of Materials Research* 26.17 (August 2011), pp. 2157–2168. DOI: 10.1557/jmr.2011.211 (cit. on pp. 88, 90).

[204] Zhihua Fang, Fabrice Donatini, Bruno Daudin, and Julien Pernot. "Axial p–n junction and space charge limited current in single GaN nanowire". en. In: *Nanotechnology* 29.1 (October 2018), 01LT01. DOI: 10/ggbhf7 (cit. on pp. 88, 131).

[205] M. D. McCluskey, N M Johnson, C. G. Van de Walle, D P Bour, M Kneissl, and W. Walukiewicz. "Metastability of Oxygen Donors in AlGaN". In: *Physical Review Letters* 80.18 (May 1998), pp. 4008–4011. DOI: 10.1103/PhysRevLett.80.4008 (cit. on p. 89).

[206] T. Mattila and R. Nieminen. "Ab initio study of oxygen point defects in GaAs, GaN, and AlN". In: *Physical Review B - Condensed Matter and Materials Physics* 54.23 (1996), pp. 16676–16682. DOI: 10.1103/PhysRevB.54.16676 (cit. on p. 89).

[207] Pramod Reddy, Isaac Bryan, Zachary Bryan, Wei Guo, Lindsay Hussey, Ramon Collazo, and Zlatko Sitar. "The effect of polarity and surface states on the Fermi level at III-nitride surfaces". In: *Journal of Applied Physics* 116.12 (2014). DOI: 10.1063/1.4896377 (cit. on p. 90).

[208] J. S. Thorp, D. Evans, M. Al-Naief, and M. Akhtaruzzaman. "The dielectric properties of aluminium nitride substrates for microelectronics packaging". In: *Journal of Materials Science* 25.12 (December 1990), pp. 4965–4971. DOI: 10.1007/BF00580114 (cit. on pp. 95, 108).

[209] Yoshitaka Taniyasu, Makoto Kasu, and Toshiki Makimoto. “An aluminium nitride light-emitting diode with a wavelength of 210 nanometres”. en. In: *Nature* 441.7091 (October 2006), pp. 325–328. DOI: 10.1038/nature04760 (cit. on p. 95).

[210] J. B. Varley, A. Janotti, and C. G. Van De Walle. “Defects in AlN as candidates for solid-state qubits”. In: *Physical Review B* 93.16 (2016), pp. 1–5. DOI: 10.1103/PhysRevB.93.161201 (cit. on p. 98).

[211] C. Stampfl and C. G. Van de Walle. “Theoretical investigation of native defects, impurities, and complexes in aluminum nitride”. In: *Physical Review B - Condensed Matter and Materials Physics* 65.15 (2002), pp. 1552121–15521210. DOI: 10.1103/PhysRevB.65.155212 (cit. on p. 98).

[212] Antonio Ferreira Da Silva, Julien Pernot, Sylvie Contreras, Bo E. Sernelius, Clas Persson, and Jean Camassel. “Electrical resistivity and metal-nonmetal transition in n -type doped 4H-SiC”. In: *Physical Review B - Condensed Matter and Materials Physics* 74.24 (2006), pp. 4–9. DOI: 10.1103/PhysRevB.74.245201 (cit. on p. 100).

[213] T. Klein, P. Achatz, J. Kacmarcik, C. Marcenat, F. Gustafsson, J. Marcus, E. Bustarret, J. Pernot, F. Omnes, Bo E. Sernelius, C. Persson, A. Ferreira Da Silva, and C. Cytermann. “Metal-insulator transition and superconductivity in boron-doped diamond”. In: *Physical Review B - Condensed Matter and Materials Physics* 75.16 (2007), pp. 1–7. DOI: 10.1103/PhysRevB.75.165313 (cit. on p. 100).

[214] Ece N. Aybeke, Alexandra-Madalina Siladie, Rémy Vermeersch, Eric Robin, Oleksandr Synhaivskyi, Bruno Gayral, Julien Pernot, Georges Brémond, and Bruno Daudin. “Nanoscale imaging of dopant incorporation in n-type and p-type GaN nanowires by scanning spreading resistance microscopy”. In: *Journal of Applied Physics* 131.7 (February 2022), p. 075701. DOI: 10.1063/5.0080713 (cit. on p. 101).

[215] Pegah Bagheri, Pramod Reddy, Seiji Mita, Dennis Szymanski, Ji Hyun Kim, Yan Guan, Dolar Khachariya, Andrew Klump, Spyridon Pavlidis, Ronny Kirste, Ramón Collazo, and Zlatko Sitar. “On the Ge shallow-to-deep level transition in Al-rich AlGaN”. In: *Journal of Applied Physics* 130.5 (2021). DOI: 10.1063/5.0059037 (cit. on p. 101).

[216] Catherine Bougerol, Eric Robin, Enrico Di Russo, Edith Bellet-Amalric, Vincent Grenier, Akhil Ajay, Lorenzo Rigutti, and Eva Monroy. “Solubility Limit of Ge Dopants in AlGaN: A Chemical and Microstructural Investigation down to the Nanoscale”. In: *ACS Applied Materials and Interfaces* 13.3 (2021), pp. 4165–4173. DOI: 10.1021/acsami.0c19174 (cit. on p. 102).

[217] Luke Gordon, Joel B. Varley, John L. Lyons, Anderson Janotti, and Chris G. Van de Walle. "Sulfur doping of AlN and AlGaN for improved n-type conductivity". In: *Physica Status Solidi - Rapid Research Letters* 9.8 (2015), pp. 462–465. DOI: 10.1002/pssr.201510165 (cit. on p. 102).

[218] Yong Bing Tang, Xiang Hui Bo, Jun Xu, Yu Lin Cao, Zhen Hua Chen, Hai Sheng Song, Chao Ping Liu, Tak Fu Hung, Wen Jun Zhang, Hui Ming Cheng, Igor Bello, Shuit Tong Lee, and Chun Sing Lee. "Tunable p-type conductivity and transport properties of AlN nanowires via Mg doping". In: *ACS Nano* 5.5 (2011), pp. 3591–3598. DOI: 10.1021/nn200963k (cit. on p. 106).

[219] Nhung Hong Tran, Binh Huy Le, Songrui Zhao, and Zetian Mi. "On the mechanism of highly efficient p-type conduction of Mg-doped ultra-wide-bandgap AlN nanostructures". In: *Applied Physics Letters* 110.3 (2017). DOI: 10.1063/1.4973999 (cit. on pp. 106, 113).

[220] P. Bogusławski, E. L. Briggs, and J. Bernholc. "Amphoteric properties of substitutional carbon impurity in GaN and AIN". In: *Applied Physics Letters* 69.2 (July 1996), pp. 233–235. DOI: 10.1063/1.117934 (cit. on p. 106).

[221] Chris G. Van de Walle, C. Stampfl, J. Neugebauer, M. D. McCluskey, and N. M. Johnson. "Doping of AlGaN Alloys". In: *MRS Internet Journal of Nitride Semiconductor Research* 4.S1 (June 1999), pp. 890–901. DOI: 10.1557/S1092578300003574 (cit. on p. 106).

[222] Gon Namkoong, Elaissa Trybus, Kyung Keun Lee, Michael Moseley, W. Alan Doolittle, and David C. Look. "Metal modulation epitaxy growth for extremely high hole concentrations above 1019 cm-3 in GaN". In: *Applied Physics Letters* 93.17 (2008), pp. 1–4. DOI: 10.1063/1.3005640 (cit. on p. 106).

[223] Habib Ahmad, Jeff Lindemuth, Zachary Engel, Christopher M. Matthews, Timothy M. McCrone, and William Alan Doolittle. "Substantial P-Type Conductivity of AlN Achieved via Beryllium Doping". In: *Advanced Materials* 33.42 (October 2021), p. 2104497. DOI: 10.1002/adma.202104497 (cit. on p. 106).

[224] Habib Ahmad, Zachary Engel, Christopher M. Matthews, and W. Alan Doolittle. "p-type AlN based heteroepitaxial diodes with Schottky, Pin, and junction barrier Schottky character achieving significant breakdown performance". In: *Journal of Applied Physics* 130.19 (November 2021), p. 195702. DOI: 10.1063/5.0069539 (cit. on pp. 106, 107).

[225] Peta Koteswara Rao, Byungguon Park, Sang Tae Lee, Young Kyun Noh, Moon Deock Kim, and Jae Eung Oh. "Analysis of leakage current mechanisms in Pt/Au Schottky contact on Ga-polarity GaN by Frenkel-Poole emission and deep level

studies". In: *Journal of Applied Physics* 110.1 (2011). DOI: 10.1063/1.3607245 (cit. on p. 108).

[226] Piotr Perlin, Marek Osiński, Petr G Eliseev, Vladimir A Smagley, Jian Mu, Michael Banas, and Philippe Sartori. "Low-temperature study of current and electroluminescence in InGaN/AlGaN/GaN double-heterostructure blue light-emitting diodes". In: *Applied Physics Letters* 69.12 (September 1996), pp. 1680–1682. DOI: 10.1063/1.117026 (cit. on p. 110).

[227] K. B. Lee, P. J. Parbrook, T. Wang, J. Bai, F. Ranalli, R. J. Airey, and G. Hill. "The origin of the high ideality factor in AlGaN-based quantum well ultraviolet light emitting diodes". In: *Physica Status Solidi (B) Basic Research* 247.7 (2010), pp. 1761–1763. DOI: 10.1002/pssb.200983617 (cit. on p. 110).

[228] Y. Garino, T. Teraji, A. Lazea, and S. Koizumi. "Forward tunneling current in {111}-oriented homoepitaxial diamond p-n junction". In: *Diamond and Related Materials* 21 (2012), pp. 33–36. DOI: 10.1016/j.diamond.2011.10.007 (cit. on p. 110).

[229] Patrick Rinke, M. Winkelnkemper, A. Qteish, D. Bimberg, J. Neugebauer, and M. Scheffler. "Consistent set of band parameters for the group-III nitrides AlN, GaN, and InN". In: *Physical Review B - Condensed Matter and Materials Physics* 77.7 (2008), pp. 1–15. DOI: 10.1103/PhysRevB.77.075202 (cit. on pp. 110, 128, XXXVII).

[230] M. Lenzlinger and E. H. Snow. "Fowler-nordheim tunneling into thermally grown SiO2". In: *Journal of Applied Physics* 40.1 (1969), pp. 278–283. DOI: 10.1063/1.1657043 (cit. on p. 116).

[231] H. P. Maruska and D. A. Stevenson. "Mechanism of light production in metal-insulator-semiconductor diodes; GaN:Mg violet light-emitting diodes". In: *Solid State Electronics* 17.11 (1974), pp. 1171–1179. DOI: 10.1016/0038-1101(74)90161-0 (cit. on p. 116).

[232] James Kolodzey, Enam Ahmed Chowdhury, Thomas N. Adam, Guohua Qui, I. Rau, Johnson Olufemi Olowolafe, John S. Suehle, and Yuan Chen. "Electrical conduction and dielectric breakdown in aluminum oxide insulators on silicon". In: *IEEE Transactions on Electron Devices* 47.1 (2000), pp. 121–128. DOI: 10.1109/16.817577 (cit. on p. 116).

[233] A. Kabulski and D. Korakakis. "Transport mechanism in aluminum nitride-metal multilayer junctions". In: *Journal of Vacuum Science & Technology B: Microelectronics and Nanometer Structures* 27.6 (2009), p. 2404. DOI: 10.1116/1.3258658 (cit. on p. 116).

[234] H. Witte, A. Rohrbeck, K. M. Günther, P. Saengkaew, J. Bläsing, A. Dadgar, and A. Krost. "Electrical investigations of AlGaN/AlN structures for LEDs on Si(111)". In: *Physica Status Solidi (A) Applications and Materials Science* 208.7 (2011), pp. 1597–1599. DOI: 10.1002/pssa.201001146 (cit. on p. 116).

[235] Ayumu Karasawa, Toshiharu MAKINO, Aboulaye Traore, Hiromitsu KATO, Masahiko Ogura, Yukako Kato, Daisuke Takeuchi, Satoshi Yamasaki, and Takeaki Sakurai. "Carrier transport mechanism of diamond p + –n junction at low temperature using Schottky–pn junction structure". In: *Japanese Journal of Applied Physics* (2021). DOI: 10.35848/1347-4065/abe33f (cit. on pp. 116, 117).

[236] G Martin, S Strite, A Botchkarev, A Agarwal, A Rockett, W R L Lambrecht, B Segall, and H Morkoç. "Valence-band discontinuity between GaN and AIN measured by x-ray photoemission spectroscopy". en. In: *Journal of Electronic Materials* 24.4 (January 1995), pp. 225–227. DOI: 10.1007/BF02659679 (cit. on p. 117).

[237] S. Satpathy, Z. S. Popovic, and W. C. Mitchel. "Theory of the composition dependence of the band offset and sheet carrier density in the GaN/AlxGa1-xN heterestructure". In: *Journal of Applied Physics* 95.10 (2004), pp. 5597–5601. DOI: 10.1063/1.1704869 (cit. on p. 117).

[238] Byung Jae Kim, Chongmin Lee, Younghun Jung, Kwang Hyeon Baik, Michael A. Mastro, Jennifer K. Hite, Charles R. Eddy, and Jihyun Kim. "Large-area transparent conductive few-layer graphene electrode in GaN-based ultra-violet light-emitting diodes". In: *Applied Physics Letters* 99.14 (2011), pp. 1–4. DOI: 10.1063/1.3644496 (cit. on p. 121).

[239] David Arto Laleyan, Songrui Zhao, Steffi Y. Woo, Hong Nhung Tran, Huy Binh Le, Thomas Szkopek, Hong Guo, Gianluigi A. Botton, and Zetian Mi. "AlN/h-BN Heterostructures for Mg Dopant-Free Deep Ultraviolet Photonics". In: *Nano Letters* 17.6 (June 2017), pp. 3738–3743. DOI: 10.1021/acs.nanolett.7b01068 (cit. on pp. 121, 125).

[240] Hideki Hirayama, Sachie Fujikawa, Jun Norimatsu, Takayoshi Takano, Kenji Tsubaki, and Norihiko Kamata. "Fabrication of a low threading dislocation density ELO-AlN template for application to deep-UV LEDs". In: *Physica Status Solidi (C) Current Topics in Solid State Physics* 6.SUPPL. 2 (2009), pp. 2–5. DOI: 10.1002/pssc.200880958 (cit. on pp. 124, 125).

[241] Norman Susilo, Sylvia Hagedorn, Dominik Jaeger, Hideto Miyake, Ute Zeimer, Christoph Reich, Bettina Neuschulz, Luca Sulmoni, Martin Guttmann, Frank Mehnke, Christian Kuhn, Tim Wernicke, Markus Weyers, and Michael Kneissl. "AlGaN-based deep UV LEDs grown on sputtered and high temperature annealed AlN/sapphire".

In: *Applied Physics Letters* 112.4 (January 2018), p. 041110. DOI: 10.1063/1.5010265 (cit. on p. 124).

[242] Hideki Hirayama, Tohru Yatabe, Tomoaki Ohashi, and Norihiko Kamata. "Remarkable enhancement of 254-280 nm deep ultraviolet emission from AlGaN quantum wells by using high-quality AlN buffer on sapphire". In: *Physica Status Solidi (C) Current Topics in Solid State Physics* 5.6 (2008), pp. 2283–2285. DOI: 10.1002/pssc.200778697 (cit. on p. 124).

[243] Nadine Tillner, Christian Frankerl, Felix Nippert, Matthew J. Davies, Christian Brandl, Rainer Lösing, Martin Mandl, Hans Jürgen Lugauer, Roland Zeisel, Axel Hoffmann, Andreas Waag, and Marc Patrick Hoffmann. "Point Defect-Induced UV-C Absorption in Aluminum Nitride Epitaxial Layers Grown on Sapphire Substrates by Metal-Organic Chemical Vapor Deposition". In: *Physica Status Solidi (B) Basic Research* 257.12 (2020), pp. 1–6. DOI: 10.1002/pssb.202000278 (cit. on p. 124).

[244] Theodore D. Moustakas, Yitao Liao, Chen-kai Kao, Christos Thomidis, Anirban Bhattacharyya, Dipesh Bhattarai, and Adam Moldawer. "Deep UV-LEDs with high IQE based on AlGaN alloys with strong band structure potential fluctuations". In: *Light-Emitting Diodes: Materials, Devices, and Applications for Solid State Lighting XVI* 8278.June 2014 (2012), p. 82780L. DOI: 10.1117/12.916213 (cit. on p. 125).

[245] Vincent Grenier, Sylvain Finot, Lucie Valera, Joël Eymery, Gwénolé Jacopin, and Christophe Durand. "UV-A to UV-B electroluminescence of core-shell GaN/AlGaN wire heterostructures". In: *Applied Physics Letters* 121.13 (September 2022), p. 131102. DOI: 10.1063/5.0101591 (cit. on p. 125).

[246] Ravi Teja Velpula, Barsha Jain, Moab Rajan Philip, Hoang Duy Nguyen, Renjie Wang, and Hieu Pham Trung Nguyen. "Epitaxial Growth and Characterization of AlInN-Based Core-Shell Nanowire Light Emitting Diodes Operating in the Ultraviolet Spectrum". In: *Scientific Reports* 10.1 (2020), pp. 1–10. DOI: 10.1038/s41598-020-59442-0 (cit. on p. 125).

[247] Valerio Piazza, Andrey V. Babichev, Lorenzo Mancini, Martina Morassi, Patrick Quach, Fabien Bayle, Ludovic Largeau, François H. Julien, Pierre Rale, Stéphane Collin, Jean-Christophe Christophe Harmand, Noelle Gogneau, and Maria Tchernycheva. "Investigation of GaN nanowires containing AlN/GaN multiple quantum discs by EBIC and CL techniques". en. In: *Nanotechnology* 30.21 (October 2019), p. 214006. DOI: 10/gf98v7 (cit. on p. 131).

[248] Leonid Chernyak, Andrei Osinsky, Vladimir Fuflyigin, and E. F. Schubert. "Electron beam-induced increase of electron diffusion length in p-type GaN and AlGaN/GaN superlattices". In: *Applied Physics Letters* 77.6 (2000), pp. 875–877. DOI: 10.1063/1.1306910 (cit. on p. 131).

[249] G. L. Pearson and J. Bardeen. "Electrical Properties of Pure Silicon and Silicon Alloys Containing Boron and Phosphorus". In: *Physical Review* 75.5 (March 1949), pp. 865–883. DOI: 10.1103/PhysRev.75.865 (cit. on p. XXXVII).

[250] W Götz, R.S Kern, C.H Chen, H Liu, D.A Steigerwald, and R.M Fletcher. "Hall-effect characterization of III–V nitride semiconductors for high efficiency light emitting diodes". In: *Materials Science and Engineering: B* 59.1-3 (May 1999), pp. 211–217. DOI: 10.1016/S0921-5107(98)00393-6 (cit. on p. XXXVII).

[251] M. Musolino, A. Tahraoui, S. Fernández-Garrido, O. Brandt, A. Trampert, L. Geelhaar, and H. Riechert. "Compatibility of the selective area growth of GaN nanowires on AlN-buffered Si substrates with the operation of light emitting diodes". In: *Nanotechnology* 26.8 (2015). DOI: 10.1088/0957-4484/26/8/085605 (cit. on p. XLIII).

[252] M Wölz, C Hauswald, T Flissikowski, T Gotschke, S Fernández-Garrido, O Brandt, H T Grahn, L Geelhaar, and H Riechert. "Epitaxial Growth of GaN Nanowires with High Structural Perfection on a Metallic TiN Film". en. In: *Nano Letters* 15.6 (October 2015), pp. 3743–3747. DOI: 10/f7gpwm (cit. on p. XLIII).

APPENDIX A

MBE calibrations by RHEED

A.1 Cells calibration by RHEED Oscillations

In order to calibrate growth rates and atomic fluxes, several techniques can be used. The technique I learned and utilized is the calibration by recording RHEED oscillations as a function of cell temperature. As discussed in paragraph 1.2.3, monitoring the RHEED intensity of the direct reflection of the electron beam on the surface, gives information on its roughness. At the beginning of the growth, the layer is complete and considered as compact. Therefore, the reflection is at its maximum giving a maximum RHEED intensity of the reflected beam. As soon as a new layer is starting to grow, the top layer gets incomplete which adds roughness and reduces the reflectivity: RHEED intensity reaches a minimum when the grown layer is half completed. Once the layer is fully grown, then the surface its initial state and RHEED signal reaches its maximum again. A schematic view of the process is drawn in figure A.1.

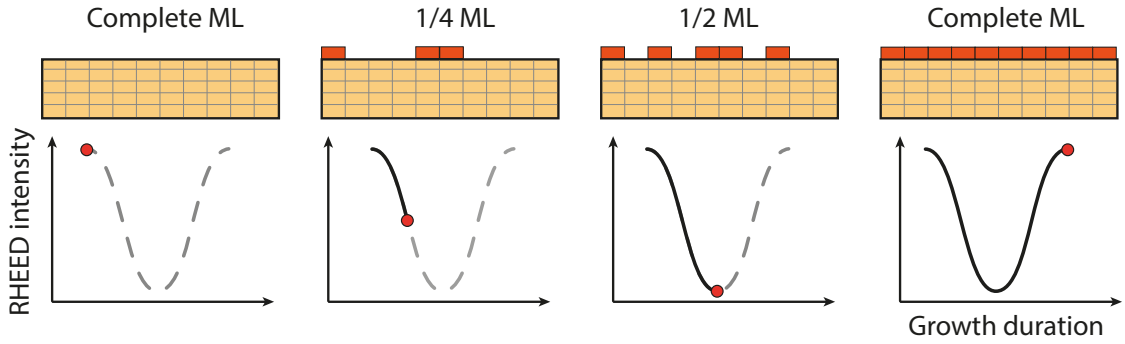

Figure A.1: Schematics of the RHEED intensity as function of the growth duration.

One can use this signal to calculate the growth rate of the layer for a given cell at a given temperature. Figure A.2 shows oscillations for a gallium cell at three different temperatures. For each of them, one can observe several oscillations with a period corresponding to the ML growth rate. As one changes growth rate by acting on the Ga flux, the growth must be Ga-limited, in other words in Nitrogen-rich conditions.

This technique seems robust and efficient. However, in practice it has to be nuanced. First, at the opening of the cell shutter, a burst of material is created which means that a higher flux is sent to the substrate. Several seconds up to some minutes can be needed to reach a steady state. Therefore, the growth rate measured by RHEED oscillation can be overestimated if one doesn't deburst the cell by opening its shutter before starting the growth. Another limitation is the substrate surface quality. As one grows layers in nitrogen rich conditions, the surface roughens. This roughness makes the reflected beam weaker and the oscillation pattern more difficult to observe. Growth of GaN under Ga rich condition can be done in order to recover the surface. However, in the case of AlN, it is more difficult to smooth the surface.

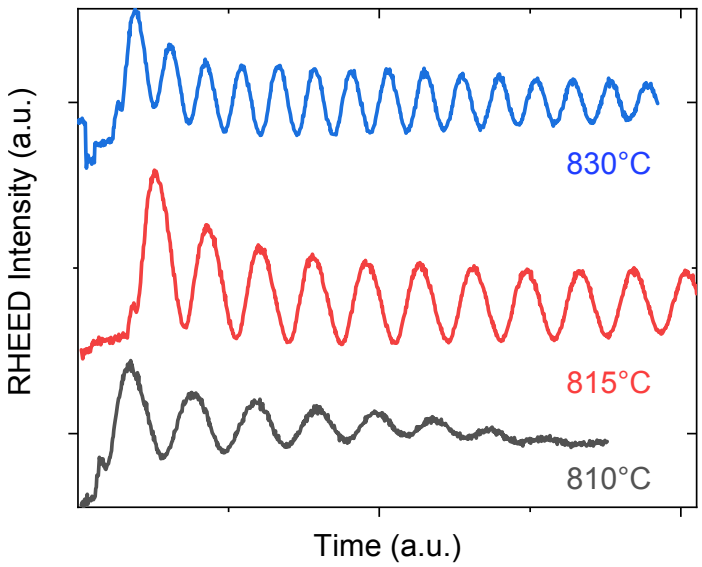

Figure A.2: RHEED oscillations during the growth of GaN layers for three different gallium cell temperatures.

Another technique can be used to calibrate the cells. In order to be closer to growth conditions of thick layers, one can grow a rather thick layer at a given cell temperature and measure its thickness afterwards, by SEM or X-ray diffraction. By doing so, surface roughness and N-rich conditions don't matter anymore and the calibration is done in a steady state.

A.2 Substrate temperature calibration with surface reconstructions

Substrate temperature in measured by a thermocouple facing the rear face of the Si wafer but not touching it directly. Temperature readout can be altered if the thermocouple moves away from the wafer for instance after a maintenance of the MBE. To ensure the growth occurs at the desired temperature, grower takes benefit from surface reconstructions of (111)-Si. Atoms at the top of the last mono-layer rearrange in a 7×7 pattern, if the surface is clean and at temperature lower than $\sim$ 860 °C [68]. This sort of sub-lattice has its a surface cell symmetry which is 7 times larger than the Si lattice. Therefore, the diffraction pattern features 7 additional lines. At higher temperature, the reconstruction vanishes and diffraction of the lattice is only seen. Recording the middle lines' RHEED intensity allows to observe their (dis-)appearance and adjust the thermocouple readout so that it matches the reconstruction temperature. Figure A.3b shows the recording of RHEED intensity of the region of interest marked on figure A.3a during cooling and heating of the Si wafer. It is also plotted the first derivative of the curves which allows to clearly see the inflexion point. The average minimum of both derivatives is taken as reference for calibration. On this example, it matches the predicted values at ±5°C.

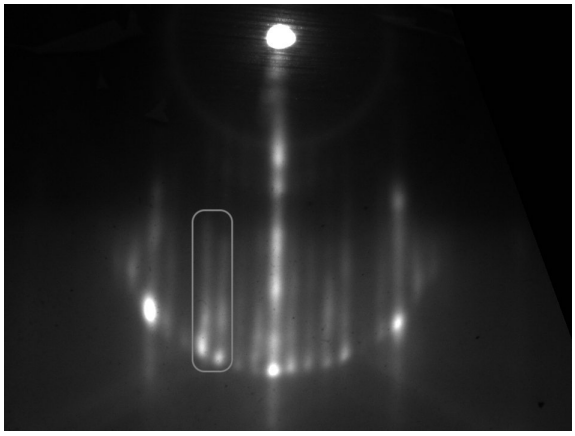

(a) (111)-Si substrate exhibiting a 7×7 surface reconstruction at T_{sub}=820°C. White rectangle shows the region of interest for RHEED intensity recording.

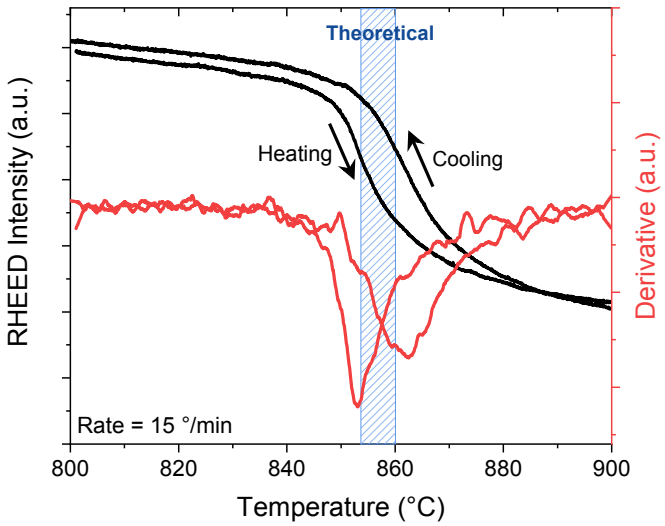

(b) RHEED intensity and its derivative as function of the temperature indicated by the thermocouple. The theoretical values are ranging between 850°C and 860°C.

Figure A.3: Substrate temperature calibration using 7×7 reconstruction of Si (111).

APPENDIX B

Quantification of carrier density

This appendix aims at giving more theoretical and analytical details on the quantification of charge carriers in doped semiconductors, based on the book of David Look [75]. It is ruled by the charge balance equation which states that the number of positive charges and negative charges must be equal:

$$n + \sum_i N_{A,i}^- = p + \sum_j N_{D,j}^+ \tag{B.1}$$

where n (resp. p) is the free electrons (resp. holes) concentration and $N_{A,i}^-$ (resp. $N_{D,i}^+$) is the number of ionized donors (resp. acceptors) of the species i. The intrinsic free carrier concentration n_i will be neglected as it is very small in AlN and GaN ($< 10^{-10}$ cm $^{-3}$). Fermi level position rules which dopant and in which proportion is ionized depending on their relative positions. If a donor energy level is below Fermi level by a few kT, it won't be ionized and if its level is above the Fermi level by few kT thus it will be assumed to be fully ionized. The opposite reasoning stands for acceptor species, giving the following set of equations:

$$\begin{cases} N_D^+ = N_D & \text{if} \quad E_D > E_F \text{ by few } kT \\ N_D^+ = 0 & \text{if} \quad E_D < E_F \text{ by few } kT \\ N_A^- = 0 & \text{if} \quad E_A > E_F \text{ by few } kT \\ N_A^- = N_A & \text{if} \quad E_A < E_F \text{ by few } kT \end{cases} \tag{B.2}$$

In the following is only considered the case of n-type doping of a semiconductor with $n \gg p$, and p will be neglected. Thus, equation B.1 can be expressed as $n+N_A = N_D^+$. Here, as we supposed aa n-doped semiconductor $E_F \gg E_A$ and $N_A^- = N_A$. Since the probability distribution followed by the ionization of dopant follows the Fermi-Dirac distribution, the charge balance can be rewritten as:

$$n + N_A = N_D^+ = \frac{N_D}{1 + \frac{1}{g}\exp\left(\frac{E_D - E_F}{kT}\right)} \tag{B.3}$$

where g is the degeneracy factor usually taken equal to 2 for electrons and 4 for holes.

Then, assuming a Boltzmann statistic, equation B.3 can be transformed using the following equation:

$$n = N_C \exp\left(\frac{E_C - E_F}{kT}\right) \tag{B.4}$$

solving the equation in E_F and replacing the solution in B.3 leads to:

$$n + N_A = \frac{N_D}{1 + \frac{1}{g}\frac{n}{N_C}\exp\left(\frac{E_D}{kT}\right)} = \frac{N_D}{1 + \frac{n}{\phi_D}} \tag{B.5}$$

$$\text{with, } \phi_D = \frac{1}{g} N_C \exp\left(-\frac{E_D}{kT}\right) \tag{B.6}$$

$$N_C = 2\left(\frac{2\pi m_e^* kT}{h^2}\right)^{3/2} \tag{B.7}$$

ending with a second order polynomial in n, which one can solve. The results is:

$$n = \frac{1}{2}(\phi_D + N_A)\left[\sqrt{1 + \frac{4\phi_D(N_D - N_A)}{(\phi_D + N_A)^2}} - 1\right] \tag{B.8}$$

with only few parameters, being m_e^*, N_A, N_D and E_D. In the limit of high temperature, N_C tends to $+\infty$ and so does ϕ_D which allows the expansion of the square root term into:

$$n \simeq \frac{1}{2}(\phi_D + N_A) \cdot \frac{2\phi_D(N_D - N_A)}{(\phi_D + N_A)^2} \simeq N_D - N_A \tag{B.9}$$

meaning that all species are ionized as expected. Calculations in the case of Si doped GaN and AlN are shown below in figure (B.1), taking effective masses of electrons reported in the table B.1, without compensation. It highlights the difficult ionization of Si donors in AlN because of its large ionization energy compared to GaN.

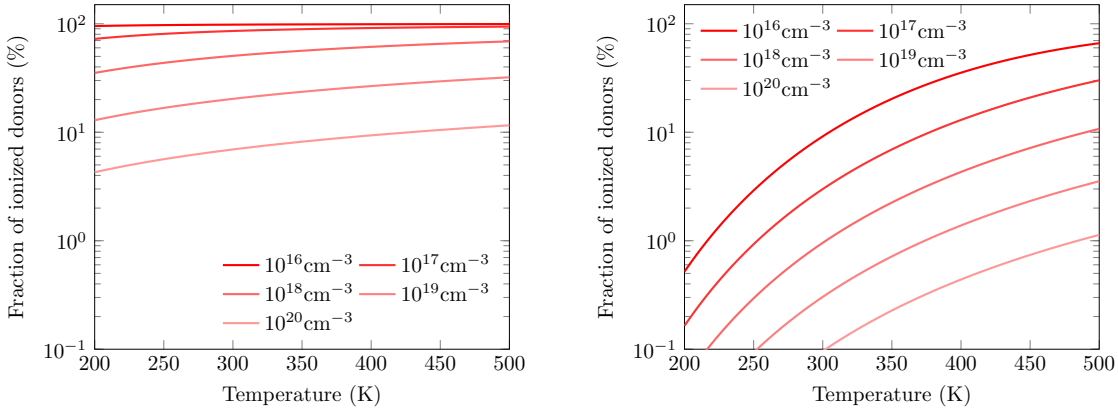

(a) GaN:Si with $E_D = 20$ meV

(b) AlN:Si with $E_D = 270$ meV

Figure B.1: Comparison of the fraction of ionized donor as function of the temperature for various dopant concentrations. Ionization energies of 20 meV and 270 meV were chosen.

This model can be seen as rather complex already, although it cannot explain the metal non-metal (or Mott) transition observed in degenerated semiconductors. GaN:Si exhibits its transition at [Si] $\sim 10^{18}$ cm^{-3} [78]. One big assumption in this model is to state that the ionization energy is constant with dopant concentration. However, depending on the spatial distribution of the atoms, dopants feel an effective medium different than the one of the pure crystal. Hence, the potential felt by the carrier between atoms is screened, translating into a lower ionization energy, as first demonstrated by *Pearson* et al in 1949 in silicon [249]. Later on, *Gotz* et al. [250] and *Brochen* et al. [100] have highlighted the same dependence in nitrides as:

$$E_D = E_{D0} - \Gamma\left(\frac{2}{3}\right)\cdot\left(\frac{4\pi}{3}\right)^{1/3}\cdot\frac{q^2}{4\pi\varepsilon}\cdot N_D^{1/3} \tag{B.10}$$

where, E_{D0} is the ionization of a single dopant, Γ is the Gamma function and ε is the dielectric constant of the material. It assumes a random distribution of atoms in the volume without any preferential direction. Figure B.2 represents the evolution of the effective ionization energy, according to this model, in the case of Si in AlN at a level of 270 meV pointing towards a metal non-metal transition occurring at several 10^{20}cm^{-3}. Figure B.3 compares the free electron concentration of this system with $N_D = 10^{19}$ cm^{-3} for the different model: without compensation, with a compensation of 10^{18} cm^{-3} and with the dependence of the ionization energy on the doping level. Taking into account this new dependance, the increase can be of more than one order of magnitude.

Table B.1: Effective masses in GaN and AlN used in the computations [229]. Values are in unit of m_0.

m_e^{GaN}	m_h^{GaN}	m_e^{AlN}	m_h^{AlN}
0.2	0.8	0.3	1.3

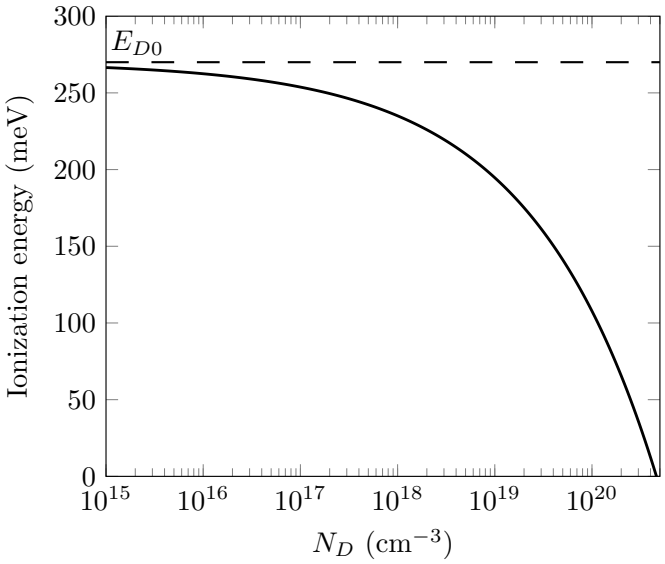

Figure B.2: Evolution of the ionization energy of a donor in AlN as function of its concentration with an base ionization energy of 270 meV as described by equation B.10.

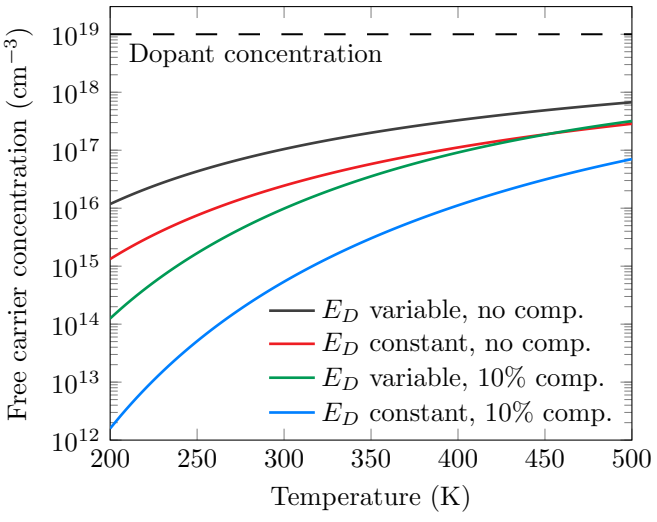

Figure B.3: Calculated free carrier concentration in AlN in various scenarios. E_{D0} of 270 meV and $N_D = 10^{19}\text{cm}^{-3}$ were used.

APPENDIX C

NextNano simulations

NextNano is a company spun out of the Walter Schottky institute of Munich and which develops a software of the same name. It allows the simulation of electronic and optoelectronic devices in order to investigate various properties. The user creates a grid on which is defined a material with its various intrinsic and extrinsic properties.

Different solvers can be used depending the results one wants to obtain. Poisson solver is used in order to solve Poisson's equation:

$$\frac{d^2\phi}{dx^2}(x) = -\frac{\rho(x)}{\varepsilon} \tag{C.1}$$

where ϕ is the potential, x the spatial coordinate, ρ the density of charges, and ε the dielectric constant of the media. It is suited to the simulation of simple band structure with no bias.

Quantum solver is used when one wants to solve Schrodinger's equation:

$$\frac{-\hbar^2}{2m}\frac{d^2\Psi}{dx^2}(x) = E\Psi(x) \tag{C.2}$$

with $\hbar$ the reduced Planck's constant, m the effective mass of the studied particle (electron or hole in our case), Ψ its wave-function and E its energy. This solver is suited to simple structure in which the focus is put on the carriers wave-function location and energy of a particle in a quantum well for instance.

Finally, Current solver is used to compute band structure and current flowing in the device when a bias is applied. It is solving the drift-diffusion current equation:

$$J_n(x) = q\left(\mu_n n(x)F(x) + D_n\frac{dn}{dx}(x)\right) \tag{C.3}$$

with, in the case of electrons, J_n the electron current density, q the electric charge, μ_n the mobility of the electron, n the density of electrons, F the electric field, D_n the diffusion coefficient, ∇n the gradient of the free electron density. These equations, and others, can be solved self-consistently when several are required in the same simulation.

In several parts of my work, *NextNano* simulation were used in order to support hypothesis. In Chapter 4, the simple Poisson solver was used in order to draw the band diagram of the structure in a 1D approximation and in 2D in order to observe the spatial distribution of charges because of Fermi level pinning on the side-walls. In this case the AlN NW was surrounded by *air* and a Fermi level pinning was applied on all NW facets. In Chapter 5 and Chapter 6, Poisson-Current solver was used in order to draw the band diagram of the NW pn-junction at different bias.

If it is a rather user-friendly software, it remains a black box and false results can be easily obtained. Indeed a lot of parameters are input prior to solve the above equations and some of them are not known with accuracy. For instance, solving Schrodinger's equation can be done using different model to approximate the band structure in k-space. One can model CB and VB only or decide to model them in a k.p-6 or k.p-8 bands model. These models rely on dispersion relations, crystal splitting and spin-orbit coupling energies, effective masses in the three directions of space and so on. Therefore, the results can be pretty dependent on unknowns. It is one reason why simulation results were not shown in Chapter 3.

In pn-junction, applying a bias on the structure implies the introduction of other dependencies because drift-diffusion current equation is used. This is highly dependant on the recombination and mobility models used and their parameters. However, since it is used to only qualitatively describe the band structure and not to predict I-V characteristics for instance, the results are not affected very much by these parameters. Figure C.1 shows two band structures of the simulation from Chapter 5 with two different mobility values. This comparison allows to justify the use of such simulation to qualitatively describe the band structure of the device under a bias.

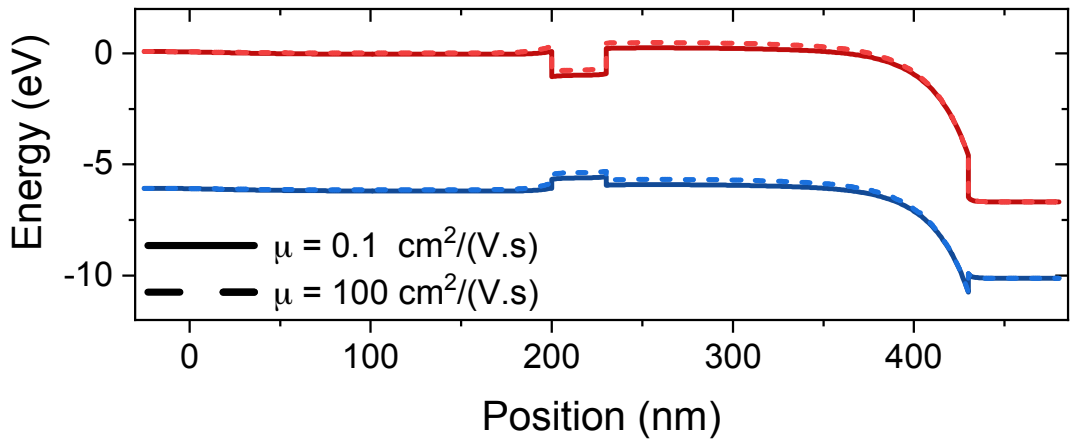

Figure C.1: NextNano simulations of the band diagram of a n-AlN — i-AlGaN — p-AlN — p-GaN structure under a +10 V bias for two mobility values in a constant mobility model. Red: Conduction band. Blue: Valence band.

APPENDIX D

Literature review on transition energy level of AlN:Si

The two following graphs show the same dataset as figure 4.14 but sorted as function of growth technique and substrate used. No trend is observed from the data.

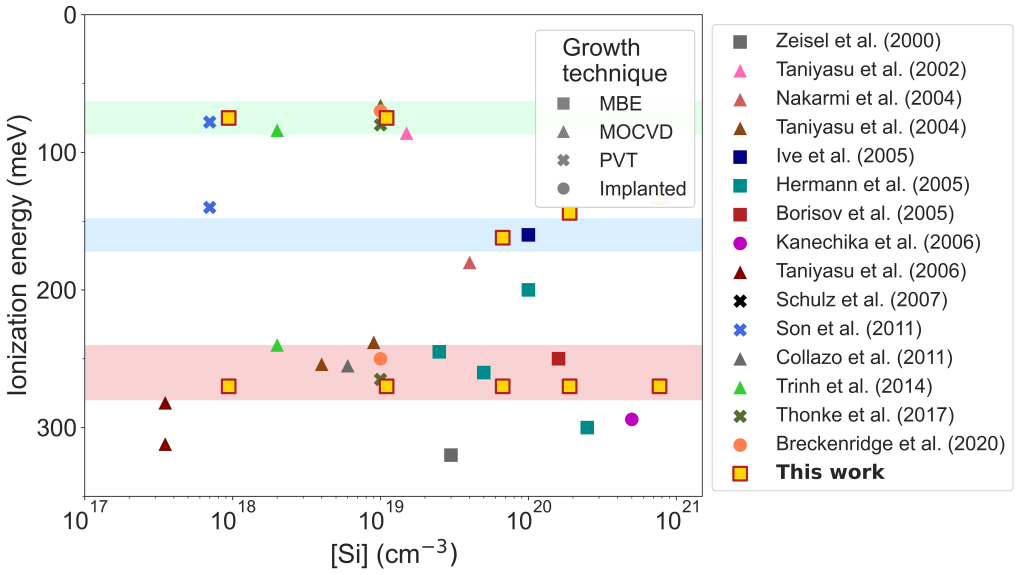

(a) As function of different growth techniques.

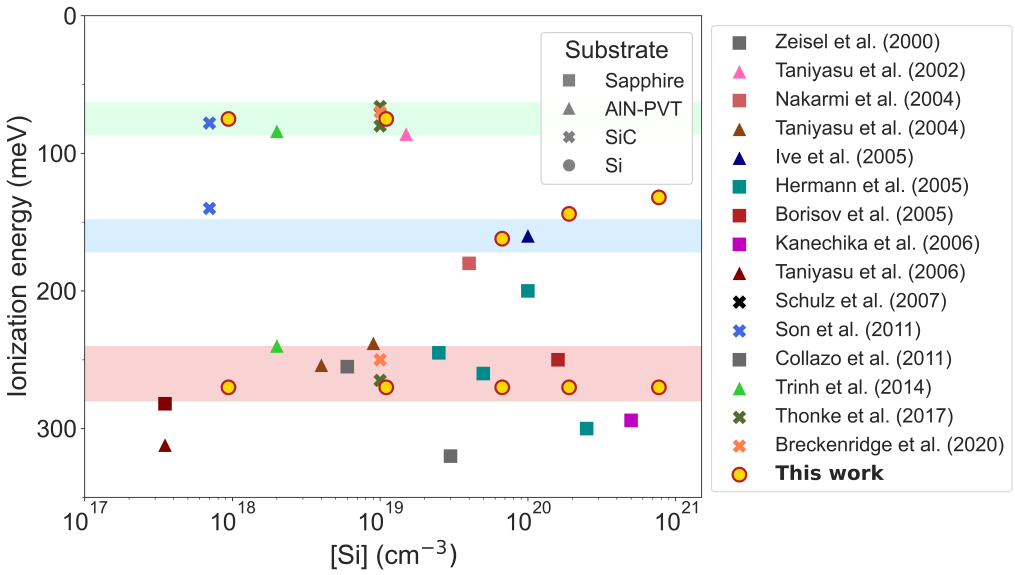

(b) As function of different substrates.

Figure D.1: Review of transition level energies of Si in AlN reported in the literature for various doping levels.

APPENDIX E

Growth on TiN buffer on (111)-Si

Growth of GaN NWs on (111)-Si substrates has its specificities in term of NWs density and diameter. If the grower wants a lower density of NWs, playing on the substrate temperature is often not enough as Ga desorption and GaN decomposition would be too large. However growing on buffer layer gives the opportunity to change few characteristics of the NWs, by acting on the surface diffusion length of adatoms. For instance the growth on AlN buffer layer is used to homogenize the NW orientation perpendicular to the surface, as well as slightly reducing NWs density [251]. Another buffer layer which has been preferred in this thesis is TiN. To do so, several groups inspired the realization of this buffer [56, 252].

First a 5 nm thin Ti layer was deposited on the (111)-Si wafer by electron-beam evaporation. Then the wafer was introduced into the growth chamber and degazed for at least 30 minutes at 300°C. A deoxidation step of 45 minutes at 650°C followed. A first nitridation of the Ti was done during 10 minutes at 450°C and a second one at the growth temperature for another 10 minutes. This nitridation was performed using our RF-plasma cell with a N flux of $\sim$ 0.9 ML/s. If the size of the Ti layer is to thick, and because of the deposition technique, the films roughens and leads to tilted NWs or no growth at all as shown in figure E.1. 5 nm seemed to be a good compromise with uncoalesced and rather straight nanowires (Figure E.2) with adjustable diameter depending on the substrate temperature and Ga flux.

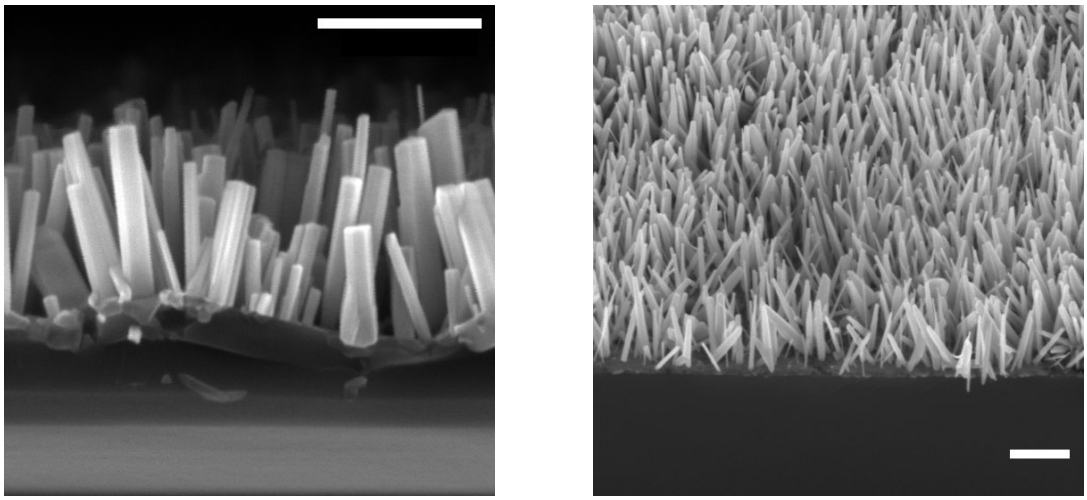

(a) (b)

Figure E.1: GaN NWs grown on (a) 20nm and (b) 50nm thick TiN buffer. Scale bar is 500 nm.

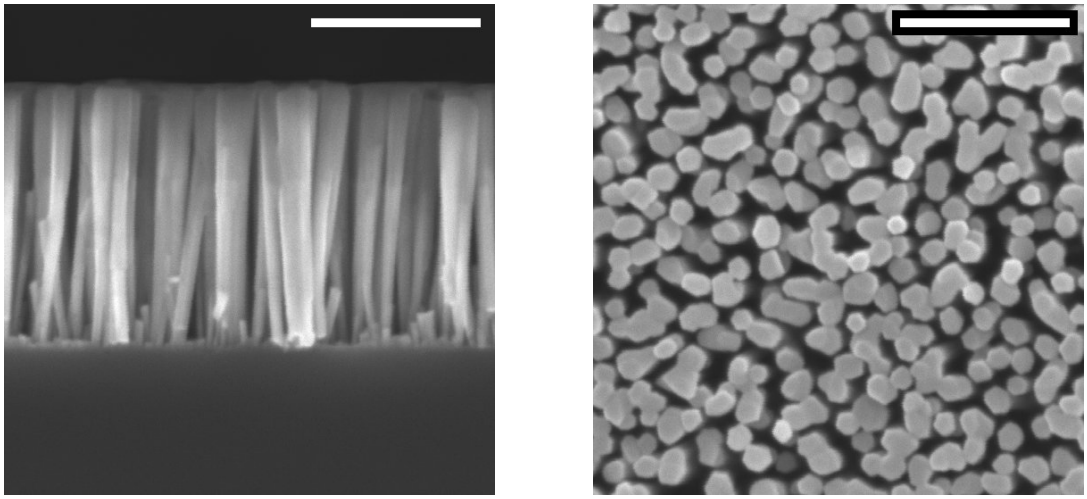

(a) (b)

Figure E.2: SE images of (a) cross sectional and (b) top view of GaN NWs on 5nm TiN buffer. Scale bar is 500 nm.